Particle Acceleration and Detection

Chuan Zhang

Radio-Frequency Quadrupole Accelerators

From Protons to Uranium Ions

Springer

Particle Acceleration and Detection

The series “Particle Acceleration and Detection” is devoted to monograph texts dealing with all aspects of particle acceleration and detection research and advanced teaching. The scope also includes topics such as beam physics and instrumentation as well as applications. Presentations should strongly emphasize the underlying physical and engineering sciences. Of particular interest are

- contributions which relate fundamental research to new applications beyond the immediate realm of the original field of research
- contributions which connect fundamental research in the aforementioned fields to fundamental research in related physical or engineering sciences
- concise accounts of newly emerging important topics that are embedded in a broader framework in order to provide quick but readable access of very new material to a larger audience

The books forming this collection will be of importance to graduate students and active researchers alike.

Chuan Zhang

Radio-Frequency Quadrupole Accelerators

From Protons to Uranium Ions

Springer

Chuan Zhang
GSI Helmholtz Centre for Heavy Ion
Research
Darmstadt, Germany

Institute for Applied Physics
Goethe-University Frankfurt
Frankfurt am Main, Germany

ISSN 1611-1052 ISSN 2365-0877 (electronic)
Particle Acceleration and Detection
ISBN 978-3-031-40966-0 ISBN 978-3-031-40967-7 (eBook)
https://doi.org/10.1007/978-3-031-40967-7

This Springer imprint is published by the registered company Springer Nature Switzerland AG
The registered company address is: Gewerbestrasse 11, 6330 Cham, Switzerland

Paper in this product is recyclable.

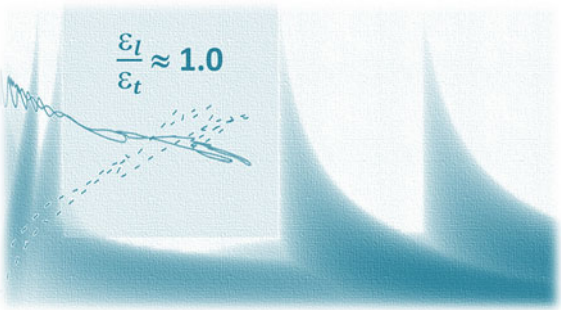
$\frac{\varepsilon_l}{\varepsilon_t} \approx 1.0$

To the memory of Prof. Dr. Horst Klein

Preface

The origins of particle accelerators, which have been developed as essential tools for numerous fields of research, can be traced back to Ising (1924) and Wideröe (1928). In the 21st century, new efforts are being made to keep improving the performance of accelerators for modern applications. An important trend is to increase the beam power even up to the order of megawatts, which can bring challenges caused by space charge effects. As space charge effects are most pronounced in low β (β is the beam velocity relative to the speed of light in vacuum) beams, this book focuses on RFQ (Radio-Frequency Quadrupole) accelerators, which operate as one of the most popular front-end structures for hadron accelerator facilities or as stand-alone machines.

Chapter 1 starts with a broad discussion of high power linacs and their applications, followed by an overview of RFQ accelerators, including historical development, mainstream resonant structures, challenges brought by modern applications, etc.

Chapter 2 is the heart of the book, addressing the physics of beams dominated by space charge effects and presenting efficient solutions for accelerating low-velocity, high-current proton and ion beams with high beam quality. Here "efficient" means as compact as possible accelerating structures with minimum RF power consumption, while "high beam quality" means high beam transmission and low emittance growth. For high power linacs of a new generation, high efficiency is extremely important for saving construction and operation costs, while high beam quality is crucial for ensuring the required availability, reliable operation, and safe hands-on maintenance (beam losses must be minimized in order to limit the activation of accelerator components to a tolerable level).

Coupling between the longitudinal and transverse planes is an important source for space-charge-induced emittance growth in linacs. Different from the usual strategies, which always try to avoid such kind of coupling, a special approach, MEGLET (Minimizing Emittance Growth via Low Emittance Transfer), has been developed to allow and even take advantage of low-level coupling. Under the condition of holding the ratio of longitudinal emittance to transverse emittance in the range of 0.9–1.4, it can achieve minimum emittance growth via two emittance transfers in opposite directions. In addition, another solution, SEGLER (Small Emittance Growth at Large

Emittance Ratios), has been proposed for those cases in which the emittance ratio cannot be held in the optimum range required by the MEGLET approach due to some given conditions. These approaches are not only important for RFQ designs but can also be of use for DTL (Drift Tube Linac) designs.

Chapters 3 and 4 will present some of the RFQ accelerators developed over the past two decades for various facilities of different dimensions (from large scale, e.g., a collider to small scale, e.g., university experimental setups) as real examples for confirming the theory in the second chapter. Among them, some recent RFQs have been designed using the MEGLET or SEGLER approach and some early ones have been revisited according to the new design guidelines. So far, a large part of these machines have been realized and successfully proven by beam experiments or even are in routine operation since many years, e.g.:

- The EBIS-based RFQ for the RHIC collider at Brookhaven National Laboratory.
- The CW HLI RFQ for the GSI Helmholtz Centre for Heavy Ion Research.
- The CW RFQ for the European ADS (Accelerator-Driven System, for nuclear waste transmutation) project MYRRHA.
- The two CW RFQs (in collaboration with Lawrence Berkeley National Laboratory) for the China ADS Injector-II project and the PXIE (now: PIP2IT) project at Fermi National Accelerator Laboratory, respectively.

Furthermore, the electrodes of the new FRANZ RFQ for Goethe University Frankfurt have been manufactured in April 2023 and will see the first beam very likely by the end of 2023.

Chapters 5 and 6 will introduce two new ideas for future development of RFQ accelerators:

- Realizing long RFQ accelerators with the so-called MUSIC (MUltiple Shorter and Independent Cavities) concept. As well known, RF tuning for long RFQs is always very demanding. Benefiting from the MEGLET and SEGLER approaches, the MUSIC concept solves the matching problems between RFQ cavities so that it is feasible to realize long RFQs consisting of short cavities with high efficiency and high beam quality.
- Frequency jump using very high frequency (e.g., 704.4 MHz) RFQ and CH (Crossbar H-mode)-DTL cavities, which is not only efficient to provide a smooth frequency jump at relatively low velocities (e.g., $\beta = 0.2$, compared to typical transition velocities for frequency jumps of $\beta = 0.4$–0.6) but also suitable for shortening large-scale linacs considerably.

It is worth mentioning that the presented RFQs cover wide ranges of different parameters, e.g.

- *Particle species*: From protons to uranium ions.
- *Resonant structures*: 4-rod, 4-vane, and IH (Interdigital H-mode).
- *Resonant frequency*: From $f = 36.136$ MHz to $f = 704.4$ MHz.
- *Duty cycle*: From $< 0.1\%$ to 100%, i.e., CW (Continuous Wave).

- *Peak beam current*: Proton beams up to 105 emA (pulsed) or 20 emA (CW), and heavy ion beams up to 20 emA (pulsed) or 5 emA (CW).
- *Beam velocity*: From $\beta = 0.0022$ to $\beta = 0.2$.

In addition, the presented studies have explored many limits from different aspects, e.g.:

- *Very long RFQs*: Single-cavity and MUSIC designs have been developed for one > 9-m-long IH RFQ and one > 6-m-long 4-rod RFQ.
- *RFQs with extremely high reliability*: For the ADS application, only very few short beam trips will be allowed (due to the coupling of the accelerator with a reactor), which is two to three orders of magnitude less than the operation performance of existing accelerators. Two CW RFQ accelerators have been successfully realized for the European ADS project MYRRHA (4-rod) and for the China ADS project (4-vane), respectively.
- *Very high frequency as well as very high β CW RFQ*: For the frequency jump study, an $f = 704.4$ MHz, $\beta = 0.2$ RFQ has been proposed (RFQs are typically operating at frequencies $f \leq 400$ MHz and $\beta \leq 0.08$). Since all dimensions of the cavity become very small at this frequency, there are many challenges to develop this 5 emA, CW RFQ that requires efficient water-cooling but allows no beam losses. For the output beam velocities of proton and ion RFQs, $\beta = 0.2$ (~20 MeV/u) is a value much larger than ever before (e.g., the β value for the 6.7 MeV LEDA RFQ is only 0.12).
- *Very high frequency normal-conducting/superconducting CHs*: Up to now, the highest frequency of the constructed CH cavities is 360 MHz. The 704.4 MHz, CW CH also proposed for the frequency jump study is a test bed for many new methodologies, e.g., the additive manufacturing (3D-printing) technology.

This book is based on the author's habilitation (a qualification for professorship in many European countries) monograph, "Beam Physics and Techniques towards Efficient Linear Accelerators with Space Charge Challenges", which was submitted to the Department of Physics, Goethe-University Frankfurt, in 2022. As a complement to existing books on accelerators and beams, e.g., "RF Linear Accelerators" (Wangler, Wiley-VCH, 2008), "Theory and Design of Charged Particle Beams" (Reiser, Wiley-VCH, 2008), and "Space Charge Physics for Particle Accelerators" (Hofmann, Springer, 2017), this book will be a helpful reference for researchers and graduate students interested in RFQ accelerators and space charge physics in low-velocity beams.

Darmstadt, Germany Chuan Zhang
June 2023

Acknowledgements

My sincere thanks go to Prof. Dr. Holger Podlech for encouraging me to complete this monograph. With his continuous support in the last 15 years, I had the opportunities to be involved in various interesting accelerator projects (e.g., MYRRHA and HBS) and to develop new ideas for beam physics and techniques. Otherwise, this monograph would not have been possible.

I am full of gratitude to Eugene Tanke for his very friendly and constant support in the last ten years. We had very nice discussions about all aspects of accelerators: beam dynamics, RF technologies, and operation issues. With his excellent help, many useful tools were developed, which allowed me to have a deep insight into the accelerator physics. Furthermore, he read through all chapters and provided very important suggestions for the improvement.

I am especially grateful to Dr. Rudolf Tiede, who has generously shared his office at IAP, Goethe University Frankfurt, with me for many years. I always benefit from his knowledge and experience about accelerators, especially the KONUS dynamics and the LORASR simulation.

Meanwhile, I would like to thank many colleagues from GSI Helmholtz Centre for Heavy Ion Research, Goethe University Frankfurt, and some other accelerator labs, among them:

- Prof. Dr. Oliver Kester (TRIUMF, Canada), Dr. Udo Weinrich, and Dr. Christina Dimopoulou for their kind support and encouragement.
- Prof. Dr. Alwin Schempp for providing me the chances to design the EBIS-based RFQ and the CW HLI RFQ.
- Prof. Dr. Robert A. Jameson and Prof. Dr. Ingo Hofmann for many inspiring discussions on the Equipartitioning Principle and on Hofmann Stability Charts, respectively.
- Prof. Dr. Ulrich Ratzinger for the valuable discussions on both the HSI RFQ and the FRANZ RFQ.
- Dr. Daniel Koser for the joint efforts in developing a new end-field compensation method for 4-rod RFQs as well as his help with the RF simulation of the 704.4 MHz, CW RFQ in the frequency jump study.

- Nils Petry for his help with the RF simulation of the 704.4 MHz, CW CH in the frequency jump study.
- Dr. Alexander Bechtold (NTG Neue Technologien GmbH, Germany) for sharing with me his experience in accelerator manufacturing.
- Dr. Hartmut Vormann for providing the information about the UNILAC, especially the two constructed HSI RFQs.
- Stefan Wunderlich for the joint efforts in developing a new dipole-compensation method for 4-rod RFQs.
- Dr. Thomas Sieber for the discussions on beam diagnostics.
- Dr. Carsten Mühle for the discussions on magnets.
- Dr. Christian Herr for the discussions on RF systems.
- Dr. Malte Schwarz for his help with my lectures and proseminars at IAP, Goethe University Frankfurt, and the discussions on the TraceWin code.
- Dr. Klaus Kümpel for his contributions to the MYRRHA RFQ project.
- Dr. Dirk Vandeplassche and Dr. Angélique Gatera (SCK-CEN, Belgium) for the discussions about the beam experiments of the MYRRHA RFQ.
- Dr. Jean-Luc Biarrotte and Dr. Frédéric Bouly (CNRS/IN2P3, France) for the information about the MYRRHA main linac.
- Dr. Derun Li, Dr. John Staples, and Dr. Steve Virostek (LBNL, USA) for the collaboration on the development of the two CW RFQs for the China ADS Injector-II project and the PXIE (now: PIP2IT) project, respectively.
- Prof. Dr. Hongwei Zhao (CAS-IMP, China) for inviting me to be a visiting professor from 2010 to 2013 (side activity).
- Dr. Hendrik Hähnel for the benchmark and the beam dynamics simulation of the IH-DTL in the redesign studies of the FRANZ RFQ.
- Michael Kaiser and Dr. Manuel Heilmann for the pleasant coffee time, a continuous power source for brainstorming.

I feel very indebted to my parents Yonglong Zhang and Qun Yao, my wife Lijing, and my children Lide and Lian, who always support me wholeheartedly. Thank you so much for accompanying me to go through the special period of completing my habilitation, which was also a hard time for the whole world (COVID-19). All of you are the fundamental driving force for my acceleration in the research field.

Last but not least, I would like to dedicate this book to my late dearest aunt Mingfang Yao.

Contents

Acronyms and Abbreviations

AC	Alternating Current
ACC, acc	Accelerator (one section of the FSP method), Acceleration (subscript)
ACCT	AC Current Transformer
ADS	Accelerator-Driven System
BEAR	Beam Experiment Aboard a Rocket
BNL	Brookhaven National Laboratory
BPM	Beam Position Monitor
C-ADS	China ADS
CERN	Européen pour la Recherche Nucléaire (European Organization for Nuclear Research)
CH	Crossbar H-mode (DTL)
CHORDIS	Cold or Hot Reflex Discharge Ion Source
CSNS	China Spallation Neutron Source
CW	Continuous Wave
dc	Duty Cycle or Direct Current
DTL	Drift Tube Linac
EBIS	Electron Beam Ion Source
ECR	Electron Cyclotron Resonance (Ion Source)
EP	Equipartitioning Principle or Equipartitioning Procedure
ESS	European Spallation Source
EU	European Union
EUROTRANS	EUROpean Research Programme for the TRANSmutation of High Level Nuclear Waste in an Accelerator Driven System
FAIR	Facility for Antiproton and Ion Research
FNAL	Fermi National Accelerator Laboratory
FRANZ	Frankfurt Neutron Source at the Stern-Gerlach-Zentrum
FSP	Four-Section Procedure
GB	Gentle Buncher (one section of the FSP method)
GSI	GSI Helmholtz Centre for Heavy Ion Research (in German: GSI Helmholtzzentrum für Schwerionenforschung)

HBS	High Brilliance Neutron Source
HLI	Hochladungsinjektor (High Charge State Injector)
HPDL	High Power Driver Linac
HSI	Hochstrominjektor (High Current Injector)
HWR	Half-Wave Resonator
IAP	Institut für Angewandte Physik (Institute for Applied Physics)
IBOF	Transverse offsets of the input beam with respect to (w.r.t.) the ideal beam axis (error studies)
IBRO	Roll-pitch-yaw rotations of the input beam w.r.t. the ideal beam axis (error studies)
IFMIF	International Fusion Materials Irradiation Facility
IH	Interdigital H-mode (DTL)
in, out	Input, output (subscripts)
J-PARC	Japan Proton Accelerator Research Complex
K-T	Kapchinsky-Teplyakov
KONUS	Kombinierte Null Grad Struktur (Combined 0° Structure)
LANL	Los Alamos National Laboratory
LBNL	Lawrence Berkeley National Laboratory
LEBT	Low Energy Beam Transport
LEDA	Low-Energy Demonstration Accelerator
LHC	Large Hadron Collider
Linac	Linear accelerator
LIPAc	Linear IFMIF Prototype Accelerator
LOFF	Transverse offsets of the magnetic lenses w.r.t. the ideal beam axis (error studies)
LORASR	Longitudinale und radiale Strahldynamikrechnungen mit Raumladung (Longitudinal and Radial Beam Dynamics Calculations Including Space Charge)
LROT	Roll-pitch-yaw rotations of the magnetic lenses w.r.t. the ideal beam axis (error studies)
MA	Main Accelerating (one section of the NFSP method)
MAX	MYRRHA Accelerator eXperiment research and development programme
max, min	Maximum, minimum (subscripts)
MB	Main Bunching (one section of the NFSP method)
MBA	Mixed Bunching-Accelerating (one section of the NFSP method)
MEBT	Medium Energy Beam Transport
MEGLET	Minimizing Emittance Growth via Low Emittance Transfer
MINERVA	MYRRHA Isotopes productioN coupling the linEar acceleRator to the Versatile proton target fAcility
MKS	Meter, kilogram, and second (system of units)
MS	Maximum-Separatrix (one section of the NFSP method)
MUSIC	MUltiple Shorter and Independent Cavities
MWS	Microwave Studio (now: CST Studio Suite)

MYRRHA	Multipurpose hYbrid Research Reactor for High-tech Applications
MYRTE	MYRRHA Research and Transmutation Endeavour
n, un	Normalized, unnormalized (subscripts)
NC	Normal Conducting
NFSP	New Four-Section Procedure
NSRL	NASA Space Radiation Laboratory
PARMTEQM	Phase And Radial Motion in Transverse Electric Quadrupoles with Multipoles
PERR	Phase errors for tanks (error studies)
PIP-II, PIP2IT	Proton Improvement Plan-II, Proton Improvement Plan-II Injector Test
PXIE	Project X Injector Experiment
QWR	Quarter-Wave Resonator
R&D	Research and Development
RAON	Rare isotope Accelerator complex for ON-line experiment
RB	Rebuncher
RF	Radio Frequency
RFQ	Radio-Frequency Quadrupole
RHIC	Relativistic Heavy Ion Colliders
RIB	Radioactive Ion Beams
RM	Radial Matcher (one section of the FSP method)
rms	Root mean square
SC	Superconducting
SEGLER	Small Emittance Growth at Large Emittance Ratios
SH	Shaper (one section of the FSP method)
SNS	Spallation Neutron Source
TE	Transverse Electric (resonant mode, also referred to as H-mode)
TEM	Transverse Electromagnetic (resonant mode)
TM	Transverse Magnetic (resonant mode)
ToF	Time of Flight
TOFF	Transverse offsets of the tanks w.r.t. the ideal beam axis (error studies)
TROT	Roll-pitch-yaw rotations of the tanks w.r.t. the ideal beam axis (error studies)
UNILAC	Universal Linear Accelerator
VERR	Voltage amplitude errors for tanks (error studies)
w., w.r.t.	With, with respect to

Symbols

A	Acceleration efficiency or mass number
a	Minimum electrode aperture of a unit cell
a_b	Radius of an unbunched beam of circular cross section
B	Dimensionless quadrupole focusing strength
$\tilde{B}$	Brilliance
C_w	Specific heat capacity of water
c	Speed of light in vacuum
d	Drift length (DTL) or gap spacing (ion source)
E	Electric field
e	Elementary electric charge
E_0	Rest energy of a particle or average longitudinal electric field for an accelerating cell
E_acc	Acceleration gradient
E_k	Kilpatrick limit
$E_\mathrm{s,\,max}$	Maximum surface electric field
E_total	Total oscillation energy (of a simple harmonic oscillator)
F	Force
f	Resonant frequency
$f(p)$	Form factor of the 3D uniform ellipsoid model
H	Height (stems)
$I,\ I_\mathrm{avg},\ I_\mathrm{peak}$	Beam current, average beam current, peak beam current
$I_0,\ I_1$	Modified Bessel function of order 0 or 1
J	Current density (ion source)
k	Phase advance per unit length or $k = \frac{\pi}{L_\mathrm{c}}$
K	Focusing strength
L	Length (if no subscript, it is the RFQ length)
L_c	Cell length
$L_\mathrm{gap,\,entrance}$	Distance between the end wall and the electrodes at the RFQ entrance
$L_\mathrm{gap,\,exit}$	Distance between the end wall and the electrodes at the RFQ exit
L_p	Length of a focusing period

m	Electrode modulation
m_0	Mass of a particle
$\dot{m}$	Water flow rate per cooling channel
N_{channel}	Number of cooling channels
N_{runs}	Ratio of runs in a batch (of simulation)
P_{avg}	Average beam power
P_{c}	RF power consumption
p	Momentum
Q	Charge state
q	Charge
R	rms beam size
R_{o}	Oscillation amplitude
R_{p}	Specific shunt impedance (RFQ)
r	Semi-axes of the 3D uniform ellipsoid model
r_0	Mid-cell electrode aperture
s	Longitudinal position on the beam axis (independent variable)
T	Beam transmission efficiency or transit time factor
t	Time (independent variable)
U	Inter-vane voltage
U_0	Extraction voltage (ion source)
u	Represents x, y, or z (as a subscript, it represents the direction; otherwise, it represents the displacement in that direction)
W	Kinetic energy of a beam
Z_{eff}	Effective shunt impedance (DTL)
Z_{ψ}	Geometric length of the separatrix (longitudinal acceptance)
α_{Twiss}, β_{Twiss}	Twiss parameters
β	Beam velocity relative to c
γ	Lorentz factor
ΔT	Temperature increase
Δ_{rf}	Dimensionless RF defocusing strength
ΔW, dW	Energy spread
$\Delta\varepsilon$	Emittance growth
$\delta\varepsilon$	Additional emittance growth
$\Delta\varphi$, $d\varphi$	Phase spread
ε_0	Permittivity of free space
ε_{l}, ε_{t}	Longitudinal and transverse emittances
ε_{x}, ε_{y}, ε_{z}	Emittances in the x, y, and z phase spaces
η	Beam duty factor
λ	Wavelength in free space
σ_{l}, σ_{t}	Longitudinal and transverse phase advance per focusing period with space charge
$\sigma_{0\text{l}}$, $\sigma_{0\text{t}}$	Longitudinal and transverse phase advance per focusing period at zero current
φ	Initial phase
φ_{exit}	Exit phase

φ_s	Synchronous phase
X	Focusing efficiency
ω_o	Angular oscillation frequency
ω	Angular frequency of the RF field

Chapter 1
Introduction

If there is no solace in the fruits of our research, there is at least some consolation in the research itself. Men and women are not content to comfort themselves with tales of gods and giants, or to confine their thoughts to the daily affairs of life; they also build telescopes and satellites and accelerators and sit at their desks for endless hours working out the meaning of the data they gather.
— Steven Weinberg
[Quote from The First Three Minutes: A Modern View of the Origin of the Universe (1977)]

Abstract Since 1924, particle accelerators have been invented and developed as essential tools for basic research, energy development, medical uses, industrial applications, national security, etc. The saying "everything is difficult at the beginning" can also be applied to accelerators to some extent, as space charge effects are most pronounced in low-velocity beams, especially at high current, which is often required for modern applications. As one of the most popular front-end structures for accelerator facilities, the RFQ accelerator is the focus of this book. This chapter will give a brief introduction to the development of RF linear accelerators as well as the challenges faced by a new generation of RFQ accelerators.

In 1911, Rutherford corrected Thomson's "plum pudding" atom model with the famous gold foil experiment, which used alpha particles emitted from radium bromide as probes for exploring the mysterious subatomic world. Encouraged by this success, Rutherford said to the Royal Society in his presidential address in 1928, "I have long hoped for a source of positive particles more energetic than those emitted from natural radioactive substances".

In the same year, Wideröe realized the first radio-frequency (RF) linac [1], which had been conceived and proposed by Ising in 1924 [2], at RWTH Aachen University in Germany. This linac, a 1 MHz, 25 kV oscillator in an 88-cm-long glass tube, accelerated potassium ions to 50 keV. This energy gain is small from today's point of view, but this attempt opened up an exciting new research field, "particle accelerator physics and technology".

C. Zhang, *Radio-Frequency Quadrupole Accelerators*, Particle Acceleration and Detection, https://doi.org/10.1007/978-3-031-40967-7_1

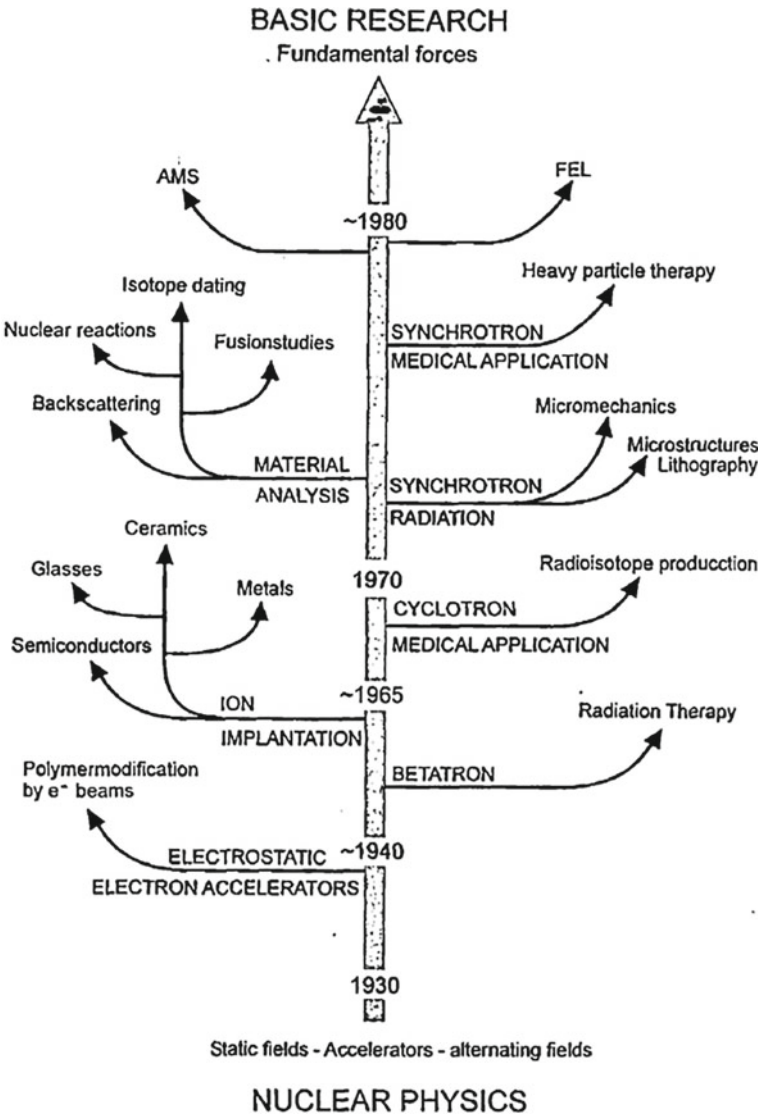

Fig. 1.1 The accelerator development "tree" with applications as "branches" [3]

In Fig. 1.1 published by Bethge in 1999, a brief overview for the development of particle accelerators in the last century is given [3]. He likened the accelerator development to a tree trunk and added many branches to represent the continuously growing number of applications based on particle accelerators (now there are many more applications). It can be seen that basic research has always been the fundamental driving force for the development of particle accelerators.

An interesting study in 2009, "Influence of Accelerator Science on Physics Research" [4], evaluated all Nobel Prize-winning research in physics back to 1939 (in that year, the first Nobel Prize related to particle accelerators was given to Lawrence due to "the invention and development of the cyclotron") and concluded that accelerator science had influenced 28% of physicists as well as 28% of physics research from 1939 to 2009. Today, particle accelerators are still continuing to contribute to the research on the frontiers of science.

1.1 RF Linear Accelerators for the 21st Century

In the 21st century, proton and ion accelerators of a new generation have been built or are being developed worldwide for modern experiments and applications. Many of them have been designed or will serve as drivers for producing various useful secondary particles as shown in Fig. 1.2.

To obtain sufficient secondary particles for required experiments or applications, one of the most remarkable new trends for the R&D of modern accelerators is to provide high power primary beams. The definition of the average beam power is given by Eq. (1.1):

$$P_{\text{avg}} = W I_{\text{avg}} = W I_{\text{peak}} \eta \tag{1.1}$$

where P_{avg} is the average beam power in kW, W is the beam energy in MeV (with the particle charge q included), I_{avg} or I_{peak} is the average or peak beam current in pmA,

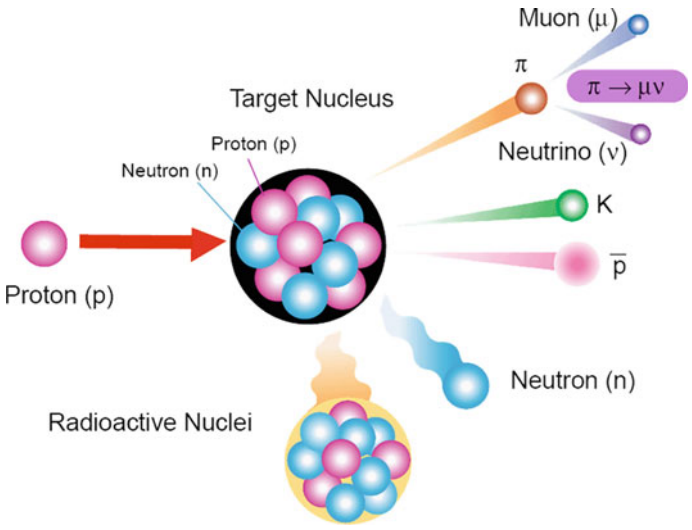

Fig. 1.2 Production of secondary particles with accelerator beams (*graph source* https://j-parc.jp)

Table 1.1 Some representative driver linacs in the world

Linac*	Particle	I_{avg} (emA)	W_{out} (MeV/u)	β_{out}	NC-SC transition β	Duty cycle	Purpose
SNS (Spallation neutron source) [5]	H^-	1.6	1000	0.88	0.55	Pulsed	Neutron production via spallation
CSNS Phase-I [6]	H^-	<1	80	0.39	–	Pulsed	Neutron production via spallation
ESS [7]	H^+	2.5	2000	0.95	0.41	Pulsed	Neutron production via spallation
MYRRHA# [8]	H^+	4	600	0.79	0.19	CW	Nuclear waste transmutation via Accelerator-Driven System (ADS)
C-ADS Phase-II [9]	H^+	5	500	0.78	0.07	CW & pulsed	Nuclear waste transmutation via ADS
FRIB# [10]	Up to uranium	<1	≥200	0.57	0.07	CW	Production of radioactive ion beams (RIB)
RAON# [11]	Up to uranium	<1	200	0.57	0.07	CW	RIB production
SPIRAL2# [12]	Up to $A/Q = 3$	5	20	0.2	0.04	CW	RIB production
PIP-II [13]	H^-	<1	800	0.84	0.07	CW & pulsed	Neutrino/muon factories
IFMIF [14]	D^+	125	20	0.2	0.07	CW	Fusion materials irradiation
J-PARC [15]	H^+	~1	400	0.71	–	Pulsed	Multi-purpose facilities
HIAF-iLinac# [16]	Up to uranium	~1	17	0.19	0.03	CW	Multi-purpose facilities

*: the linacs with the names in italic are under construction; otherwise, they are existing
#: the data are for the cases with the highest beam power

and η is the beam duty factor. As $q = eQ$ with e being the elementary electric charge and Q being the charge state, the beam current in Eq. (1.1) is the particle current in pmA, not the electric current in emA. The relationship between the particle current and the electric current is I (pmA) $= I$ (emA)/Q.

This book focuses on proton and ion linacs (electron linacs are out of the scope for the following discussions), so hereinafter the word "linacs" always refers to as "proton and ion linacs". Table 1.1 lists some representative modern linacs, where β is the beam velocity relative to the speed of light in vacuum c. If a machine has no data in the column "NC-SC transition β", it is a full normal conducting (NC) one; otherwise, it uses a mixture of NC and superconducting (SC) cavities.

An overview for the beam power of the above-mentioned linacs (also including some other well-known linacs) is given in Fig. 1.3. To avoid a too crowded plot, only the machines with an output beam velocity of $\beta_{out} > 0.1$ are shown.

It can be seen that the average beam power P_{avg} values of the linacs for the IFMIF, China ADS (C-ADS) Phase-II, MYRRHA, SNS, and ESS projects are beyond 1 MW (the C-ADS driver linac is even aiming to reach 10 MW in Phase III [9]). The

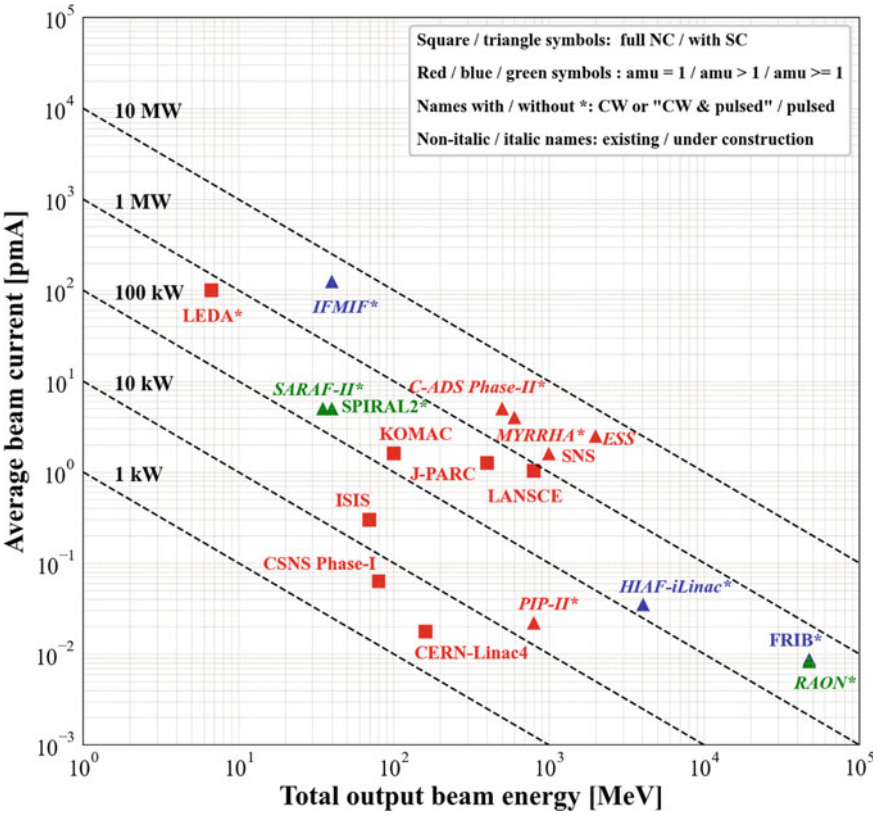

Fig. 1.3 Beam power of some representative driver linacs ($\beta_{out} > 0.1$) in the world

schematic layouts of these high power driver linacs (HPDL) are plotted in Fig. 1.4, where the first MW-class linac in the world, i.e., the LAMPF (now: LANSCE [17]) linac with $P_{\mathrm{avg}} = 0.8$ MW is also shown for a comparison. Except the LAMPF linac realized in the last century is a full NC machine, all the newer HPDLs use a mixture of NC and SC cavities. One trend for the HPDL development is to continuously lower the NC-SC transition β. Thanks to the superconducting RF technology, the beam power of a modern HPDL can be increased with a dramatically shortened overall length (see the beam power and overall length values in Fig. 1.4). For all these modern HPDLs, an NC radio-frequency quadrupole (RFQ) accelerator has been adopted as the injector structure. This is because the beam physics is usually most complicated at the low energy end of an HPDL and beam losses are difficult to be completely avoided inside the RFQ, especially at high current (see Sect. 1.3).

More generally, Fig. 1.5 shows a schematic layout of a typical modern HPDL, which can be roughly divided into the following three parts:

- Very low β (0.01 ~ 0.1): the NC RFQ accelerator is a kind of dominating injector structure in this part.
- Low and medium β (0.1 ~ 0.5): different combinations of various NC and SC drift-tube linac (DTL) structures, e.g., Alvarez-type DTL, H-type structures, Half Wave Resonator (HWR), Quarter Wave Resonator (QWR), and spoke cavities can be used.
- High β (>0.5): the SC elliptical cavity is a popular structure for this part (some HPDLs, e.g., MYRRHA and ESS will also use double-spoke cavities for the transition from low and medium β to high β).

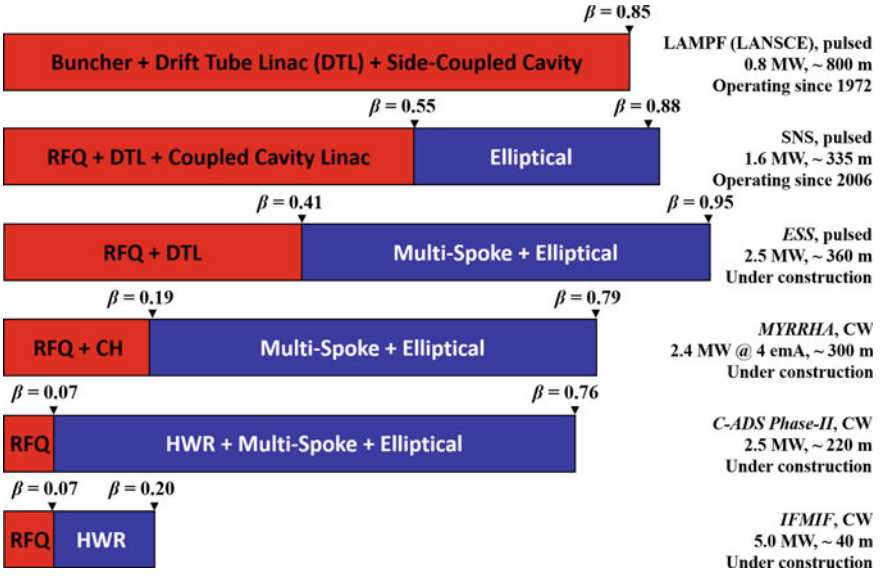

Fig. 1.4 $P_{\mathrm{avg}} \geq 0.8$ MW driver linacs (the bar length is scaled by β, not by the machine length)

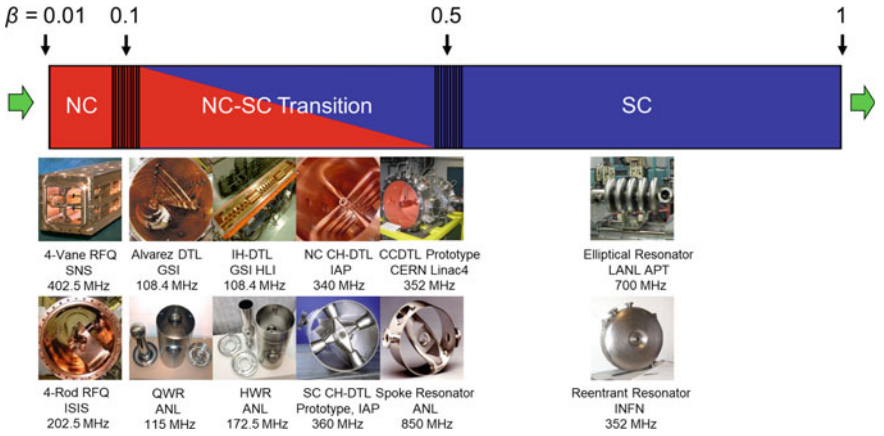

Fig. 1.5 Typical layout of a modern large-scale HPDL with different kinds of RF structures for different β ranges

1.2 Radio-Frequency Quadrupole Accelerators

Figure 1.6 shows a schematic plot of the typical front end of a modern proton or ion linac. For most cases, the beam energy at the exit of an ion source and a low energy beam transport (LEBT) section is $\leq$100 keV/u, i.e., $\beta \leq 0.015$. At 350 MHz, a relatively high resonant frequency for the front end, the length of the first accelerating cell will be $\leq$0.625 cm (for $\beta\lambda/2$ structures) or $\leq$1.250 cm (for $\beta\lambda$ structures). If one directly applies a DTL as the first accelerating structure, the entrance drift tubes would be too short to be physically constructed and to be easily cooled if the duty cycle is high.

Furthermore, according to the Lorentz force equation, Eq. (1.2), the magnetic force is proportional to the particle velocity and the electric force is velocity-independent. Even if quadrupole magnets can be integrated into such small drift tubes, they cannot provide sufficient focusing to overcome the RF defocusing effect and the space charge effects, especially at high beam current.

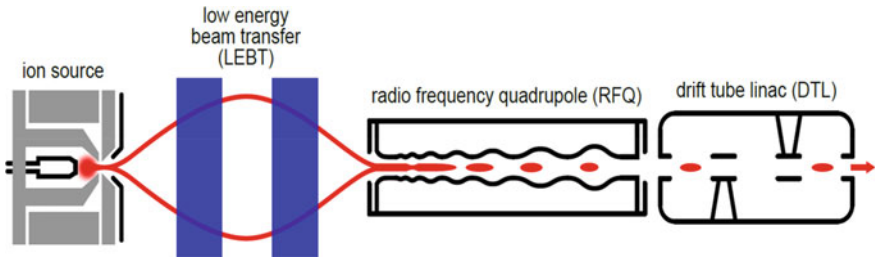

Fig. 1.6 Schematic plot of the typical front end for modern proton and ion linacs (graph from [18] with small modifications)

$$\boldsymbol{F} = q\,(\boldsymbol{E} + \boldsymbol{v} \times \boldsymbol{B}) \tag{1.2}$$

In addition, to convert a dc beam provided by an ion source to a bunched input beam required for the acceleration in a DTL, a single-gap RF cavity or a double-harmonic bunching system was often used (before 1980s), but there were many limitations, e.g., low bunching efficiency and low reliability, especially at high current [19].

The "missing link" between the ion source and the DTL was not filled until the invention of the RFQ accelerator by Kapchinsky and Teplyakov (K-T) in 1968 (formally published in 1969 [20]). A brief history for the development of the RFQ accelerators is given in Table 1.2.

Different from Paul's RFQ trap with four unmodulated electrodes for mass separation [32], the RFQ accelerator has a quasi-periodic modulation of the electrodes

Table 1.2 Milestones in the RFQ development

1960s	Kapchinsky conceived the first idea to modulate an RF electric quadrupole and to add a longitudinal field component for bunching and acceleration [19]
1968–1969	A double-H resonator was invented by Teplyakov to drive "Kapchinsky's electrodes" and the first paper introducing the RFQ accelerator was published by K-T (in Russian) [20]
1972	First beam was accelerated by the Demo RFQ at Institute for High Energy Physics, Protvino (148.5 MHz, 0.0025% dc, 100–620 keV, ~200 emA, H^+) [21]
1977	The RFQ concept was introduced to LANL [19]
1980	The Proof-of-Principle 4-vane RFQ (425 MHz, ~5% dc, 100–640 keV, 38 emA, H^+) was developed as the first RFQ outside of Soviet Union [22]
1980–1983	The "Proton Model" RFQ using a split-coaxial resonator was operated with beams at IAP, Goethe University (54 MHz, CW, 2.4–55 keV, <1 emA, H^+) [23]
1982–1983	The first 0-mode-$\lambda/2$ rod-type RFQ was operated with beams at IAP, Goethe University (108.5 MHz, CW, 10–360 keV, 0.5 emA, H^+) [23, 24]
1982	The first acceleration of heavy ions was done by the "LITL" 4-vane RFQ in Japan (100 MHz, CW, 5–138 keV/u, 4 emA, $A/Q < 7$) [23]
1989	The "BEAR" RFQ was operated with beams in sub-orbital flight (425 MHz, <1% dc, 0.03–1 MeV, 20 emA, H^-) [25]
1993	The CERN RFQ2 with > 200 emA was installed for Linac2, the former injector to the LHC [26] (202.56 MHz, < 1% dc, 90–750 keV, H^+) [27]
1998	The > 9-m-long HSI RFQ was built for GSI (36 MHz, ≤20 emA, ≤25% dc for $A/Q \leq 26$ and <1% dc for $A/Q > 26$, H^+ to U^{4+}) [28]
1999–2000	The most powerful RFQ in the world, "LEDA", was built and tested (8 m long, 350 MHz, CW, 75 keV–6.7 MeV, 100 emA, 670 kW, resonantly coupled, H^+) [29]
2000	Two SC RFQs were tested at liquid helium temperature at INFN (4-rod Nb-Ti resonator, 80 MHz, CW, 37.1–585.4 keV/u, very low current, heavy ions) [30]
2018	Beam commissioning of a very high frequency RFQ for particle therapy (750 MHz, very low dc, 0.04–5 MeV, 250 eμA, H^+) [31]
2019–2021	Beam commissioning of the longest RFQ in the world, "IFMIF-LIPAc", (9.78-m-long, 175 MHz, CW, 0.1–5 MeV, 125 emA, D^+) [14]

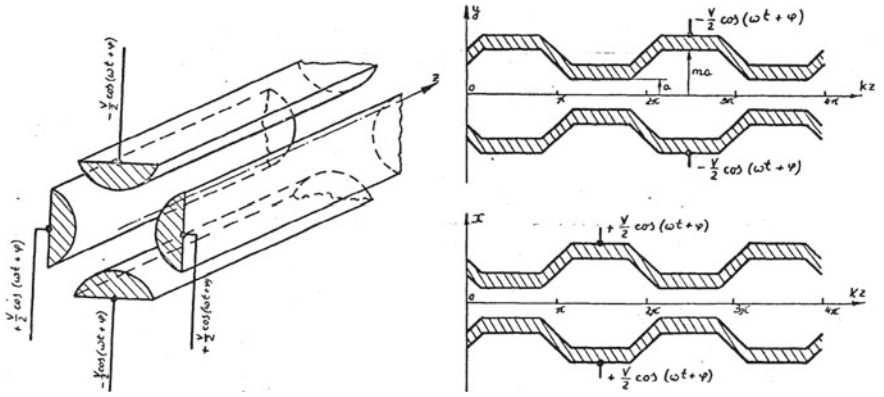

Fig. 1.7 RFQ electrodes without (left) and with (right) modulation (graphs from the first RFQ publication [20]), where a is the minimum electrode aperture, m is the modulation parameter, and ma is the maximum electrode aperture

along the beam axis so that the longitudinal electric field can be produced while retaining the quadrupole focusing field (as shown in Fig. 1.7).

On the one hand, the velocity-independent electric force is very efficient for focusing very low β beams, and on the other hand, if the modulation parameter and the synchronous phase can be changed properly along the accelerating channel, a progressive bunching and acceleration with high beam transmission and good beam quality is feasible. Therefore, the RFQ accelerator is a kind of ideal structure for simultaneously focusing, bunching, and accelerating low-β (typically 0.01 ~ 0.08) beams only with the RF field, even at high current.

In the last several decades, various resonant structures have been developed for driving the four electrodes. A brief overview of the characteristics of various RFQ resonant structures is given in Table 1.3, where 4-vane and 4-rod are the two kinds of most popular structures.

As shown in Fig. 1.8, the 4-vane structure consists of a cavity loaded with four vane-like electrodes, which divide the cavity into four quadrants. Operated in a TE_{210}-like mode, this kind of cavity excites the transverse electric field near the vane tips and the magnetic field in the quadrants longitudinally. The RF properties of a 4-vane RFQ are determined not only by the electrodes but also by the cavity wall, so this structure is relatively sensitive to mechanical machining errors. Mechanical errors and cavity auxiliaries, e.g., coupler loops, tuners and vacuum ports can cause a quadrupole asymmetry and bring dipole and longitudinal field tilt problems. Therefore, the RF tuning of a 4-vane RFQ is often demanding.

In a 4-vane RFQ cavity, the lowest mode is a dipole mode (TE_{110}-like mode), which has a resonant frequency often close to the required mode, i.e., the lowest-order quadrupole mode (TE_{210}-like mode). In order to enlarge the frequency gap and avoid the mixing of these two modes, various solutions e.g. to strap alternate

Table 1.3 A glance at RFQ resonant structures

Type	Resonant mode	Ion species	Typical f (MHz)	Cavity dimension dependence of f	Variants
4-vane [33]	TE_{210}-like	Mainly light ions	100–400	Mainly on radial dimension	4-vane with windows, 4-chamber, cloverleaf
4-rod [24]	π–0	Light and heavy ions	≤200	Theoretically independent to cavity dimensions	Spiral [34], split-ring, ladder [35]
Interdigital H-type (IH) [28]	TE_{110}-like	Mainly heavy ions	≤100	Mainly on radial dimension	–
Split-coaxial resonator [36]	TEM-like	Mainly heavy ions	≤100	Mainly on longitudinal dimension	–
Double-H [20]	$2 \cdot TE_{110}$-like	Mainly light ions	100–400	Mainly on radial dimension	–

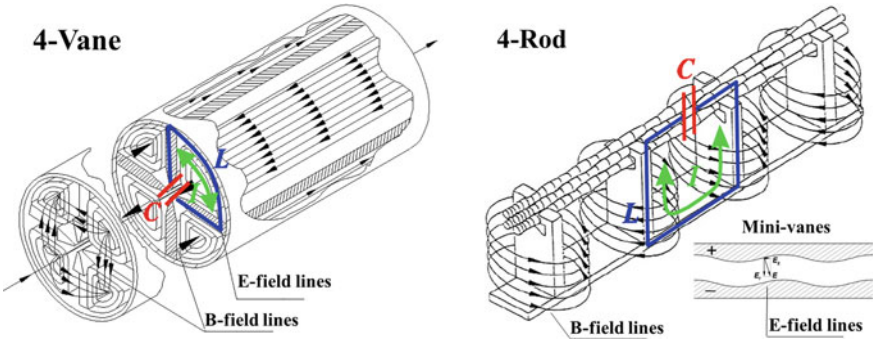

Fig. 1.8 4-vane RFQ and 4-rod RFQ (now often with mini-vane type electrodes) [37]

vane tips together with vane coupling rings [38] or to install π-mode stabilizing loops [39], have been invented.

The longitudinal field tilt sensitivity is proportional to $(L/\lambda)^2$, where L is the RFQ structure length and λ is the wavelength in free space [40–42]. A rule of thumb for the limitation of the RFQ length is as follows [19]:

- $L < 2\lambda \rightarrow$ not a big concern
- $2\lambda < L < 4\lambda \rightarrow$ needs particular care
- $L > 4\lambda \rightarrow$ requires segmentation and resonant coupling.

The resonant coupling technology to separate an RFQ into several individually driven structures and then to couple them together was developed by Los Alamos National Laboratory (LANL) for the construction of the 8-m-long LEDA (Low-Energy Demonstration Accelerator) RFQ [29]. This technology can successfully solve the longitudinal field tilt problem for a long RFQ, but more manufacturing difficulties and costs have to be considered. An alternative solution for realizing long RFQs with multiple shorter and independent cavities will be presented in Chap. 5. This method can provide good longitudinal stability and allow easy RF tuning without additional manufacturing difficulties related to the coupling (more advantages can be found in Chap. 5).

Mainly developed at Goethe University Frankfurt, the 4-rod RFQ can be described as a chain of interlaced $\lambda/2$-resonators in a π-0-mode [43]. This structure has undergone many modifications. The right picture in Fig. 1.8 shows the most popular version, with an equidistant arrangement of straight stems. In 1990s, mini-vane-like electrodes were introduced to replace the original rod shape because of the better water-cooling capability and mechanical stability for working at high beam current and high duty cycle. It can be seen that the resonant frequency of a 4-rod RFQ is mainly determined by its inner structure and theoretically independent from the tank dimensions. This brings the following pros and cons:

- At the same frequency, a 4-rod RFQ, which has only about a half of the radial dimension of a 4-vane one, is more compact.
- Auxiliaries like tuners and RF couplers can be easily added to the vacuum tank.
- It also permits to open a long groove on the cavity wall for making the installation, alignment, and RF tuning conveniently.
- However, under similar conditions, the RF power density is normally approximately 2–4 times higher in case of the 4-rod RFQ, which can bring challenges for CW operation or working at high frequencies, e.g., >300 MHz.

The 4-rod RFQ shown in Fig. 1.8 can be also described by a chain of capacitively shortened $\lambda/4$ transmission line resonators (see Fig. 1.9), in which the voltage distribution along the stem is a quasi-linear function of the height of the stem. Therefore, the height difference between the upper and lower electrodes causes a difference in voltage, i.e., the dipole problem for a 4-rod RFQ.

A natural idea for overcoming this dipole problem is to balance the length difference of the current paths from the ground plate to the electrodes at different heights. As shown in Graph (b) of Fig. 1.10, the classic method is to make a cut between the two "arms" of the stem. In this way, the current path from the ground plate to the upper electrode is shortened, while that to the lower electrode is lengthened. Because tuning plates need to be installed between stems, the size of the cutting angle is limited.

In case the compensation provided by the classic method is not sufficient, the following solutions with the same goal to balance the length difference of the current paths to the upper and lower electrodes can be used (see Fig. 1.10):

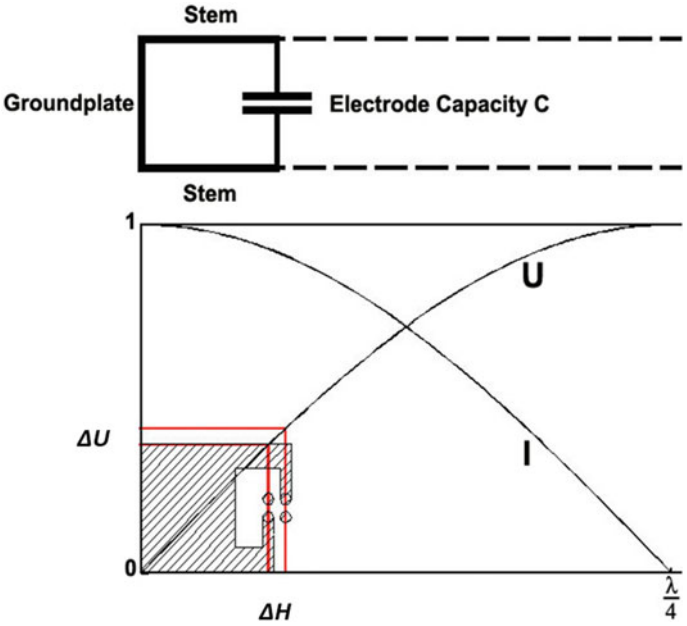

Fig. 1.9 Principle of a capacitively loaded λ/4 transmission line resonator [44]

- A solution developed for the 4-rod version of the 325.224 MHz FAIR p-Linac RFQ [44] by rotating the stem "arms", as shown in Graph (c).
- A solution developed for the MYRRHA RFQ [45] by widening the stem on the lower "arm" side, and Graph (d).
- A solution, which was proposed very recently, by shifting or rotating the top part of the lower "arm" in the plane perpendicular to the stem [46], as shown in Graph (e).

End fields are another problem caused by the asymmetry of a 4-rod RFQ. As shown in Graph (a) of Fig. 1.11, the electrodes mounted on the second to last stem (red) have longer overhangs than those mounted on the end stem (gray), which means the current paths (dashed lines) have different lengths. This can result in non-zero longitudinal electric field components between the electrodes and the end-plates at both the entrance and the exit of a 4-rod RFQ (see the left graph in Fig. 1.12). These unwanted end fields can change the nominal beam properties, e.g., energy and can cause mismatching problems. This has been a known problem for a long time but was not paid enough attention to in the past. For high power linacs, especially when there are superconducting accelerating structures downstream of a 4-rod RFQ, this issue has to be addressed.

The end fields at the entrance and exit gaps of a 4-rod RFQ can more or less change the beam energy. If the deviation from the nominal output energy exceeds the longitudinal acceptance of the following DTL linac, significant beam losses can

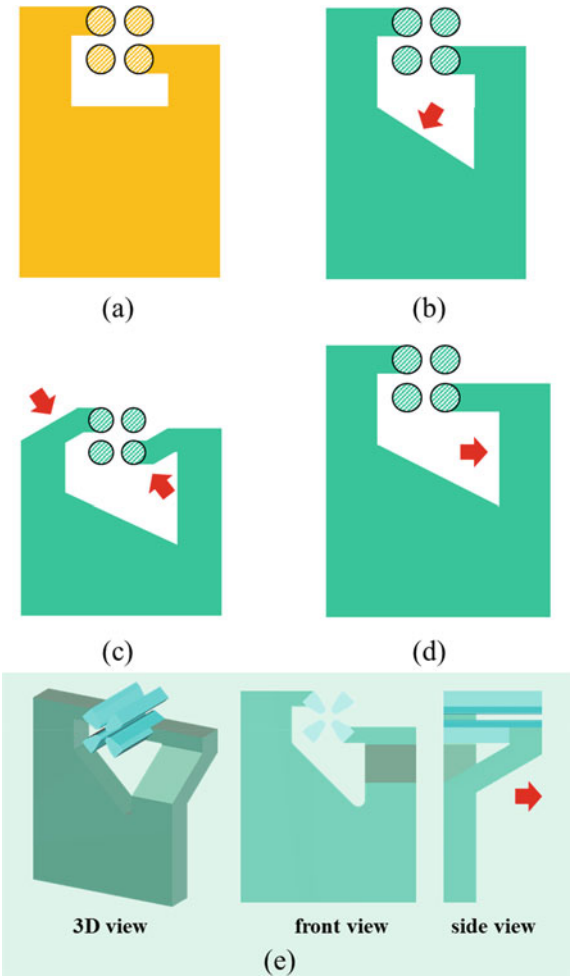

Fig. 1.10 Dipole problem for 4-rod RFQs: **a** stem without dipole optimization; **b** classic dipole optimization method; **c** method proposed for the 4-rod version of the FAIR p-Linac RFQ [44]; **d** method used for the MYRRHA RFQ [45]; **e** solution by shifting or rotating the top part of the lower "arm" in the plane perpendicular to the stem [46]

occur. For example, tremendous efforts had to be made to correct the output beam energy during the commissioning of the 4-rod RFQ for Fermi National Accelerator Laboratory (FNAL) [48].

Recently, two solutions have been proposed to solve this problem without influencing the beam dynamics itself (no additional drift space at the two RFQ end gaps will be required). As shown in Graph (b) of Fig. 1.11, the first method is based on a principle similar to adjusting the lengths of the current paths (but for the electrodes with long and short overhangs). In Graph (c), a new-type of end stem with inductively coupled side-stems is presented as the second method. Taking advantage of the combination of these two methods, full end-field compensation with preserved shunt impedance can be achieved [47]. Figure 1.12 compares the end fields of a

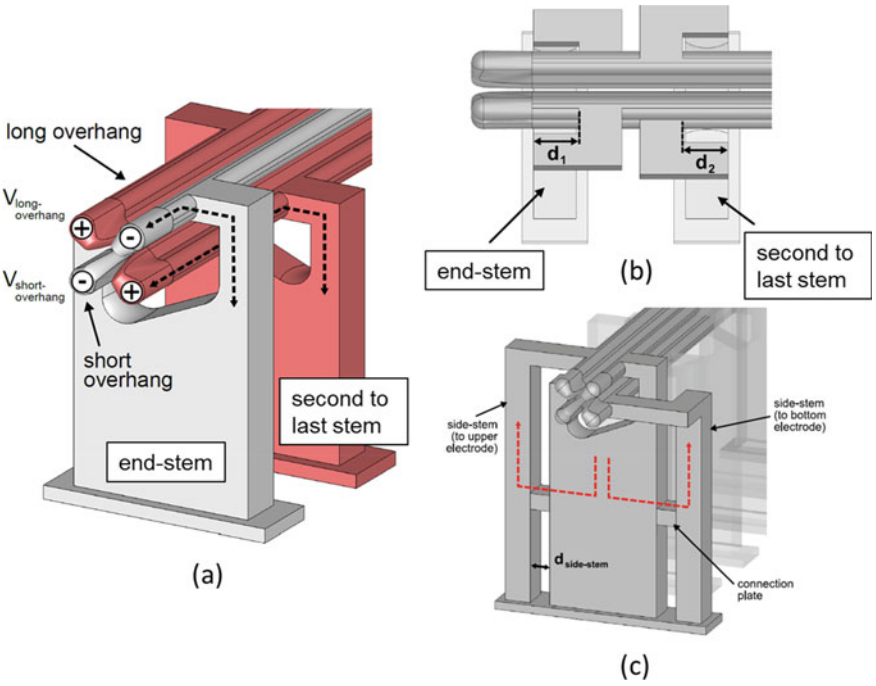

Fig. 1.11 End field problem of 4-rod RFQs: **a** long electrode overhangs are mounted on the second to last stem (red) and short electrode overhangs are mounted on the end stem (gray) with current paths of different lengths (dashed lines); **b** solution 1: to balance the length difference of the current paths by the modified electrode-mounting brackets at the last two stems; **c** solution 2: to use inductively coupled side-stems lateral to the end stem [47]

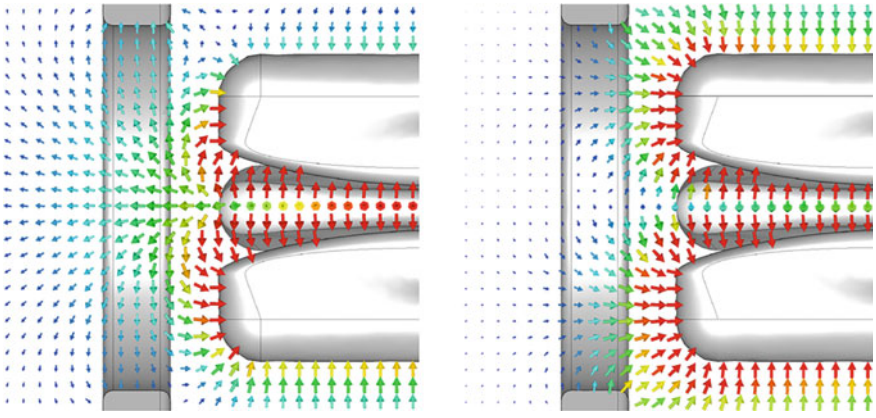

Fig. 1.12 End fields of a 4-rod RFQ before (left) and after (right) optimization [47]

6-stem 4-rod RFQ model (a shortened version of the MYRRHA RFQ) before and after optimization [47].

1.3 Front Ends for High Power Linacs

To reach high beam power, typically there are the following ways to combine the three factors in Eq. (1.1):

- Using high beam energy and high average current (modest peak current and low duty factor): e.g., SNS and ESS.
- Using also high beam energy and high average current (but low peak current and CW mode): e.g., MYRRHA and PIP-II.
- Using low beam energy and very high average current (very high peak current and CW mode): e.g., LEDA and IFMIF.

Increasing the peak beam current will directly bring challenges caused by space charge effects. There are two kinds of space charge forces from the self fields of the charged particles in a beam (see Fig. 1.13):

- The electric force between the particles will lead to a Coulomb repulsion (defocusing) effect.
- The force from the magnetic fields of parallel travelling particles (which can be regarded as parallel currents) can provide an attraction (focusing) effect.

The relativistic form of Newton's second law reads:

$$\boldsymbol{F} = \frac{d\boldsymbol{p}}{dt} = \frac{d\gamma m_0 \boldsymbol{v}}{dt} = \gamma m_0 \frac{d\boldsymbol{v}}{dt} + m_0 \boldsymbol{v} \frac{d\gamma}{dt} \tag{1.3}$$

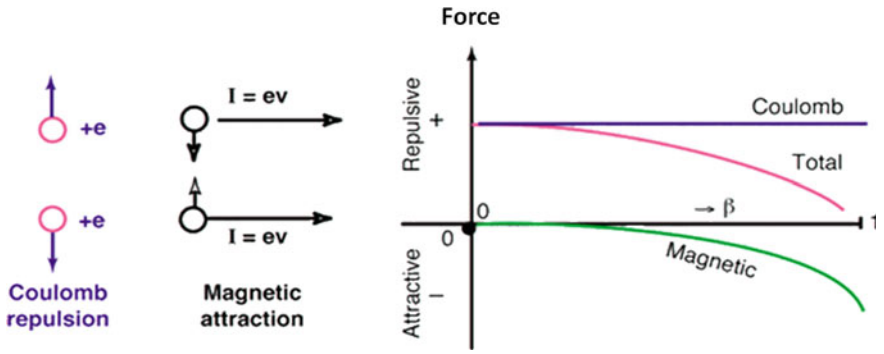

Fig. 1.13 Space charge forces between two equal-charge particles as a function of β [49]

where $\boldsymbol{F}$ is the force; $\boldsymbol{p}$, m_0, and $\boldsymbol{v}$ are the momentum, the mass, and the velocity of the particle, respectively; and $\gamma = \frac{1}{\sqrt{1-\beta^2}}$ is the Lorentz factor. Using the cylindrical-polar coordinates (r, ϕ, z, t), the longitudinal (corresponding to the beam propagation direction) and radial forces can be written as Eqs. (1.4) and (1.5), respectively:

$$\begin{aligned} F_z &= \gamma m_0 \frac{dv_z}{dt} + m_0 v_z \frac{d\gamma}{dt} = \gamma m_0 \frac{dv_z}{dt} + m_0 v_z \beta \gamma^3 \frac{d\beta}{dt} \\ &= \gamma m_0 \frac{dv_z}{dt} + m_0 \beta^2 \gamma^3 \frac{dv_z}{dt} = \gamma^3 m_0 \frac{dv_z}{dt} \end{aligned} \tag{1.4}$$

$$F_r = \gamma m_0 \frac{dv_r}{dt} \tag{1.5}$$

According to the Lorentz force equation, Eq. (1.2), the longitudinal and radial forces can be also written as Eq. (1.6) and (1.7), respectively:

$$F_z = qE_z \tag{1.6}$$

$$F_r = q\left(E_r - v_z B_\phi\right) \tag{1.7}$$

Using Schindl's model, i.e., an unbunched beam of circular cross section (radius a_b) and uniform charge density (a total current of I) moving with constant velocity $v = \beta c$, one can derive the radial electric self field and the azimuthal magnetic self field as Eqs. (1.8) and (1.9) [49]:

$$E_r = \frac{I}{2\pi\varepsilon_0 \beta c} \frac{r}{a_b^2} \tag{1.8}$$

$$B_\phi = \frac{I}{2\pi\varepsilon_0 c^2} \frac{r}{a_b^2} \tag{1.9}$$

where ε_0 is the permittivity of free space.

By substituting Eqs. (1.8) and (1.9) into Eq. (1.7), one gets:

$$F_r = qE_r\left(1 - \beta^2\right) = \frac{qE_r}{\gamma^2} \tag{1.10}$$

In the $(1 - \beta^2)$ term, the "1" represents the electric force which is always defocusing, and the "β^2" represents the magnetic force that can cancel the defocusing effect. The higher the β is, the larger the cancellation will be (see Fig. 1.13). A full cancellation will happen at $\beta = 1$, i.e., $v = c$.

Taking into account Eqs. (1.3)–(1.8) and using u to represent z or r, we may describe the particle motions in both longitudinal and radial directions by the following equation:

$$\frac{dv_u}{dt} = \frac{qE_u}{\gamma^3 m_0} \tag{1.11}$$

It is clear that the space charge effects are proportional to the beam current ($E_u \propto I$) and are most critical in the low-β range. If one includes the influence from accelerator components, e.g., image current, the defocusing effect will be even stronger.

Space charge effects can cause beam quality degradation (e.g., formation of halo particles and emittance growth) and even beam losses. Beam losses may lead to the following problems:

- Damage of accelerator components
- Activation of the machine
- Quenches in superconducting cavities and magnets.

Based on the experience at LANSCE, a commonly used beam loss limit for safe operation (hands-on maintenance) of modern high power linacs is 1 W/m [50].

Increasing the duty cycle will bring another challenge for realizing a high power linac, i.e., the reliability problem. For reliable operation at high duty cycle, especially in the CW mode, the heat load induced by RF power dissipation in NC accelerating structures is a primary concern. For example, Fig. 1.14 shows one connection between a tuning plate and a stem of the SARAF RFQ, which was burnt during the CW operation [51]. For high power linacs, therefore, not only efficient water-cooling concepts but also how to minimize RF power consumption from the physics (both RF structure and beam dynamics) design point of view are important.

RF breakdown is another issue for reliable operation. The maximum achievable electric field as a function of RF frequency was first investigated by Kilpatrick in the 1950s and the results could be expressed as [52]:

Fig. 1.14 One burnt connection between a tuning plate and a stem of the SARAF RFQ [51]

$$f = 1.64E_{\mathrm{k}}^{2}e^{-8.5/E_{\mathrm{k}}} \tag{1.12}$$

where f is the frequency in MHz and E_k is known as the Kilpatrick limit in MV/m. Along with the progress in technologies, e.g., electrode surface processing and vacuum conditions, higher maximum surface electric fields are achievable. For example, up to 2.5 times the Kilpatrick limit is feasible for pulsed operations, according to the operation experience of the CERN RFQ2 [27]. The Kilpatrick factor of the CW LEDA RFQ is 1.8, a safe value proven by experiments and commonly taken as a guideline for operating CW RFQs [29].

However, Fig. 1.15 shows that many beam trips occurred inside the LEDA RFQ [53]. Beam trips are the interruptions of beam delivery to the target. For the ADS application, which requires an extremely high reliability and has a very strict limit on beam trips (e.g., for MYRRHA, only very limited beam trips with a duration longer than 3 seconds are allowed [8]), the accelerator design has to be more conservative.

As a kind of standard injector structure for modern high power driver linacs, the RFQ has a decisive influence on the beam performance of the entire linac. For modern HPDLs, the RFQ often needs to work at both high peak current and high duty cycle, which makes the RFQ design very challenging (see Fig. 1.16):

- As the first accelerating structure, the RFQ has the lowest beam velocity in the entire linac, so it always sees the most pronounced space charge effects.
- Most RFQs are operating at room temperature, so the cooling problem at high duty cycle has to be solved carefully, especially for the 4-rod structure.

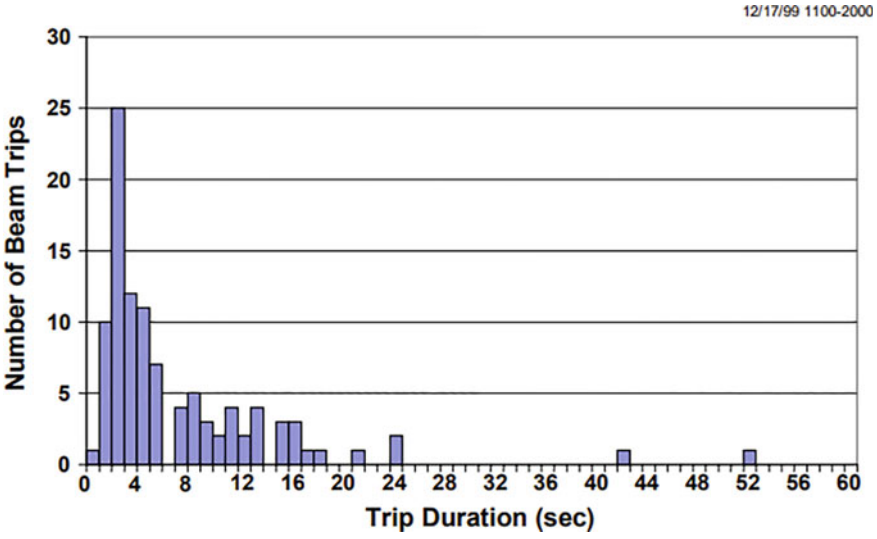

Fig. 1.15 The number of beam trips versus trip duration (data archived in 1 s intervals) for a 9-h CW operation of the LEDA RFQ [53]

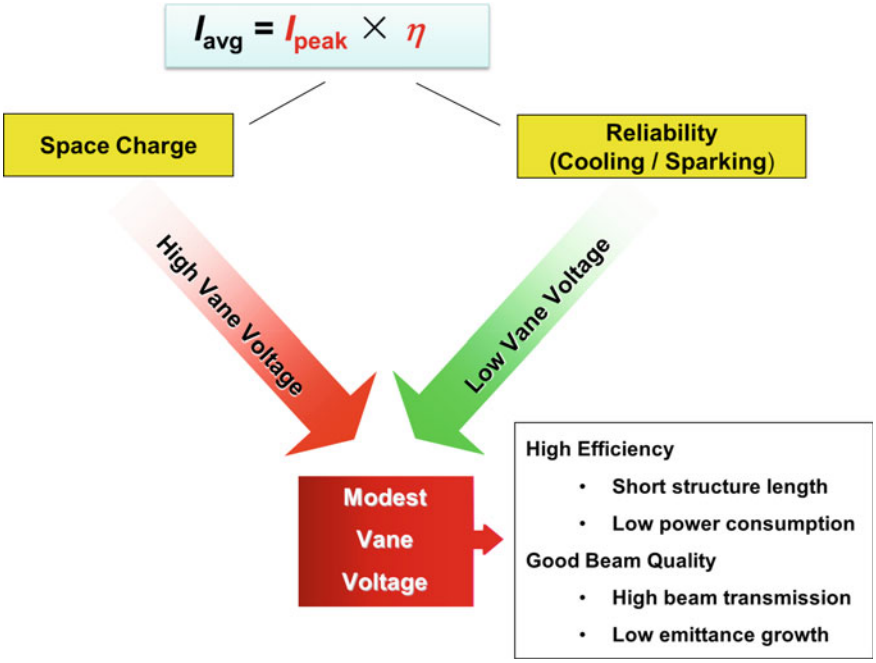

Fig. 1.16 High power challenges for modern RFQ accelerators

- Last but not least, the RFQ has a very small distance between electrodes (typically several mm), so the sparking risk requires great attention in case the inter-vane voltage is high.

To overcome strong space charge effects, a high inter-vane voltage is preferred, but this is not favorable for achieving high reliability. Therefore, to increase the duty cycle will also bring space charge challenges, but indirectly.

This book will present some unconventional beam physics concepts and new techniques developed to realize efficient high current RFQs with high beam quality. So far, there is no clearly defined criterion for "high current". For protons, usually ~100 emA and ~1 emA are considered as high values for I_{peak} and I_{avg}, respectively [54]. For other kinds of ions (with charge state Q and mass number A), the Child–Langmuir law (see Sect. 2.7 or [55]), which shows that the achievable beam current I from an ion source is limited by the extraction voltage U_0 as $I \propto \left(\frac{Q}{A}\right)^{1/2} U_0^{3/2}$ due to space charge effects, might be taken as a scaling law. Usually, input energies, W_{in} ($W_{\mathrm{in}} \propto U_0$), of heavy ion RFQs (typically a few keV/u) are much lower than those of proton RFQs (typically several tens of keV/u). Therefore, several emA and several tens of eμA can be regarded as high I_{peak} and I_{avg} values for heavy ion beams, respectively.

References

1. R. Wideröe, *Über ein neues Prinzip zur Herstellung hoher Spannungen*, vol. 21. Ph.D. thesis, Technischen Hochschule Aachen, Archiv für Elektrotechnik (1928)
2. G. Ising, Prinzip einer Methode zur Herstellung von Kanalstrahlen hoher Voltzahl. Ark. Mat. Astron. Fys. **18**, 30 (1924)
3. K. Bethge, Industrial applications of accelerators. Nucl. Phys. News **9/1** (1999)
4. E. Haussecker, A. Chao, Influence of accelerator science on physics research. Phys. Perspect. **13**, Article Number: 146 (2011)
5. N. Holtkamp, Status of the SNS linac: an overview, in *Proceedings of LINAC* (2004)
6. S.N. Fu, S. Wang, Operation status and upgrade of CSNS, in *Proceedings of IPAC* (2019)
7. I.D. Kittelmann et al., Ionisation chamber based beam loss monitoring system for the ESS linac, in *Proceedings of IBIC* (2019)
8. H. Podlech et al., The MYRRHA-project, in *Proceedings of NAPAC* (2019)
9. S. Fu et al., Chinese plan for ADS and CSNS, in *Proceedings of SRF* (2011)
10. J. Wei et al., The FRIB project – accelerator challenges and progress, in *Proceedings of HIAT* (2012)
11. M. Kwon, Y.S. Chung, Y.K. Kwon, T.S. Shin, Y.U. Sohn, RAON, Korean heavy ion accelerator facility. Kasokuki **17**(4) (2020)
12. T. Junquera et al., Status of the construction of the SPIRAL2 accelerator at GANIL, in *Proceedings of LINAC* (2008)
13. V. Lebedev (ed.), *The PIP-II reference design report*. FNAL report no. FERMILAB-DESIGN-2015-01 (2015)
14. D. Jimenez-Rey et al., Commissioning of test bench at LIPAc accelerator/BI commissioning LIPAc, in *Proceedings of ARIES Workshop* (2021)
15. Y. Liu et al., Progresses of J-PARC linac commissioning, in *Proceedings of the 14th Annual Meeting of Particle Accelerator Society of Japan* (2017)
16. J.C. Yang et al., High intensity Heavy Ion Accelerator Facility (HIAF) in China. Nucl. Instrum. Methods Phys. Res. Sect. B: Beam Interact. Mater. Atoms **317**(Part B), 15 (2013)
17. R.W. Garnett, LANSCE accelerator update and future plans. IOP Conf. Ser.: J. Phys.: Conf. Ser. **1021** (2018)
18. D. Koser, Development of a 108 MHz 4-rod CW RFQ-design for high duty cycle acceleration of heavy ion beams at the GSI-HLI. Ph.D. thesis, Goethe University Frankfurt (2020)
19. M. Vretenar, The radio frequency quadrupole. CERN Accelerator School: High Power Hadron Machines (2011)
20. I.M. Kapchinsky, V.A. Teplyakov, A linear ion accelerator with spatially uniform hard focusing. SLAC report no. SLAC-TRANS-0099 (Transl. T. Watt from Preprint ITEP-673) (1969)
21. N.I. Golosai et al., Tests on the initial section of an accelerator with quadrupole HF focusing (Transl. Soviet Atomic Energy) (1975) (in Russian)
22. R.W. Hamm, K.R. Crandall, C.W. Fuller, RF quadrupole linac: a new low-energy accelerator. LANL report no. LA-UR-80-1091 (1980)
23. H. Klein, Development of the different RFQ accelerating structures and operation experience, in *Proceedings of PAC* (1983)
24. A. Schempp et al., Status of the Frankfurt zero-mode proton RFQ. IEEE Trans. Nucl. Sci. **30**(4) (1983)
25. D. Schrage et al., A flight-qualified RFQ for the BEAR project, in *Proceedings of LINAC* (1988)
26. https://home.cern/science/accelerators/large-hadron-collider
27. E. Tanke, M. Vretenar, M. Weiss, Measurement of the CERN high intensity RFQ, in *Proceedings of EPAC* (1992)
28. U. Ratzinger, K. Kaspar, E. Malwitz, S. Minaev, R. Tiede, The GSI 36 MHz high-current IH-type RFQ and HIIF–relevant extensions. Nucl. Instrum. Methods Phys. Res. Sect. A **415** (1998)
29. L.M. Young, Operations of the LEDA resonantly coupled RFQ, in *Proceedings of PAC* (2001)

30. G. Bisoffi et al., First results with the full niobium superconducting RFQ resonator at INFN-LNL, in *Proceedings of EPAC* (2000)
31. M. Vretenar et al., High-frequency compact RFQs for medical and industrial applications, in *Proceedings of LINAC* (2016)
32. W. Paul, H. Steinwedel, Ein neues Massenspektrometer ohne Magnetfeld. Z. Naturforschung **8a** (1953)
33. R.H. Stokes, K.R. Crandall, J.E. Stovall, D.A. Swenson, RF quadrupole beam dynamics, in *Proceedings of PAC* (1979)
34. R.E. Laxdal, RFQ-IH radioactive beam linac for ISAC. AIP Conf. Proc. **473**, 546 (1999)
35. M. Syha, Beam dynamics design of the FAIR proton-linac RFQ and design study of a compact 325MHz RFQ. Ph.D. thesis, Goethe University Frankfurt (2021)
36. R.W. Müller, Layout of a high-intensity linac for very heavy ions with RFQ focusing. GSI report no. 79-7 (1979)
37. A. Schempp, 4-rod RFQs. Talk at GSI (2008)
38. H. Lancaster, R. Gough, D. Howard, H.R. Schneider, Vane coupling rings simplify tuning of the LBL RFQ accelerator, in *Proceedings of 12th International Conference on High-Energy Accelerators* (1983)
39. A. Ueno, T. Kato, Y. Yamazaki, The π-mode stabilizing loop for four-vane type RFQs, in *Proceedings of LINAC* (1990)
40. D.D. Armstrong, W.D. Cornelius, F.O. Purser, R.A. Jameson, T.P. Wangler, RFQ development at Los Alamos. LANL report no. LA-UR-84-498 (1984)
41. R.A. Jameson, Introduction to RFQ session, in *Proceedings of LINAC* (1984)
42. L.M. Young, Tuning and stabilization of RFQ's, in *Proceedings of LINAC* (1990)
43. A. Schempp, Overview of recent RFQ projects, in *Proceedings of LINAC* (2008)
44. B. Hofmann, Untersuchungen an einem RFQ-Beschleuniger für hohe Betriebsfrequenzen. Diplomarbeit, Goethe University Frankfurt (2004)
45. K. Kümpel, C. Lenz, N.F. Petry, H. Podlech, A. Bechtold, C. Zhang, Dipole compensation of the 176 MHz MYRRHA RFQ, in *Proceedings of IPAC* (2017)
46. S. Wunderlich, C. Zhang, New method for overcoming dipole effects of 4-rod RFQs, in *Proceedings of HIAT* (2022)
47. D. Koser, C. Zhang, H. Podlech, K. Kümpel, A new method to compensate the longitudinal component of the end-fields in 4-Rod RFQ accelerators. Nucl. Instrum. Methods Phys. Res. Sect. A **961** (2020)
48. J.S. Schmidt, B. Koubek, A. Schempp, Simulations on the boundary fields of 4-rod RFQ electrodes, in *Proceedings of IPAC* (2013)
49. K. Schindl, Space Charge. CERN Accelerator School: Intermediate Course on Accelerator Physics (2003)
50. F. Gerigk, K. Bongardt, I. Hofmann, High current linac design with examples of resonances and halo, in *Proceedings of LINAC* (2002)
51. I. Mardor et al., Status of the SARAF CW 40 MeV proton/deuteron accelerator, in *Proceedings of PAC* (2009)
52. T.J. Boyd Jr., Kilpatrick's criterion. Los Alamos Group AT-1 report no. AT-1:82-28 (1982)
53. H. Vernon Smith Jr., J.D. Schneider, Status report on the Low-Energy Demonstration Accelerator (LEDA), in *Proceedings of LINAC* (2000)
54. T.P. Wangler, *RF Linear Accelerators* (Wiley-VCH Verlag GmbH & Co. KGaA, 2008). ISBN: 978-3-527-40680-7
55. M. Reiser, *Theory and Design of Charged Particle Beams*, Second, Updated and Expanded edn. (Wiley-VCH Verlag GmbH & Co. KGaA, 2008). Print ISBN: 9783527407415

Chapter 2
Beam Physics with Space Charge Challenges

Abstract Coupling between the longitudinal and transverse planes is an important source for space-charge-induced emittance growth in linacs. An RFQ accelerator working with low-velocity (typically $\beta = 0.01 \sim 0.08$) beams is an ideal test bench for studying beam physics dominated by space charge effects. This chapter will discuss the physics behind four important design methods for RFQ accelerators.

Two of these methods are already well known:

- The Four-Section Procedure (FSP) originally developed by Los Alamos National Laboratory (LANL) requires constant longitudinal and transverse oscillation frequencies at zero current (space charge forces are neglected).
- The Equipartitioning Procedure (EP) requires constant oscillation energies between transverse and longitudinal degrees of freedom.

The other two methods, which allow and even take advantage of low-level emittance transfer, have been proposed recently:

- The MEGLET (Minimizing Emittance Growth via Low Emittance Transfer) approach tries to hold the ratio of longitudinal emittance to transverse emittance in the range of 0.9–1.4 in order to keep the emittance transfer at low levels and uses two emittance-transfer periods (in which the emittance transfer is in opposite directions) for achieving almost zero net emittance growth.
- The SEGLER (Small Emittance Growth at Large Emittance Ratios) approach is another solution for achieving small emittance growth when a large emittance ratio (beyond the optimum range required for MEGLET) is inevitable due to some given conditions.

2.1 Basic Equations

The essential parts of an RFQ accelerator are the four electrodes, which are surrounding the beam axis and in alternating polarities. Figure 2.1 shows a cross-section view of a pair of adjacent RFQ electrodes and their surface electric-field components schematically, where a is the minimum electrode aperture of a unit cell

C. Zhang, *Radio-Frequency Quadrupole Accelerators*, Particle Acceleration and Detection, https://doi.org/10.1007/978-3-031-40967-7_2

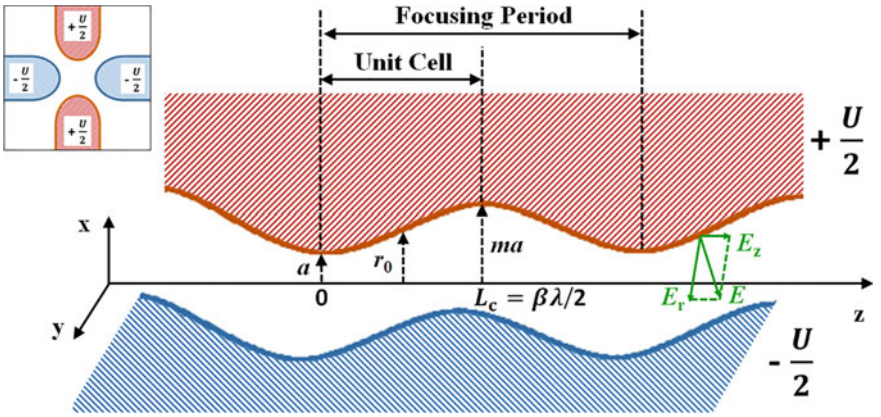

Fig. 2.1 Schematic cross-section view of a pair of adjacent RFQ electrodes and their surface electric-field components

(often abbreviated as "cell"), m is the electrode modulation, r_0 is the mid-cell electrode aperture, $L_c = \frac{\beta\lambda}{2}$ is the cell length, and U is the inter-vane voltage. In different longitudinal positions of the RFQ, one can adjust a, m, U, and the synchronous phase φ_s to adapt the transverse and longitudinal electric-field components for meeting different demands on focusing, bunching, and acceleration, respectively. These are the main parameters to design an RFQ structure.

As RFQs typically work for very low-velocity ($\gamma \approx 1$) beams, it allows describing the motion of a particle with charge q and mass m_0 in all three planes with the following equation:

$$m_0 \ddot{u} = F_{\mathrm{rf},u} + F_{\mathrm{sc},u} \tag{2.1}$$

where $\ddot{u} = \frac{d^2u}{dt^2}$, $F_{\mathrm{rf},u} = qE_{\mathrm{rf},u}$ is the external electric-field force, and $F_{\mathrm{sc},u} = qE_{\mathrm{sc},u}$ is the space-charge force from the self-field of particles (the contribution from the self-magnetic field can be ignored at $\gamma \approx 1$ [1]). In Eq. (2.1) as well as in the following discussions, u represents x, y or z (as a subscript, it represents the direction; otherwise, it represents the displacement in that direction).

Proposed by the RFQ inventors, Kapchinsky and Teplyakov, the well-known two-term potential function is the basics for the RFQ beam dynamics analyses. Using the Cartesian coordinates, it can be written as [2, 3]:

$$V(x, y, z, t) = \frac{U}{2}\left[\frac{X}{a^2}\left(x^2 - y^2\right) + AI_0(kr)\cos(kz)\right]\sin(\omega t + \varphi) \tag{2.2}$$

where $\frac{X}{a^2}\left(x^2 - y^2\right) + AI_0(kr)\cos(kz) = \pm 1$, I_0 is the 0 order modified Bessel function, $k = \frac{\pi}{L_c} = \frac{2\pi}{\beta\lambda}$, $r^2 = x^2 + y^2$, ω is the angular frequency of the RF field, and φ is the initial phase; X is the focusing efficiency defined by:

$$X \equiv \frac{I_0(ka) + I_0(kma)}{m^2 I_0(ka) + I_0(kma)} \tag{2.3}$$

and A is the acceleration efficiency defined by:

$$A \equiv \frac{m^2 - 1}{m^2 I_0(ka) + I_0(kma)} \tag{2.4}$$

Accordingly, the two terms in Eq. (2.2) are called as the quadrupole focusing term and the acceleration term, respectively.

Analytically, the electric-field components can be obtained from the gradients of the potential function as [4]:

$$E_{\mathrm{rf},x} = \left[-\frac{XU}{a^2} x - \frac{kAU}{2} I_1(kr) \frac{x}{r} \cos(kz) \right] \sin(\omega t + \varphi) \tag{2.5}$$

$$E_{\mathrm{rf},y} = \left[\frac{XU}{a^2} y - \frac{kAU}{2} I_1(kr) \frac{y}{r} \cos(kz) \right] \sin(\omega t + \varphi) \tag{2.6}$$

$$E_{\mathrm{rf},z} = \left[\frac{kAU}{2} I_0(kr) \sin(kz) \right] \sin(\omega t + \varphi) \tag{2.7}$$

where I_1 is the modified Bessel function of order 1.

To study the space charge effects in a linac beam bunch analytically, a 3D uniform ellipsoid model with the following linear space-charge electric-field components is often adopted [3–5]:

$$E_{\mathrm{sc},x} = \frac{3}{4\pi\varepsilon_0 c} \frac{I_{\mathrm{avg}}\lambda[1 - f(p)]}{(r_x + r_y) r_z} \frac{x}{r_x} \tag{2.8}$$

$$E_{\mathrm{sc},y} = \frac{3}{4\pi\varepsilon_0 c} \frac{I_{\mathrm{avg}}\lambda[1 - f(p)]}{(r_x + r_y) r_z} \frac{y}{r_y} \tag{2.9}$$

$$E_{\mathrm{sc},z} = \frac{3}{4\pi\varepsilon_0 c} \frac{I_{\mathrm{avg}}\lambda f(p)}{r_x r_y} \frac{z}{r_z} \tag{2.10}$$

where ε_0 is the permittivity of free space, I_{avg} is the average beam current, r_x, r_y, r_z are the semi axes of the ellipsoid, $f(p) \approx \frac{\sqrt{R_x R_y}}{3\gamma R_z}$ is the ellipsoid form factor with R_x, R_y, and R_z as the rms (root mean square) beam sizes, and the semi-axes are related to the rms beam sizes by $r_u = \sqrt{5} R_u$ [3, 4].

Using the longitudinal position on the beam axis s instead of t as the independent variable, we may rewrite Eq. (2.1) as:

$$u'' + K_u u = 0 \tag{2.11}$$

where $u'' = \frac{d^2u}{ds^2}$ and K_u denotes the focusing strength provided by all (external and self-field) applied forces. Equation (2.11) shows that the particle motion satisfies the equation of a simple harmonic oscillator in both transverse and longitudinal planes.

Based on the smooth approximation, the phase advance per unit length k_u, an effective wave number for transverse or longitudinal oscillations, is related to K_u by $k_u = \sqrt{|K_u|}$ and the phase advance per focusing period L_p (for RFQs: $L_\mathrm{p} = \beta\lambda$) is $\sigma_u = k_u L_\mathrm{p}$ [4].

Only considering the external forces, one can get the phase advance per focusing period without space charge from the external electric-field components as:

$$\sigma_{0\mathrm{t}} = \sqrt{\frac{B^2}{8\pi^2} + \Delta_\mathrm{rf}} \tag{2.12}$$

$$\sigma_{0\mathrm{l}} = \sqrt{-2\Delta_\mathrm{rf}} \tag{2.13}$$

where B is the dimensionless quadrupole focusing strength defined by:

$$B \equiv \frac{qXU\lambda^2}{m_0c^2a^2} \tag{2.14}$$

and Δ_{rf} is the dimensionless RF defocusing strength defined by:

$$\Delta_\mathrm{rf} \equiv \frac{\pi^2 qAU\sin\varphi_\mathrm{s}}{2m_0c^2\beta^2} \tag{2.15}$$

For Eqs. (2.12) and (2.13), the subscripts "0", "t", and "l" refer to zero current, the transverse planes (x and y), and the longitudinal plane (z), respectively.

The relationship between the angular oscillation requency $\omega_{\mathrm{o},u}$ and σ_u is [4]:

$$\omega_{\mathrm{o},u} = \frac{\sigma_u c}{\lambda} \tag{2.16}$$

To calculate the phase advance with space charge analytically, one can follow Sacherer's procedure [7] to convert the single-particle equation Eq. (2.11) to the following rms envelope equation:

$$R_u'' + K_u R_u - \frac{\varepsilon_u^2}{R_u^3} = 0 \tag{2.17}$$

where $R_u = \sqrt{\overline{u^2}}$ is the rms beam size, K_u is now the focusing strength for the beam (in the above equation, the external-focusing term and the space-charge term are combined into one for simplifying the analysis), and ε_u is the unnormalized rms emittance defined by $\varepsilon_u \equiv \sqrt{\overline{u^2}\ \overline{u'^2} - \overline{uu'}^2}$. This rms envelope equation is widely applicable for all particle distributions [6]. For matched beams ($R_u'' = 0$) [7], one obtains k_u and σ_u as:

$$k_u = \frac{\varepsilon_u}{R_u^2} \tag{2.18}$$

$$\sigma_u = \frac{\varepsilon_u \beta\lambda}{R_u^2} \tag{2.19}$$

More generally, the phase advance with space charge can be obtained from the beam dynamics simulation with the following definition [4]:

$$\sigma_u \equiv \int_0^{L_p} \frac{ds}{\beta_{\text{Twiss},u}(s)} = \int_0^{L_p} \frac{\varepsilon_u}{R_u^2} ds \tag{2.20}$$

where $\beta_{\text{Twiss},u}$ is one of the Twiss parameters and satisfies $R_u = \sqrt{\beta_{\text{Twiss},u}\,\varepsilon_u}$.

2.2 LANL Four-Section Procedure and New Four-Section Procedure

For designing RFQ accelerators, the "Four-Section Procedure" (FSP) [3] developed by LANL is a conventional technique. As shown in Fig. 2.2, the FSP method divides an RFQ into four sequential sections: Radial Matcher (RM), Shaper (SH), Gentle Buncher (GB), and Accelerator (ACC).

The RM section adapts the time-independent characteristics of a dc input beam from an ion source (or an LEBT) to the time-varying focusing system in an RFQ [8]. Typically several focusing periods long, this section has $\varphi_s = -90°$ (which provides a full 360° phase acceptance [4]) and $m = 1$ (i.e., no modulation). If one increases B according to Eq. (2.21), usually a good radial matching with negligible emittance increase can be reached [9]:

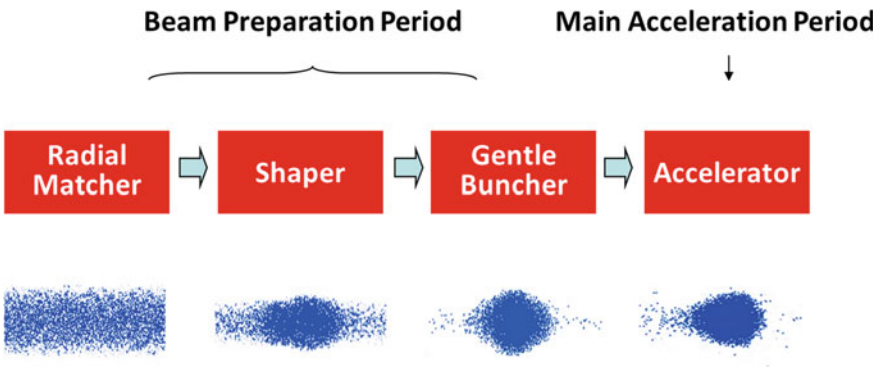

Fig. 2.2 LANL four-section procedure

$$B(s) = B_{\mathrm{RM,out}}\left[\frac{3}{4}\sin\left(\frac{\pi}{2}\frac{s}{L_{\mathrm{RM}}}\right) - \frac{1}{4}\sin\left(\frac{3\pi}{2}\frac{s}{L_{\mathrm{RM}}}\right)\right] \tag{2.21}$$

where L_{RM} and $B_{\mathrm{RM,\,out}}$ are the length and the output B value of the RM section, respectively.

Serving as a non-adiabatic pre-bunching section, the SH section increases φ_{s} and m to the starting values required for the main bunching section as linear functions of s.

The GB section is the "heart" of the FSP method. In order to reach an adiabatic bunching, K-T suggested holding the longitudinal small oscillation frequency of the beam $\omega_{\mathrm{o,1}}$ and the geometric length of the separatrix Z_{ψ} constant [2].

$$\omega_{\mathrm{o,1}} = \text{constant (for GB)} \tag{2.22}$$

$$Z_{\psi} = \text{constant (for GB)} \tag{2.23}$$

From Eqs. (2.13), (2.15), to Eq. (2.16), one can get:

$$\omega_{\mathrm{o,1}}^2 = \frac{\pi^2 q A U \sin(-\varphi_{\mathrm{s}})}{m_0 \beta^2 \lambda^2} \tag{2.24}$$

The definition of Z_{ψ} is as follows [4]:

$$Z_{\psi} \equiv \frac{\psi\beta\lambda}{2\pi} \tag{2.25}$$

where ψ is the phase width of the separatrix and is only related to φ_{s} with $\tan\varphi_{\mathrm{s}} = \frac{\sin\psi - \psi}{1-\cos\psi}$.

However, a bunching process strictly satisfying these two conditions would be slow (see Fig. 2.3). Especially if the GB section is directly started with $\varphi_{\mathrm{s}} = -90°$, it would become infinitely long. That is why the non-adiabatic SH section is needed to ramp φ_{s} and the acceleration efficiency A quickly to suitable values, e.g., $-85°$ ~ $-88°$ and 0.02 ~ 0.04, respectively, for starting the GB section. At the end of the GB section, the beam bunch is maximally compressed longitudinally and the real acceleration is not yet started, so this position would be most important for the space charge effects and could become a bottleneck for the whole RFQ design.

When the bunching is completed, the ACC section in which a, m and φ_{s} are kept constant starts the real acceleration until the required output beam energy is reached.

In addition, the FSP method holds B constant throughout the RFQ channel (except the short RM section) in order to lead to a constant mid-cell aperture r_0, i.e., a position-independent capacitance. This constraint was helpful for simplifying machining and RF tuning (due to the technical limitations at the time when the FSP method was invented).

$$B = \text{constant (after RM)} \tag{2.26}$$

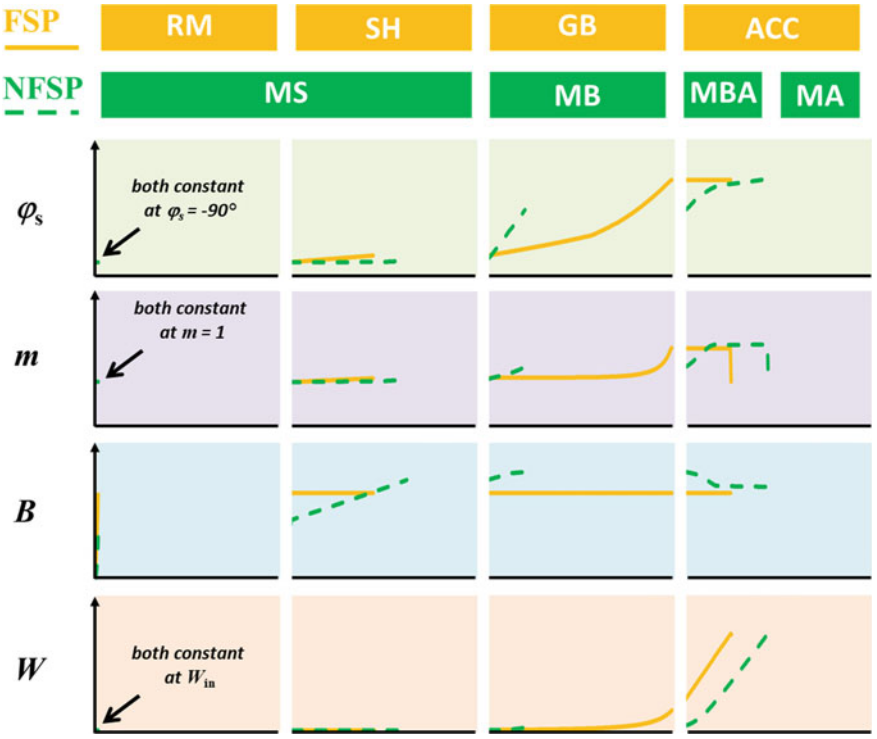

Fig. 2.3 Comparison of the evolution of the main beam dynamics parameters along an RFQ between FSP (orange solid curves) and NFSP (green dashed curves)

Equations (2.22), (2.23), and (2.26) are only determined by structure-related parameters, so it can be seen that "the space charge forces have been neglected" by the FSP method [4].

Along an RFQ, the space charge situation is always changing. When the beam is gradually bunched longitudinally, the space charge effects are getting stronger with the decreasing bunch size and behave most significantly at the end of the bunching. Afterwards, the real acceleration will begin and the transverse defocusing effect will be naturally weakened. Apparently, it is not reasonable to hold B constant like the FSP method. In addition, the FSP-style two-stage bunching should also be improved, not only because the fast non-adiabatic pre-bunching can be a potential source for unstable particles but also because the slow main bunching is not efficient and usually leads to a long structure. The higher the beam current is, the more critical these problems will be.

To overcome the disadvantages of the conventional method, a so-called "New Four-Section Procedure" (NFSP) [10] has been developed. It varies B along the RFQ according to the space charge condition at different positions—namely during the bunching, B should be increased to overcome the stronger and stronger space charge

effects until the transverse defocusing force can be weakened by acceleration, and afterwards it should fall down accordingly—and tries to keep the whole beam development under balanced space charge forces and external focusing forces. "Protected" by the increasing B, a fast main bunching becomes feasible so that the pre-bunching can be performed more gently still with a shortened overall RFQ length.

The NFSP method also divides an RFQ into four sequential sections, but differently:

- Maximum-Separatrix (MS) Section: covering the original RM and SH sections but keeping $\varphi_s \approx -90°$. It forms the initial beam bunch via a gentle and symmetrical pre-bunching (m, B, and A can be increased more gently, compared to the FSP method) with an almost full 360° phase acceptance.
- Main Bunching (MB) Section: it continues decreasing the phase spread of the initial bunch to be close to the target value. B is kept rising to balance the continuously growing space charge effects, so φ_s and m are allowed to be increased much more rapidly than in the original GB section. This can shorten the whole bunching process considerably without degrading the beam quality.
- Mixed Bunching-Accelerating (MBA) Section: when the real acceleration starts, B can also start to fall down accordingly. Meanwhile, φ_s and m can be increased continuously to tune the bunch parameters as desired and provide some acceleration.
- Main Accelerating (MA) Section: if at the end of the MBA section, the required output beam energy is not yet reached, a section with constant (similar to the original ACC section) or slowly changing B, φ_s, and m can be added.

The new way of evolving the main beam dynamics parameters along an RFQ is schematically shown in Fig. 2.3. For an easier comparison with the FSP method, another version of section-dividing is adopted here for the NFSP method (in which the RM section is taken out from the MS section as a separate section and the MBA and MA sections are merged into one section).

Typically, the NFSP method uses a higher maximum B than the FSP method for designing the same machine. However, the NFSP method usually needs a lower U for reaching comparable or better beam quality, so the achieved maximum surface electric field $E_{s,\,max}$ is not necessary higher than that given by the FSP method. A detailed comparison between the FSP and NFSP methods can be found in [11].

The NFSP method has enabled several efficient RFQ designs with both high beam transmission efficiency and short structure length, even at very high current, e.g., 200 emA [10, 12].

2.3 Equipartitioning Principle and Hofmann Stability Charts

The longitudinal and transverse oscillations of the beam in a linac are not independent of each other. When certain conditions are met, longitudinal and transverse coupling can occur.

In 1968, the longitudinal-transverse coupling was identified by Chasman as an important mechanism for space-charge-induced emittance growth in high intensity proton linacs [13] and Lapostolle proposed that this kind of emittance growth could be minimized by equipartitioning (at that time, it was only a concept) [14].

In 1981, Jameson published the Equipartitioning Principle (EP) and suggested minimizing space-charge-induced emittance growth by removing free oscillation energy (often abbreviated as "free energy") between the transverse and longitudinal degrees of freedom [15]. As mentioned above, the motion of beam particles in the RFQ satisfies the equation of a simple harmonic oscillator in both transverse and longitudinal planes. The total oscillation energy of a simple harmonic oscillator is:

$$E_{\text{total}} = \frac{1}{2} m_0 \omega_{\text{o}}^2 R_{\text{o}}^2 \tag{2.27}$$

with ω_{o} being the angular oscillation frequency and R_{o} being the oscillation amplitude (for a beam, it is the rms beam size). No free oscillation energy implies a balance of the longitudinal and transverse oscillation energies, i.e.:

$$\frac{E_{\text{total,l}}}{E_{\text{total,t}}} = \frac{\omega_{\text{o,l}}^2 R_{\text{l}}^2}{\omega_{\text{o,t}}^2 R_{\text{t}}^2} = 1 \tag{2.28}$$

Substituting Eqs. (2.16) and (2.19) into Eq. (2.28), we get the following EP equation:

$$\frac{\varepsilon_{\text{l}} \sigma_{\text{l}}}{\varepsilon_{\text{t}} \sigma_{\text{t}}} = 1 \tag{2.29}$$

Also in 1981, Hofmann reported the stability thresholds for different coupling modes in linear devices [16]. The calculation was performed using the Vlasov equation for an initial Kapchinsky–Vladimirsky distribution with arbitrary emittance ratios, tune ratios, and intensity [16]. These thresholds had been originally obtained for continuous beams in the two transverse directions, but it was found that they could also be applied to investigate the longitudinal-transverse emittance transfer in bunched beams [17]. Hofmann visualized the thresholds including the growth rates of coupling resonances in the form of charts and suggested that these charts could give a useful orientation for controlling the longitudinal-transverse coupling in linacs

[18]. The detailed theory about the Hofmann charts and some experimental evidence can be found in the book [19].

Equation (2.29) implies $\frac{\sigma_l}{\sigma_t} = \frac{\varepsilon_t}{\varepsilon_l}$, where $\frac{\sigma_l}{\sigma_t}$ is the tune ratio (i.e., the ratio of longitudinal phase advance σ_l to transverse phase advance σ_t) and $\frac{\varepsilon_t}{\varepsilon_l}$ is the ratio of transverse emittance ε_t to longitudinal emittance ε_l. Figure 2.4 shows several Hofmann charts for different emittance ratios in the range of $\frac{\varepsilon_l}{\varepsilon_t} = 0.2-2.0$, where the abscissa is the tune ratio $\frac{\sigma_l}{\sigma_t}$ and the ordinate is the tune depression ratio $\frac{\sigma_t}{\sigma_{0t}}$ or $\frac{\sigma_l}{\sigma_{0l}}$. They are the same as $\frac{k_l}{k_t}$ and $\frac{k_t}{k_{0t}}$ $\left(\frac{k_l}{k_{0l}}\right)$ originally used by Hofmann, because $\frac{\sigma_l}{\sigma_t} = \frac{k_l}{k_t}$ and $\frac{\sigma_t}{\sigma_{0t}} = \frac{k_t}{k_{0t}}$ $\left(\frac{\sigma_l}{\sigma_{0l}} = \frac{k_l}{k_{0l}}\right)$. A smaller tune depression ratio means stronger space charge effects and vice versa.

On a Hofmann chart, the darker the color is, the higher the growth rate of coupling resonance. The major resonance peaks usually appear at the positions where $\frac{\sigma_l}{\sigma_t} = \frac{i}{j}$ (i and j are integers), e.g., $\frac{\sigma_l}{\sigma_t} = \frac{1}{2}$, $\frac{1}{1}$, and $\frac{2}{1}$, while the maximum spread of the safe tune depression is always available at a location where the EP equation is satisfied (see the blue dashed lines in Fig. 2.4). On a Hofmann chart for a certain emittance ratio $\frac{\varepsilon_l}{\varepsilon_t}$, if originally there is a resonance peak located at $\frac{\sigma_l}{\sigma_t} = \frac{\varepsilon_t}{\varepsilon_l}$, this peak will vanish due to the lack of the free energy to drive resonances. However, this peak disappears only in the case where the EP condition is exactly met. Any deviation will result in the return of the vanished peak (the larger the deviation is, the more the peak regrows). For example, the $\frac{\sigma_l}{\sigma_t} = 1.0$ resonance peak disappears on the $\frac{\varepsilon_l}{\varepsilon_t} = 1.0$ Hofmann chart, but it grows again on the neighboring charts gradually (see Fig. 2.4).

We may revisit the FSP method from the point of view of the tune chart. Equations (2.22) and (2.2)–(2.26) imply that:

$$\omega_{o,l} = \text{constant (for GB)} \overset{\text{Eqs. (2.13), (2.15) and (2.16)}}{\Longleftrightarrow} \sigma_{0l} = \text{constant (for GB)} \tag{2.30}$$

$$B = \text{constant (after RM)} \overset{\text{Eqs. (2.12) to (2.14)}}{\Longleftrightarrow} \sigma_{0t} = \text{constant (after RM)} \tag{2.31}$$

Therefore, the FSP method requires the following condition to be satisfied for the main part of an RFQ:

$$\frac{\sigma_{0l}}{\sigma_{0t}} = \text{constant} \overset{\text{if longitudinal and transverse tune depressions are similar}}{\Longleftrightarrow} \frac{\sigma_l}{\sigma_t} = \text{constant} \tag{2.32}$$

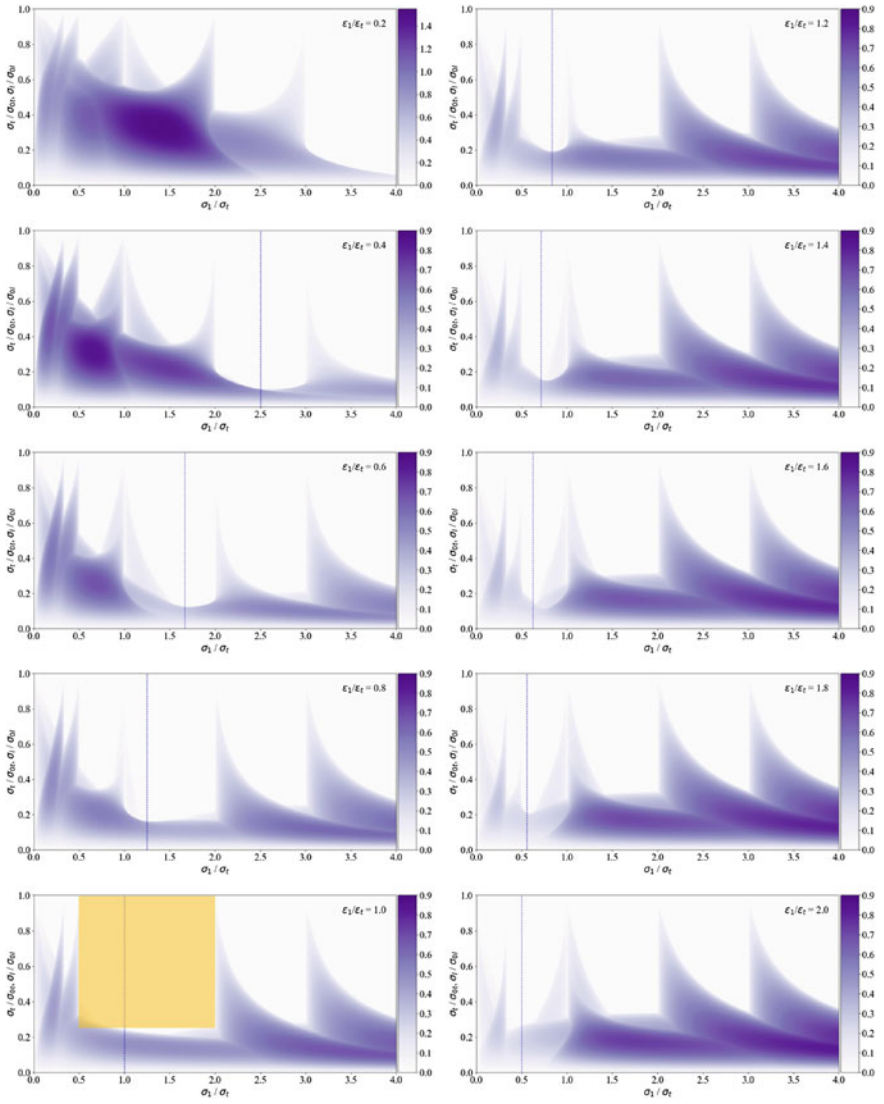

Fig. 2.4 Hofmann charts (generated using TraceWin [20]) for $0.2 \leq \frac{\varepsilon_1}{\varepsilon_t} \leq 2.0$. The blue dashed lines mark the locations where the EP equation is satisfied. The rectangle marked in orange covers a large safe area for tune footprints

Similar to the EP method, the FSP method tries to focus the tune footprints on one fixed σ_1/σ_t (actually σ_{0l}/σ_{0t}) line, but the σ_1/σ_t value is not specified. If this σ_1/σ_t line is by chance close to the EP line, an FSP design can behave like an EP design and good beam performance can also be achieved.

2.4 MEGLET: Minimizing Emittance Growth via Low Emittance Transfer

It is true that if the EP condition is satisfied, the coupling resonance can be maximally avoided. However, free energy does not necessarily cause resonances, and resonances do not necessarily cause instabilities.

It can be seen in Fig. 2.4 that there are sufficient clean (resonance-free) areas on a Hofmann chart besides the EP line. In addition, usually emittance transfer cannot be avoided completely in reality, and a changed emittance ratio will move the EP line in the tune space. Therefore, it makes more sense to choose the clean area on the Hofmann charts instead of sticking to the EP line for the beam motion.

A previous study [21] showed that the Hofmann chart which met the condition given in Eq. (2.33) could provide a quasi-rectangular clean area with wide ranges of tune ratio ($\frac{\sigma_l}{\sigma_t} = 0.5-2.0$) and tune depression ratio ($\frac{\sigma}{\sigma_0} = \sim 0.25-1.0$), respectively. To avoid large emittance transfer, it was recommended using this "safe rectangle" (see the area marked in orange in Fig. 2.4 or Fig. 2.5) to the greatest extent for the beam motion [21].

$$\frac{\varepsilon_l}{\varepsilon_t} = 1.0 \tag{2.33}$$

However, it will be almost impossible to keep the emittance ratio $\frac{\varepsilon_l}{\varepsilon_t}$ exactly equal to one in real machines. A more practical design guideline is to keep $\frac{\varepsilon_l}{\varepsilon_t}$ close to one. Although the $\frac{\sigma_l}{\sigma_t} = 1.0$ resonance peak will regrow when a deviation from $\frac{\varepsilon_l}{\varepsilon_t} = 1.0$ starts, fortunately the $\frac{\sigma_l}{\sigma_t} = 1.0$ resonance peak would not be significant and its resonance growth rates would be low, if $\frac{\varepsilon_l}{\varepsilon_t}$ can be held in the range of $0.9 \leq \frac{\varepsilon_l}{\varepsilon_t} \leq 1.4$

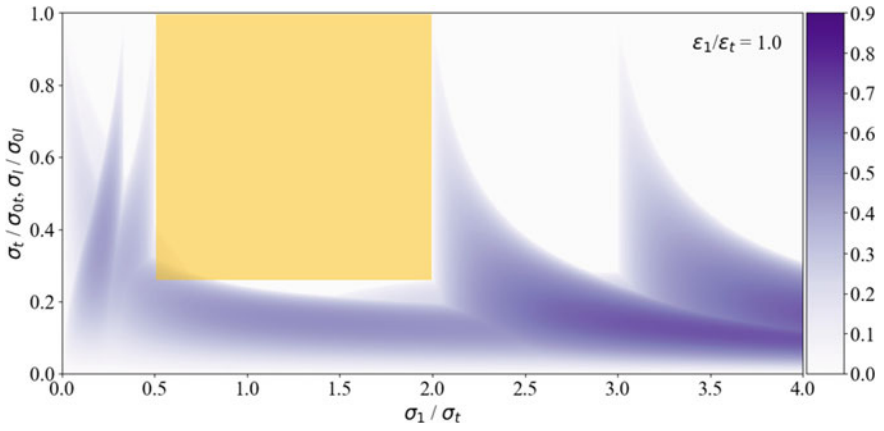

Fig. 2.5 Hofmann chart (generated using TraceWin) for $\frac{\varepsilon_l}{\varepsilon_t} = 1.0$. The rectangle marked in orange covers the safe area for tune footprints

(see Fig. 2.6) [22]. If more emittance transfer is acceptable, this range can be properly relaxed.

An emittance ratio range leading to low emittance transfer, $0.9 \leq \frac{\varepsilon_l}{\varepsilon_t} \leq 1.4$, has been determined. The next steps will be to place and maintain the tune trajectories of the beam inside this range (not necessary to use the whole range) and to take advantage of the low emittance transfer in order to minimize emittance growth.

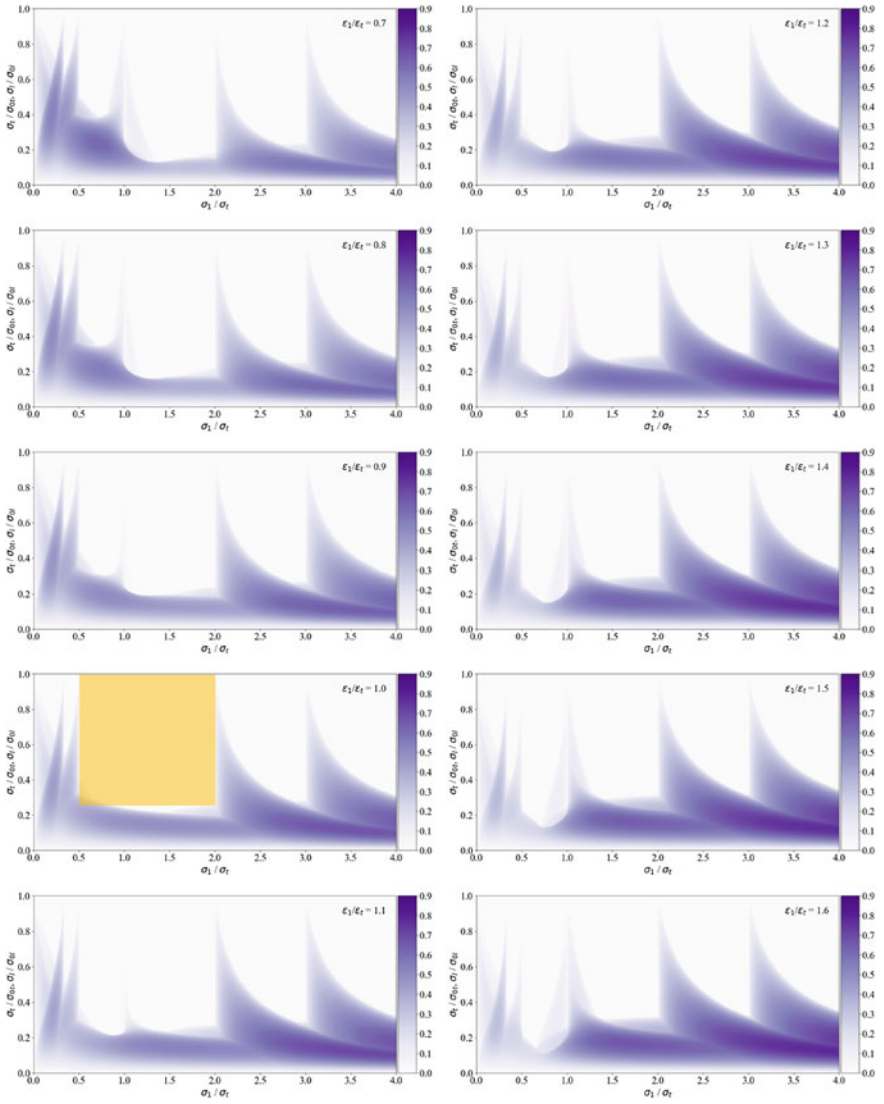

Fig. 2.6 Hofmann charts (generated using TraceWin) for $0.7 \leq \frac{\varepsilon_l}{\varepsilon_t} \leq 1.6$

Typically, an RFQ accelerator receives a continuous beam from an ion source (or an LEBT) with very small energy spread ΔW_{in} but very large phase spread $\Delta\varphi_{\text{in}}$. For RFQ beam dynamics design studies, therefore, it is usually assumed that $\Delta W_{\text{in}} = 0$ and $\Delta\varphi_{\text{in}} = \pm 180°$, respectively, which leads to $\varepsilon_{\text{l, in}} = 0$. If the very short RM section (typically several cells long) is ignored, the input beam will go through three sequential stages in an NFSP-style RFQ (see Fig. 2.3):

- MS Section: during this period, ε_{l} is being increased from 0 to a certain value which can be regarded as the "actual" $\varepsilon_{\text{l, in}}$. Meanwhile, $\frac{\sigma_{\text{l}}}{\sigma_{\text{t}}}$ also starts to increase from 0. Before the beam bunch is initially formed, no significant emittance transfer between the longitudinal and transverse planes will occur.
- MB Section: as the longitudinal electric field is still mainly used for bunching in this stage, the acceleration is small. Therefore, this part is most critical for space charge, especially at its end. During the longitudinal beam compression, $\frac{\sigma_{\text{l}}}{\sigma_{\text{t}}}$ is increasing and emittance transfer can occur from the longitudinal plane to the transverse ones.
- MBA Section and MA Section: the real acceleration will be started and the longitudinal focusing force as well as the transverse defocusing effect will be weakened as natural consequences. In this stage, $\frac{\sigma_{\text{l}}}{\sigma_{\text{t}}}$ will start decreasing again and the emittance transfer will also reverse direction (i.e., the emittance transfer will occur from the transverse planes to the longitudinal one).

Dividing an RFQ also into three stages, a new approach, so-called Minimizing Emittance Growth via Low Emittance Transfer (MEGLET), has been proposed [22] as a further development of the NFSP method. Based on the evolution of the tune trajectories on the Hofmann charts, the three new (MEGLET) stages can be divided as follows [22]:

- Before entering the "safe rectangle": it includes the initial bunching and the starting part of the second stage of bunching with $\frac{\sigma_{\text{l}}}{\sigma_{\text{t}}} < 0.5$. To see the emittance transfer effect more clearly, one can choose a relatively large $\frac{\varepsilon_{\text{l}}}{\varepsilon_{\text{t}}}$ in the range of 0.9–1.4, e.g., 1.3, for the end of the initial bunching, because the subsequent emittance transfer can lower $\frac{\varepsilon_{\text{l}}}{\varepsilon_{\text{t}}}$ down to ~1.0 when the tune trajectories are approaching the "safe rectangle".
- "Travelling" inside the "safe rectangle": it covers the part around the end of the second stage of bunching with $0.5 \leq \frac{\sigma_{\text{l}}}{\sigma_{\text{t}}} \leq 2.0$. This stage is most critical for space charge, especially at high current, so this part of the tune trajectories should be well kept inside the "safe rectangle". It is also important to keep the oscillation of the tune trajectories at the turning point (where the tune trajectories are turning around) away from the position $\frac{\sigma_{\text{l}}}{\sigma_{\text{t}}} = 1$ where the resonance peak can regrow. A proper position to place the oscillation of the tune trajectories could be at $\frac{\sigma_{\text{l}}}{\sigma_{\text{t}}} = 1.2$.
- After leaving the "safe rectangle": in this stage, the tune trajectories will go back to the $\frac{\sigma_{\text{l}}}{\sigma_{\text{t}}} < 0.5$ region and move further towards $\frac{\sigma_{\text{l}}}{\sigma_{\text{t}}} = 0$, and at the same time the emittance transfer will reverse the direction and increase $\frac{\varepsilon_{\text{l}}}{\varepsilon_{\text{t}}}$. It can be seen in Fig. 2.6 that the growth rates of the $\frac{\sigma_{\text{l}}}{\sigma_{\text{t}}} < 0.5$ resonance peaks are low and they are

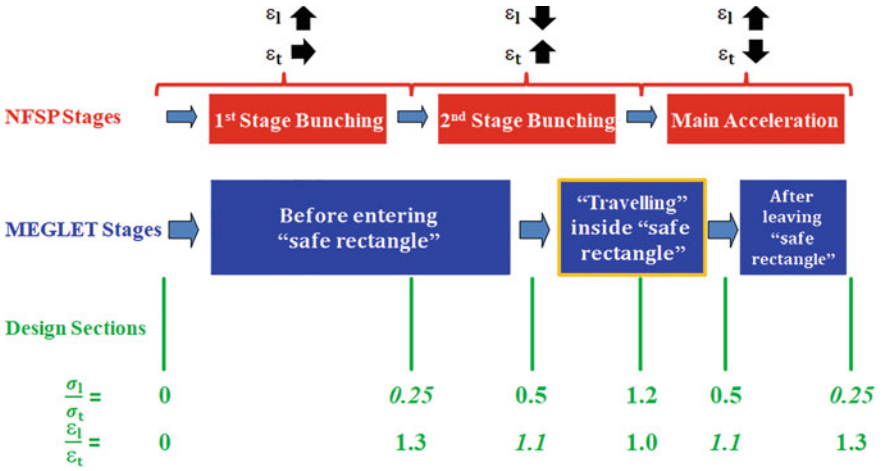

Fig. 2.7 Design sections for an MEGLET-style RFQ (the very short RM section is not shown). The numbers are some typical target values for the tune ratio and the emittance ratio (if they are in italics, relatively larger deviations are acceptable) [22]

decreasing with an increasing $\frac{\varepsilon_l}{\varepsilon_t}$. Therefore, the emittance transfer will be not very significant here. The low emittance transfer will be favorable to help bringing the ε_l, ε_t, and $\frac{\varepsilon_l}{\varepsilon_t}$ values back to what they were before the emittance transfer started.

In this way, the originally harmful emittance transfer can be used as a beneficial tool for minimizing the emittance growth in both transverse and longitudinal planes.

In Fig. 2.7, the NFSP stages and the MEGLET stages are shown together schematically. In total, there are six key points for dividing all these stages and for designing a MEGLET-style RFQ accelerator section by section. The target values $\frac{\sigma_l}{\sigma_t}$ and $\frac{\varepsilon_l}{\varepsilon_t}$ will be obtained from the simulation. The tune ratio at zero current $\frac{\sigma_{0l}}{\sigma_{0t}}$ is determined by the structure-related parameters (e.g., a, m, U, and φ_s) and can be calculated by using Eqs. (2.12) and (2.13). Therefore, it is convenient to take $\frac{\sigma_{0l}}{\sigma_{0t}}$ as a good estimation of $\frac{\sigma_l}{\sigma_t}$ for the design. The typical evolution of the structure-related parameters along the RFQ can be found in Fig. 2.3. To avoid abrupt changes of the parameters, the transitions between the sections can be properly smoothed.

2.5 MEGLET Versus Equipartitioning Principle

To apply the new design approach, a 324 MHz, 3 MeV proton RFQ has been taken as an example. For the convenience of description, this RFQ is hereafter referred to as the MEGLET RFQ.

Table 2.1 Basic design parameters of the MEGLET RFQ

Parameter	Value
Particle	H^+
Frequency f (MHz)	324
Input energy W_{in} (keV)	50
Output energy W_{out} (MeV)	3.0
Input beam current I_{in} (emA)	60
Input emittance $\varepsilon_{t,\,in,\,n,\,rms}$ (π mm mrad)	0.20
Inter-vane voltage U (kV)	75

Table 2.1 lists its basic parameters. The design goal for the MEGLET RFQ is to achieve high transmission using a short structure with the focus especially on minimizing emittance growth.

Table 2.2 lists some 3 MeV H^+ or H^- RFQ accelerators constructed or being constructed worldwide in the 21st century (so far). From the beam dynamics point of view, the difference between H^+ and H^- ions can be ignored. It can be seen that the chosen basic parameters of the MEGLET RFQ are representative. Except for the inter-vane voltage U, they are identical to those of the J-PARC epRFQ [23], which was designed as a "fully equipartitioned" machine. This will allow a comparison between the MEGLET approach and the EP method.

Table 2.2 Some modern 3 MeV H^+ or H^- RFQ accelerators in the world (sorted by the input beam current used for the beam dynamics simulation)

Parameter	KOMAC (PEFP) [24]	CSNS [25]	J-PARC RFQ-III [26]	J-PARC epRFQ [23]	CPHS [27]	CERN Linac4 [28]	FAIR p-Linac [29]
Particle	H^+	H^-	H^-	H^-	H^+	H^-	H^+
f (MHz)	350	324	324	324	325	352.2	325.224
W_{in} (keV)	50	50	50	50	50	45	95
W_{out} (MeV)	3.0	3.0	3.0	3.0	3.0	3.0	3.0
I_{in} (emA)	22	40	60	60	60	70	100
$\varepsilon_{t,\,out,\,n,\,rms}$ (π mm mrad)	0.20	0.20	0.20	0.20	0.20	0.25	0.30
U (kV)	85	80	81	61.3−143	60−135	78	88.43
$\varepsilon_{t,\,out,\,n,\,rms}$ (π mm mrad)	0.22	0.20	0.21	0.24	0.25	0.25	0.32 (95%*)
$\varepsilon_{l,\,out,\,n,\,rms}$ (π MeV deg)	0.112	0.1143	0.11	0.11	0.14	0.13	0.21 (95%*)
L (m)	3.21	3.603	3.623	3.073	2.969	3.06	3.3
T (%)	98.3	97.1	98.5	99.1	97.2	95.0	88.5

*: 95% of transported particles

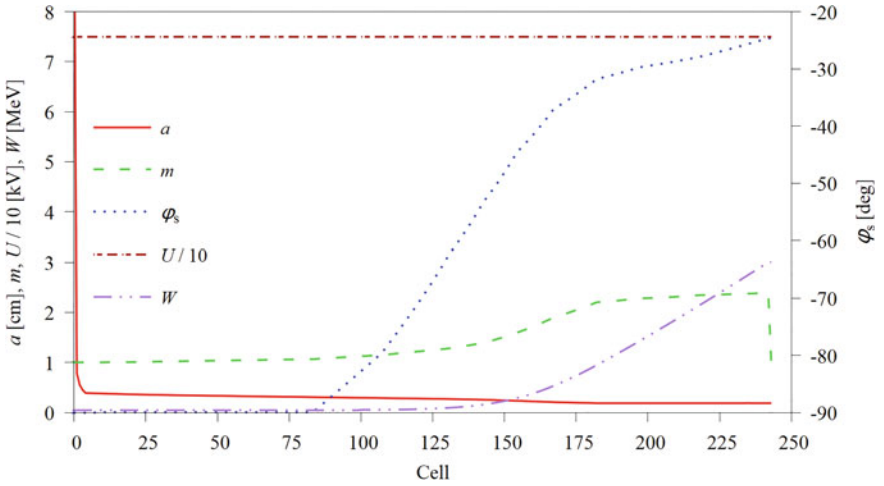

Fig. 2.8 Main design parameters of the MEGLET RFQ, where a is the minimum electrode aperture, m is the electrode modulation, φ_s is the synchronous phase, U is the inter-vane voltage, and W is the beam energy [22]

Following the new approach, the beam dynamics design of the MEGLET RFQ has been made. Figure 2.8 shows the evolution of the main design parameters along the MEGLET RFQ.

The beam dynamics simulation of the MEGLET RFQ has been performed using the PARMTEQM code [30] with 10^5 input macro-particles. Same as for the J-PARC epRFQ, a 4D Waterbag input distribution (particles are generated randomly in a 4D transverse hyperspace with a uniform phase spread and no energy spread) has been adopted for the MEGLET RFQ.

It can be seen in Fig. 2.9 that no matter with or without space charge, the phase advance values along the MEGLET RFQ are all smaller than 45°. They are well below the stopbands of both the 2nd to 4th order parametric resonances and the 4th and 6th order single-particle resonances [31], so for the MEGLET RFQ, only the longitudinal-transverse coupling resonance is important.

Figure 2.10 shows the tune trajectories of the beam in the MEGLET RFQ, where the red and green curves are corresponding to the transverse and longitudinal tune depression ratios, $\frac{\sigma_t}{\sigma_{0t}}$ and $\frac{\sigma_l}{\sigma_{0l}}$, as functions of tune ratio $\frac{\sigma_l}{\sigma_t}$, respectively. The arrows indicate the moving directions of the tune trajectories. Each arrow represents one step. For small steps, the size of the arrows has been reduced to avoid crowding the figure. As the tune trajectories enter and leave the "safe rectangle" at Cell 95 and Cell 163, respectively, the MEGLET RFQ can be divided into the following three stages:

- Stage 1: from the RFQ entrance up to Cell 95.
- Stage 2: between Cell 95 and Cell 163.
- Stage 3: the remaining part after Cell 163.

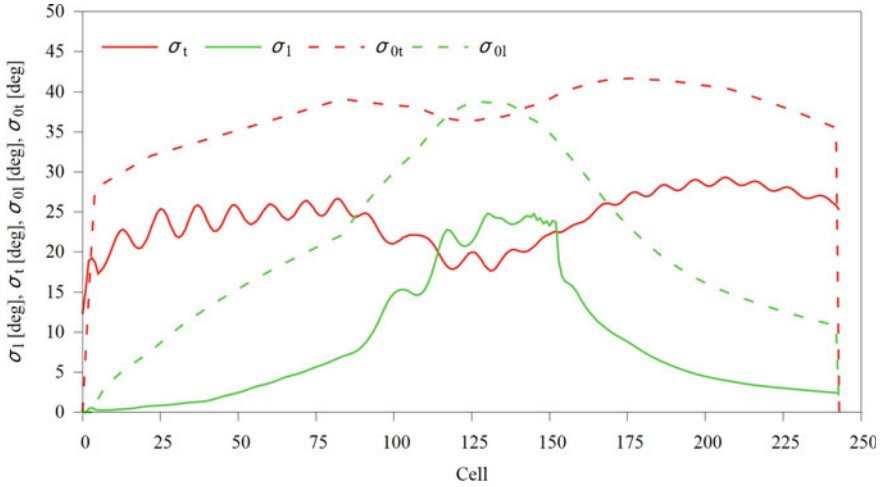

Fig. 2.9 Phase advance values with and without space charge along the MEGLET RFQ [22]

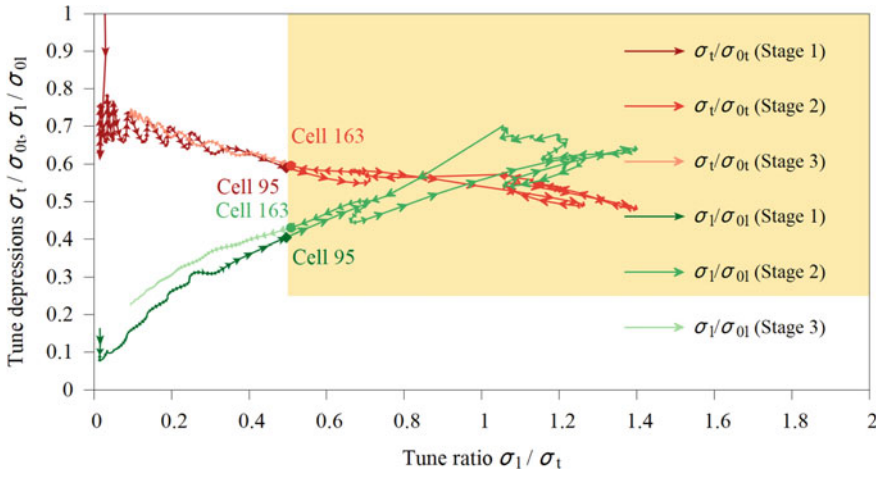

Fig. 2.10 Evolution of tune depression ratios along the MEGLET RFQ. The tune trajectories of the three stages are showed in red (transverse) and green (longitudinal) colors from dark to light. The "safe rectangle" marked in orange covers Stage 2 where the space charge effects are most critical [22]

In Fig. 2.11, the longitudinal and transverse emittances are plotted as functions of cell number, where the emittance curves for 99% of particles are used to show the evolution of the main beam by excluding 1% outmost particles. In the figure, all emittances are in units of π mm mrad and are normalized (after the normalization, the emittance ratio is kept unchanged, i.e., $\frac{\varepsilon_{l,n}}{\varepsilon_{t,n}} = \frac{\varepsilon_l}{\varepsilon_t}$). An often adopted unit of the longitudinal emittance in linacs is π MeV deg. The conversion formula for the

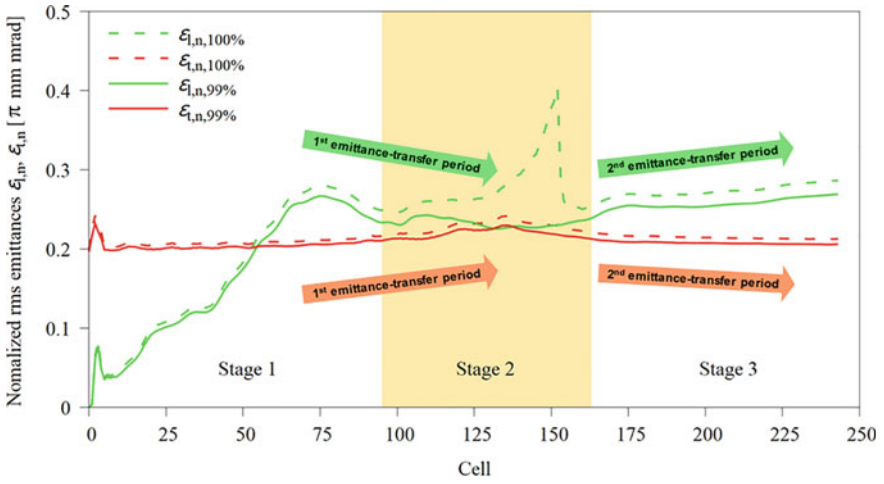

Fig. 2.11 Evolution of longitudinal and transverse emittances for 100% and 99% of particles along the MEGLET RFQ [22]

longitudinal emittance unit from π MeV deg to π mm mrad is:

$$\varepsilon_{l,n}(\pi \text{ mm mrad}) = \frac{10^6}{360}\frac{\lambda(\text{m})}{E_0(\text{MeV})}\varepsilon_{l,n}(\pi \text{ MeV deg}) \tag{2.34}$$

where E_0 is the rest energy of the beam particle in MeV.

Figure 2.11 shows that the formation of the initial beam bunch is completed around Cell 75 where the synchronous phase starts to move away from −90° (see Fig. 2.8). The emittance ratio $\frac{\varepsilon_l}{\varepsilon_t}$ (in this study, it always refers to $\frac{\varepsilon_{l,100\%}}{\varepsilon_{t,100\%}}$ or $\frac{\varepsilon_{l,n,100\%}}{\varepsilon_{t,n,100\%}}$) at this position has been chosen as ~1.3. Afterwards, the emittance transfer occurs from the longitudinal plane to the transverse ones, so the emittance ratio is being decreased and reaches ~1.1 at the end of Stage 1.

In the second MEGLET stage, the $\varepsilon_{l,n,100\%}$ curve starts to have a "jump" around Cell 135 (see Fig. 2.11) where the real acceleration starts (see Fig. 2.8). This "jump" is caused by the less than 1% of particles which are outside of the separatrix and cannot catch the right acceleration. After they are lost, the $\varepsilon_{l,n,100\%}$ curve comes back to flat again. The real acceleration also reverses the direction of the emittance transfer so that the transverse and longitudinal emittances will be decreased and increased, respectively. "Protected" by the "safe rectangle", the emittance transfer in the whole Stage 2 is relatively low and the emittance ratio at the end of this stage can be still held at ~1.1.

Entering into the third MEGLET stage, the beam will see the $\frac{\sigma_l}{\sigma_t} \leq 0.5$ resonance peaks again, so the emittance transfer will become stronger. However, Fig. 2.6 shows that the growth rates of the $\frac{\sigma_l}{\sigma_t} \leq 0.5$ resonance peaks on the Hofmann charts for $\frac{\varepsilon_l}{\varepsilon_t} = 1.1-1.4$ are relatively low and they are decreasing with an increasing $\frac{\varepsilon_l}{\varepsilon_t}$. Therefore, the emittance transfer in this stage will be slow.

Table 2.3 Emittance values before and after emittance transfers

Emittance (π mm mrad)	Cell 75 (start of 1st emittance-transfer period)	Cell 137 (end of 1st/ start of 2nd emittance-transfer period)	Cell 243 (end of 2nd emittance-transfer period/exit of the RFQ)
$\varepsilon_{\mathrm{l,\,n,\,rms,\,100\%}}$	0.280	0.285	0.286
$\varepsilon_{\mathrm{l,\,n,\,rms,\,99\%}}$	0.267	0.228	0.269
$\varepsilon_{\mathrm{t,\,n,\,rms,\,100\%}}$	0.211	0.239	0.213
$\varepsilon_{\mathrm{t,\,n,\,rms,\,99\%}}$	0.206	0.228	0.206

In total, there are two emittance-transfer periods:

- 1st emittance transfer period: from Cell 75 to Cell 137.
- 2nd emittance transfer period: from Cell 137 to Cell 243, i.e., the RFQ exit.

The 100% and 99% emittance values at these three cells are listed in Table 2.3. If we take the 99% emittances (to remove the noise from the <1% tail particles), one can observe that:

- In the 1st emittance transfer period $\varepsilon_{\mathrm{l,\,n,\,rms}}$ is decreased by ~17%, while $\varepsilon_{\mathrm{t,\,n,\,rms}}$ is increased by ~9%.
- In the 2nd emittance transfer period $\varepsilon_{\mathrm{t,\,n,\,rms}}$ is increased by ~18% and $\varepsilon_{\mathrm{t,\,n,\,rms}}$ is decreased by ~10%.

There are one longitudinal plane and two transverse planes, so the emittance transfer between the longitudinal plane and each transverse plane is ~9% for both periods, which is low.

Both transverse and longitudinal emittances values at Cell 243, i.e., the exit of the MEGLET RFQ are very close to those at Cell 75 (before the emittance transfer starts), so there is almost no net emittance growth. Shown in Fig. 2.12, the emittance ratio $\frac{\varepsilon_{\mathrm{l}}}{\varepsilon_{\mathrm{t}}}$ is well inside the range from 0.9 to 1.4 for most positions along the MEGLET RFQ.

The main simulation results of the MEGLET RFQ are summarized in Table 2.4. The RFQ length L is about 3 m and the beam transmission efficiency is 99.1%. Both are very comparable to those of the J-PARC epRFQ.

As the J-PARC epRFQ uses a non-constant inter-vane voltage U, one needs to find an equivalent value for the comparison. The specific shunt impedance of an RFQ, R_{p}, is defined as:

$$R_{\mathrm{p}} = \frac{U^2 L}{P_{\mathrm{c}}} \tag{2.35}$$

where P_{c} is the RF power consumption. For the J-PARC epRFQ, the nominal P_{c} is 380 kW [32]. Because the J-PARC epRFQ and its predecessor, the J-PARC RFQ III [26], have the same frequency and similar design specifications, it is

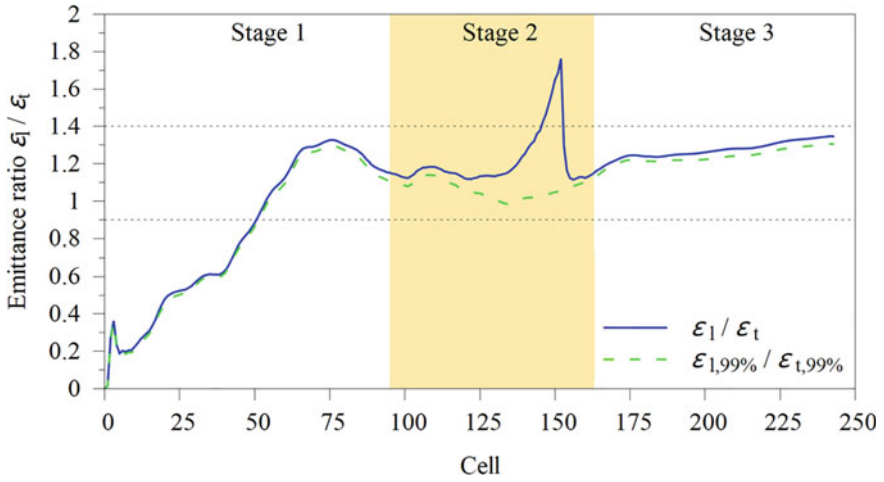

Fig. 2.12 Emittance ratio $\frac{\varepsilon_l}{\varepsilon_t}$ as a function of cell number

Table 2.4 Main design results of the MEGLET RFQ

Parameter	MEGLET RFQ [22]	J-PARC epRFQ [23]
Particle	H^+	H^-
f (MHz)	324	324
W_{in} (keV)	50	50
W_{out} (MeV)	3.0	3.0
I_{in} (emA)	60	60
U (kV)	75	61.3–143
$\varepsilon_{t,\,in,\,n,rms}$ (π mm mrad)	0.20	0.20
$\varepsilon_{t,\,out,\,n,rms}$ (π mm mrad)	0.21	0.24
$\varepsilon_{l,\,out,\,n,rms}$ (π MeV deg)	0.10	0.11
L (m)	3.067	3.073
T (%)	99.1	99.1

appropriate to assume that the two RFQs have the same R_p value. For the J-PARC RFQ III, $P_c = 400$ kW, $U = 81$ kV, and $L = 3.623$ m [26, 33]. Based on all these data, the calculated equivalent inter-vane voltage for the J-PARC epRFQ is 85.7 kV, which is ~14% higher than that adopted for the MEGLET RFQ.

For the J-PARC epRFQ, most of the tune trajectories have been indeed successfully concentrated with the EP line as the focus (see the 5th figure in [23]). However, the tune trajectories intensively oscillate around $\frac{\sigma_l}{\sigma_t} = 0.77$, the EP line for $\frac{\varepsilon_l}{\varepsilon_t} = 1.3$, and touch the main resonance peak at $\frac{\sigma_l}{\sigma_t} = 1.0$ many times (especially the transverse tune trajectory) so that the resonance can be accumulated. It can be seen in the 2nd

figure in [23] that the transverse emittance is gradually increasing along the J-PARC epRFQ and $\frac{\varepsilon_l}{\varepsilon_t}$ is not constant after the shaper but varies within the range of 1.2–1.5.

In the MEGLET case, the tune trajectories have much less oscillations with much smaller amplitudes (see Fig. 2.10). Its main oscillation has been well confined around $\frac{\sigma_l}{\sigma_t} = 1.2$ in order to avoid touching the $\frac{\sigma_l}{\sigma_t} = 1.0$ major resonance peak repeatedly. More importantly, both longitudinal and transverse output emittance values have been brought back to the levels before the two emittance-transfer periods (see Fig. 2.11 and Table 2.3).

In this way, the MEGLET RFQ reaches smaller output emittance values in both transverse and longitudinal planes (see Table 2.4).

2.6 MEGLET RFQ with Off-Design Input Beams

In the real world, the manufacture and operation of accelerators cannot be done perfectly. Therefore, it is very important for an accelerator design to have sufficient tolerance for off-design situations.

The MEGLET RFQ has been tested for two cases with both input beam currents and input emittances (see Table 2.5) different from the nominal case. To some degree, they can also be regarded as two mismatching cases.

The I_{in} and $\varepsilon_{t,\,in,\,n,\,rms}$ values for Case 1 and Case 2 are the same as those for the CERN Linac4 RFQ [28] and for the FAIR p-Linac RFQ [29], respectively. For a comparison, the nominal case (hereafter referred to as Case 0) is also listed in the table. All three input beams have a Waterbag-type distribution including 10^5 macro-particles. One difference is that the input beam for Case 1 has an input energy spread $\Delta W_{in} = \pm 2\%$, because the simulation results for the Linac4 RFQ are based on this condition [34]. No matter for Case 1 or Case 2, the same MEGLET RFQ has been used, so all structure-related parameters, e.g., f, W_{in}, and U, have been kept fixed in the simulation.

Table 2.5 Input beam intensities and emittances of the MEGLET RFQ for different cases

Parameter	Case 0 (nominal case)	Case 1	Case 2
I_{in} (emA)	60	70	100
$\varepsilon_{t,\,in,\,n,\,rms}$ (π mm mrad)	0.20	0.25	0.30
ΔW_{in} (%)	0	± 2	0

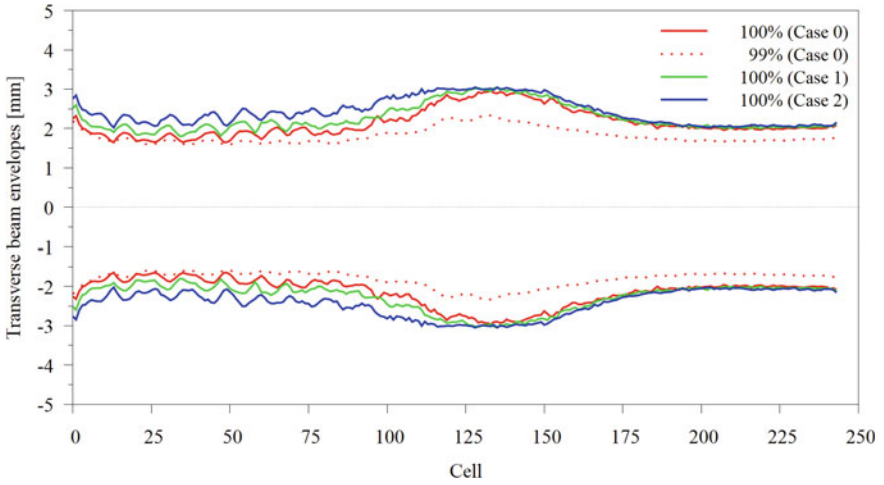

Fig. 2.13 Transverse beam envelopes of the MEGLET RFQ in different cases

Figure 2.13 compares the simulated transverse beam envelopes of the MEGLET RFQ for the three cases. From Case 0 to Case 2, the input beam current and the input emittance are increasing, and so does the beam size. The MEGLET RFQ has been designed for an input beam with $I_{in} = 60$ emA and $\varepsilon_{t,\,in,\,n,\,rms} = 0.2\ \pi$ mm mrad, so there are more beam losses in the two off-design cases. The simulated beam transmission efficiency for all transported particles is 97.6% and 89.4% for Case 1 and Case 2, respectively. For both cases, ~99% of the transported particles are well clustered around synchronous particle with phase differences <30° and energy differences <30 keV.

The evolution of the longitudinal and transverse emittances is shown in Fig. 2.14 for the three cases. As mentioned, the MEGLET approach uses two periods of emittance transfer after the initial bunching: (1) in the first transfer period, the transverse emittance increases and the longitudinal emittance decreases; (2) in the second transfer period, it is just the opposite. All transverse emittance curves show the two emittance-transfer periods clearly. For the longitudinal emittance, it can be seen that the green dashed curve (the $\varepsilon_{l,\,n}$ curve for Case 1) does not start with 0 because of the ±2% of input energy spread. In general, the three longitudinal emittance curves are still similar and from them the second emittance-transfer period can be distinctly seen. For Case 1 and Case 2, due to the larger input beam currents and input emittances, the initial bunching cannot capture as many particles as in the nominal case. These small numbers of particles outside of the separatrix (longitudinal acceptance) make the first transfer period of the green and blue dashed curves less obvious.

The main simulation results for the two MEGLET off-design cases as well as the design values of the Linac4 RFQ and the p-Linac RFQ are listed in Table 2.6. It can be seen that the MEGLET RFQ can still achieve comparable beam transmission efficiency as well as better output emittances by using a lower U, although the input

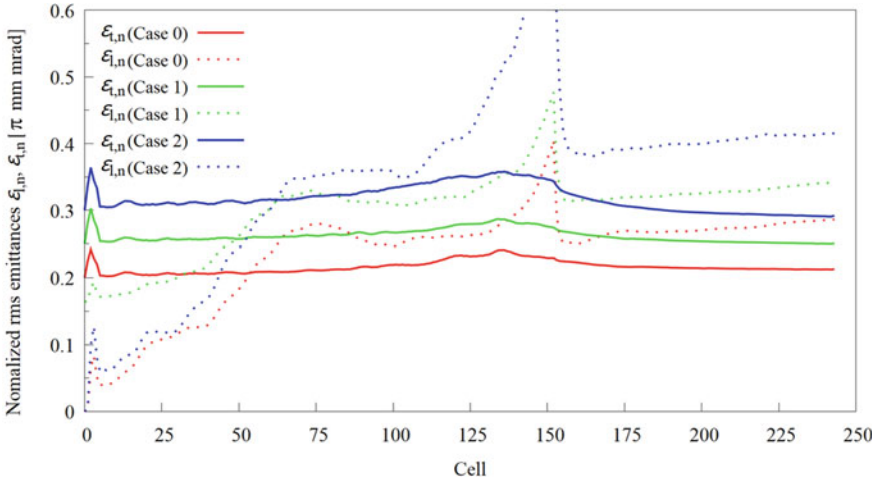

Fig. 2.14 Comparison of the longitudinal and transverse emittances (for 100% of particles) of the MEGLET RFQ in different cases

Table 2.6 Main simulation results of the MEGLET RFQ with off-design input beams

Parameter	MEGLET case 1 [22]	CERN Linac4 [28, 34]	MEGLET Case 2 [22]	FAIR p-Linac [29]
Ion	H^+	H^-	H^+	H^+
f (MHz)	324	352.2	324	325.224
W_{in} (keV)	50 (± 2%)	45 (± 2%)	50	95
W_{out} (MeV)	3.0	3.0	3.0	3.0
U (kV)	75	78	75	88.43
I_{in} (emA)	70	70	100	100
$\varepsilon_{t,\,in,\,n,\,rms}$ (π mm mrad)	0.25	0.25	0.30	0.30
$\varepsilon_{t,\,out,\,n,\,rms}$ (π mm mrad)	0.25	0.25	0.29	0.32 (95%*)
$\varepsilon_{l,\,out,\,n,\,rms}$ (π MeV deg)	0.12	0.13	0.15	0.21 (95%*)
L (m)	3.067	3.06	3.067	3.3
T (%)	97.6	95.0	89.4	88.5

*: 95% of transported particles

beams are not optimum. It is worth mentioning that for the two off-design cases, the emittance ratio $\frac{\varepsilon_l}{\varepsilon_t}$ is still mainly inside the range from 0.9 to 1.4 along the MEGLET RFQ so that good performance in emittance growth is kept.

2.7 SEGLER: Small Emittance Growth at Large Emittance Ratios

For using the MEGLET approach, one needs to hold the emittance ratio inside the optimum range, i.e., $0.9 \leq \frac{\varepsilon_l}{\varepsilon_t} \leq 1.4$. At given conditions, which kind of $\frac{\varepsilon_l}{\varepsilon_t}$ values can be achieved is determined by the bunching process. Generally speaking, the RFQ bunching needs to achieve the following goals:

- To capture as many particles as possible and reduce the beam phase spread to a suitable value for efficient acceleration, e.g., $\pm 30°$.
- To minimize energy spread during the bunching.
- To avoid a too long structure for the bunching.

In a linac beam bunch, the particles perform synchrotron oscillations with respect to the synchronous particle. Such oscillations can be described using the following "Synchrotron Equations":

$$\frac{d\Delta\varphi_{i,\mathrm{s}}}{ds} = \omega\left(\frac{dt_i}{ds} - \frac{dt_\mathrm{s}}{ds}\right) = \frac{\omega}{c}\left(\frac{1}{\beta_i} - \frac{1}{\beta_\mathrm{s}}\right) \approx -\frac{\omega}{\beta_\mathrm{s} c}\frac{\Delta\beta_{i,\mathrm{s}}}{\beta_\mathrm{s}} = -\frac{\omega\Delta W_{i,\mathrm{s}}}{m_0 c^3 \beta_\mathrm{s}^3 \gamma_\mathrm{s}^3} \tag{2.36}$$

$$\frac{d\Delta W_{i,\mathrm{s}}}{ds} = qE_0T(\cos\varphi_i - \cos\varphi_\mathrm{s}) \tag{2.37}$$

where E_0 is the average longitudinal electric field for an accelerating cell, T is the transit time factor, and $W_{i,\mathrm{s}} = W_i - W_\mathrm{s}$ and $\Delta\varphi_{i,\mathrm{s}} = \varphi_i - \varphi_\mathrm{s}$ are the energy difference and the phase difference between a test particle and the synchronous particle, respectively. If a minimum energy spread is required, the change in $W_{i,\mathrm{s}}$ should be small (like for adiabatic bunching). In this case, the variation of $\Delta\varphi_{i,\mathrm{s}}$ is inversely proportional to $\sim\beta_\mathrm{s}^3\gamma_\mathrm{s}^3$ according to Eq. (2.36). For RFQs, $\gamma \approx 1$, so the length of such a bunching section is proportional to $\sim\beta_\mathrm{s}^3$. In addition, the length of a bunching cell is longer at a higher β_in. Clearly, a lower W_in is usually more favorable to avoid a too long structure for bunching.

If a high beam current is needed for an RFQ, however, usually one should also have a high W_in because of space charge forces being lower at higher energies. The formula for the space-charge electric field limits in ion sources is known as the Child–Langmuir law [35, 36]. For a planar electrode geometry with a gap spacing d between the two plates and an applied voltage U_0, the limiting current density J in A/m^2 is determined by [37]:

$$J = 1.67 \times 10^{-3}\left(\frac{q}{m_0c^2}\right)^{1/2}\frac{U_0^{3/2}}{d^2} \tag{2.38}$$

where q and m_0 are the charge and mass of the particle, respectively, and c is the speed of light in vacuum (all in MKS units). Applying Eq. (2.38) to a round uniform

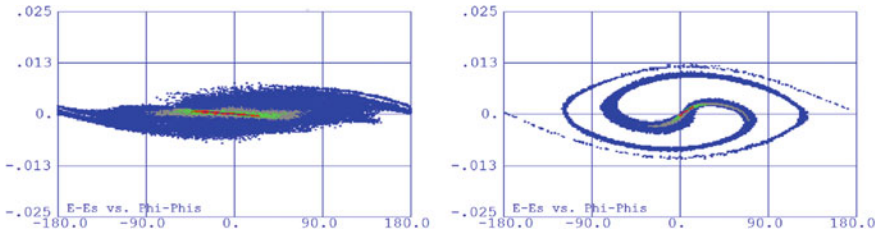

Fig. 2.15 Longitudinal output particle distributions for Cell 75 (end of the pre-bunching) of the MEGLET RFQ at 60 emA (left) and 0 emA (right)

beam emitted from a circular area with radius r_s, one gets the beam current limit due to space charge as follows [37]:

$$I = 1.67\pi \times 10^{-3}\left(\frac{q}{m_0c^2}\right)^{1/2} U_0^{3/2}\left(\frac{r_s}{d^2}\right)^2 \tag{2.39}$$

Equation (2.39) implies that W_{in} is a limiting factor for increasing I_{in}.

In addition, the space charge effects also play a very important role in the bunching process. Figure 2.15 shows the longitudinal output particle distributions at Cell 75 (the end of the pre-bunching) of the MEGLET RFQ for both 60 emA (design I_{in}) and 0 emA cases. The corresponding normalized rms emittance at 0 emA is 0.450 π mm mrad, much larger than the nominal one, 0.280 π mm mrad. Because the same RFQ is used, the bunching field designed for 60 emA becomes too strong for a zero current beam and will cause a lot of empty area inside the emittance ellipse. To some degree, the space charge effects can help to reduce the growth rate of the energy spread and lead to a smooth and progressive bunching. Although the resulting "actual" $\varepsilon_{l,in}$ at the end of the pre-bunching can be smaller, the length of the pre-bunching section may be longer.

Besides the above-mentioned factors, many other parameters, e.g., the input emittance, the inter-vane voltage, the resonant frequency, and the required RFQ structure length, can also influence the bunching quality and the length of the bunching section. In reality, therefore, one needs often to make trade-offs in choosing the design parameters for an RFQ accelerator and it is possible to reach larger emittance ratios, which are beyond the optimum $\frac{\varepsilon_l}{\varepsilon_t}$ range required by the MEGLET method.

As a continuation of Fig. 2.4, Fig. 2.16 shows the Hofmann charts for the emittance ratios $\frac{\varepsilon_l}{\varepsilon_t}$ from 2.2 to 4.0. Due to the remarkable $\frac{\sigma_l}{\sigma_t} = 1.0$ resonance peak, the "safe rectangle" used by the MEGLET method is not available any more. On these $2.0 \leq \frac{\varepsilon_l}{\varepsilon_t} \leq 4.0$ Hofmann charts, however, a relatively large safe area for tune footprints (see the ¼ ellipse marked in orange in Fig. 2.16) can be still found.

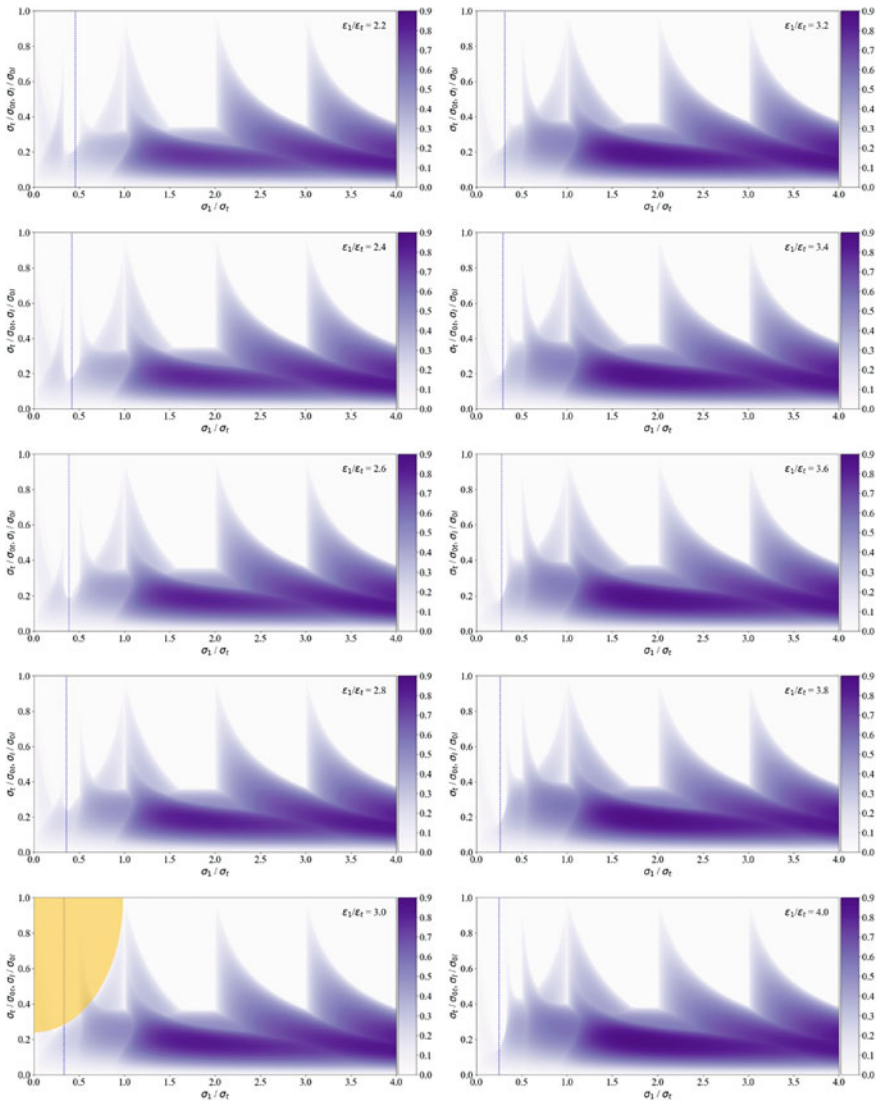

Fig. 2.16 Hofmann charts (generated using TraceWin) for $2.2 \leq \frac{\varepsilon_1}{\varepsilon_t} \leq 4.0$. The ¼ ellipse marked in orange covers a relatively safe area for tune footprints

In Fig. 2.17, one can see more clearly that the semi axes of this "safe ¼ ellipse" are $\frac{\sigma_1}{\sigma_t} = 0.0$–$1.0$ and $\frac{\sigma}{\sigma_0} = 0.25$–$1.0$, so the area of the "safe ¼ ellipse" is smaller than that of the "safe rectangle". With several resonance peaks inside, this "safe ¼ ellipse" is also not as clean as the "safe rectangle". Nevertheless, the most remarkable $\frac{\sigma_1}{\sigma_t} = 0.5$ resonance peak is fortunately relatively weak, so to use this area is a good compromise for achieving small emittance growth at large emittance ratios

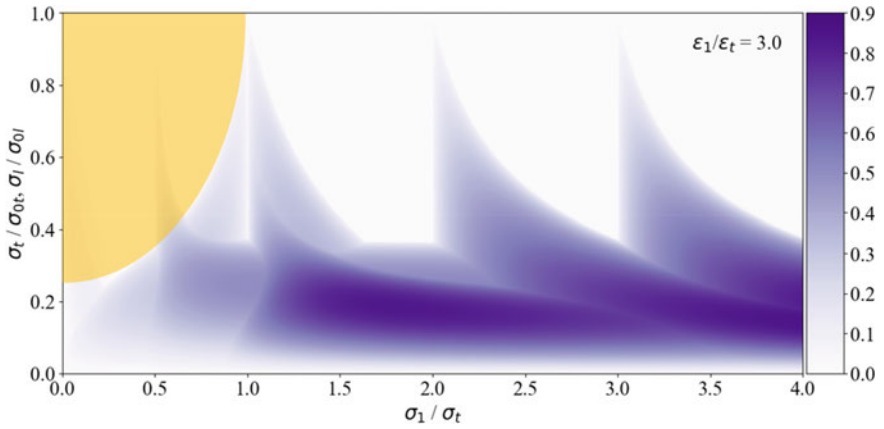

Fig. 2.17 Hofmann chart (generated using TraceWin) for $\frac{\varepsilon_1}{\varepsilon_t} = 3.0$ with the "safe ¼ ellipse"

$(2.0 \leq \frac{\varepsilon_1}{\varepsilon_t} \leq 4.0)$. This method is therefore named as "SEGLER" (Small Emittance Growth at Large Emittance Ratios).

When applying the SEGLER method, it is important to keep $\frac{\sigma_1}{\sigma_t} \leq 1.0$, which means that the longitudinal focusing strength should be smaller than the transverse one. One can tune different dynamics parameters to realize this. For example, a smaller electrode modulation can provide larger transverse electric field components and smaller longitudinal electric-field components.

This method has been applied for the redesign of the FRANZ (Frankfurt Neutron Source at the Stern-Gerlach-Zentrum) RFQ and the design of the two-cavity HBS (High Brilliance Neutron Source) RFQ. More details can be found in Chaps. 3 and 5.

2.8 A General Comparison of the Four RFQ Design Methods

From the point of view of tune footprints, the above-mentioned four RFQ design methods can be divided into two groups (also see Fig. 2.18 and Table 2.7):

- FSP and EP:
  - At the beginning of an RFQ, the tune footprints have typically less but larger oscillations (fast parameter variations for a fast pre-bunching).
  - In the main part of an RFQ, the tune footprints have very intense and large oscillations around a certain $\frac{\sigma_l}{\sigma_t}$ line (slow parameter variations so that a slow main bunching).
  - The realized RFQs have relatively more cells (i.e., longer structures), as compared to those realized using the following two newer methods.

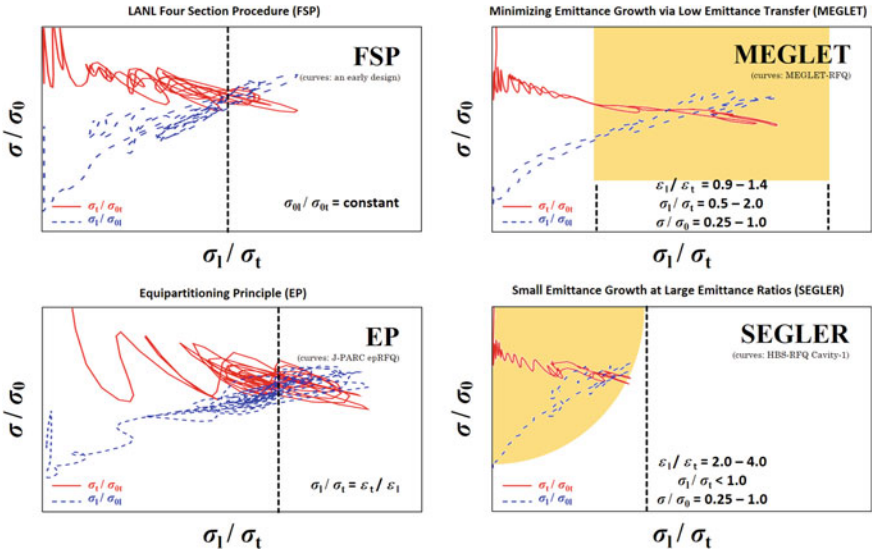

Fig. 2.18 Schematic plots of the typical tune charts for the four RFQ design methods. The tune footprints for the graphs have been taken from an unpublished design (FSP), the J-PARC epRFQ design [24] (EP), the MEGLET RFQ design (MEGLET, see Sect. 2.5) and the design for the HBS RFQ Cavity-1 (SEGLER, see Sect. 5.5), respectively

Table 2.7 Characteristics of the four RFQ design methods

	FSP	EP	MEGLET	SEGLER
Hofmann charts as guidelines	No	Yes	Yes	Yes
$\varepsilon_l/\varepsilon_t$ *	Not specified	Not specified	0.9–1.4 #	2.0–4.0
σ_l/σ_t*	($\frac{\sigma_{0l}}{\sigma_{0t}}$ = constant)	$\varepsilon_t/\varepsilon_l$	0.5–2.0	0.0–1.0
σ/σ_0 *	Not specified	Not specified	0.25–1.0	0.25–1.0
Tune footprints for pre-bunching	Less but large oscillations	Less but large oscillations	More but small oscillations	More but small oscillations
Tune footprints for main bunching	Intensive and large oscillations	Intensive and large oscillations	Less and small oscillations	Less and small oscillations

*: for the main part of the RFQ
#: this range can be properly relaxed, if more emittance transfer is acceptable

- MEGLET and SEGLER:
  - At the beginning of an RFQ, the tune footprints have typically more but very small oscillations (due to the more gentle pre-bunching).
  - In the main part of an RFQ, the tune footprints have few small oscillations (a fast main bunching) and one avoids these being localized at a certain $\frac{\sigma_l}{\sigma_t}$ line.
  - Usually the realized RFQs have in total less cells (shorter structures).

Some general conclusions can be made as follows:

- Freedom for changing parameters: MEGLET > SEGLER > FSP > EP
  - FSP requires constant longitudinal and transverse oscillation frequencies at zero current, i.e., $\frac{\sigma_{0l}}{\sigma_{0t}} =$ constant (roughly one can take it as $\sigma_l/\sigma_t =$ constant) and EP requires equal longitudinal and transverse oscillation energies, i.e., $\sigma_l/\sigma_t = \varepsilon_t/\varepsilon_l$.
  - MEGLET and SEGLER aim to keep $\varepsilon_l/\varepsilon_t$ in certain safe ranges instead of requiring a specified σ_l/σ_t.
  - The "safe rectangle" of MEGLET is larger and cleaner than the "safe ¼ ellipse" of SEGLER.
- Expected beam quality:
  - Usually EP > FSP. The EP line has always the maximum spread of the safe tune depression, and the fixed σ_l/σ_t line used by FSP can locate in a resonance peak. If the fixed σ_l/σ_t line used by a FSP design is by chance overlapped with an EP line, this FSP design can also achieve the EP-level beam quality.
  - MEGLET > SEGLER, as MEGLET has a larger and cleaner safe area than SEGLER.
  - MEGLET > EP in the case of similar RFQ length and similar RF power consumption.

The main differences between the EP and MEGLET methods can be summarized as follows:

- The EP method emphasizes equal longitudinal and transverse oscillation energies, but for the MEGLET approach, close longitudinal and transverse emittances are important.
- To minimize the emittance growth, the EP method tries to avoid the longitudinal-transverse coupling. On the contrary, the MEGLET method allows and even takes advantage of low emittance transfer for achieving minimum emittance growth (see Fig. 2.19).
- For both methods, the tune trajectories will have oscillations when the tune trajectories are turning around in the tune space. An EP design usually has an intensive oscillation around the EP line, but in the MEGLET case, the oscillation will be much smaller and one avoids the position where the main resonance peak can regrow.
- The MEGLET approach does not force the tune trajectories to stay on or closely around the EP line, so it allows changing the beam dynamics parameters more quickly with more freedom, which is helpful for leading to a shorter RFQ accelerator with lower RF power consumption.
- Last but not least, the EP method usually requires a big variation in inter-vane voltage along the RFQ, e.g., 61.3–143 kV for the J-PARC epRFQ, while the MEGLET method adopts the conventional way, i.e., keeps the inter-vane voltage constant throughout the RFQ, which is favorable for an easy RF tuning.

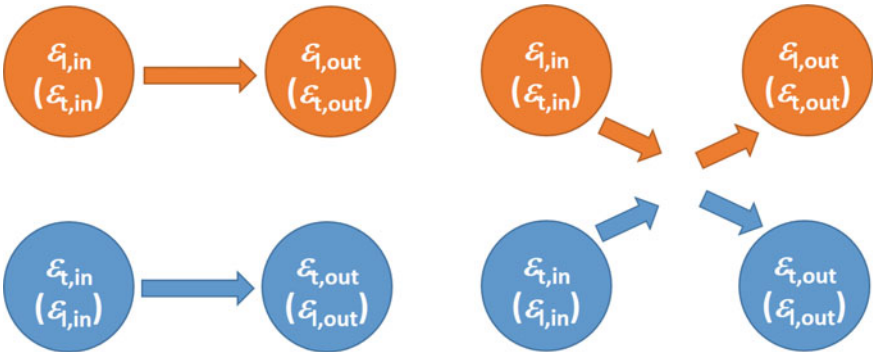

Fig. 2.19 Different strategies for dealing with the longitudinal-transverse coupling (left: EP, right: MEGLET)

References

1. K. Schindl, Space charge. CERN Accelerator School: Intermediate Course on Accelerator Physics (2003)
2. I.M. Kapchinsky, V.A. Teplyakov, A linear ion accelerator with spatially uniform hard focusing. SLAC report no. SLAC-TRANS-0099 (Transl. by T. Watt from Preprint ITEP-673) (1969)
3. R.H. Stokes, K.R. Crandall, J.E. Stovall, D.A. Swenson, RF quadrupole beam dynamics, in *Proceedings of* PAC (1979)
4. T.P. Wangler, *RF Linear Accelerators* (Wiley-VCH Verlag GmbH & Co. KGaA, 2008). ISBN: 978-3-527-40680-7
5. P.M. Lapostolle, Effects of the space charge in a proton linear accelerator. CERN report no. AR/Int. SG/65-15 (1965)
6. F.J. Sacherer, RMS envelope equations with space charge, in *Proceedings of PAC* (1971)
7. P.M. Lapostolle, M. Weiss, Formulae and procedures useful for the design of linear accelerators. CERN report no. CERN-PS-2000-001 (DR) (2000)
8. K.R. Crandall, Proposal for a new radial matching section for RFQ linacs. LANL technical report no. AT-1:83:3 (1983)
9. J.W. Staples, RFQ's – an introduction. LBL report no. LBL-29472 (1990)
10. C. Zhang, A. Schempp, Beam dynamics studies on a 200 mA proton radio frequency quadrupole accelerator. Nucl. Instrum. Methods Phys. Res. Sect. A **586** (2008)
11. C. Zhang, Linac design for intense hadron beams. Ph.D. thesis, Goethe University Frankfurt (2009)
12. C. Zhang et al., HSI RFQ upgrade for the UNILAC injection to FAIR, in *Proceedings of IPAC* (2016)
13. R. Chasman, Numerical calculations of the effects of space charge on six dimensional beam dynamics in proton linear accelerators, in *Proceedings of LINAC* (1968)
14. L. Smith et al., Round table discussion of space charge and related effects, in *Proceedings of LINAC* (1968)
15. R.A. Jameson, Equipartitioning in linear accelerators, in *Proceedings of LINAC* (1981)
16. I. Hofmann, Emittance growth of beams close to the space charge limit, in *Proceedings of PAC* (1981)
17. I. Hofmann, I. Bozsik, Computer simulation of longitudinal transverse space charge effects in bunched beams, in *Proceedings of LINAC* (1981)
18. I. Hofmann, Stability of anisotropic beams with space charge. Phys. Rev. E **57**, 4713 (1998)
19. I. Hofmann, *Space Charge Physics for Particle Accelerators* (Springer, 2017). ISBN: 9783319621562 (Print) & 9783319621579 (eBook)

20. TraceWin code, http://irfu.cea.fr/dacm/logiciels/
21. C. Zhang, H. Podlech, Design approach for a 325 MHz, 3 MeV, 70 – 100 mA proton radio-frequency quadrupole accelerator with low emittance transfer. Nucl. Instrum. Methods Phys. Res. Sect. A **947** (2019)
22. C. Zhang, Minimizing emittance growth via low emittance transfer. Phys. Rev. Accel. Beams **25**, 034201 (2022)
23. Y. Kondo, T. Morishita, R.A. Jameson, Development of a radio frequency quadrupole linac implemented with the equipartitioning beam dynamics scheme. Phys. Rev. Accel. Beams **22**, 120101 (2019)
24. Y.S. Cho, J.H. Jang, H.S. Kim, H.J. Kwon, and K.T. Seol, Design and Fabrication of PEFP 350 MHz RFQ, in *Proceedings of the KNS Spring Meeting* (2005)
25. H.F. Ouyang and S. Fu, Study of CSNS RFQ design, in *Proceedings of LINAC* (2006)
26. Y. Kondo, K. Hasegawa, T. Morishita, R.A. Jameson, Beam dynamics design of a new radio frequency quadrupole for beam-current upgrade of the japan proton accelerator research complex linac. Phys. Rev. ST Accel. Beams **15**, 080101 (2012)
27. Q.Z. Xing et al., A 3-MeV RFQ accelerator for the compact pulsed hadron source at Tsinghua University. Phys. Procedia **26**, 36 (2012)
28. C. Rossi et al., The radiofrequency quadrupole accelerator for the Linac4, in *Proceedings of LINAC* (2008)
29. M. Syha, Beam dynamics design of the FAIR proton-linac RFQ and design study of a compact 325MHz RFQ. Ph.D. thesis, Goethe University Frankfurt (2021)
30. Manual of the LANL RFQ design codes, LANL report no. LA-UR-96-1836 (2005)
31. I. Hofmann, O. Boine-Frankenheim, Parametric instabilities in 3D periodically focused beams with space charge. Phys. Rev. Accel. Beams **20**, 014202 (2017)
32. T. Morishita, Y. Kondo, Electromagnetic design and tuning of the four-vane radio frequency quadrupole with nonuniform intervane voltage profile. Phys. Rev. Accel. Beams **23**, 111003 (2020)
33. T. Morishita et al., High-power test results of the RFQ III in J-PARC Linac, in *Proceedings of LINAC* (2014)
34. C. Rossi, Private communications (2021)
35. C.D. Child, Discharge of hot CaO. Phys. Rev. (Ser. I) **32**, 492 (1911)
36. I. Langmuir, The effect of space charge and residual gases on thermionic currents in high vacuum. Phys. Rev. **2**, 450 (1913)
37. M. Reiser, *Theory and Design of Charged Particle Beams*, Second, Updated and Expanded edn. (Wiley-VCH Verlag GmbH & Co. KGaA, 2008). Print ISBN: 9783527407415

Chapter 3
Injectors for Modern Science Facilities

Abstract Designed or revisited according to the theory introduced in Chap. 2, six RFQ accelerators, the injectors to the following modern science facilities at different scales, will be discussed as real examples:

- Large scale: Relativistic Heavy Ion Collider (RHIC) at Brookhaven National Laboratory (BNL).
- Medium to large scale: Facility for Antiproton and Ion Research (FAIR) at GSI (GSI Helmholtz Centre for Heavy Ion Research).
- Medium scale: High Brilliance Neutron Source (HBS) for Forschungszentrum Jülich.
- Small scale: Frankfurt Neutron Source at the Stern-Gerlach-Zentrum (FRANZ) for Goethe University Frankfurt.

So far, two of them have been built and put into routine operation for many years, two have been proposed, one will be tested with beams in the near future, and another one is under development. For designing the RFQ for the HBS facility, a special two-cavity solution has been applied. Its R&D study will be presented therefore in Chap. 5, introducing this special solution in details.

3.1 EBIS-Based RFQ for RHIC at BNL

The RHIC facility constructed in 1999 is one of the large-scale operating accelerators in the world. The collisions of gold ions were achieved first at a beam energy of 28 GeV/u in 2000 and then at the design beam energy of 100 GeV/u in 2001 [1]. To replace the original pre-injector, tandem Van de Graaff electro-static accelerators (see the bottom right corner of Fig. 3.1), an EBIS (Electron Beam Ion Source) based RF linac was proposed (near the booster in Fig. 3.1). Besides the advantage of a much shorter transport line to the booster, the modern pre-injector can provide a wide range of ion species from Helium to Uranium with various desired charge states and can meet all experiment needs of RHIC and the NASA Space Radiation Laboratory (NSRL) [2].

C. Zhang, *Radio-Frequency Quadrupole Accelerators*, Particle Acceleration and Detection, https://doi.org/10.1007/978-3-031-40967-7_3

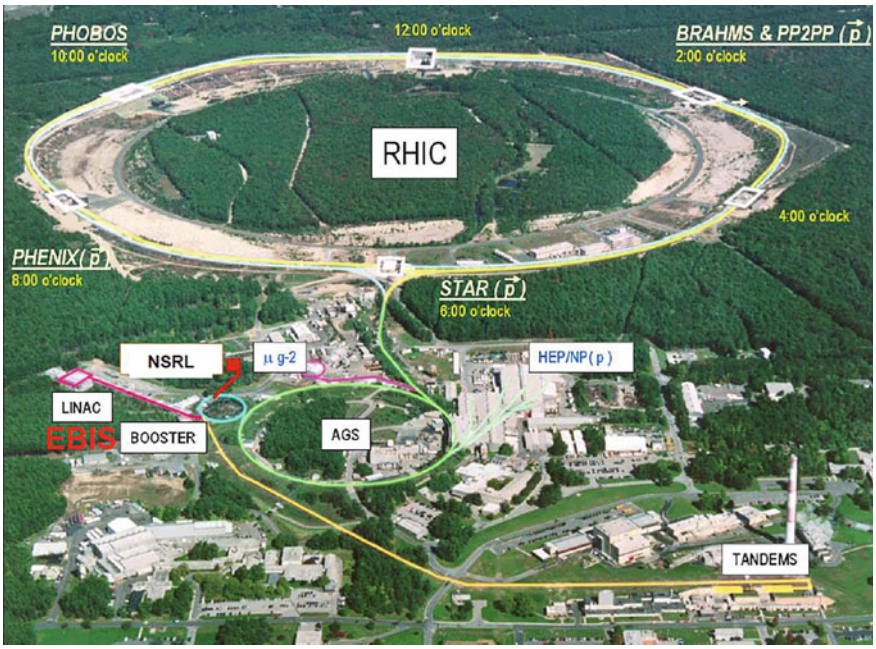

Fig. 3.1 Overview of the RHIC accelerator facility at BNL [2]

As shown in Fig. 3.2, the new pre-injector consists of a high current electron beam ion source, an RFQ accelerator and an IH-DTL. The design requirements for the EBIS-based pre-injector and the RFQ part are given in Tables 3.1 and 3.2, respectively.

To meet the design goal of the EBIS-based RFQ accelerator, i.e., to get a rather short structure with $L = 3.1$ m using a moderate inter-vane voltage of 70 kV [3], an NFSP-style design has been developed (see Fig. 3.3).

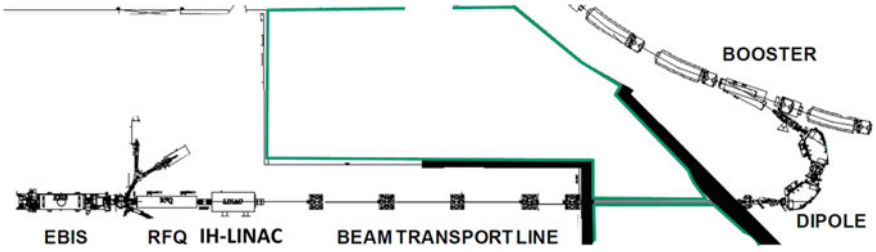

Fig. 3.2 Layout of the EBIS-based heavy ion pre-injector [2]

Table 3.1 Top-level requirements of the EBIS-based pre-injector [2]

Parameter	Value
Particle	Helium to Uranium
Q/A	$\geq$1/6
Beam current (emA)	>1.5
Pulse length (μs)	10–40 (for few-turn injection)
Repetition rate (Hz)	5
EBIS output energy (keV/u)	17
RFQ output energy (keV/u)	300
Linac output energy (MeV/u)	2
Time to switch species (s)	1

Table 3.2 Design specifications of the EBIS-based RFQ [2]

Parameter	Value
A/Q	6.25 ($\approx Au^{32+}$)
f (MHz)	100.625
W_{in} (keV/u)	17
W_{out} (keV/u)	300
I_{in} (emA)	10
$\varepsilon_{\text{t, in, n, rms}}$ (π mm mrad)	0.09
$\Delta\varepsilon_{\text{t}}$ (%)	$\leq$20
$\varepsilon_{z,\text{ out, n, rms}}$ (90%) (π keV/u deg)	$\leq$172
T (%)	>90

For some reasons, the design was optimized for $\varepsilon_{t,\text{ in, }n,\text{ rms}} = 0.0582$ π mm mrad (not the design value mentioned in Table 3.2), but later checked with larger input emittances. Using a Waterbag-type input distribution with 4000 macro-particles, the PARMTEQM simulation of the EBIS-based RFQ has been performed. The main results of the RFQ design are summarized in Table 3.3.

Table 3.4 shows that the EBIS-based RFQ still has high beam transmission efficiency with lager input emittances, which are ~1.5 or 2 times the adopted design value, respectively. In Case 2b ($I_{\text{in}} = 10$ emA, $\varepsilon_{\text{t, in, n, rms}} = 0.09$ π mm mrad), i.e., the required design case (see Table 3.2), the transverse emittance growth is 18.7% in the x plane or 16.6% in the y plane and the longitudinal output emittance is 21.6 π keV/u deg for 99% of transported particles. All of them are well inside the required ranges.

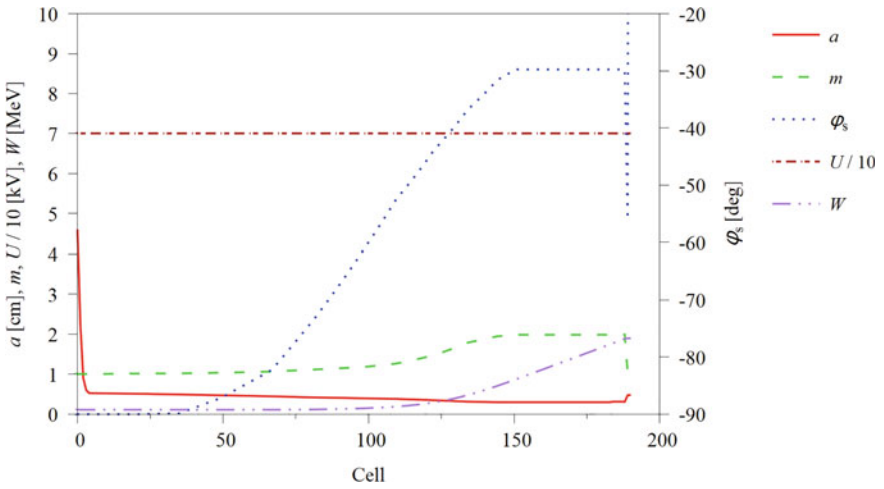

Fig. 3.3 Evolution of the main parameters along the EBIS-based RFQ

Table 3.3 Main design parameters and simulation results of the EBIS-based RFQ

Parameter	Design CZ10
U (kV)	70
$\varepsilon_{t,\,in,\,n,\,rms}$ (π mm mrad)	0.0582
I_{in} (emA)	10
Kilpatrick factor	1.9
$\varepsilon_{x,\,out,\,n,\,rms}$ (π mm mrad)	0.0921
$\varepsilon_{y,\,out,\,n,\,rms}$ (π mm mrad)	0.0953
$\varepsilon_{z,\,out,\,n,\,rms}$ (π MeV deg)	0.1646
$\Delta\varphi_{out}$ (deg) (99% of transported particles)	$\pm$29
$\Delta\varphi_{out}$ (deg) (90% of transported particles)	$\pm$20
ΔW_{out} (keV/u) (99% of transported particles)	$\pm$9.0
ΔW_{out} (keV/u) (90% of transported particles)	$\pm$5.6
L (cm)	307.6
Total number of cells	191
T (%)	99.0

However, Fig. 3.4 shows that there are some halo particles in the output distribution especially in the longitudinal phase space. As mentioned, the design goals were focused on achieving good transmission and a short RFQ length with a moderate inter-vane voltage, so no special attention was paid to halo particles and emittance growths.

Table 3.4 Simulation results of the EBIS-based RFQ with different input beams

Case	$\varepsilon_{t,\,in,\,n,\,rms}$	I_{in} (emA)	T (%)	$\varepsilon_{x,\,out,\,n,\,rms}$ (π mm mrad)	$\varepsilon_{y,\,out,\,n,\,rms}$ (π mm mrad)	$\varepsilon_{z,\,out,\,n,\,rms}$ (π MeV deg)
1a	0.0582 (adopted design value)	0	98.5	0.064	0.062	0.284
1b	0.0582 (adopted design value)	10	99.0	0.092	0.095	0.165
2a	0.0900 (required design value)	0	98.5	0.098	0.096	0.294
2b	0.0900 (required design value)	10	98.8	0.117	0.114	0.331
3a	0.1164 (2 × adopted design value)	0	98.4	0.126	0.124	0.271
3b	0.1164 (2 × adopted design value)	10	98.7	0.150	0.154	0.330

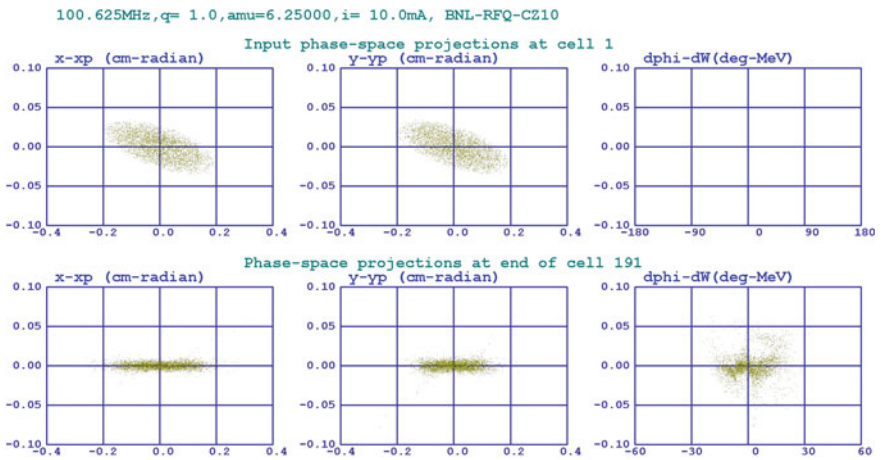

Fig. 3.4 Input (top) and output (bottom) distributions of the EBIS-based RFQ

Revisiting this design, one can see in Fig. 3.5 that the emittance ratio for the main part of the RFQ is between 2.0 and 4.0, which is beyond the optimum range required by the MEGLET method and should be the suitable range for the SEGLER method.

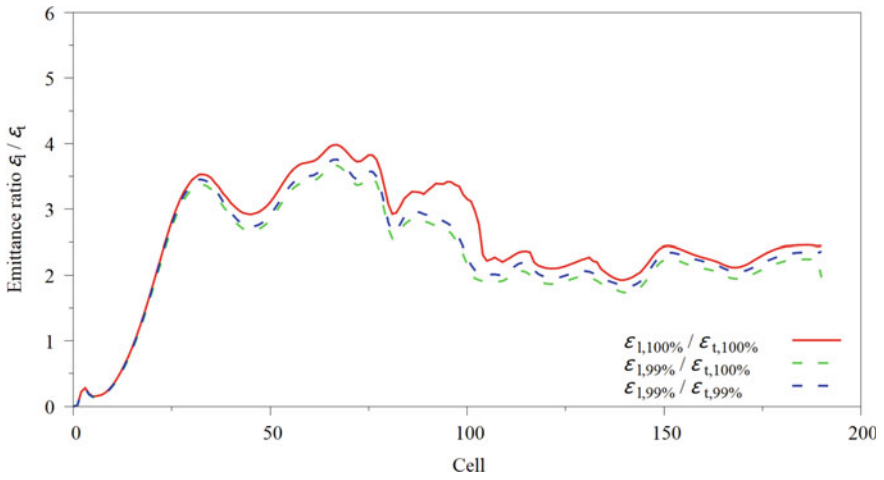

Fig. 3.5 Evolution of emittance ratios along the EBIS-based RFQ

In Fig. 3.6, one can see more clearly that:

- The pre-bunching is ended at Cell 32 with $\frac{\varepsilon_l}{\varepsilon_t} \approx 3.6$.
- Afterwards, the first emitance transfer period starts and continues until the exit of the RFQ (there is no second emittance transfer, as the required energy gain of the RFQ is relatively low).
- Significant emittance transfer starts at Cell 70, as the tune footprints enter the $\frac{\sigma_l}{\sigma_t} = 0.5$ resonance peak (see Fig. 3.7).

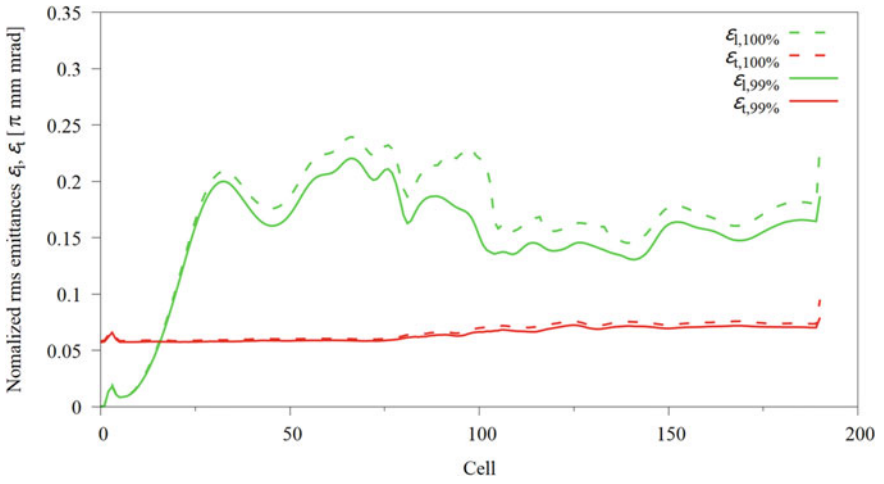

Fig. 3.6 Evolution of longitudinal and transverse emittances for 100% and 99% of particles along the EBIS-based RFQ

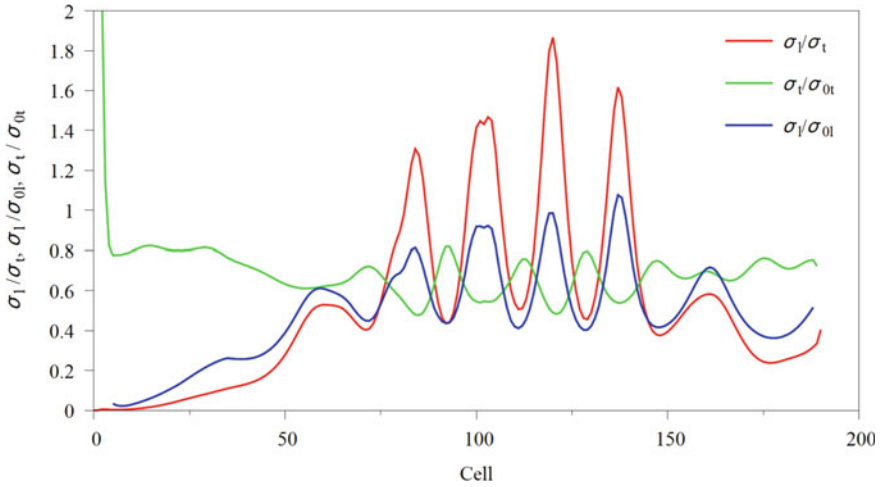

Fig. 3.7 Tune ratio and tune depressions along the EBIS-based RFQ

- At Cell 80, the tune footprints leave the "safe ¼ ellipse" of the SEGLER method.
- At Cell 105, $\frac{\varepsilon_1}{\varepsilon_t}$ is decreased to 2.0 (see the $\frac{\varepsilon_{1,99\%}}{\varepsilon_{t,100\%}}$ curve) and the emittance transfer is slowed down.
- The tune footprints return to the "safe ¼ ellipse" after Cell 140, so the emittance transfer is not obvious any more.

From today's point of view, this design can be improved by:

- Optimizing the pre-bunching by ending it with a smaller emittance ratio.
- Reducing $\frac{\sigma_1}{\sigma_t}$ to be below 1 between Cell 80 and Cell 140 so that the tune footprints can stay inside the "safe ¼ ellipse" as required by the SEGLER method.

During the beam commissioning, Au^{32+}, He^{1+} and Fe^{20+} ions were successfully accelerated by the constructed EBIS-based RFQ (see Fig. 3.8) and a good agreement between the measurements and the simulations has been found [2, 4]. In addition, the required matching conditions into the IH-DTL can be well fulfilled (see Fig. 3.9). The EBIS-based RFQ has been in routine operation for more than 10 years.

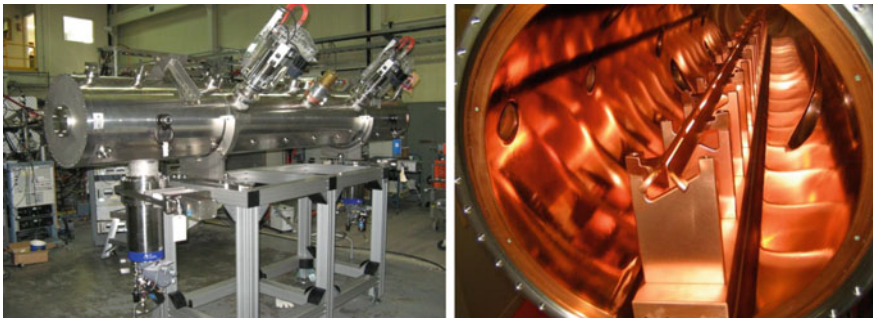

Fig. 3.8 The constructed EBIS-based RFQ [2]

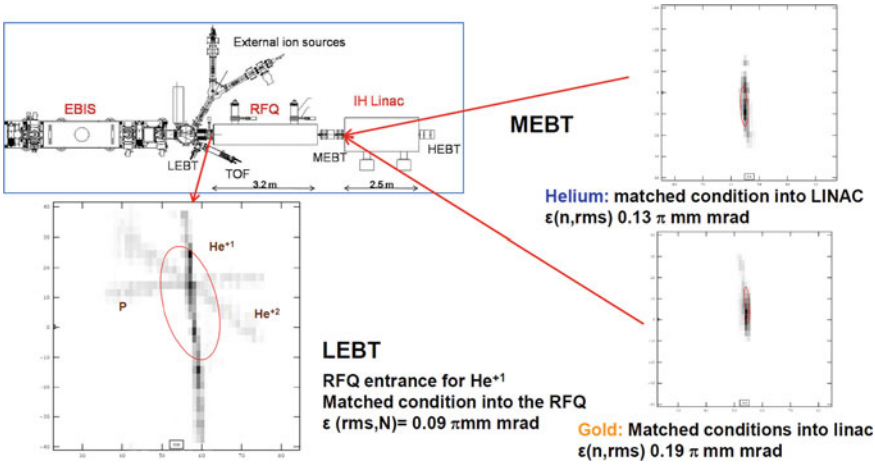

Fig. 3.9 Beam measurements for the EBIS-based RFQ [2]

3.2 CW HLI RFQ for GSI

Figure 3.10 shows the existing accelerator complex at GSI (marked in blue) and the accelerator facilities under construction for the future Facility for Antiproton and Ion Research (FAIR, marked in red) [5]. In the figure, two linacs can be seen. One is the existing UNILAC that can provide a wide range of ion species from protons to Uranium ions, and another one is the proposed p-Linac dedicated for providing high current protons. This section and the next two sections will present two RFQ designs made for the two injectors to the UNILAC, i.e., the high charge state injector (in German: Hochladungsinjektor, HLI) and the high current injector (in German: Hochstrominjektor, HSI), respectively, as well as several RFQ designs proposed for the p-Linac.

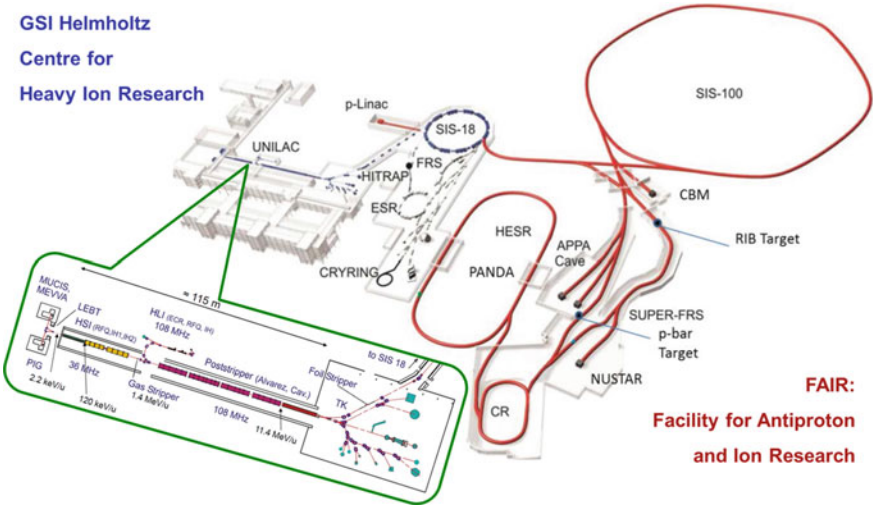

Fig. 3.10 Overview of the accelerator facilities for GSI (blue) and FAIR (red)

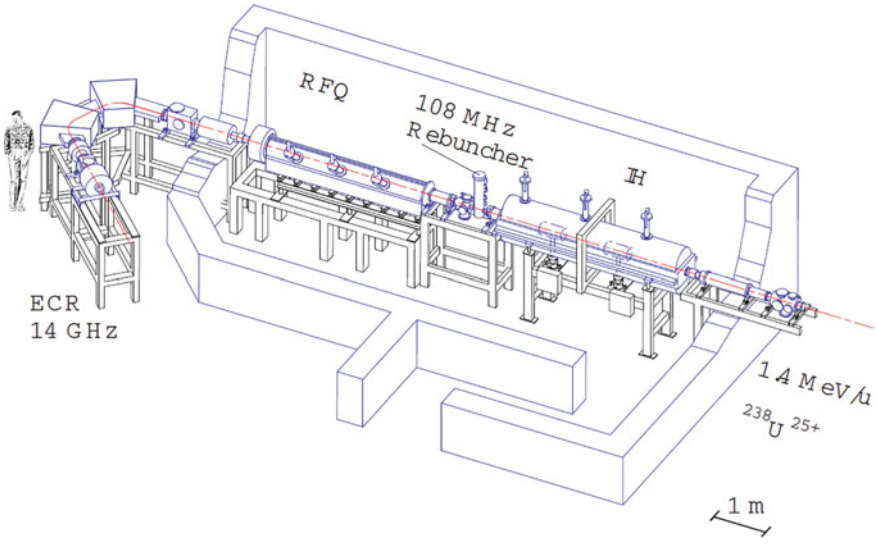

Fig. 3.11 The high charge state injector HLI at GSI [6]

Consisting of an ECR (Electron Cyclotron Resonance Source) ion source, an RFQ, and an IH-DTL, the HLI linac (see Fig. 3.11) needs to accelerate highly charged ion beams to 1.4 MeV/u at high duty cycle for the further acceleration in the Alvarez cavities of the UNILAC. The ion beams from the HLI have enabled many important

Table 3.5 Design specifications of the first HLI RFQ and the CW HLI RFQ

Parameter	First HLI RFQ [7]	CW HLI RFQ [9]
Design A/Q	8.5	6.0
f (MHz)	108.48	108.48
W_{in} (keV/u)	2.5	4
W_{out} (keV/u)	300	300
I_{in} (emA)	0	5
$\varepsilon_{\text{t, in, n, rms}}$ (π mm mrad)	0.05	0.1
U (kV)	80	55
L (m)	3	2
Duty cycle	25–50	100

Table 3.6 Main design parameters and simulation results of the CW HLI RFQ

Parameter	Design	CZA6
I_{in} (emA)	5	0
$\varepsilon_{\text{t, in, n, rms}}$ (π mm mrad)	0.1	0.1
$\varepsilon_{x,\text{ out, n, rms}}$ (π mm mrad)	0.105	0.102
$\varepsilon_{y,\text{ out, n, rms}}$ (π mm mrad)	0.101	0.102
$\varepsilon_{z,\text{ out, n, rms}}$ (π keV/u deg)	9.5	16.1
$\Delta\varphi_{\text{out}}$ (deg) (100% of transported particles)	$\pm$35.0	$\pm$19.6
$\Delta\varphi_{\text{out}}$ (deg) (99% of transported particles)	$\pm$20.0	$\pm$17.2
ΔW_{out} (keV/u) (100% of transported particles)	$\pm$5.5	$\pm$5.7
ΔW_{out} (keV/u) (99% of transported particles)	$\pm$4.1	$\pm$5.2
L (m)	2	2
Total number of cells	153	153
T (%)	91.3	98.6

experiments at GSI, e.g., discovery of new elements, super heavy element research, and heavy ion cancer therapy.

Designed for a duty cycle up to 50%, the first HLI injector was built and tested with beams in 1991 [7, 8]. To meet the growing demand for higher (average) beam currents, two upgrade measures were decided: (1) to upgrade the ion source for directly increasing the beam current; and (2) to upgrade the entire injector from pulsed to CW operation [6].

The replacement of the RFQ was the first step towards a CW capable injector. In Table 3.5, a comparison of the design specifications between the first pulsed RFQ and the new CW RFQ is listed. Besides increasing the maximum duty cycle by a factor of two, the design goal was to shorten the RFQ length by ~30% whilst using a ~30% lower U. Meanwhile, high beam transmission, small energy spread, and small transverse emittance growth for a good matching to the IH-DTL were also required.

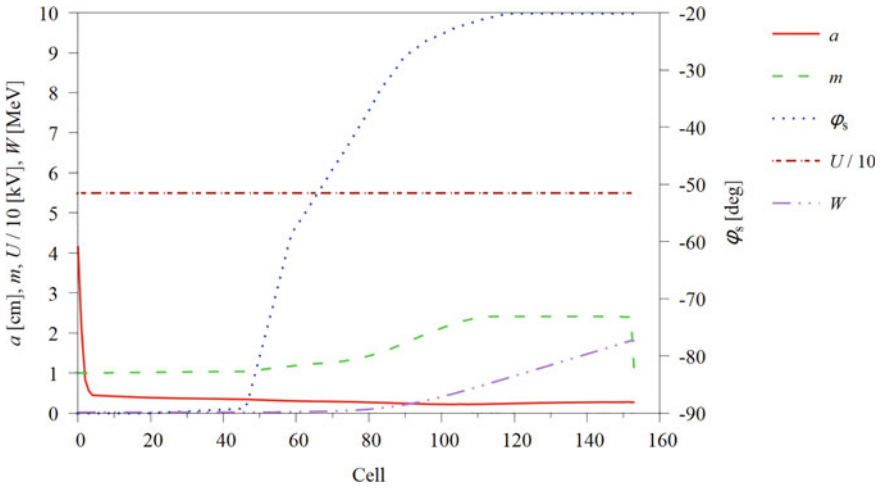

Fig. 3.12 Evolution of the main design parameters along the CW HLI RFQ

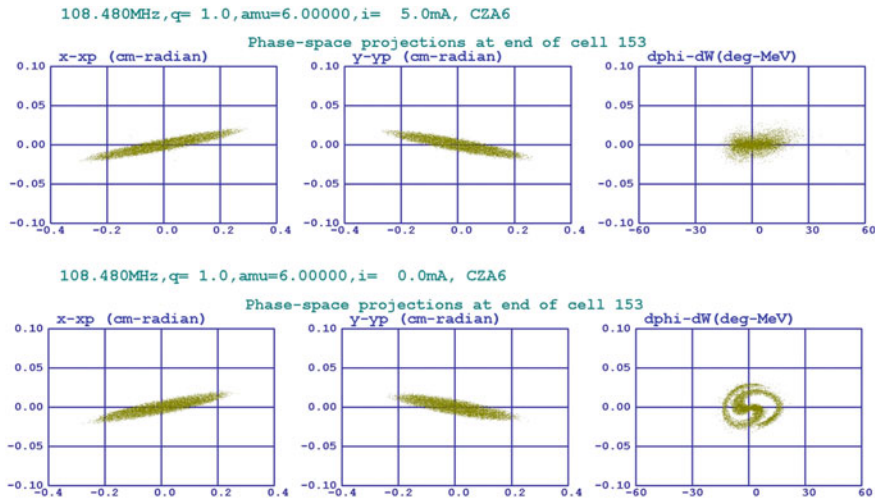

Fig. 3.13 Output distributions of the CW HLI RFQ at 5 emA (top) and 0 emA (bottom)

The evolution of the main parameters along the realized CW HLI RFQ is plotted in Fig. 3.12, and the detailed simulation results are summarized in Table 3.6.

For both the design case (5 emA) and the zero-current case (0 emA), the beam transmission efficiency is higher than 90%. The transverse emittance growth is insignificant, and the energy spread and the phase spread of the output beam are small.

Figure 3.13 shows the output phase spaces for both 5 emA and 0 emA. The transverse particle distributions are similar, while the longitudinal particle distribution at

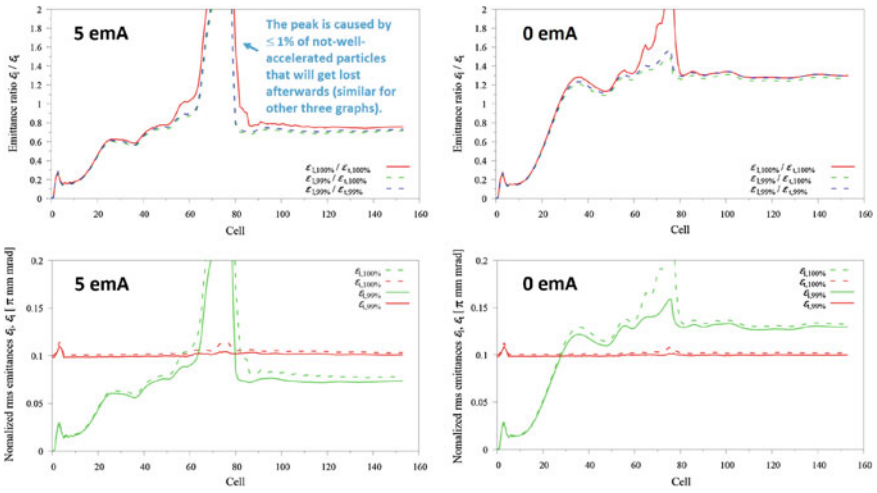

Fig. 3.14 Evolution of emittance ratios (top) as well as evolution of longitudinal and transverse emittances for 100% and 99% of particles (bottom)

0 emA has a larger emittance (with a lot of empty area inside) than that at 5 emA. This is because the bunching force designed for 5 emA was applied to a zero-current beam.

The emittance ratios as well as the emittance values are plotted in Fig. 3.14 as a function of cell number. At zero current, emittance transfer can also occur (e.g., around Cell 35 where the beam enters the $\frac{\sigma_l}{\sigma_t} = 0.5$ resonance peak). The CW HLI RFQ has mainly $\frac{\varepsilon_l}{\varepsilon_t} \approx 1.3$ at 0 emA, which is inside the optimum emittance ratio range of the MEGLET method, so the emittance transfer is not obvious. For the case of 5 emA ($\frac{\varepsilon_l}{\varepsilon_t} \approx 0.8$ for the main part of the RFQ, which is very close to the optimum range), also no significant emittance transfer can be observed.

There is another reason for the low emittance transfer. In order to get a short structure, φ_s was increased very fast after Cell 45 and many particles were excluded from the rapidly shrinking longitudinal acceptance (see the longitudinal particle distributions for Cell 55 in Fig. 3.15), especially in the 5 emA case. These particles did not contribute to the emittance transfer and were going to be lost in the later cells (the transmission efficiency is ~7% lower at 5 emA).

The CW HLI RFQ has been built and tested with different kinds of beams [6, 9]. Although a stable CW operation cannot yet be reached due to mechanical and thermal instabilities of the RF structure, the measurements showed that "the beam dynamics performed well" [6]. To fix the flaws in the RF structure design, a dedicated PhD study has been recently done [10].

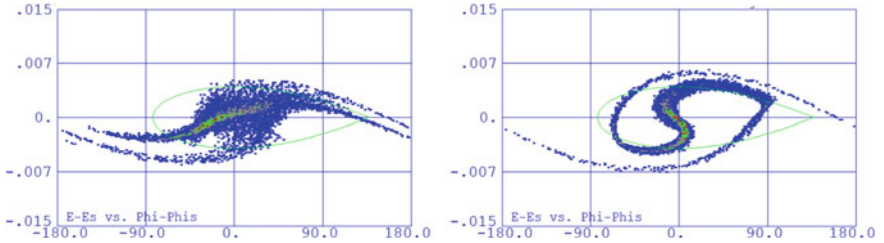

Fig. 3.15 Longitudinal phase spaces at Cell 55 for 5 emA (left) and 0 emA (right), where the green curves indicate the longitudinal acceptances

3.3 HSI RFQ Upgrade for FAIR

In order to enable various unique physics experiments, the FAIR facility will need to provide particle beams with unprecedented intensity and quality [5]. The existing UNILAC and the proposed p-Linac will be responsible for providing high current ion and proton beams to the FAIR facility, respectively.

Accelerating a wide variety of particle species from protons to uranium ions in the energy range of 2.2–120 keV/u, the 36.136 MHz HSI RFQ is a starting accelerating structure of the UNILAC, so it has a decisive influence on the beam performance of the whole machine.

Some major milestones in the development of the HSI RFQ are as follows:

- In 1996, the design of the first HSI RFQ for U^{4+} ions with a design current of $I_{in} = 16.5$ emA was started [11].
- In 1998, the first HSI RFQ (hereafter referred to as Version-1998) was constructed [12].
- In 1999, the Version-1998 RFQ was put into operation.
- In 2004, the electrodes were renewed with a modified radial matching section for a larger acceptance.
- In 2008, the second HSI RFQ (hereafter referred to as Version-2008) was designed (still for U^{4+} but I_{in} was increased to 20 emA) and constructed [13]. For this upgrade, the inter-vane voltage U was increased from 125 to 155 kV.
- In 2009, the Version-2008 RFQ was put into operation.
- From 2009 until now, the Version-2008 RFQ is in routine operation (in 2019, the electrodes were renewed but still based on the same design).
- Since 2015, in order to meet the beam intensity requirement for FAIR, the R&D for a third version of the HSI RFQ has been started.

The main design parameters of the two constructed HSI RFQs can be found in Table 3.7 (see the later part of this section for a comparison with a design made for the third version of the HSI RFQ). The design goals for the new version are as follows:

Table 3.7 Comparison of HSI-RFQ designs

	Design CZ2016	Version-2008	Version-1998
W_{in} (keV/u)	2.2	2.2	2.2
W_{out} (keV/u)	120	120	120
U (kV)	125	155	125
$r_{0,\text{avg}}$ (cm)	0.58	0.60	0.61
$E_{\text{s, max}}$ (MV/m)	30.2	31.2	31.8
g_{min} (cm)	0.53	0.60	0.49
I_{in} (emA)	20	20	16.5
$\varepsilon_{\text{t, in, un, total}}$ (π mm-mrad)	210	210	138
$\varepsilon_{\text{t, in, n, rms}}$ (π mm-mrad)	0.076	0.076	0.050
$\alpha_{\text{Twiss, t, in}}$	0.6	0.6	0.43
$\beta_{\text{Twiss, t, in}}$ (cm/rad)	13.6	13.6	4.6
Total number of cells	384	409	357
L (cm)	916.4	921.7	921.749
T (%)	94.1	88.5	89.5

- $I_{\text{in}} = 20$ emA with $T \geq 90\%$ (for real operation, 18 emA and 16.2 emA will be expected at the entrance and the exit of the RFQ, respectively).
- The maximum surface electric field $E_{\text{s, max}}$ should be lower than that of the Version-2008 RFQ.
- L should be kept same so that the same tank can be used.
- Last but not least, a high brilliance of the output beam is expected. The brilliance is an important index to measure the beam quality. There are different definitions for the brilliance $\widetilde{B}$ and the one used by this study is given as follows:

$$\widetilde{B} \equiv \frac{I}{\varepsilon_x \varepsilon_y} \quad \text{or} \quad \widetilde{B} \equiv \frac{I}{\varepsilon_{\text{t}}^2} \tag{3.1}$$

  where I is the beam current in mA, ε_x and ε_y are the transverse emittances in π mm mrad, and $\varepsilon_{\text{t}} = \left(\varepsilon_x + \varepsilon_y\right)/2$ (for $\widetilde{B}$, the factor $1/\pi^2$ can be left out). No matter which definition is used, for a given input beam, a design with a high $\widetilde{B}$ requires both high beam transmission and low emittance growth.

As the Version-1998 RFQ was designed for a lower current, i.e., 16.5 emA, the following discussions will focus on the Version-2008 RFQ and two new designs proposed for the third version of the HSI RFQ with $I_{\text{in}} = 20$ emA. For completeness, however, the design parameters of the Version-1998 RFQ will be also included in the figures and tables.

Using the same design input beam as the Version-2008 RFQ, a new design made in 2016 (hereafter referred to as Design CZ2016) [14] is based on the NFSP method (see Fig. 3.16).

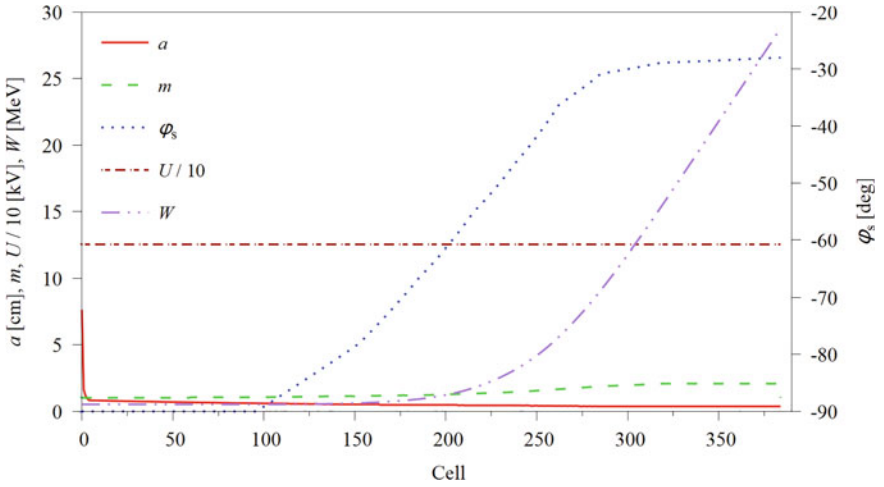

Fig. 3.16 Main design parameters of the Design-CZ2016 HSI RFQ

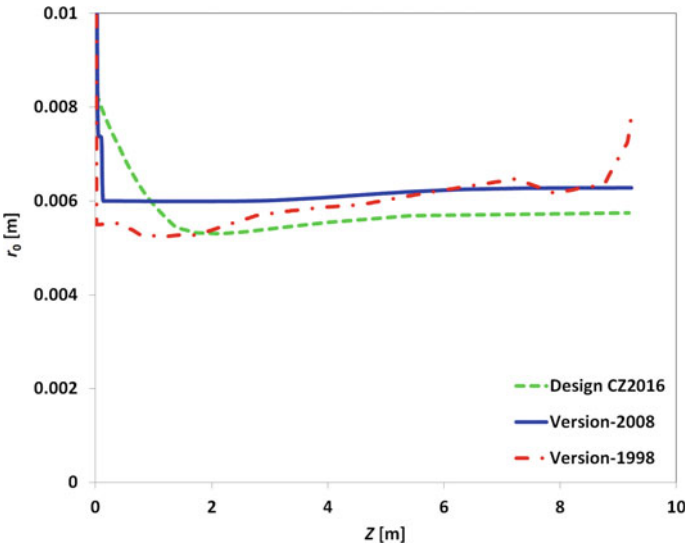

Fig. 3.17 Evolution of the mid-cell aperture of electrodes r_0 along the HSI RFQ

Figure 3.17 compares the evolution of the mid-cell aperture of the electrodes, r_0, along the RFQ. Different from the Version-1998 RFQ, which r_0 is always changing, the Version-2008 RFQ and the Design-CZ2016 RFQ have a relatively constant r_0 along the main part of the structure. This can help to make the RF tuning easier, especially for a > 9-m-long machine. The average r_0 of the Design-CZ2016 RFQ is only 0.02 cm smaller than that of the Version-2008 RFQ, but it allows reducing

the inter-vane voltage from 155 to 125 kV with still sufficient focusing. This change will not only lower $E_{s,\,max}$ but also save the RF power significantly. In addition, a special feature of the Design-CZ2016 RFQ is that it decreases r_0 gradually (not sharply) at the entrance, which can improve the transverse acceptance considerably (see Fig. 3.17).

In Fig. 3.18, the acceleration efficiency, A, which is defined in Eq. (2.4), is plotted as a function of the longitudinal position. It can be seen that the Design-CZ2016 RFQ has a more gentle pre-bunching but a much faster main bunching than the Version-2008 RFQ. In this way, the Design-CZ2016 RFQ can achieve the same energy gain over an almost identical distance (see Fig. 3.19) despite a ~20% lower inter-vane voltage. As shown in Table 3.7, the Design-CZ2016 RFQ is ~5 cm shorter, which leaves some room for the fine-tuning of the design.

The detailed parameters of the Design-CZ2016 RFQ together with the two constructed HSI RFQs are compared in Table 3.7. It can be seen that the Design-CZ2016 RFQ has not only the highest beam transmission efficiency, but also the lowest $E_{s,\,max}$ (favorable for reducing the risk of sparking) among the three designs. In addition, the average mid-cell aperture of the electrodes $r_{0,\,avg}$ of the Design-CZ2016 RFQ is only 0.02 cm smaller that of the Version-2008 RFQ so that the current rings for carrying electrodes should be still applicable as well as no big tuning efforts will be needed.

The two constructed HSI RFQs were designed many years ago, so most of the simulation data cannot be found any more. Fortunately, the simulated output particle distributions of these two designs based on an off-design input beam with $I_{in} = 25$ emA and the unnormalized total transverse input emittance

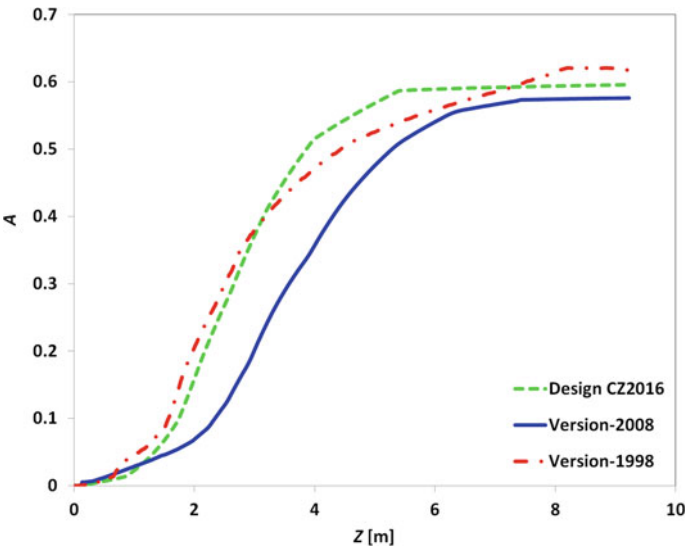

Fig. 3.18 Evolution of the acceleration efficiency A along the HSI RFQ

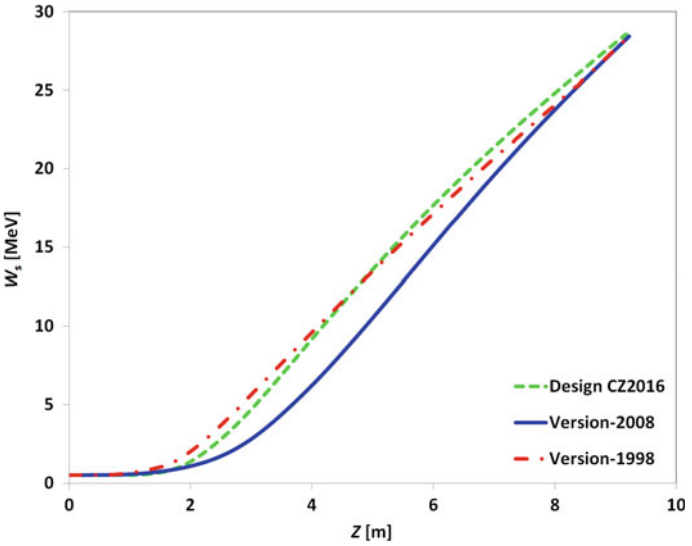

Fig. 3.19 Evolution of the synchronous energy along the HSI RFQ

$\varepsilon_{\text{t, in, un, total}} = 210\ \pi$ mm mrad (equivalent $\varepsilon_{\text{t, in, n, rms}} = 0.076\ \pi$ mm mrad) are still available. For a comparison, the Design-CZ2016 RFQ was also simulated with this input beam. The output distributions for all three versions are plotted together in Fig. 3.20. It should be mentioned that for the Version-1998, only 2000 input macro-particles were used, and for the two newer versions, 10^4 input macro-particles were used.

The results from this comparison are given in Table 3.8. Although the transverse output emittance values of the newest design are larger than those of the previous designs (because of the much higher beam transmission efficiency), actually the emittance growth is $\leq$0%. Meanwhile, the longitudinal output emittance of the new design is much smaller than that of the Version-1998 RFQ and comparable to that of the Version-2008 RFQ.

Furthermore, some other off-design cases have been also checked for the Design-CZ2016 RFQ. For example, I_{in} and $\varepsilon_{\text{t, in, un, total}}$ were increased from 20 to 35 emA and from 210 to 280 π mm mrad, respectively, both calculated beam transmission efficiencies were still 84%. All these results indicated the robustness of the new design.

Very recently in 2022, a new design for the HSI RFQ (hereafter referred to as Design CZ2022) [17] has been developed with the following motivations:

- To decrease U from 125 to 120 kV for further lowering $E_{\text{s, max}}$ and saving more RF power (the power is proportional to U^2).
- To apply the recently developed MEGLET approach for further improving the brilliance.

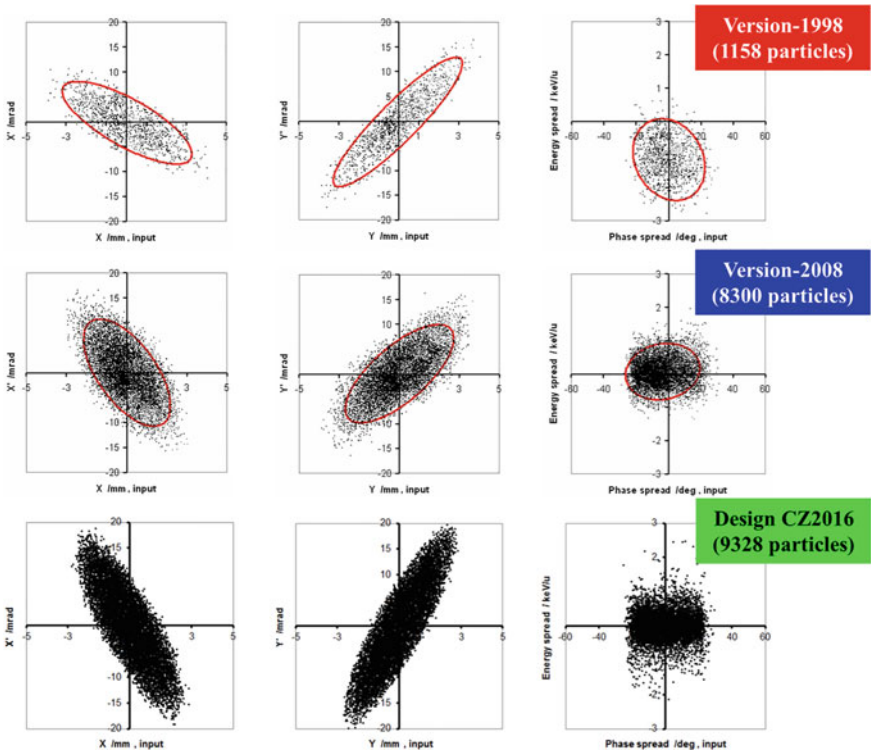

Fig. 3.20 Output phase spaces for $I_{\text{in}} = 25$ emA and $\varepsilon_{\text{t, in, un, total}} = 210$ π mm mrad (the graphs for Version-1998 and Version-2008 are from [15, 16])

Table 3.8 Comparison of simulated output distributions of the HSI-RFQ designs (for an off-design input beam: $I_{\text{in}} = 25$ emA and $\varepsilon_{t,\text{ in, un, total}} = 210$ π mm mrad)

	Design CZ2016 @ 25 emA	Version-2008 @ 25 emA	Version-1998 @ 25 emA
$\varepsilon_{\text{t, in, un, total}}$ (π mm mrad)	210	210	210
$\varepsilon_{\text{t, in, n, rms}}$ (π mm mrad)	0.076	0.076	0.076
Number of input macro-particles	10,000	10,000	2000
Number of output macro-particles	9328	8300	1158
T (%)	93.3	83	57.9
$\varepsilon_{x,\text{ out, n, rms}}$ (π mm mrad)	0.076	0.066	0.064
$\varepsilon_{y,\text{ out, n, rms}}$ (π mm mrad)	0.074	0.069	0.063
$\varepsilon_{z,\text{ out, n, rms}}$ (π keV/u ns)	0.327	0.325	0.472

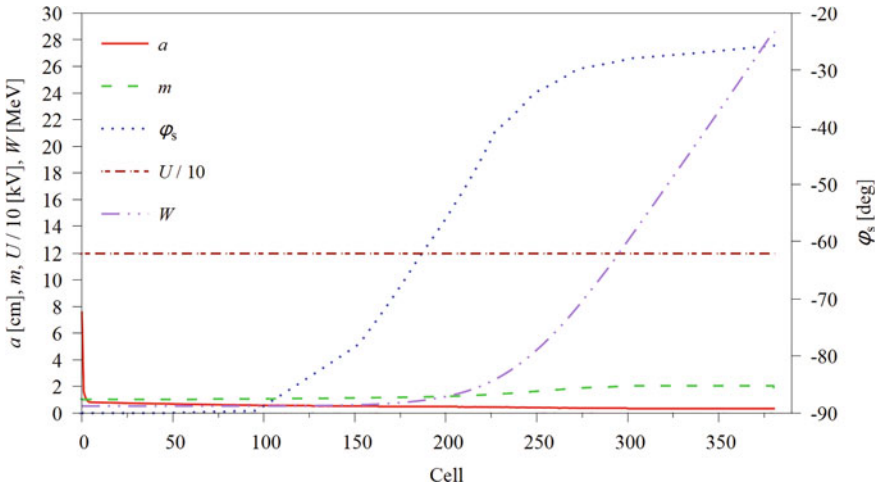

Fig. 3.21 Main design parameters of the Design-CZ2022 HSI RFQ

For the Design-CZ2022 RFQ, the same input emittances ($\varepsilon_{t,\,in,\,un,\,total} = 210\ \pi$ mm mrad or $\varepsilon_{t,\,in,\,n,\,rms} = 0.076\ \pi$ mm mrad) and Twiss parameters (see Table 3.7) as the Version-2008 RFQ were adopted. Comparing Fig. 3.21 with Fig. 3.16, one can see that the MEGLET-style Design-CZ2022 RFQ is quite similar to the Design-CZ2016 RFQ, which means the Design-CZ2016 RFQ based on the NFSP method met the requirements of the MEGLET approach inadvertently.

The beam dynamics simulation of the Design-2022 HSI RFQ was firstly performed using PARMTEQM with a 4D Waterbag input distribution. In Fig. 3.22, it can be seen that that the emittance ratio evolves well within the range of $0.9 \leq \frac{\varepsilon_l}{\varepsilon_t} \leq 1.4$ along the main part of the Design-CZ2022 HSI RFQ.

The tune footprints of the Design-CZ2022 HSI RFQ are shown in Fig. 3.23. According to the definition used by MEGLET, the RFQ can be divided into the following three stages:

- Stage 1: from the RFQ entrance to Cell 110.
- Stage 2: between Cell 110 and Cell 242.
- Stage 3: from Cell 242 to the RFQ exit.

It can be seen that the tune footprints of Stage 2 have been covered by the "safe rectangle".

Table 3.9 compares the main parameters between Design CZ2022 and Design CZ2016. One can see that:

- The Design-CZ2022 RFQ will be more efficient, as U is 5 kV lower (the RF power is proportional to U^2).
- The Design-CZ2022 RFQ will be more reliable, as $E_{s,\,max}$ becomes <30 MV/m.

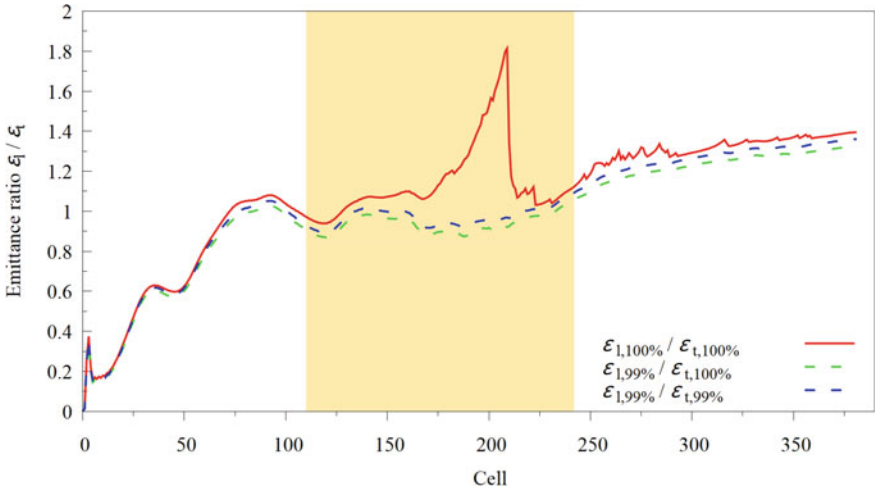

Fig. 3.22 Evolution of emittance ratios along the Design-CZ2022 HSI RFQ

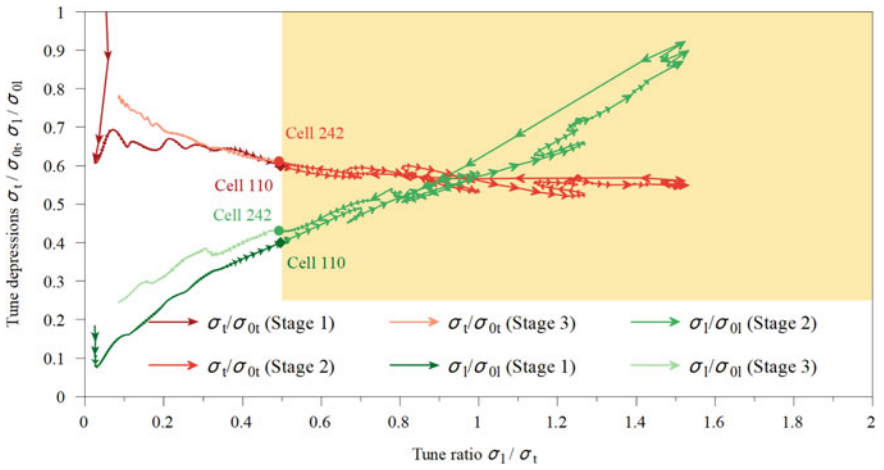

Fig. 3.23 Tune chart of the design-CZ2022 HSI RFQ

- The Design-CZ2022 RFQ has higher beam transmission and smaller output emittances, so the brilliance of the output beam has been also improved.

The Design CZ2022 is also checked with an input distribution generated by the DYNAC code with $\varepsilon_{t,\,\mathrm{in},\,n,\,\mathrm{rms}} = 0.076\ \pi$ mm mrad and the same Twiss parameters (but in the transverse directions, the distributions are Gaussian). The transverse phase spaces of the two used input distributions are shown in Fig. 3.24, which shows that the beam size and the maximum divergence angle are much larger those in the Gaussian case.

Table 3.9 Design CZ2022 versus Design CZ2016 for the HSI RFQ

	Design CZ2022	Design CZ2016
U (kV)	120	125
$r_{0,\,\mathrm{avg}}$ (cm)	0.58	0.58
$E_{\mathrm{s,\,max}}$ (MV/m)	29.9	30.2
g_{min} (cm)	0.53	0.53
I_{in} (emA)	20	20
$\varepsilon_{x,\,\mathrm{out,\,n,\,rms}}$ (π mm mrad)	0.070	0.071
$\varepsilon_{y,\,\mathrm{out,\,n,\,rms}}$ (π mm mrad)	0.072	0.072
$\varepsilon_{z,\,\mathrm{out,\,n,\,rms}}$ (π mm mrad)	0.0995	0.0998
Total number of cells	381	384
L (cm)	920.1	916.4
T (%)	96.2	94.1

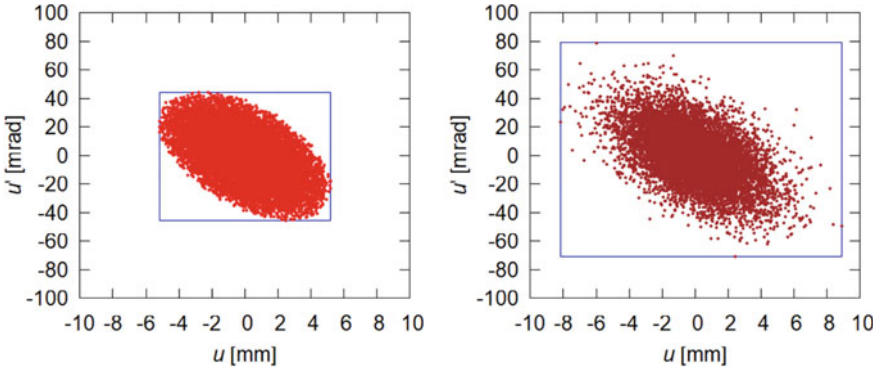

Fig. 3.24 4D Waterbag (left) and Gaussian (right) transverse input distributions (u represents the x or y direction)

In Figs. 3.25 and 3.26, the longitudinal and transverse emittances are plotted as functions of cell number for the Waterbag and Gaussian cases, respectively, where the emittance curves for 99% of particles are used to show the performance of the main beam by excluding 1% outmost particles. In the figures, the two emittance transfer periods, which are typical for a MEGLET-style RFQ, can be easily identified. It can be also seen that in order to obtain a high $\tilde{B}$ for the new HSI RFQ, the emittance transfer in the second period has been designed to be stronger than that in the first period so that one can get smaller transverse output emittances.

In the part marked in orange (see Figs. 3.25 and 3.26), the tune footprints of the beam are inside the "safe rectangle". Generally speaking, these two figures are similar. For the Waterbag case, the emittance ratio of the main beam is well held in the range of $0.9 \leq \frac{\varepsilon_{\mathrm{l}}}{\varepsilon_{\mathrm{t}}} \leq 1.4$ along the main part of the RFQ, as required by

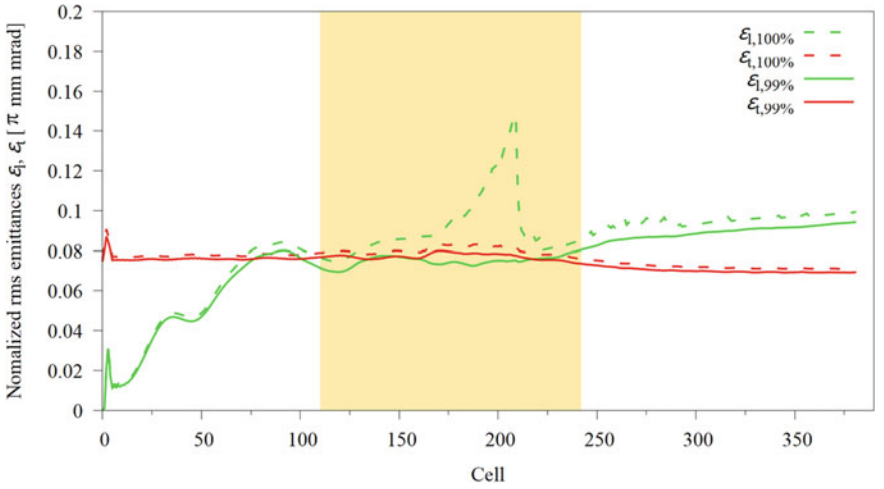

Fig. 3.25 Evolution of emittances for 100% and 99% of particles along the Design-2022 HSI RFQ (Waterbag case)

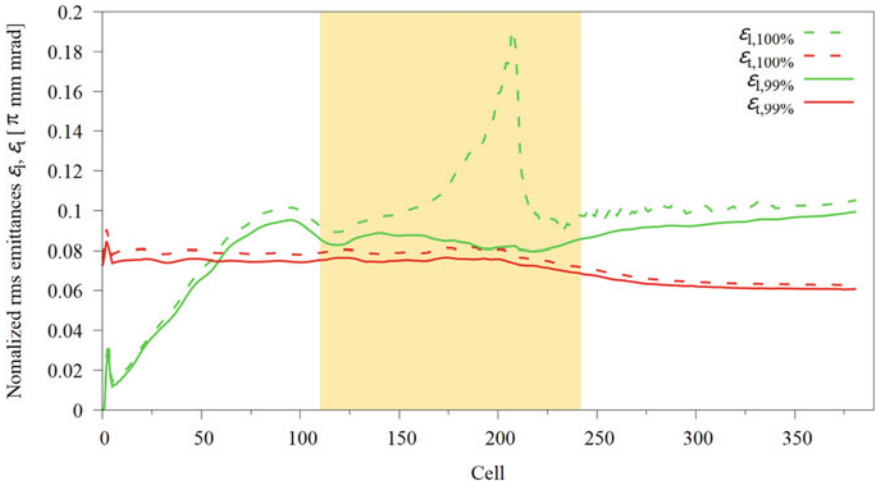

Fig. 3.26 Evolution of emittances for 100% and 99% of particles along the Design-2022 HSI RFQ (Gaussian case)

the MEGLET method. For the Gaussian case, the emittance transfer is stronger, but the maximum emittance ratio of the main beam is 1.7, still not far away from the optimum range.

Table 3.10 Simulated beam transmission and output emittances

	PARMTEQM waterbag	PARMTEQM Gaussian	DYNAC waterbag	DYNAC Gaussian
T (%)	96.2	90.3	96.1	90.9
$\varepsilon_{x,\,\mathrm{out,\,n,\,rms}}$ (π mm mrad)	0.070	0.063	0.079	0.068
$\varepsilon_{y,\,\mathrm{out,\,n,\,rms}}$ (π mm mrad)	0.072	0.063	0.077	0.068
$\varepsilon_{z,\,\mathrm{out,\,n,\,rms}}$ (π mm mrad)	0.099	0.105	0.088	0.097

For a benchmark, the DYNAC code has been taken. The main simulation results given by the two codes are compared in Table 3.10, which shows that no matter the beam transmission or the output emittances are comparable.

With the Gaussian input beam, more losses happened due to the larger total emittance (see Fig. 3.24). Nevertheless, for all cases, the beam transmission is still >90%. Except the transverse emittances of the DYNAC simulation in the Waterbag case are slightly larger than $\varepsilon_{\mathrm{t,\,in,\,n,\,rms}}$, all other transverse emittance values are much smaller than $\varepsilon_{\mathrm{t,\,in,\,n,\,rms}}$. This indicates a high brilliance of the Design-2022 HSI RFQ.

Figure 3.27 shows that the output particle distributions simulated by DYNAC are similar to those given by PARMTEQM for both the Waterbag case and the Gaussian case, especially in the transverse planes.

So far, several solutions have been proposed for the third version of the HSI RFQ:

- In 2016 (Design CZ2016), using one cavity with $U = 125$ kV and $E_{s,\,\mathrm{max}} = 30.2$ MV/m [14].
- In 2020 (see Chap. 5), using multiple short and independent cavities with $E_{\mathrm{s,\,max}} = 30.9$ MV/m (U varies from 120 to 147 kV, but it is constant in each cavity) [18].
- In 2022 (Design CZ2022), using one cavity with $U = 120$ kV and $E_{\mathrm{s,\,max}} = 29.9$ MV/m [17, 19].

However, a final decision to launch the upgrade project of the HSI RFQ has not yet been made.

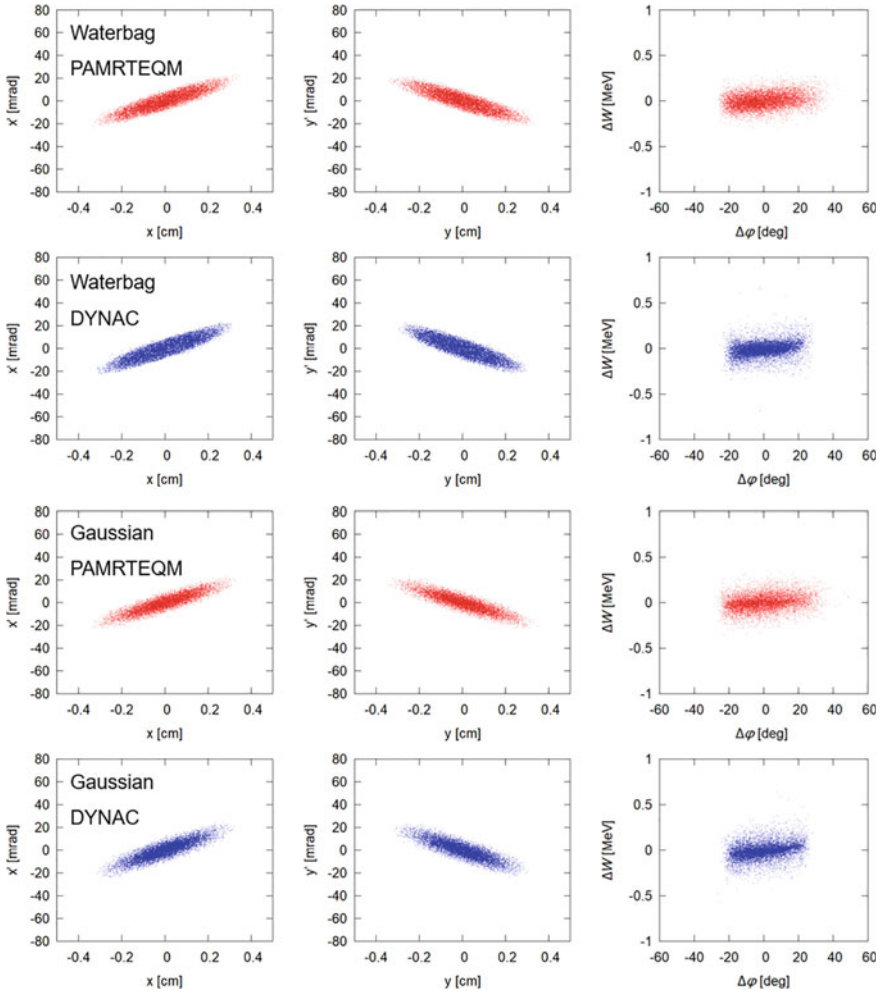

Fig. 3.27 Simulated output particle distributions of the Design-2022 HSI RFQ

3.4 p-Linac RFQ for FAIR

The p-Linac will be another important injector for the FAIR facility. The FAIR antiproton physics program demands a rate of 7×10^{10} cooled antiprotons per hour. The existing UNILAC can also deliver protons, but it is not capable to provide a proton beam with sufficient current for the production of the required antiprotons. Therefore, a dedicated proton linac, the so-called p-Linac, has been proposed to serve as a new injector for the FAIR facility.

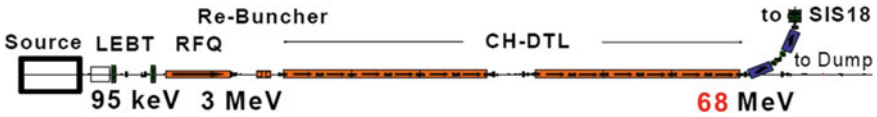

Fig. 3.28 Schematic layout of the FAIR p-Linac [20] (the original output energy 70 MeV was changed to 68 MeV in 2017)

As shown in Fig. 3.28, the planned p-Linac mainly consists of an RFQ accelerator and a chain of CH-DTL cavities operating at 325.224 MHz. It needs to provide a $\geq$35 emA, 68 MeV proton beam for the downstream synchrotrons at a duty cycle of 0.0144%.

The first reference design for the p-Linac RFQ was published in 2009 [21]. This RFQ (hereafter referred to as CZ2009) was optimized for 45 emA and could provide $\geq$95% transmission efficiency also at 70 emA or even at 100 emA.

This 3.2-m-long RFQ is very compact when considering the relatively high input energy W_{in} of 95 keV (compared with the W_{in} values adopted by other modern 3 MeV, >300 MHz H^+ or H^- RFQ accelerators, e.g., CERN Linac4 RFQ and J-PARC RFQ-III, see Table 2.2), as the length of the adiabatic bunching section is proportional to β^3 according to Eq. (2.36). At that time, it was required to achieve high transmission efficiency with a rather short structure, so no special attention was paid to halo particles and emittance growths. In the top graphs of Fig. 3.29, one can see that the CZ2009 p-Linac RFQ (the 70 emA matched case is taken for a comparison with the later designs optimized for 70 emA) has many halo particles in its output distribution.

In 2014, also based on the NFSP method, a design hereafter referred to as CZ2014a was developed with improved beam quality [22]. The CZ2014a RFQ is 10 cm shorter and the halo particles have been significantly reduced (see the second row of graphs in Fig. 3.29). In 2018, the CZ2014a design was further tuned by following the MEGLET strategy to minimize the number of halo particles. The resulting design hereafter referred to as CZ2018 [23] has an even smaller RFQ length, and the tail particles in the longitudinal phase space have almost disappeared at both 70 and 100 emA.

For all these simulations, 10^5 input macro-particles have been used and all transported particles have been included, i.e., no tail particles are removed from the simulation in the longitudinal plane. In addition, for this comparison, the input beam adopted by the CZ2014a design (slightly different to the design input beam for the CZ2018 p-Linac RFQ) was applied to the simulation for the CZ2018 design. Therefore, the presented results for the CZ2018 design have very small (ignorable) differences from those listed in [23].

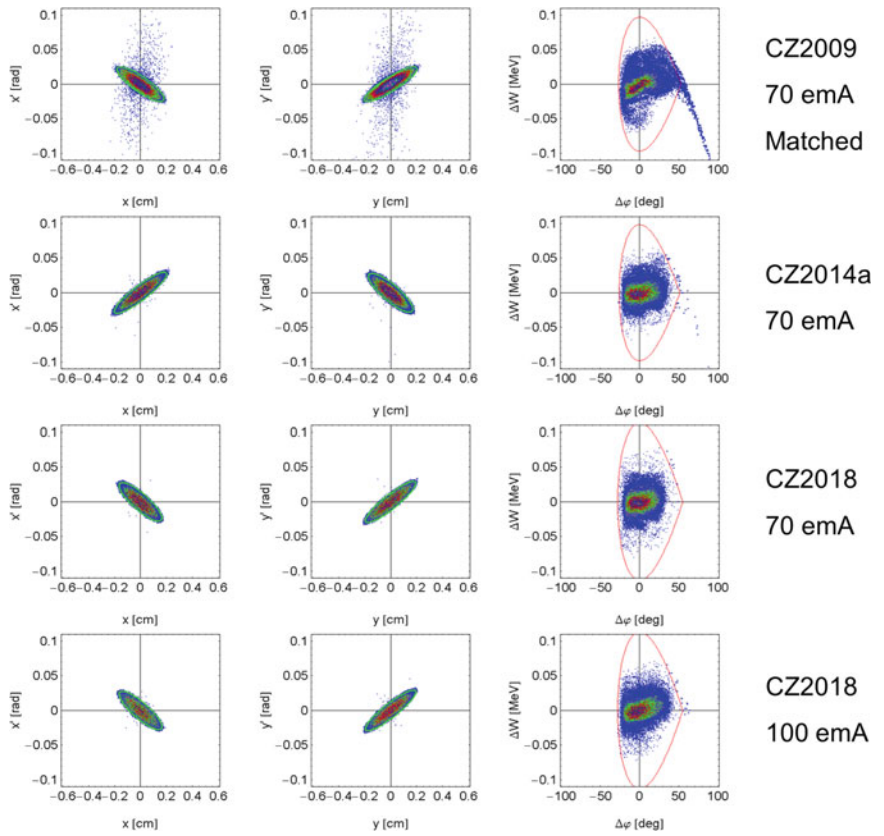

Fig. 3.29 Output particle distributions of different designs for the p-Linac RFQ, where the green ellipses include 99% of the beam and the red curves indicate the separatrix. The x and y output distributions of the CZ2014a design could be exchanged by rotating the RFQ by 90°

It can be seen that the evolution of the main design parameters of the CZ2018 RFQ in Fig. 3.30 is similar to that of the MEGLET RFQ in Fig. 2.8. The CZ2018 RFQ also has the two emittance transfer periods of MEGLET-style (see Fig. 3.31).

Recently, the p-Linac RFQ has been constructed but with another design (hereafter referred to as IAP2018) proposed by Institut für Angewandte Physik (IAP) of Goethe University Frankfurt [24]. One reason was that the construction costs of this RFQ had been provided by third-party funding and it could save the p-Linac project budget.

Some detailed results of all these four designs are compared in Table 3.11. From a physics point of view, the MEGLET-style CZ2018 RFQ has more advantages, not only in terms of beam quality (e.g., beam transmission and emittances) but also in terms of RF efficiency (e.g., RFQ length and inter-vane voltage).

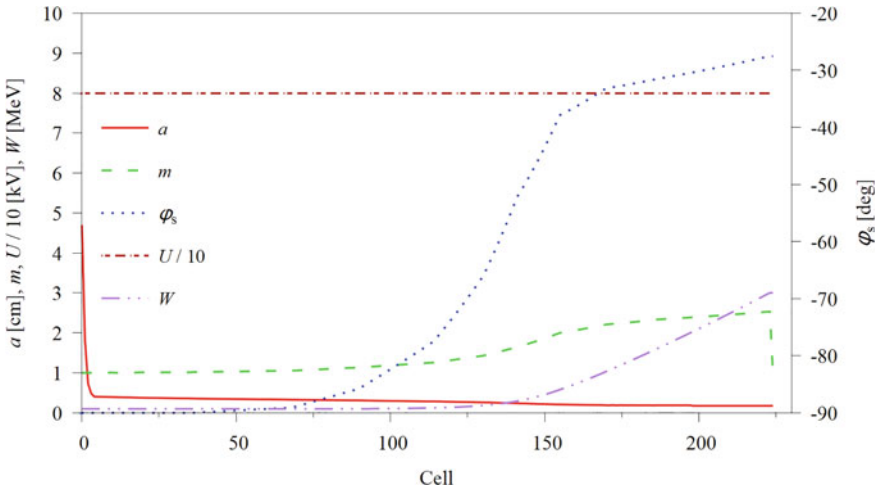

Fig. 3.30 Main design parameters of the CZ2018 p-Linac RFQ

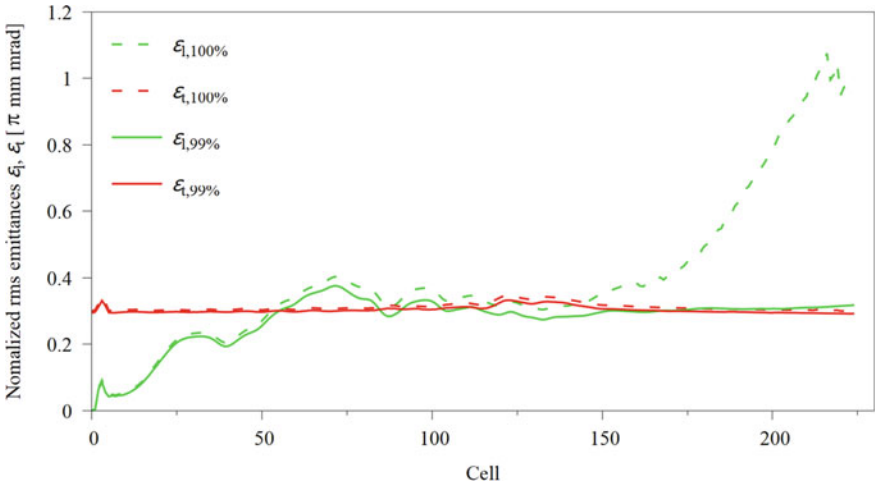

Fig. 3.31 Emittance evolution along the CZ2018 p-Linac RFQ

Table 3.11 Comparison of the designs for the p-Linac RFQ

	CZ2009 matched *NFSP* [21, 22]	CZ2014a *NFSP* [22]	CZ2018 *MEGLET* [23]	CZ2018 *MEGLET* [23]	IAP2018 *Modified FSP* [24]
I_{in} (emA)	70*	70	70	100	100
U (kV)	80	80	80	80	88.43
$\varepsilon_{t,\,in,\,n,\,rms}$ (π mm mrad)	0.30	0.30	0.30	0.30	0.30
$\varepsilon_{x,\,out,\,n,\,rms}$ (π mm mrad)	0.390 (all) 0.299 (acc.)	0.305 (all) 0.303 (acc.)	0.299 (all) 0.298 (acc.)	0.301 (all) 0.300 (acc.)	0.323 (95%#)
$\varepsilon_{y,\,out,\,n,\,rms}$ (π mm mrad)	0.415 (all) 0.303 (acc.)	0.307 (all) 0.305 (acc.)	0.300 (all) 0.299 (acc.)	0.302 (all) 0.301 (acc.)	0.321 (95%#)
$\varepsilon_{z,\,out,\,n,\,rms}$ (π keV deg)	6078 (all) 153 (acc.)	556 (all) 125 (acc.)	367 (all) 126 (acc.)	666 (all) 143 (acc.)	205 (95%#)
L (m)	3.2	3.1	3.0	3.0	3.3
T (%)	99.4 (all) 97.2 (acc.)	96.5 (all) 96.4 (acc.)	95.81 (all) 95.78 (acc.)	90.21 (all) 90.12 (acc.)	88.47

*: The design current for the CZ2009 RFQ was 45 emA
#: 95% of transported particles

3.5 FRANZ RFQ Redesign for Goethe University Frankfurt

As a successor of the retired neutron source based on a 3.7 MV Van-de-Graaff accelerator at Forschungszentrum Karlsruhe, the FRANZ facility has been planned to increase the neutron intensity from 10^4 n/cm^2/s to 10^7 n/cm^2/s [25] by using modern linacs. The produced high intensity neutrons in the energy range from around 1 keV up to 500 keV will allow experiments of interest to nuclear astrophysics.

As shown in Fig. 3.32, this small-scale but ultra-intense neutron source should consist of a volume-type plasma ion source that was recently replaced by a CHORDIS (Cold or Hot Reflex Discharge Ion Source) type ion source, a 250 kHz chopper to shape the beam time structure as required, a novel inductively coupled RFQ-IH combination to accelerate the proton beam to 2 MeV, a short rebuncher cavity to allow the adjustment of the final energy by $\pm$0.2 MeV, a bunch compressor to push several linac beam bunches into a 1 ns time slot, and finally a ^{7}Li target for the neutron generation via the ^{7}Li (p, n) Be^7 reaction.

The original plan for the FRANZ linac was to deliver a 200 emA, CW beam. So far, the CERN RFQ2, the former injector to the Large Hadron Collider, seems to have been the only RFQ that has provided $\geq$200 emA protons [27, 28]. However, its duty cycle is $\ll$1%.

From the Child–Langmuir law, Eq. (2.39), one can deduct that the available beam current I from an ion source is limited by the extraction voltage U_0 as $I \propto U_0^{3/2}$.

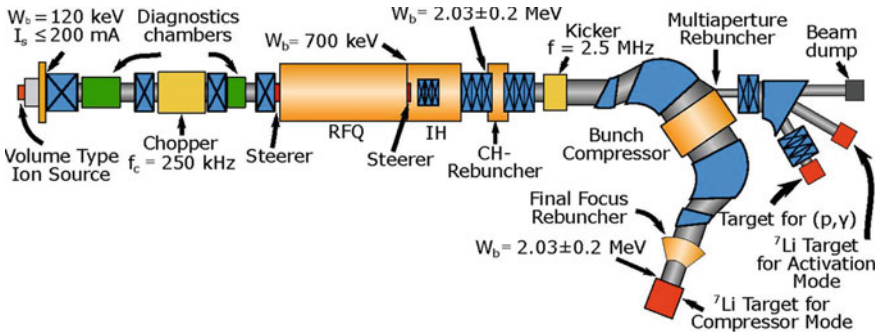

Fig. 3.32 Overview of the planned FRANZ facility at Goethe University Frankfurt [26]. Recently, W_b (W_{in}) and I_s (I_{in}) were updated to 60 keV and 30–60 emA, respectively

Therefore, the higher the required beam current is, the higher the output energy of the ion source should be. For the 200 emA, CW ion source of FRANZ, the output beam energy was chosen to be 120 keV. To provide a stable proton beam at this current is very challenging, even with the most advanced ion source technologies.

Published in 2006 [29] and afterwards in 2008 with some improvements [30], the first reference design for the 200 emA, CW FRANZ RFQ (hereafter referred to as Design CZ2008) can achieve >98% of beam transmission efficiency, a relatively short structure, and a reasonable Kilpatrick factor by using approximately half the inter-vane voltage of the CERN RFQ2 (see Table 3.12).

Later, the R&D of the FRANZ ion source showed that the design goal to provide 200 emA, CW beams would not be reachable in the short term. It was decided to realize the FRANZ linac in two steps: (1) to first accelerate a 50 emA beam from

Table 3.12 Comparison between the 200 emA, pulsed CERN RFQ2 and the 200 emA, CW FRANZ RFQ

	CERN RFQ2 [27, 28]	FRANZ RFQ Design CZ2008 [29, 30]
f (MHz)	202.56	175
W_{in} (keV)	90	120
W_{out} (keV)	750	700
I_{in} (emA)	200 (output)	200 (input)
U (kV)	178	85
$\varepsilon_{t,\,in,\,n,\,rms}$ (π mm mrad)	0.40	0.40
Kilpatrick factor	2.45	1.59
m_{max}	1.62	1.51
Duty cycle (%)	0.036	100
L (cm)	178.5	197.89
T (%)	~90 (measured)	98.3 (simulated)

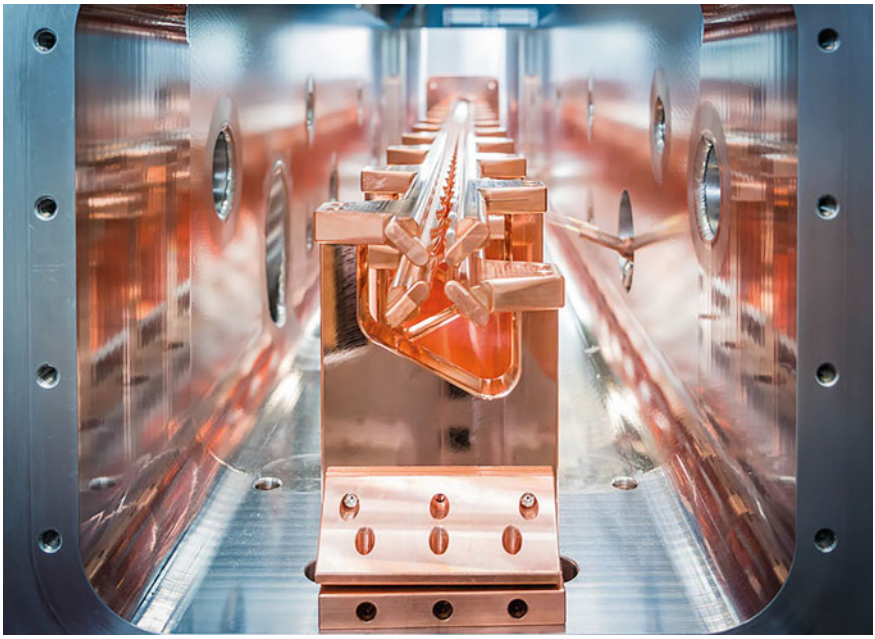

Fig. 3.33 Front view of the fabricated FRANZ RFQ (Design FraCZAScm) for 50 emA [25]

120 keV to 2 MeV at the CW mode; (2) to upgrade it later for 140 emA by exchanging the RFQ electrodes [26].

Shown in Fig. 3.33, a 50 emA RFQ (hereafter referred to as Design FraCZAScm) was built (but no suitable input beam could be used for the tests) [25, 26]. Its design parameters [25] are listed in Table 3.15 (in the later part of this section for a comparison with a new design recently made for an available ion source).

The FRANZ linac could not obtain a usable ion source until 2019 when a CHORDIS type ion source from GSI became available. At the design extraction voltage of 35 kV, this ion source can provide up to 60 emA of H^+, H^{2+}, and H^{3+} particles (in which the H^+ fraction is up to 50%). Behind the ion source, a compact electrostatic post-accelerator was mounted to increase the beam energy to 60 keV. Due to the new input beam parameters ($I_{in} = 30$ emA, $W_{in} = 60$ keV), the RFQ electrodes should be redesigned and replaced, but all the other parts, e.g., the tank, the RFQ stems, the internal quadrupole triplet, and the constructed IH-DTL were decided to be kept (see Fig. 3.34). Therefore, the output distribution of the new FRANZ RFQ should be as close as possible to the design input distribution used for the downstream IH-DTL (see Fig. 3.35).

The design requirements for the input and output data of the new $W_{in} = 60$ keV FRANZ RFQ are specified in Tables 3.13 and 3.14, respectively.

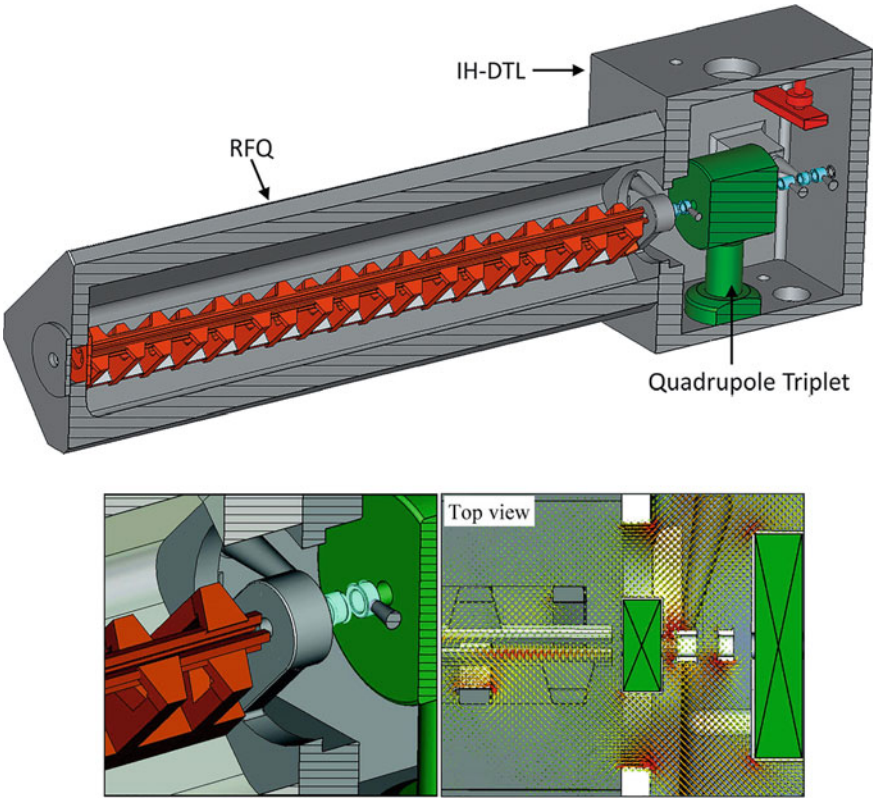

Fig. 3.34 The inductively coupled RFQ-IH combination (top) [26] and the MWS simulation of the RFQ-IH coupling (bottom, graph by Manuel Heilmann)

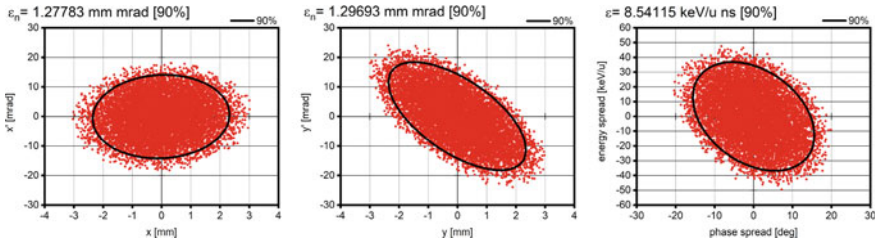

Fig. 3.35 Required input distribution for the FRANZ IH-DTL [31]

To make a redesign of this coupled RFQ, which should satisfy all these listed conditions, is much more complicated than to design a stand-alone new RFQ. Especially, some constraints must be met precisely, for example, the exit RF phase of the RFQ, i.e., the RF phase at the starting position of the steerer magnet, should be

Table 3.13 Design requirements for the input data of the new $W_{\text{in}} = 60$ keV FRANZ RFQ and the values finally adopted by Design CZ2022c

	Given	Design CZ2022c
f (MHz)	175	175
W_{in} (keV)	60	60
I_{in} (emA)	30	30
U (kV)	65 ± 5	60
$\varepsilon_{\text{t, in, n, rms}}$ (π mm mrad)	0.25	0.25
$\alpha_{\text{Twiss, }x\text{, in}}$	0.75	0.75
$\beta_{\text{Twiss, }x\text{, in}}$ (cm/rad)	5.2	5.2
$\alpha_{\text{Twiss, }y\text{, in}}$	0.75	0.75
$\beta_{\text{Twiss, }y\text{, in}}$ (cm/rad)	5.2	5.2

Table 3.14 Design requirements for the output data of the new $W_{\text{in}} = 60$ keV FRANZ RFQ and the corresponding results given by Design CZ2022c

	Expected	Accepted range	Design CZ2022c
W_{out} (keV)	700	± 10	706
Kilpatrick factor	≤ 1.6	–	1.27
$\varepsilon_{x\text{, out, n, rms}}$ (π mm mrad)	0.36	–	0.308 (100%) 0.294 (99%)
$\varepsilon_{y\text{, out, n, rms}}$ (π mm mrad)	0.36	–	0.332 (100%) 0.314 (99%)
$\varepsilon_{z\text{, out, n, rms}}$ (π keV ns)	2	$-0.3, +0.1$	2.220 (100%) 1.881 (99%)
Exit phase φ_{exit} (deg)	-63.4	± 2	-63.29
L_{total} (mm) (from inner wall to the steerer start)	1762	± 0.0	1761.9918
$L_{\text{gap, entrance}}$ (mm)	8	± 1	8.4571
$L_{\text{gap, exit}}$ (mm)	6.9	± 1	9.9016
$L_{\text{electrode}}$ (mm)	1747	± 2	1743.6331
T (%)	≥ 95	–	98.30

controlled at $-63.4°$ ($\pm 2°$) in order to ensure that the beam will see the correct RF field at the RFQ-IH transition.

Due to the very limited flexibility, the strategy for the redesign is to give the priority to the strict requirements, e.g., L_{total} over the relatively relaxed ones, e.g., emittance growths. Shown in Fig. 3.36, a new RFQ design (so-called Design CZ2022c) with many trade-offs has been developed for a $W_{\text{in}} = 60$ keV input beam. Almost all parameters are within the required ranges. Although $\varepsilon_{z\text{, out, n, rms}}$ and $L_{\text{gap, exit}}$ are above the given limits, they were finally accepted, after being checked with the RF simulation of the FRANZ linac and the beam dynamics simulation of the downstream IH [31].

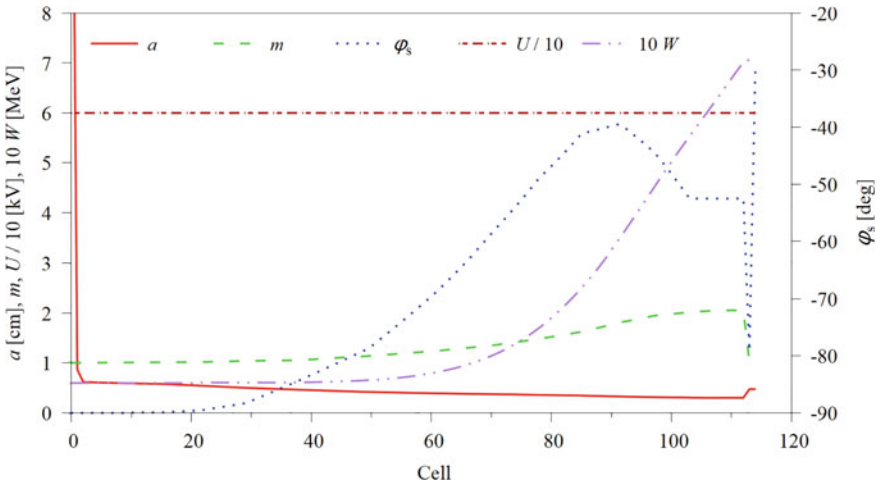

Fig. 3.36 Main design parameters of the Design-CZ2022c FRANZ RFQ

For this design, the emittance ratio at the end of pre-bunching (see Cell 45 in Fig. 3.37) has to be $\frac{\varepsilon_l}{\varepsilon_t} > 2$. Therefore, the SEGLER method instead of the MEGLET method should be used in order to still achieve good beam quality for the new design. The tune footprints have been carefully confined in the "safe ¼ ellipse" needed for the SEGLER method (see Fig. 3.38). It can be seen in Fig. 3.37 that the longitudinal and transverse emittances have been kept almost constant along the main part of the RFQ.

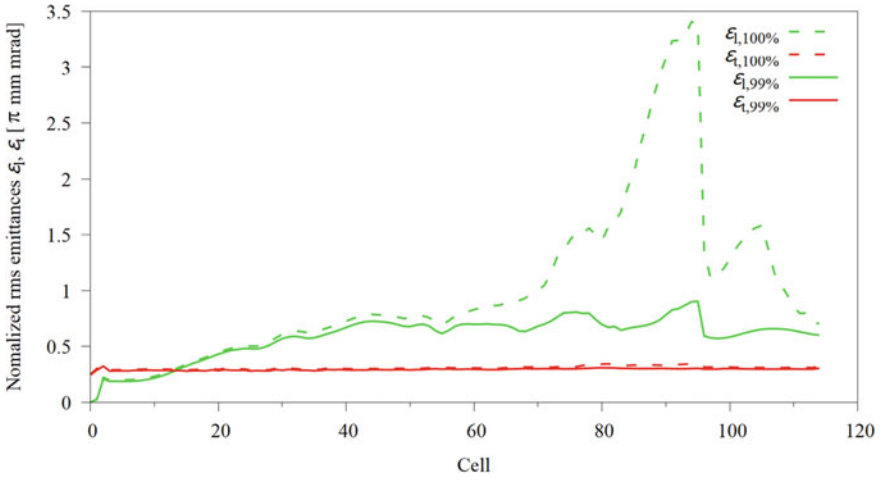

Fig. 3.37 Evolution of longitudinal and transverse emittances for 100% and 99% of particles along the Design-CZ2022c FRANZ RFQ

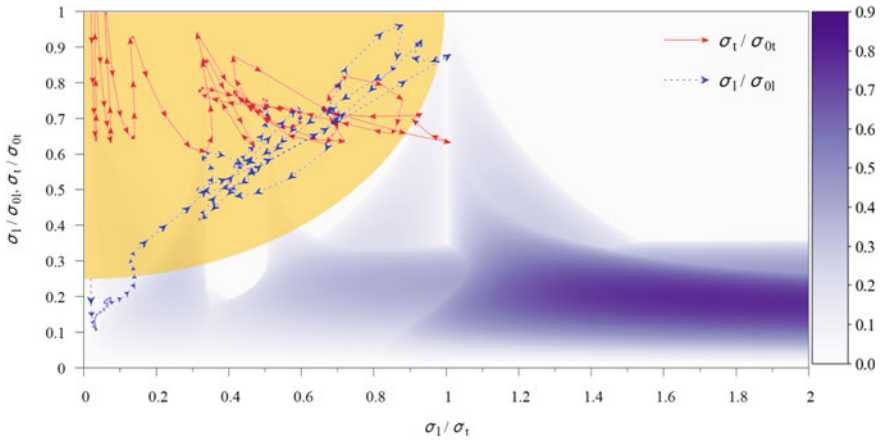

Fig. 3.38 Tune chart of the Design-CZ2022c FRANZ RFQ (overlapped with the Hofmann chart for $\frac{\varepsilon_l}{\varepsilon_t} = 2.3$)

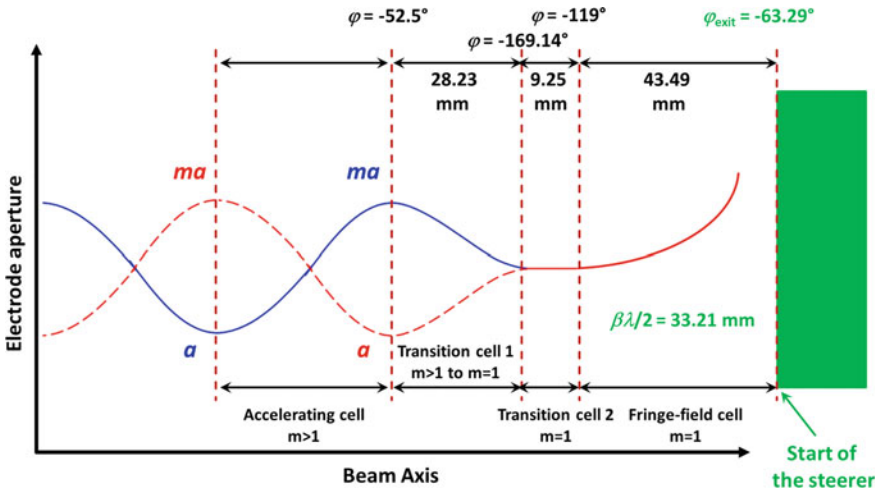

Fig. 3.39 The end cells of the Design-CZ2022c RFQ and their exit RF phases (all phases in cosine convention)

Figure 3.39 shows the end cells of the Design-CZ2022c RFQ, where the values in black are available in the PARMTEQM output files, while those in green have been additionally calculated. The second transition cell and the fringe-field cell have no modulation, so there is no acceleration. Using their β value, one can get that the geometric length for half an RF period (180°) in this region is 33.21 mm. The geometric lengths of the last two cells are known, so the RFQ exit phase can be easily calculated.

Table 3.15 Comparison between the already constructed Design FraCZAScm and the Design CZ2022c at 50 emA

	Design FraCZAScm (built) [25]	Design CZ2022c @ 50 emA
f (MHz)	175	175
W_{in} (keV)	120	60
W_{out} (keV)	700	700
I_{in} (emA)	50	50
U (kV)	62	60
Kilpatrick factor	1.5	1.27
a (mm)	3.3	2.98
m_{max}	2.2	2.054
$\varepsilon_{\text{t, in, n, rms}}$ (π mm mrad)	0.20	0.25
$\varepsilon_{\text{t, out, n, rms}}$ (π mm mrad)	0.36	0.32 (x) 0.35 (y)
$\varepsilon_{\text{l, out, n, rms}}$ (π keV deg)	0.41[a]	0.26
L (m)	1.762	1.762
T (%)	96	97.4

[a] In [25], the unit for this value is π keV ns. However, according to the longitudinal distribution in the 17th figure of [25], the correct unit seems to be π keV deg

In Table 3.15, the simulation results of the Design-CZ2022c RFQ with a 50 emA input beam are given. This design also shows good performance in transmission efficiency and emittance growths at this higher current, which is favorable for the future upgrade.

The vane geometry of the Design-CZ2022c RFQ was imported into the TracwWin code (actually the TOUTATIS code [32] that was run inside TraceWin as a subroutine) for a benchmark [31]. The x- and y-vanes were switched due to the different definitions used by the TOUTATIS and PARMTEQM codes. All results have a good agreement, e.g., the simulated output distributions are very similar (see Fig. 3.40).

This output distribution was used as the input distribution of the IH-DTL and the LORASR [33] simulation gave a beam transmission efficiency of 98.54% at the end of the IH-DTL [31].

The electrodes of the Design-CZ2022c FRANZ RFQ have been manufactured in April 2023 and will see the first beam very likely by the end of 2023.

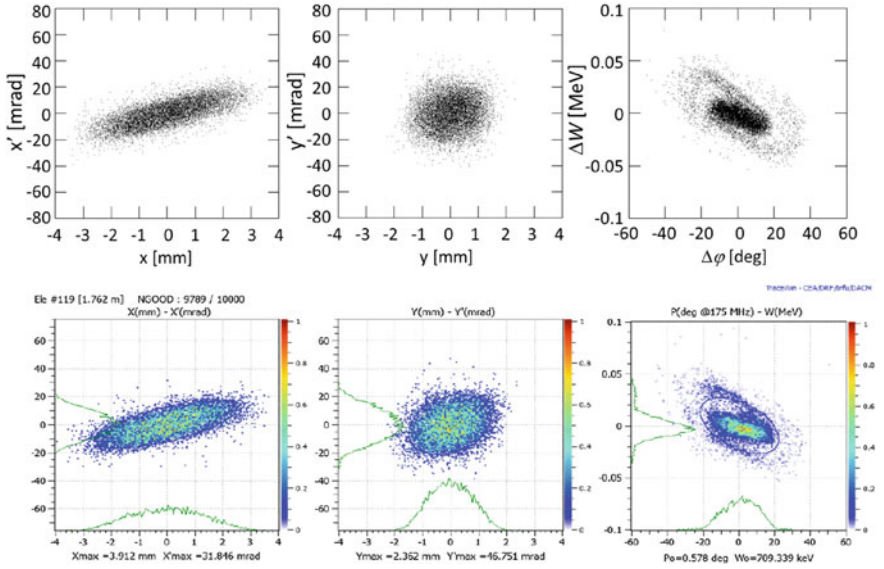

Fig. 3.40 Simulated output distributions of the Design-CZ2022c RFQ by PARMTEQM (top graphs with *x*- and *y*-planes switched) and TraceWin/TOUTATIS (bottom graphs from [31])

References

1. M. Harrison, T. Ludlam, S. Ozaki, RHIC project overview. Nucl. Instrum. Methods Phys. Res. A **499** (2003)
2. J. Alessi et al., Commissioning of the EBIS-based heavy ion preinjector at Brookhaven (including talk), in *Proceedings of LINAC* (2010)
3. A. Schempp et al., RFQ and IH accelerators for the new EBIS injector at BNL, in *Proceedings of PAC* (2007)
4. M. Okamura et al., Beam commissioning results for the RFQ and MEBT of the EBIS based preinjector for RHIC, in *Proceedings of LINAC* (2010)
5. O. Kester et al., Status of the FAIR-facility, in *Proceedings of IPAC* (2013)
6. P. Gerhard et al., Status and perspectives of the CW upgrade of the UNILAC HLI at GSI, in *Proceedings of HIAT* (2015)
7. J. Friedrich et al., Properties of the GSI HLI-RFQ structure, in *Proceedings of PAC* (1991)
8. J. Klabunde, The high charge state injector for GSI, in *Proceedings of LINAC* (1992)
9. M. Vossberg, A. Schempp, C. Zhang, L. Dahl, W. Barth, The new GSI HLI-RFQ for CW-operation, in *Proceedings of LINAC* (2010)
10. D. Koser, Development of a 108 MHz 4-rod CW RFQ-design for high duty cycle acceleration of heavy ion beams at the GSI-HLI, Ph.D. thesis, Goethe University Frankfurt (2020)
11. A. Schempp, Design of compact RFQ's, in *Proceedings of LINAC* (1996)
12. U. Ratzinger, K. Kaspar, E. Malwitz, S. Minaev, R. Tiede, The GSI 36 MHz high-current IH-Type RFQ and HIIF–relevant extensions. Nucl. Instrum. Methods Phys. Res. Sect. A **415** (1998)
13. A. Kolomiets et al., Upgrade of the unilac high current injector RFQ, in *Proceedings of LINAC* (2008)
14. C. Zhang et al., HSI RFQ upgrade for the UNILAC injection to FAIR, in *Proceedings of IPAC* (2016)

15. R. Tiede, Tracking of the RFQ output distribution based on the new HSI-RFQ electrodes design through the HSI MEBT Using LORASR, Internal note no. IAP-DYNA-170308, IAP Frankfurt (2008)
16. R. Tiede, Matching to IH-section, Talk at final meeting of European community INTAS project (ref. no. 06-1000012-8782 2006) (2009)
17. C. Zhang, H. Podlech, Efficient heavy ion acceleration with high brilliance, in *Proceedings of HIAT* (2022)
18. C. Zhang, H. Podlech, E. Tanke, Realizing long radio-frequency quadrupole accelerators with multiple shorter and independent cavities. Phys. Rev. Accel. Beams **23**, 042003 (2020)
19. C. Zhang, Minimizing emittance growth via low emittance transfer. Phys. Rev. Accel. Beams **25**, 034201 (2022)
20. G. Clemente, The room temperature CH-DTL and its application for the FAIR proton injector, Ph.D. thesis, Goethe University Frankfurt (2007)
21. C. Zhang, Linac design for intense hadron beams, Ph.D. thesis, Goethe University Frankfurt (2009)
22. C. Zhang, H. Podlech, New reference design of the European ADS RFQ accelerator for MYRRHA, in *Proceedings of IPAC* (2014)
23. C. Zhang, H. Podlech, Design approach for a 325 MHz, 3 MeV, 70 – 100 mA proton radio-frequency quadrupole accelerator with low emittance transfer. Nucl. Instrum. Methods Phys. Res. Sect. A **947** (2019)
24. M. Syha, Beam dynamics design of the FAIR proton-linac RFQ and design study of a compact 325MHz RFQ, Ph.D. thesis, Goethe University Frankfurt (2021)
25. S. Alzubaidi et al., The Frankfurt neutron source FRANZ. Eur. Phys. J. Plus **131**, 124 (2016)
26. R. Tiede et al., A coupled RFQ-IH-DTL cavity for FRANZ: a challenge for RF technology and beam dynamics, in *Proceedings of HB* (2016)
27. E. Tanke, M. Vretenar, M. Weiss, Measurement of the CERN high intensity RFQ, in *Proceedings of EPAC* (1992)
28. M. Weiss, The RFQ2 complex: the future injector to CERN linac 2, in *Proceedings of EPAC* (1992)
29. C. Zhang, A. Schempp, Development of a high current proton linac for FRANZ, in *Proceedings of EPAC* (2006)
30. C. Zhang, A. Schempp, Beam dynamics studies on a 200 mA proton radio frequency quadrupole accelerator. Nucl. Instrum. Methods Phys. Res. Sect. A **586** (2008)
31. H. Hähnel, FRANZ RFQ CZ2022c TraceWin simulations & compatibility assessment, Summary report, IAP Frankfurt (2022)
32. TOUTATIS code, http://irfu.cea.fr/dacm/logiciels/
33. R. Tiede et al., LORASR code development, in *Proceedings of EPAC* (2006)

Chapter 4
Injectors for Accelerator-Driven Systems

Abstract Following the previous chapter, several other real examples also for confirming the theory introduced in Chap. 2 will be presented. Listed as follows, these RFQ accelerators have been developed for the Accelerator-Driven System (ADS) technology to solve the nuclear waste problem:

- A MEGLET-style CW 4-rod RFQ developed for the European ADS project MYRRHA.
- In collaboration with Lawrence Berkeley National Laboratory (LBNL), two CW 4-vane RFQs developed using a modified NFSP method (the NFSP method is the predecessor of the MEGLET approach) for the China ADS Injector II Project and the Project X Injector Experiment (PXIE, now PIP2IT, i.e., Proton Improvement Plan-II Injector Test) at Fermi National Accelerator Laboratory (FNAL), respectively. The PXIE RFQ was not planned for the ADS use. However, because its physics design is based on a same root as the design adopted by the China ADS Injector-II RFQ, it is included in this chapter.

For the ADS application, the driver linac is required to have an extremely high reliability, e.g., beam trips longer than 3 seconds must be very rare, which brings big challenges to the beam dynamics of the linac especially in the RFQ part. So far, all these three machines have been constructed and tested with beams. High beam transmission efficiency ($\geq$95%) and reliable CW operation have been experimentally proven.

4.1 CW RFQ for European ADS Project MYRRHA

Nuclear fission is one known technology, which is providing a large fraction of electricity for the world, but a public worry is how to treat the produced waste, especially the long-lived, high-level radioactive ones, e.g., minor actinides. Figure 4.1 shows the evolution of the radiotoxicity of spent nuclear fuel relative to that of the natural uranium ore as a function of time for various nuclear-waste management options. It can be seen that the transmutation process offers the possibility to shorten the lifetime as well as to reduce the volume of the nuclear waste considerably.

C. Zhang, *Radio-Frequency Quadrupole Accelerators*, Particle Acceleration and Detection, https://doi.org/10.1007/978-3-031-40967-7_4

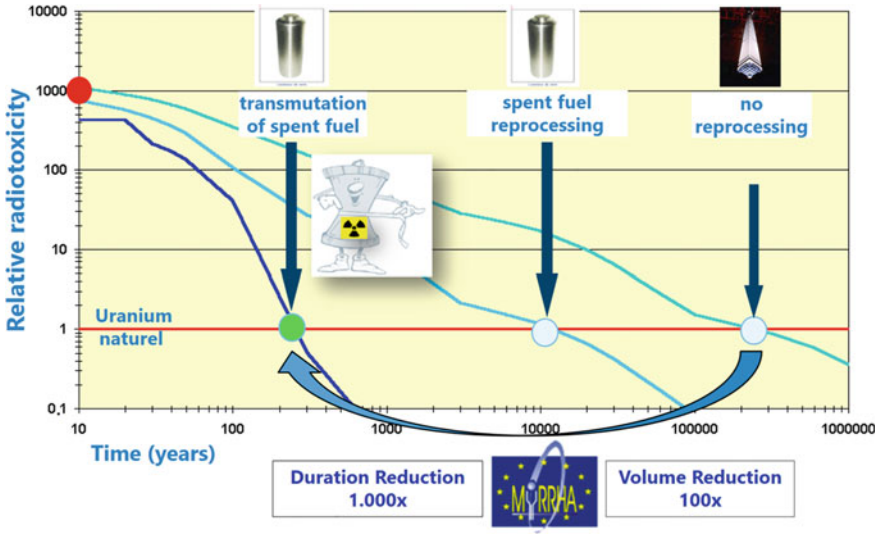

Fig. 4.1 Decrease in the relative radiotoxicity of nuclear waste as a function of time (*graph source* SCK · CEN, with small modifications)

The "energy amplifier" [1] proposed by the Nobel laureate Rubbia can be a promising candidate for such transmutation systems. Shown in Fig. 4.2, this kind of accelerator-driven system employs a high power proton accelerator as a spallation neutron source to drive a sub-critical fission reactor. To minimize thermal stress and material fatigue on the target window, reactor structures, and fuel assemblies as well as to ensure a high availability, unwanted beam trips (i.e., beam interruptions on the target) longer than 3 seconds must be very rare [2]. This means that for the driver linac of such an accelerator-driven system, an extremely high reliability has to be ensured.

Figure 4.3 shows the specification on beam trips for the MYRRHA ADS linac [2], which is far above the performance of present high power proton accelerators, e.g., the mean time between failures of the SNS linac is a couple of hours. Furthermore, different from the SNS linac that is a pulsed machine, the MYRRHA ADS linac will work at the CW mode, so the situation will become more challenging.

Therefore, all components of the MYRRHA linac have to be designed conservatively so that they will be operated well below their physical limits. For a demonstration of the accelerator-driven system, great efforts have been made over decades, but the R&D studies are still ongoing.

A brief history of the R&D activities for the ADS application in Europe is as follows:

- 2001: "A European Roadmap for Developing Accelerator Driven Systems for Nuclear Waste Incineration" was issued by the European Technical Working Group on ADS [3].

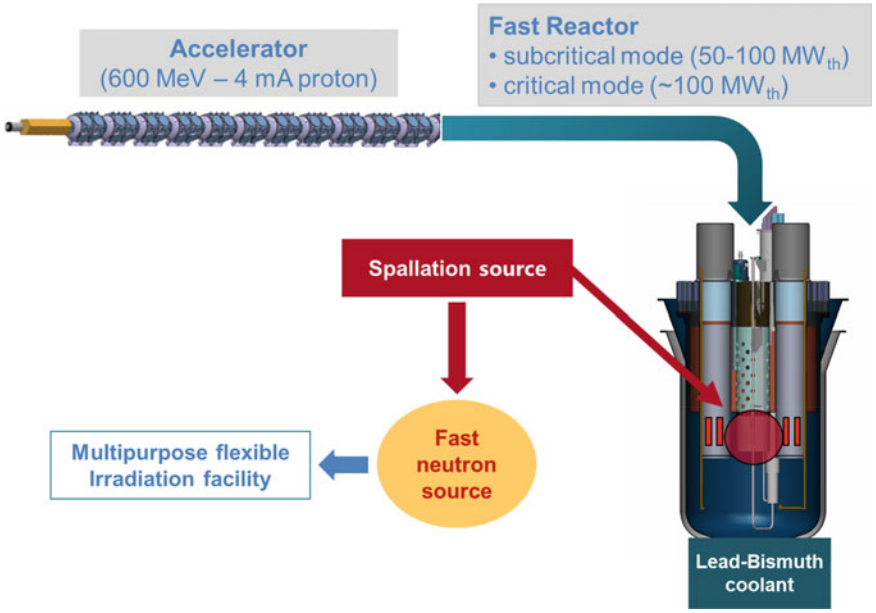

Fig. 4.2 Schematic layout of an accelerator-driven system (*graph source* SCK · CEN)

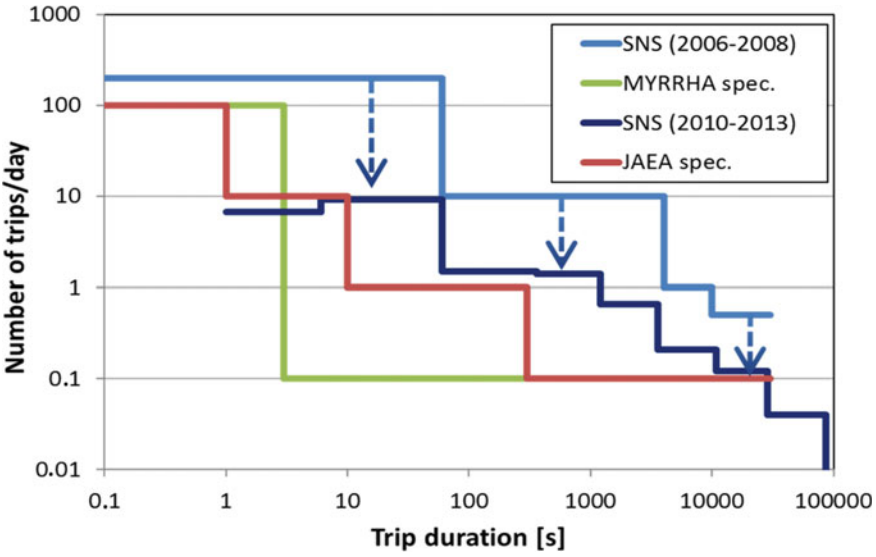

Fig. 4.3 Beam trips occurred in the SNS linac, required by the Japanese ADS project (JAEA), and accepted for the MYRRHA linac [2]

- 2002–2004 (EU-FP5): Preliminary Design Study for an eXperimental Accelerator Driven System (PDS-XADS).
- 2005–2010 (EU-FP6): EUROpean Research Programme for the TRANSmutation of High Level Nuclear Waste in an Accelerator Driven System (EUROTRANS) [4].
- 2010: Belgian government declared support for the construction of MYRRHA.
- 2010–2015 (EU-FP7): MYRRHA Accelerator eXperiment (MAX) [5].
- 2016–2020 (EU-Horizon2020): MYRRHA Research and Transmutation Endeavour (MYRTE).
- 2018: Belgian government decided to start the construction of MYRRHA in Mol and opened it to international participation.
- 2019–2026 (MYRRHA Phase 1): MINERVA (MYRRHA Isotopes productioN coupling the linEar acceleRator to the Versatile proton target fAcility) for building and testing the first part of the MYRRHA linac up to 100 MeV and a proton target facility for this energy.

A schematic overview of the MYRRHA driver linac is given in Fig. 4.4. To reach the goal of extremely high reliability, the design strategies for the entire linac are conservative designs and redundancy. The redundancy for the main linac can be ensured in series, i.e., the function of a faulty element, e.g., amplifier module or accelerating cavity, will be taken over by one or more neighboring elements so that the delivery of the proton beam with nominal parameters to the target will not be interrupted longer than 3 seconds. In the injector part, the failure of a long accelerating cavity with a frozen β profile cannot be easily compensated by its neighbors, so parallel redundancy has been adopted (as shown in Fig. 4.4, in case of a failure in the main injector, a hot stand-by injector should be able to take over the beam-delivery task with a switching time < 3 seconds).

As mentioned in Sect. 1.3, usually $I_{\mathrm{avg}} \approx 1$ emA is already considered as a high value for proton linacs [7]. The MYRRHA linac will work for up to 4 emA, CW

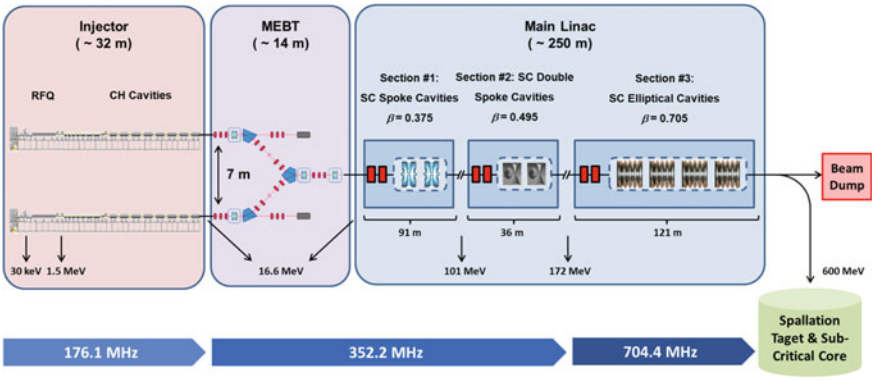

Fig. 4.4 Overview of the MYRRHA facility (the plot was remade according to [6])

proton beams. It is challenging to ensure a very reliable CW operation for such a high current linac.

Table 4.1 summaries three important versions made for the design of the European ADS RFQ.

In the EUROTRANS project [4], the driver linac was specified to deliver a 2.5–4 emA, 600 MeV proton beam and a 20 emA, 800 MeV proton beam for a prototype-scale demonstration phase and an industrial-scale phase, respectively. For an easy upgrade without additional R&D costs, the 3 MeV EUROTRANS RFQ was designed to achieve almost 100% beam transmission with very good beam quality at both 5 and 30 emA (the design beam currents for the two phases, respectively) [8]. For the EUROTRANS RFQ, the 4-vane structure was chosen due to the design working frequency of 352 MHz.

Different from EUROTRANS such a pure research project, the successor project, MAX, was pursuing not only to continue the R&D studies but also to deliver a consolidated design for the real construction and demonstration in Mol, Belgium. To further improve the design for the MYRRHA RFQ, some new ideas were applied [9].

Firstly, the RF frequency was halved from 352 to 176 MHz with the following considerations:

- It allows replacing the 4-vane RFQ structure by the more cost-saving 4-rod one.
- To obtain a higher specific shunt impedance R_p. Figure 4.5 plots the measured R_p values of ten built CW RFQ accelerators as a function of f. The fitting curve in the figure can be expressed by the following formula [11]:

$$R_p(\mathrm{M\Omega m}) = 16/f(\mathrm{MHz}) \tag{4.1}$$

Table 4.1 Designs for the European ADS RFQ

	EUROTRANS [8]		MYRRHA Design CZ2011 [9]	MYRRHA Design CZ2013 [10] (built)
I_{in} (emA)	5	30	5	5
RF structure	4-vane	4-vane	4-rod	4-rod
f (MHz)	352	352	176	176.1
W_{in} (keV)	50	50	30	30
W_{out} (MeV)	3	3	1.5	1.5
U (kV)	65	65	40	44
Kilpatrick factor	1.69	1.69	1.01	1.05
$\varepsilon_{t,\,in,\,n,\,rms}$ (π mm mrad)	0.20	0.20	0.20	0.20
$\varepsilon_{x,\,out,\,n,\,rms}$ (π mm mrad)	0.21	0.21	0.22	0.21
$\varepsilon_{y,\,out,\,n,\,rms}$ (π mm mrad)	0.20	0.20	0.22	0.21
$\varepsilon_{z,\,out,\,n,\,rms}$ (π keV deg)	109	88.9	64.6	41
L (m)	4.32	4.32	3.99	4.03
T (%)	~100	99.9	~100	98.6

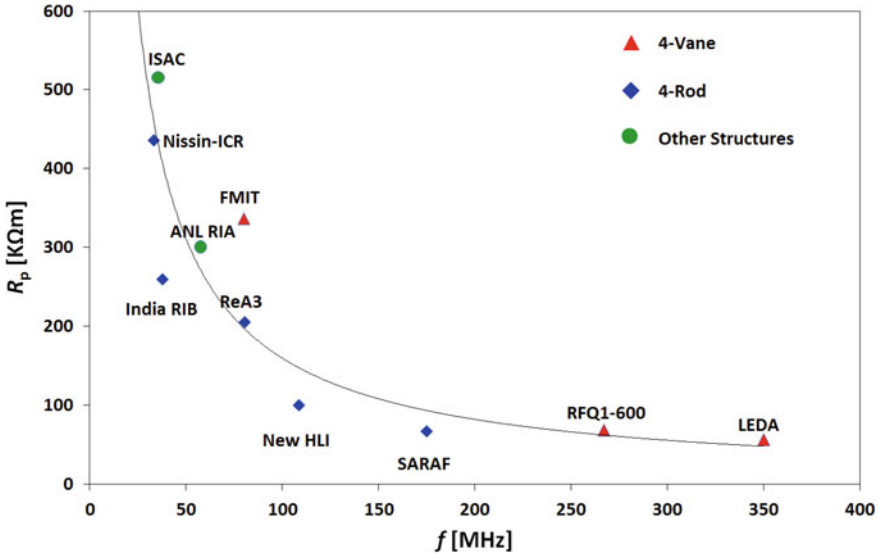

Fig. 4.5 Measured shunt impedance of ten built CW RFQs in the world [11]

As a result of this change, the RF power consumption P_c was reduced from 69.8 kW/m to 23.5 kW/m [10]. The P_c value of the EUROTRANS RFQ was calculated by the CST Microwave Studio software [12] with a safety margin of 20% [9], while that of the MYRRHA RFQ was estimated using the measured shunt impedance, 67 kΩm, of the SARAF RFQ (another 176 MHz, CW, 4-rod RFQ with a similar length) [13, 14]. In the SARAF experiments, a stable CW operation with a thermal load of 47.5 kW/m has been reached [13]. Therefore, 23.5 kW/m is a very conservative value.

- The minimum gap between electrodes can be enlarged and the sparking risk can be reduced.

Secondly, the higher design beam current, 30 emA, was not required for the MAX project, so the inter-vane voltage U was lowered from 65 to 40 kV. Accordingly, the Kilpatrick factor of the RFQ was decreased from 1.69 to 1.01.

Last but not least, for keeping the RFQ length still at ~4 m, the RFQ-CH transition energy was reduced from 3 MeV to 1.5 MeV. This is also favorable for the downstream NC CH cavities, because for H-type DTLs, the lower the β value at the input is, the higher the shunt impedance will be [15].

The resulting MYRRHA RFQ design is hereafter referred to as Design CZ2011.

In 2013, for the final optimization before the construction of the MYRRHA RFQ, it was decided to increase U by 10% (P_c can be still <30 kW/m) but keep the transverse beam dynamics (e.g., the B values of the cells) almost unchanged [10]. This can lead to a larger electrode aperture and consequently smaller capacitance

between the electrodes so that higher stems, which are favorable for a better Q value and smaller dipole effects (see Fig. 1.9), can be used.

Another motivation for further improving the Design CZ2011 was to minimize the longitudinal output emittance $\varepsilon_{z,\,\mathrm{out}}$ (by reducing the number of transported but poorly accelerated particles) even at the cost of some transverse beam losses. This is important for avoiding beam losses downstream of the accelerator especially in the SC cavities. In Table 4.1, one can see that the beam transmission efficiency of this design (Design CZ2013) is only ~1% lower but the emittances in all phase spaces are smaller. As the RFQ output energy, 1.5 MeV, is lower than the threshold energy of the ^{65}Cu (p, n) ^{65}Zn reaction, 2.16 MeV, these beam losses in the RFQ part will not threaten hands-on maintenance.

The Design CZ2013 (see Fig. 4.6) was made using the NFSP method [16] without foreseeing the MEGLET guidelines for controlling the emittance transfers. Nevertheless, one can see that the two emittance transfer periods are started at Cell 60 (see Fig. 4.7) with an emittance ratio of ~1.1 (see Fig. 4.8) and afterwards the emittance ratio varies along the main part of RFQ in the range of 0.8–1.2 (see Fig. 4.8). Therefore, the Design-CZ2013 MYRRHA RFQ achieved good beam quality like a MEGLET-style RFQ.

Figure 4.9 shows the built MYRRHA RFQ with the lid opened as well as the setup for the high power tests in Louvain-la-Neuve, Belgium. The main RF parameters of the RFQ are summarized in Table 4.2. The dipole component of the MYRRHA RFQ was lowered to be <2% due to the efficient compensation enabled by the method shown in Graph (d) of Fig. 1.10 [17].

Based on the successful conditioning of the RFQ cavity up to 142 kW in the full CW mode, the first beam commissioning of the MYRRHA RFQ was carried in 2020. All measured results presented in [18] have good agreements with the design

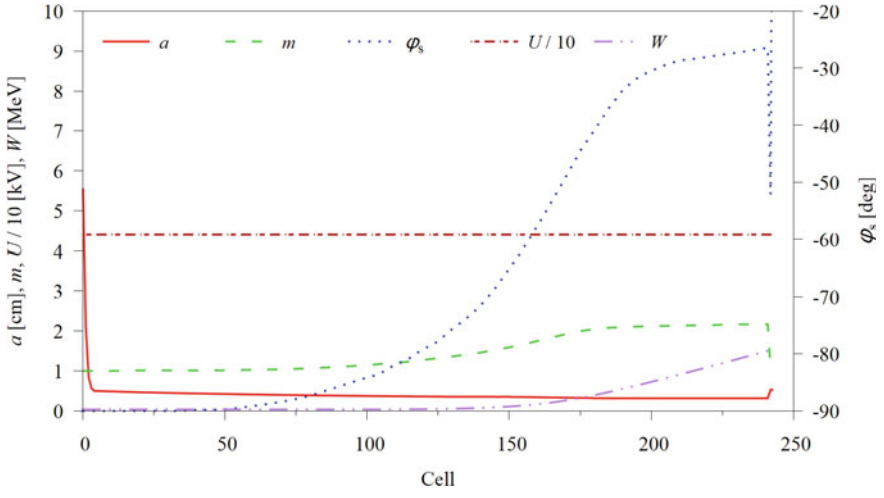

Fig. 4.6 Design parameters of the built MYRRHA RFQ (Design CZ2013)

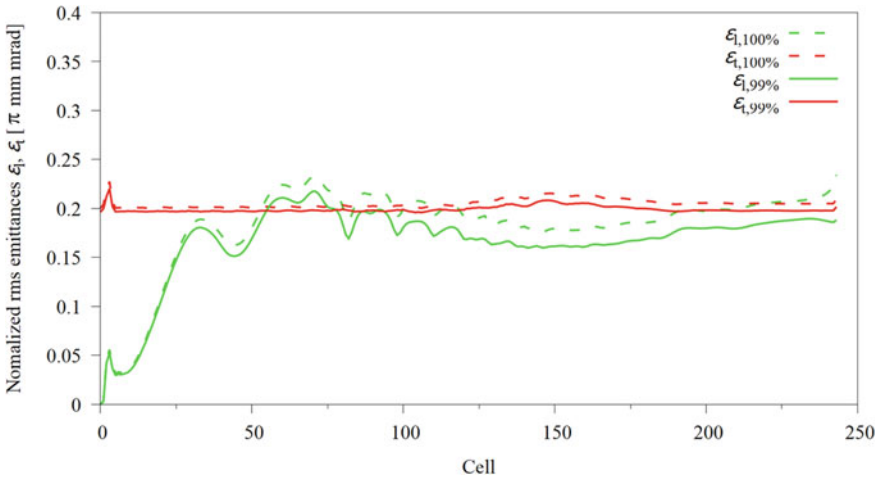

Fig. 4.7 Evolution of longitudinal and transverse emittances for 100% and 99% of particles along the Design-CZ2013 MYRRHA RFQ

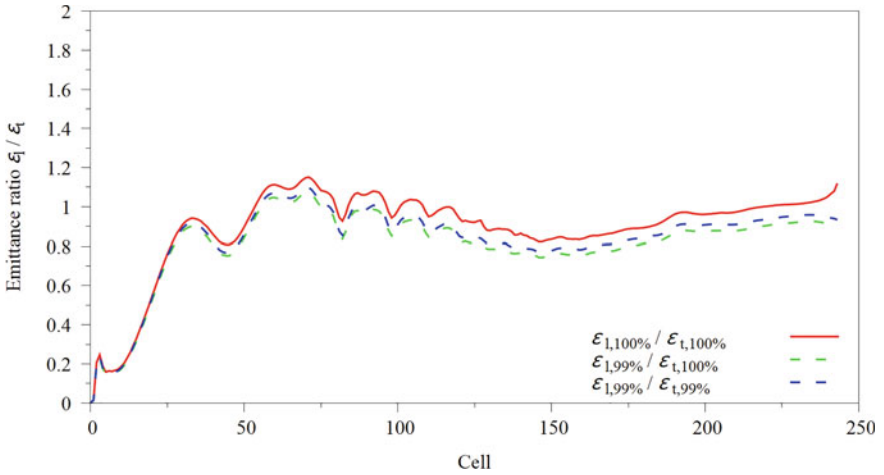

Fig. 4.8 Evolution of emittance ratios along the Design-CZ2013 MYRRHA RFQ

expectations [10]. As shown in Fig. 4.10, the measured transmission was 95% at nominal power (110 kW or 44 kV) and could be improved by increasing the RF power (until reaching a plateau at $T = 98\%$ from 125 kW upwards). The measured curves [18] are close to the design expectations based on the PARMTEQM simulation [10]. The TOUTATIS model (translated from the PARMTEQM model) of the MYRRHA RFQ predicted even higher transmission (see Fig. 4.10). Over the time that RFQ was operated, the transmission was further improved. Finally, 120 kW at which the measured $T = 98.9\%$ was adopted as the working point [18].

Fig. 4.9 The inner structure of the built MYRRHA RFQ (main picture), the front view of electrodes (top left corner), and the setup for the high power tests (bottom right corner) [2]

Table 4.2 Summary of the RF parameters of the built MYRRHA RFQ [2]

Parameter	Value
f (MHz)	176.1
Duty cycle (%)	100
U (kV)	44
Kilpatrick factor	1.05
R_p (kΩm)	72
P_c (kW)	108
P_c per meter (kW/m)	26.5
Dipole component (%)	<2

In 2021, the second beam commissioning campaign for the MYRRHA RFQ was performed with the focus on the measurement of the output beam energy with the time of flight (ToF) method. As shown in Fig. 4.11, the measured value at 120 kW, 1.494 ± 0.003 MeV, is fairly close to the expected 1.5 MeV and is fully in the acceptance of downstream cavities (the missing 6 keV can also be easily recovered by using the neighboring rebuncher cavities) [19].

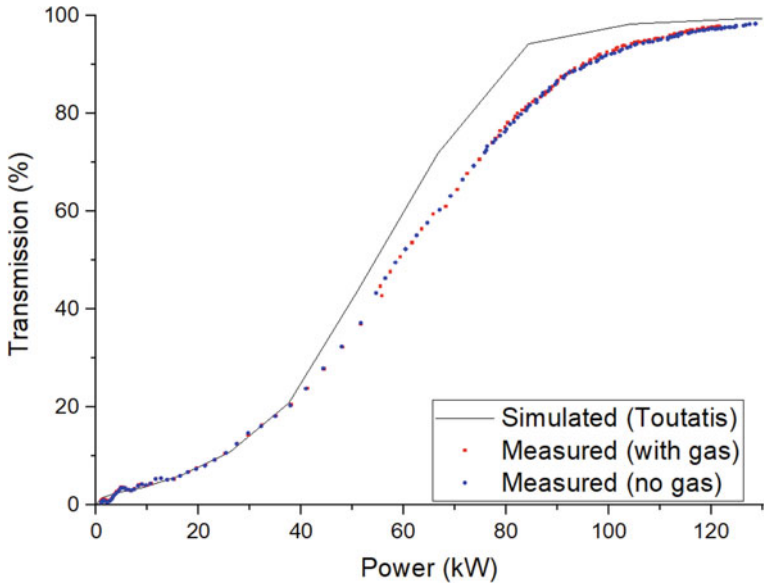

Fig. 4.10 Measured beam transmission of the MYRRHA RFQ with and without Argon injection into the LEBT (close to the design expectations based on the PARMTEQM simulation), compared with the simulated transmission by TOUTATIS [18]

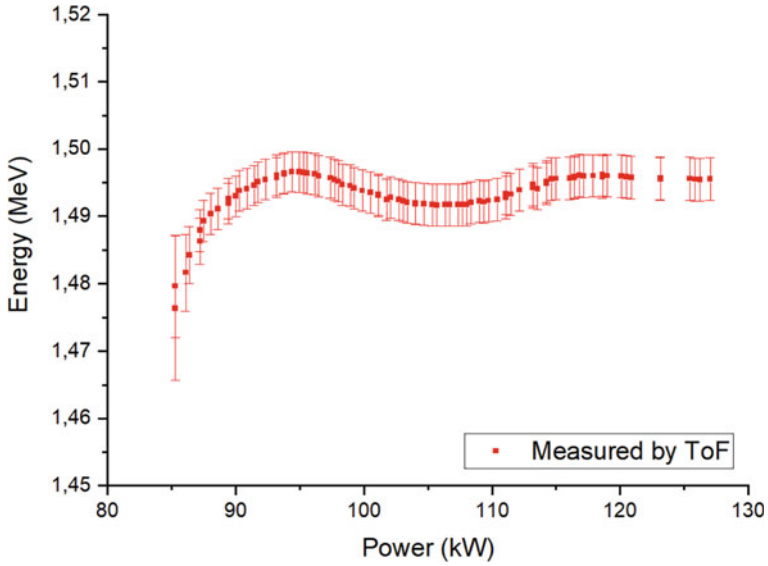

Fig. 4.11 Measured output beam energy of the MYRRHA RFQ as a function of RF power [19]

4.2 CW RFQ for China ADS Injector II

In China, active R&D studies on ADS were started in 2010 and a roadmap for the long-term ADS development was proposed in 2011 [20]. For the 10 MeV injector of the China ADS driver linac, two versions were developed in parallel. The 325 MHz Injector-I mainly consists of an NC RFQ and several SC spoke cavities, while the 162.5 MHz Injector-II mainly consists of an NC RFQ and several SC HWR/SC CH cavities.

The design requirements for the 162.5 MHz Injector-II RFQ are listed in Table 4.3. The design beam current is 15 emA (in real operation, 10 emA will be required), and the design should show good performance up to 20 emA. The output energy was chosen as 2.1 MeV for two reasons: (1) to keep the RFQ length shorter than 4.5 m; (2) to keep the energies of lost particles lower than 2.16 MeV, the threshold energy of the copper-proton reaction. Different from the MYRRHA RFQ, behind which NC CH cavities are used to cover the acceleration up to 16.6 MeV, the Injector-II RFQ is directly followed by superconducting cavities. Therefore, more design constraints with respect to the beam quality, e.g., very small longitudinal output emittance, have been specified for the Injector-II RFQ. In addition, for easier matching at the two ends of the RFQ, the Twiss α parameters of the transverse input and output distributions have been limited to $\leq$1.5. The Twiss α parameter is a measure of the focalization of the beam: (1) $\alpha_{\text{Twiss}} < 0$: diverging; (2) $\alpha_{\text{Twiss}} = 0$: waist; (3) $\alpha_{\text{Twiss}} > 0$: converging.

Developed for Institute of Modern Physics, Chinese Academy of Sciences, the physics design of the Injector-II RFQ was based on a collaboration between Chuan Zhang and LBNL [21, 22]. To take advantage of the existing LBNL expertise for the construction of RFQ accelerators, e.g., the SNS RFQ, it was required by LBNL to use the 4-vane structure with a constant mid-cell aperture r_0 (i.e., a constant B) for the Injector-II RFQ.

Table 4.3 Design requirements of the China ADS Injector-II RFQ and the MYRRHA RFQ

Parameters	Injector-II RFQ	MYRRHA (Design CZ2013)
Particle species	H^+	H^+
RF structure	4-vane	4-rod
f (MHz)	162.5	176.1
W_{in} (keV)	35	30
W_{out} (MeV)	2.1	1.5
Duty cycle (%)	100	100
I_{in} (emA)	15 (up to 20)	5
$\varepsilon_{\text{t, in, n, rms}}$ (π mm mrad)	0.30	0.20
$\Delta\varepsilon_{\text{t}}$ (%)	$\leq$10	As small as possible
$\varepsilon_{z\text{, out, n, rms}}$ (π keV ns)	$\leq$1.0	–
T (%)	95	As high as possible
$\alpha_{\text{Twiss, t, in, max}}$ & $\alpha_{\text{Twiss, t, out, max}}$	$\leq$1.5	–

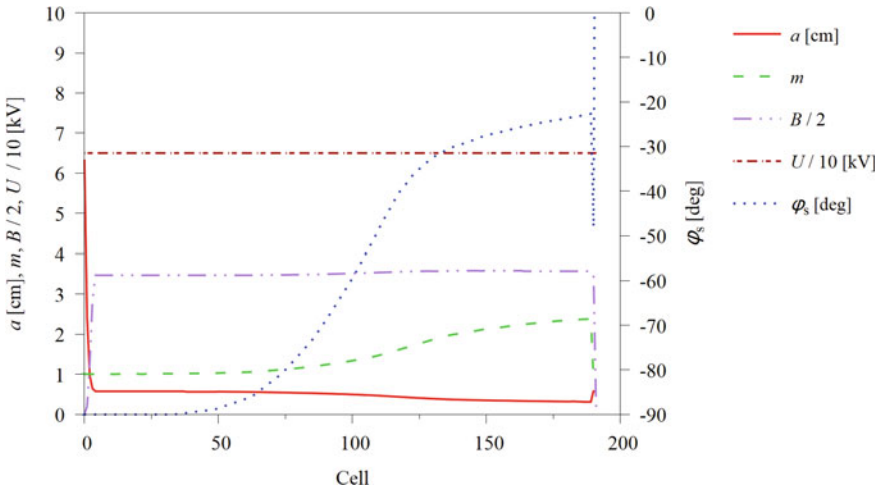

Fig. 4.12 Main design parameters of the China ADS Injector-II RFQ

The Injector-II RFQ has been designed with a modified NFSP method: φ_s and m evolve in the NFSP way, but B is kept constant (see Fig. 4.12). As mentioned in Chap. 2, it is not reasonable to hold B constant from the beam physics point of view, but at relatively low peak beam current, the price paid for this, some beam quality degradation, is often still acceptable.

As shown in Fig. 4.13, to obtain $\alpha_{\text{Twiss, t, out, max}} \leq 1.5$ as desired, two transition cells were added at the RFQ end: (1) the first one (also called as Crandall Cell) can lead to a smooth transition from $m > 1$ to $m = 1$ and end the electrode tips with quadrupole symmetry; (2) the second one with $m = 1$, which length can be adjusted to change the orientations of the transverse emittance ellipses.

Using a 4D Waterbag input distribution, the beam transport along the designed Injector-II RFQ was simulated using the PARMTEQM code. The beam envelopes and the input/output distributions are shown in Figs. 4.14 and 4.15, respectively.

In Fig. 4.14, a blowup in the transverse beam envelopes can be observed near Cell 100. It is a natural result of the application of a constant B. But it is still acceptable in this case, because (1) though it causes $\leq$0.5% beam losses, no activation danger exists at such low energies; (2) afterwards, the transverse beam size is almost constant along the RFQ.

Figure 4.16 shows that the emittance ratio varies along the main part of the RFQ in the range of 0.8–1.2 (similar to the MYRRHA RFQ, see Fig. 4.8). As a very small longitudinal output emittance was required for the Injector-II RFQ, a relatively small longitudinal emittance was achieved at the end of the pre-bunching that resulted in an emittance ratio of ~1.0 for starting the two emittance transfer periods (see Fig. 4.17).

A further simulation with $I_{\text{in}} = 20$ emA showed that the transmission of the Injector-II RFQ was still >99% as required. A comparison of the design results between the China ADS Injector-II RFQ and the MYRRHA RFQ is given in Table 4.4.

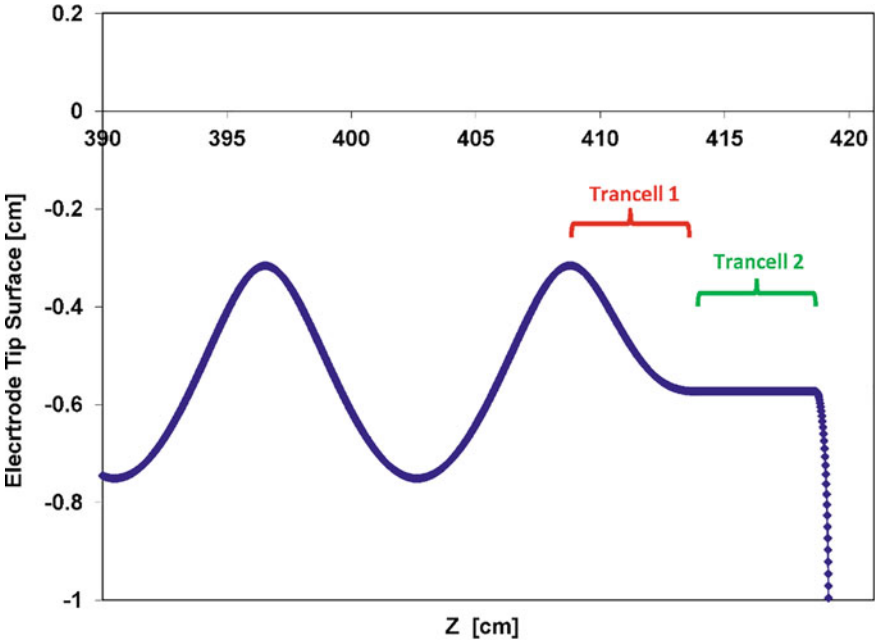

Fig. 4.13 End cells of the China ADS Injector-II RFQ

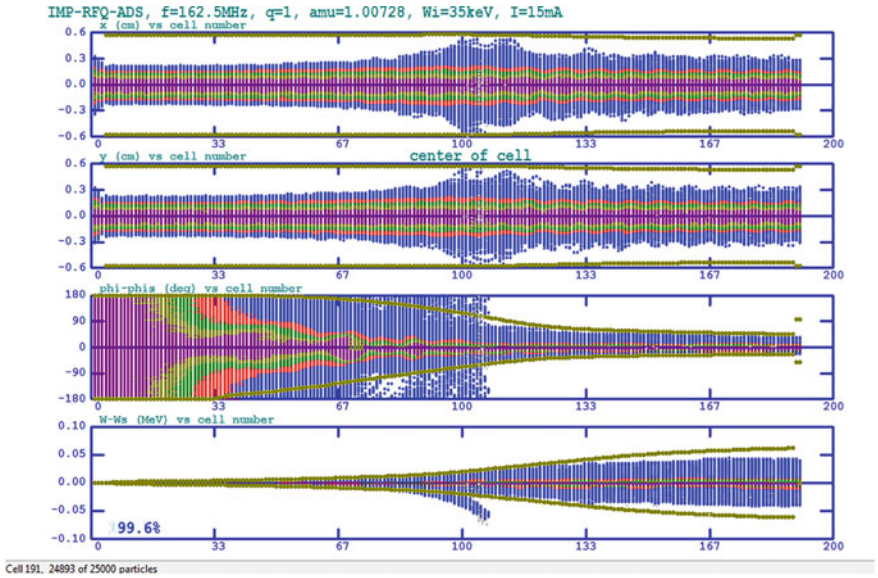

Fig. 4.14 Beam envelopes of the China ADS Injector-II RFQ [23]

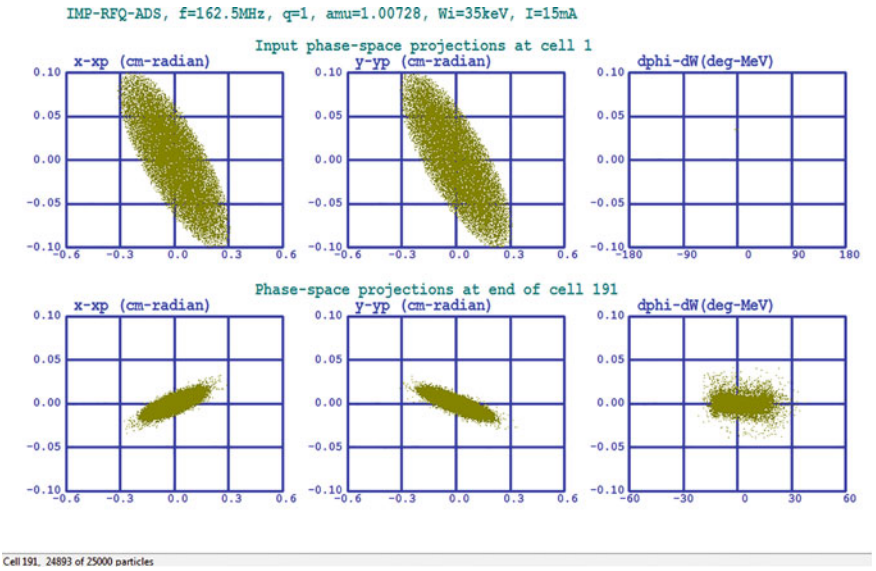

Fig. 4.15 Input (top) and output (bottom) particle distributions of the China ADS Injector-II RFQ [23]

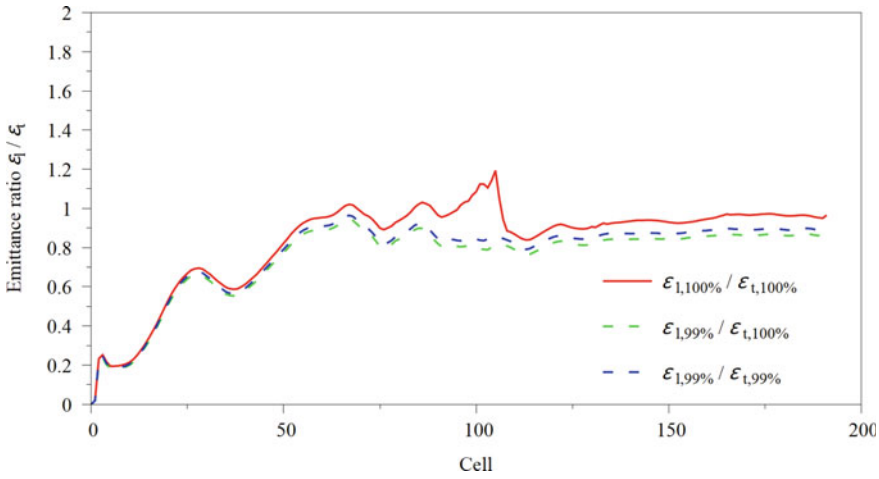

Fig. 4.16 Evolution of emittance ratio along the China ADS Injector-II RFQ

Both RFQ designs have shown good performances, e.g., $\varepsilon_{z,\,\mathrm{out,\,n,\,rms}} < 1\ \pi$ keV ns. The China ADS Injector-II RFQ has 1% higher transmission, but the inter-vane voltage of the MYRRHA RFQ is ~30% lower.

The RF conditioning of the built Injector-II RFQ was started at an RF power of 2 kW, which was ramped up gradually and carefully [22]. The nominal RF power

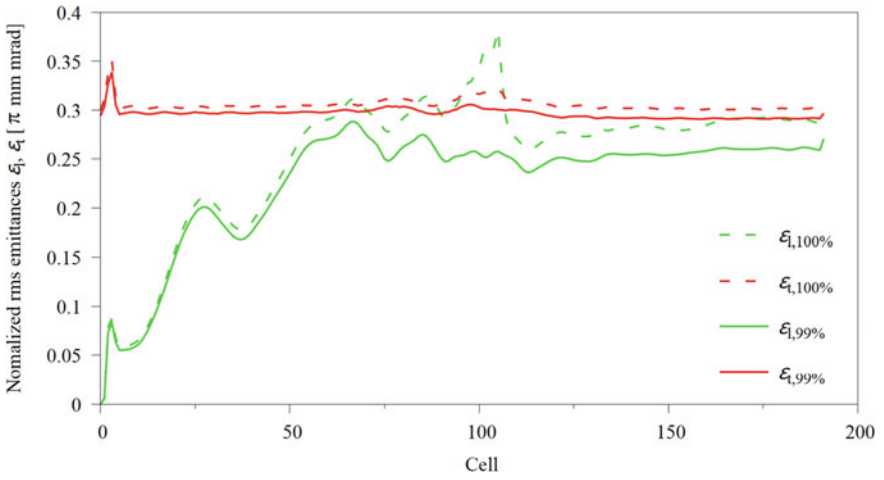

Fig. 4.17 Evolution of longitudinal and transverse emittances for 100% and 99% of particles along the China ADS Injector-II RFQ

Table 4.4 Designs for the China ADS Injector-II RFQ and the MYRRHA RFQ

Parameters	Injector-II RFQ	MYRRHA (Design CZ2013)
f (MHz)	162.5	176.1
W_{in} (keV)	35	30
W_{out} (MeV)	2.1	1.5
Duty cycle (%)	100	100
I_{in} (emA)	15 (20)	5
U (kV)	65	44
Kilpatrick factor	1.16	1.05
$\varepsilon_{t,\,in,\,n,\,rms}$ (π mm mrad)	0.30	0.20
$\Delta\varepsilon_x$ (%)	3	5
$\Delta\varepsilon_y$ (%)	3	5
$\varepsilon_{z,\,out,\,n,\,rms}$ (π keV ns)	0.92	0.73
$\alpha_{Twiss,\,t,\,in,\,max}/\alpha_{Twiss,\,t,\,out,\,max}$	1.21/1.43	0.88/0.06
L (m)	4.21	4.03
T (%)	99.6 (15 emA) 99.1 (20 emA)	98.6

92.7 kW or the nominal inter-vane voltage 65 kV (110 kW or 44 kV for the MYRRHA RFQ, because usually the 4-vane RFQ has a better R_p than the 4-rod RFQ at the same frequency) was reached after 45 days [22]. The beam commissioning was started in 2014 [22, 24] with 2 emA pulsed beams. The beam current was increased gradually

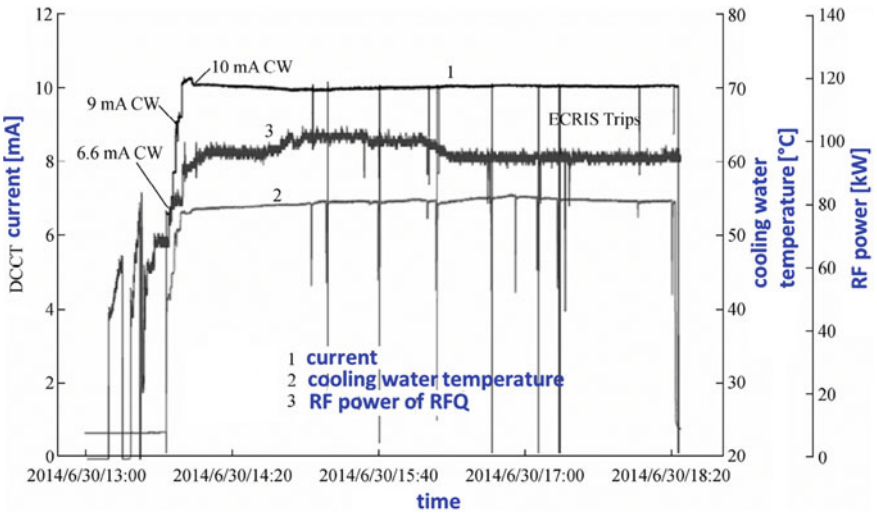

Fig. 4.18 CW beam operation of the China ADS Injector-II RFQ in 2014 [22]

to the required value of 10 emA and afterwards the duty cycle was also increased to 100%.

Figure 4.18 [22] shows the CW beam operation results (at 10 emA for ~4.5 h). The measurement results at 10 emA were as follows: the transmission efficiency was 95.3%, the output beam energy was 2.165 MeV (± 1.9%), and the transverse output emittances were 0.33 π mm mrad. At an input power of 93.6 kW, the measured beam transmission efficiency can be increased to 96.9% for a 10.5 emA input beam [24].

4.3 CW RFQ for Project X Injector Experiment at FNAL

This section introduces another 162.5 MHz, CW RFQ, which is very similar to the China ADS Injector-II RFQ. Also, based on the collaboration between Chuan Zhang and LBNL [25–27], this RFQ was developed for the Project X Injector Experiment (PXIE) [28] at FNAL.

Project X was proposed as a multi-functional proton accelerator complex, which should support FNAL's leading role in the intensity frontier research over many decades [28]. The purpose of PXIE was to test the technologies selected for the Project X front end and to mitigate the primary technical risks of the whole facility [28]. Project X was later changed to Proton Improvement Plan-II (PIP-II), and PXIE was accordingly renamed as PIP-II Injector Test (PIP2IT).

Table 4.5 shows that the design requirements of the PXIE RFQ are very similar to those of the China ADS Injector-II RFQ, except the particle species, the input energy,

Table 4.5 Design requirements of the PXIE RFQ and the China ADS Injector-II RFQ

Parameter	PXIE RFQ [27]	Injector-II RFQ
Particle species	H^-	H^+
RF structure	4-vane	4-vane
f (MHz)	162.5	162.5
W_{in} (keV)	30	35
W_{out} (MeV)	2.1	2.1
Duty cycle (%)	100	100
I_{in} (emA)	5 (up to 10)	15 (up to 20)
$\varepsilon_{t,\,in,\,n,\,rms}$ (π mm mrad)	–	0.30
$\Delta\varepsilon_t$ (%)	–	$\leq$10
$\varepsilon_{t,\,out,\,n,\,rms}$ (π mm mrad)	0.25	–
$\varepsilon_{z,\,out,\,n,\,rms}$ (π keV ns)	0.8–1.0	$\leq$1.0
T (%)	95	95
$\alpha_{Twiss,\,t,\,in,\,max}/\alpha_{Twiss,\,t,\,out,\,max}$	$\leq$0.6	$\leq$1.5

and the input beam current. From the beam dynamics point of view, the difference between H^+ and H^- ions can be ignored.

Due to the good performance of the Injector-II RFQ design and the similar design specifications (even a lower I_{in}), the design adopted by the Injector-II RFQ was also applied to the PXIE RFQ with some adaptions for the slightly lower W_{in} [29]. If the main dynamics parameters are plotted as functions of cell number, one can see that the two designs are almost identical (see Fig. 4.19 and Fig. 4.12), except the PXIE RFQ has a slightly lower U (60 kV instead of 65 kV for a lower I_{in}) and has 16 more cells.

In Table 4.6, the design parameters and simulation results of the two 162.5 MHz, CW RFQs are compared. For the PXIE RFQ at the design current 5 emA, one obtained that [27]:

- $T = 99.8\%$
- $\varepsilon_{t,\,out,\,n,\,rms} = 0.15\ \pi$ mm mrad
- $\varepsilon_{z,\,out,\,n,\,rms} = 0.64\ \pi$ keV ns.

A later simulation with new Twiss parameters for the input beam (the RFQ design itself was unchanged) gave the following results [30]:

- $T = 99.9\%$
- $\varepsilon_{t,\,out,\,n,\,rms} = 0.15\ \pi$ mm mrad
- $\varepsilon_{z,\,out,\,n,\,rms} = 0.7\ \pi$ keV ns.

The beam dynamics simulation of the PXIE RFQ was performed using a beam distribution derived from ion source emittance measurements (see the top graphs in Fig. 4.20). The data of this distribution was provided by Staples [29]. It can be seen that the transverse input beam distributions for the two RFQs have noticeable

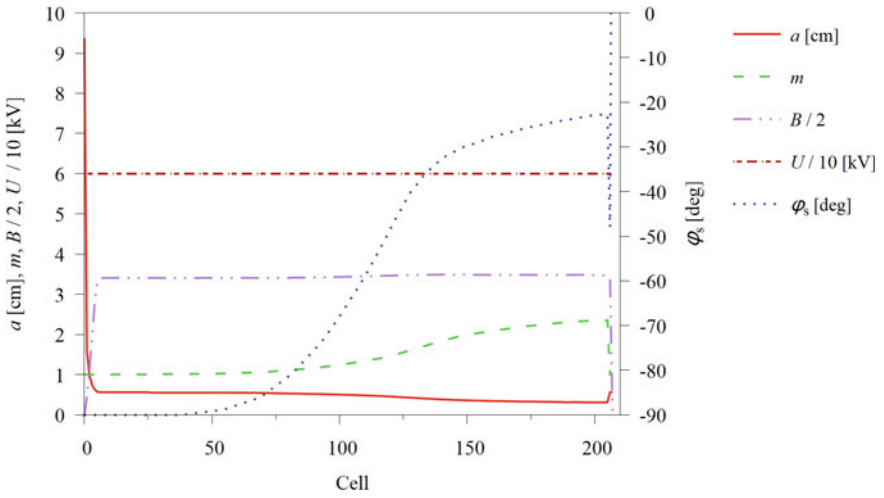

Fig. 4.19 Main design parameters of the PXIE RFQ (now: PIP2IT RFQ)

Table 4.6 Design parameters and simulation results of the PXIE RFQ and the China ADS Injector-II RFQ

Parameters	PXIE RFQ	Injector-II RFQ
f (MHz)	162.5	162.5
W_{in} (keV)	30	35
W_{out} (MeV)	2.1	2.1
Duty cycle (%)	100	100
I_{in} (emA)	5	15
U (kV)	60	65
Kilpatrick factor	1.11	1.16
$\varepsilon_{t,\,in,\,n,\,rms}$ (π mm mrad)	0.115	0.30
$\varepsilon_{x,\,out,\,n,\,rms}$ (π mm mrad)	0.155	0.307
$\varepsilon_{y,\,out,\,n,\,rms}$ (π mm mrad)	0.151	0.308
$\varepsilon_{z,\,out,\,n,\,rms}$ (π keV ns)	0.64	0.92
$\alpha_{Twiss,\,t,\,in,\,max}/\alpha_{Twiss,\,t,\,out,\,max}$	1.34/1.41	1.21/1.43
L (m)	4.45	4.21
T (%)	99.8 (5 emA) 99.6 (10 emA)	99.6 (15 emA) 99.1 (20 emA)

differences. The original design was optimized for the input beam of the China ADS Injector-II RFQ, so beam mismatching at the beginning of the PXIE RFQ will be inevitable.

In Fig. 4.21, the oscillated transverse beam envelopes up to Cell 100 confirmed the prediction for the mismatching (in the case of the Injector-II RFQ, this situation

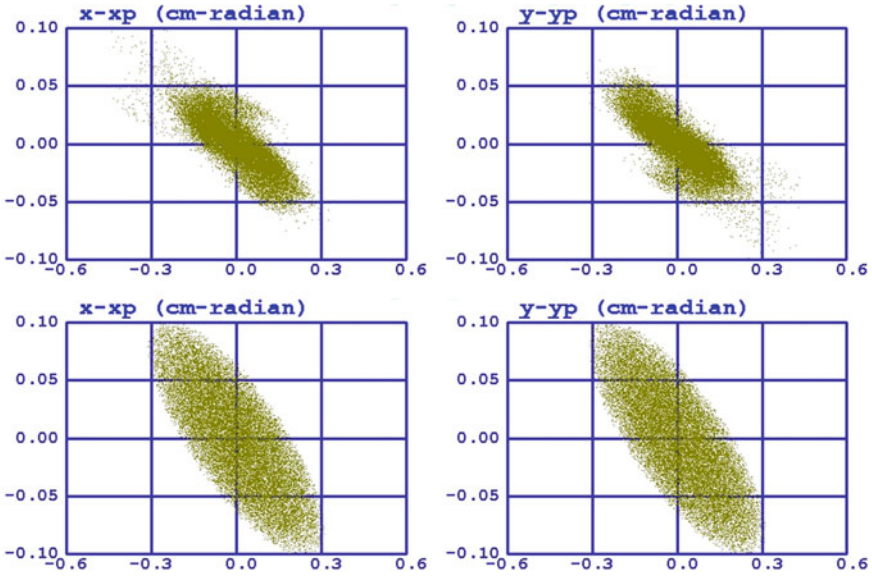

Fig. 4.20 Input particle distributions of the PXIE RFQ (top) and the Injector-II RFQ (bottom)

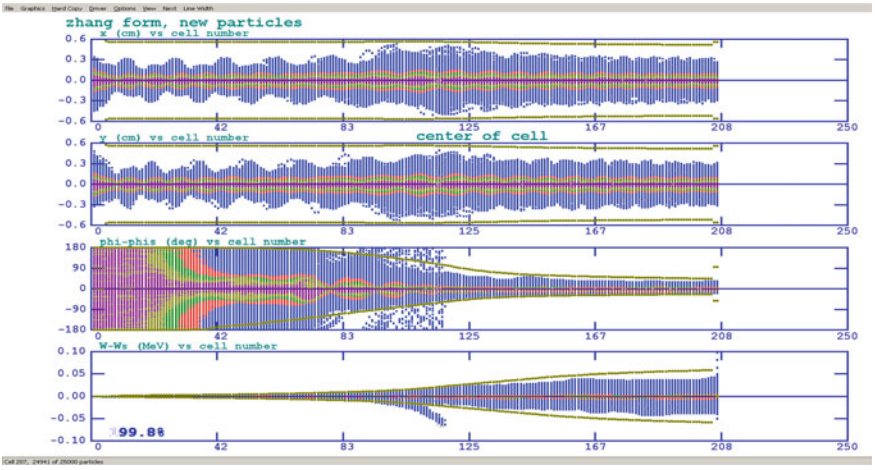

Fig. 4.21 Beam transport simulation of the PXIE RFQ [27]

could not be seen in Fig. 4.14). Furthermore, the input emittance of the PXIE RFQ, $\varepsilon_{t,\,in,\,n,\,rms} = 0.115\ \pi$ mm mrad, is only ~40% of that of the Injector-II RFQ, so the evolution of the emittance ratio will also be very different. Figure 4.22 shows that at the pre-bunching end of the PXIE RFQ, $\frac{\varepsilon_l}{\varepsilon_t}$ reached even ~2.3 instead of ~1.0 (the original value for the Injector-II RFQ).

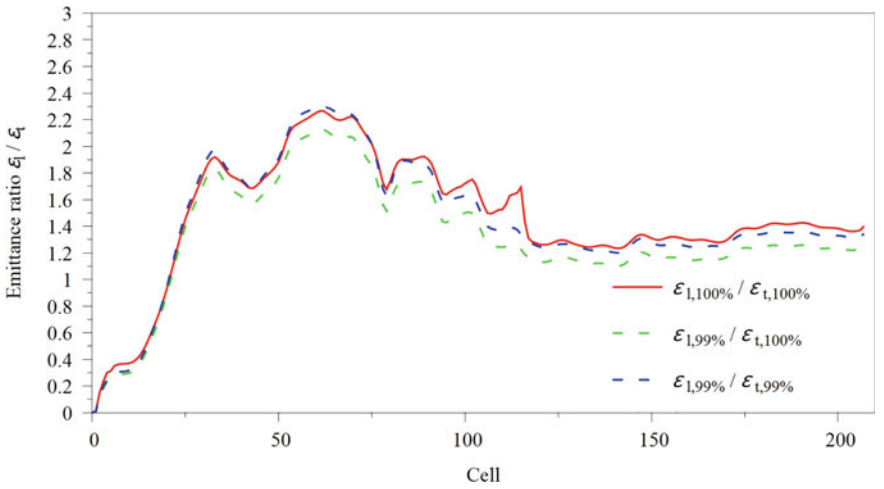

Fig. 4.22 Evolution of emittance ratios along the PXIE RFQ

In Fig. 4.23, one can see that in the PXIE RFQ:

- Obvious emittance transfer started at ~ Cell 65 and stopped at ~ Cell 120 until the emittance ratio entered the MEGLET optimum range.
- Afterwards, the emittance ratio stayed in the range of 1.2–1.4 and there was no large emittance transfer any more.

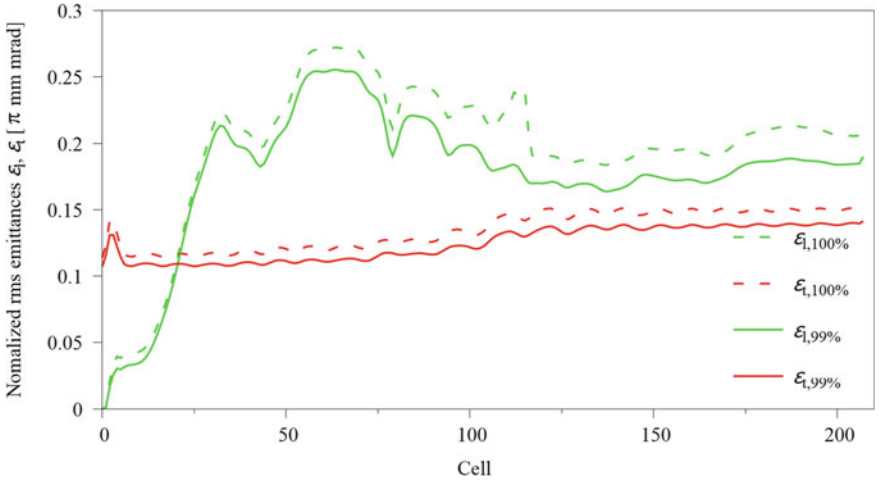

Fig. 4.23 Evolution of longitudinal and transverse emittances for 100% and 99% of particles along the PXIE RFQ

The PXIE RFQ (now: PIP2T RFQ) has been commissioned and has been operational for several years. It demonstrated stable RF operation in both pulsed and CW modes and beam measurement results were in good agreement with the RFQ beam design specifications [31] e.g.:

- The measured beam transmission efficiency of a 5 emA, H^- beam through the CW RFQ operating at 60 kV was 98%.
- Measured using the ToF method, the output beam energy was 2.1 MeV $\pm$ 1%.
- The measured beam emittances were also within the design specifications.

References

1. F. Carminati, R. Klapisch, I.P. Revol, Ch. Roche, J.A. Rubio, C. Rubbia, An energy amplifier for cleaner and inexhaustible nuclear energy production driven by a particle beam accelerator. CERN report AT/93-47 (ET) (1993)
2. H. Podlech et al., The MYRRHA-project, in *Proceedings of NAPAC* (2019)
3. The European technical working group on ADS, A European roadmap for developing Accelerator Driven Systems (ADS) for nuclear waste incineration. ENEA (2001). ISBN: 88-8286-008-6
4. H. Podlech et al., The EUROTRANS project. AIP Conf. Proc. **1265**, 355 (2010)
5. http://ipnwww.in2p3.fr/MAX/
6. F. Bouly, M. Baylac, A. Gatera, D. Uriot, Superconducting linac design upgrade in view of the 100 MeV MYRRHA phase I, in *Proceedings of IPAC* (2019)
7. T.P. Wangler, RF Linear Accelerators (Wiley-VCH Verlag GmbH & Co. KGaA, 2008). ISBN: 978-3-527-40680-7
8. C. Zhang et al., Reliability and current-adaptability studies of a 352 MHz, 17 MeV, continuous-wave injector for an accelerator-driven system. Phys. Rev. ST Accel. Beams **13**, 080101 (2010)
9. C. Zhang et al., From EUROTRANS to MAX: new strategies and approaches for the injector development, in *Proceedings of IPAC* (2011)
10. C. Zhang, H. Podlech, New reference design of the European ADS RFQ accelerator for MYRRHA, in *Proceedings of IPAC* (2014)
11. C. Zhang, H. Podlech, Efficient focusing, bunching, and acceleration of high current heavy ion beams at low energy. Nucl. Instrum. Methods Phys. Res. Sect. A **879** (2018)
12. Microwave Studio (now: CST Studio Suite), https://www.3ds.com/de/produkte-und-services/simulia/produkte/cst-studio-suite/
13. A. Bechtold, A. Schempp, M. Vossberg, Recent high power RFQ development, in *Proceedings of International Topical Meeting on Nuclear Research Applications and Utilization of Accelerators* (2009)
14. I. Mardor et al., Status of the SARAF CW 40 MeV proton/deuteron accelerator, in *Proceedings of PAC* (2009)
15. U. Ratzinger, H-type linac structures. CERN Accelerator School: Radio Frequency Engineering (2000)
16. C. Zhang, A. Schempp, Beam dynamics studies on a 200 mA proton radio frequency quadrupole accelerator. Nucl. Instrum. Methods Phys. Res. Sect. A **586** (2008)
17. K. Kümpel, C. Lenz, N. F. Petry, H. Podlech, A. Bechtold, C. Zhang, Dipole compensation of the 176 MHz MYRRHA RFQ, in *Proceedings of IPAC* (2017)
18. A. Gatera et al., MINERVA (MYRRHA Phase 1) RFQ beam commissioning, in *Proceedings of IPAC* (2021)
19. A. Gatera et al., MYRRHA-MINERVA injector status and commissioning, in *Proceedings of HB* (2021)

20. S. Fu et al., Chinese plan for ADS and CSNS, in *Proceedings of SRF* (2011)
21. Z. Zhang et al., Design of a four-vane RFQ for China ADS project, in *Proceedings of LINAC* (2012)
22. Z. Zhang et al., Development and test of ADS injector II RFQ accelerator. At. Energy Sci. Technol. **B10** (2015)
23. D. Li, IMP RFQ beam dynamics and RF design. Talk at IMP RFQ design review, Lanzhou, China (2011)
24. Z.-J. Wang et al., Beam commissioning for a superconducting proton linac. Phys. Rev. Accel. Beams **19**, 120101 (2016)
25. S. Virostek et al., Design and Analysis of the PXIE CW Radio-Frequency Quadrupole (RFQ), in *Proceedings of IPAC* (2012)
26. D. Li et al., Progress of the front-end system development for project X at LBNL, in *Proceedings of IPAC* (2012)
27. D. Li, S. Virostek for the PXIE RFQ team, PXIE RFQ design overview. Talk at PXIE program review meeting (2012)
28. S. Nagaitsev et al., PXIE: project X injector experiment, in *Proceedings of IPAC* (2012)
29. J.W. Staples, Email on August 29th (2011)
30. D. Li, PXIE RFQ. Talk at PXIE program review meeting (2013)
31. A. Saini et al., Beam tests of the PIP-II Injector test radio frequency quadrupole. Nucl. Instrum. Methods Phys. Res. Sect. A **978** (2020)

Chapter 5
Towards Efficient Long RFQ Accelerators

Abstract This chapter presents new solutions, which use multiple shorter and independent cavities, for the realization of future long RFQ accelerators. From the RF point of view, the use of shorter cavities has many advantages, e.g., the longitudinal field stability can be improved, the RF tuning can be simplified, and a large power amplifier that usually needs to be customized can be replaced by several small ones already available on the market. However, the beam matching between cavities can become an issue, especially at high current and low energies, because the RFQ has rather small electrode apertures and its focusing system always varies with time. Benefiting from the new design approaches introduced in Chap. 2 and some other special ideas, two efficient multi-cavity RFQ accelerators have been designed:

- One > 9-m-long MEGLET-style RFQ accelerator based on the IH structure for 20 emA uranium ions.
- One > 6-m-long SEGLER-style RFQ accelerator based on the 4-rod structure for 105 emA protons.

This kind of multi-cavity RFQ accelerators can also be used for the experimental demonstration of MEGLET- or SEGLER-style emittance transfers.

5.1 MUSIC: Realizing Long RFQs Using Multiple Shorter and Independent Cavities

The RFQ accelerator is excellent in capturing, focusing, and bunching a dc beam from an ion source (or an LEBT), but is not very efficient for accelerating it to high beam energy (the electric field in an RFQ has a large component in the transverse direction). Typically, the output beam energy of an RFQ accelerator is lower than 3 MeV/u, and its structure length is shorter than 4 m. For some projects (see Fig. 5.1), however, longer RFQs have been constructed or operated. Except for the ISAC RFQ [1] and the HSI RFQ [2], they are all using the 4-vane structure based on the TE_{210} mode.

One important reason for having a long RFQ can be due to the accelerating structure behind the RFQ, usually a DTL. The accelerating cells at the low energy

C. Zhang, *Radio-Frequency Quadrupole Accelerators*, Particle Acceleration and Detection, https://doi.org/10.1007/978-3-031-40967-7_5

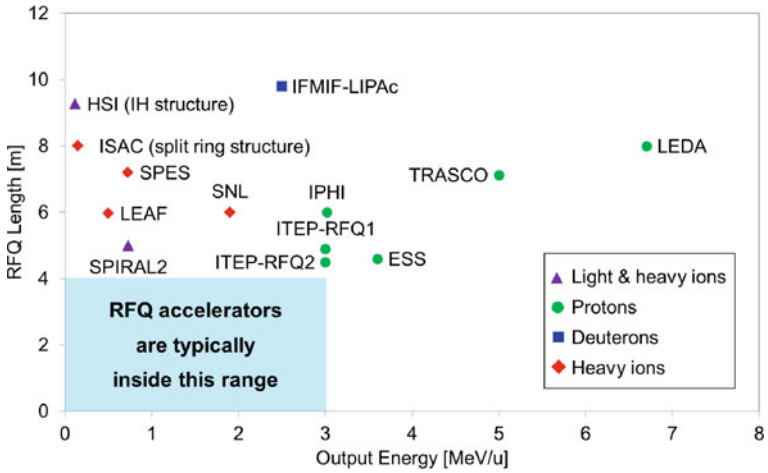

Fig. 5.1 Overview of some long (> 4 m) RFQ accelerators constructed or operated worldwide [3]

end of a DTL need a reasonable length so that the tubes can be physically constructed and also can be easily cooled if the duty cycle is high. Typically, the length of the first DTL cell should be longer than 3 cm in case no integrated quadrupole magnet is necessary for the tube; otherwise, the RFQ needs to provide an output beam with even higher beam velocity. Furthermore, for some very high current machines, higher output energy of the RFQ can make the beam dynamics of the downstream DTL less challenging.

For an RFQ accelerator, it is very important to keep a good frequency separation between the operating mode and the nearest unwanted mode. In case of the 4-vane structure operating in the TE_{210} mode, the sensitivity to tuning errors can be expressed as proportional to $(L/\lambda)^2$, where L is the RFQ length and λ is the free-space wavelength [4–6]. It implies that the longer the 4-vane RFQ is, the more difficult the RF tuning is. The HSI RFQ uses the IH-RFQ structure based on the TE_{110} mode. Similar to the 4-vane structure, the magnetic field lines in the HSI RFQ are parallel to the beam axis and turning around at the two ends of the cavity. The 4-rod structure does not have such a longitudinal stability problem, but the RF tuning also becomes complicated, when the structure is longer than 4 m.

To address the difficulties in realizing long RFQs, several solutions have been proposed and developed. One is the so-called "resonant coupling" approach, which divides a long RFQ accelerator into short (e.g., 1–2 m) sections and couples them together by short (a few mm) gaps between the end regions [7]. The RF simulation of a 4-m-long, 425 MHz RFQ showed that the frequency difference between the mode of interest and the neighboring mode could be increased from 1.9 to 6.6 MHz via resonant coupling [7]. After the successful application to the 8-m-long LEDA RFQ [8], this approach has been taken for many later long 4-vane RFQs, e.g., TRASCO [9]. This kind of coupled structure needs only one RF power source and one beam dynamics design, so it is still one RFQ.

Another idea is to use a so-called "Tandem-RFQ", i.e., two sequential RFQ cavities with independent RF systems. Three examples are: (1) the constructed SNL RFQ with a total length $L_{\text{total}} = 6$ m [10], the constructed superconducting PIAVE RFQ with $L_{\text{total}} = \sim 2$ m [11] (it is not a long RFQ, but uses a similar idea), and the proposed EURISOL RFQ with $L_{\text{total}} = 7.8$ m [12]. A challenge for using this concept is the beam matching issue between the RFQ cavities, especially in the transverse direction. Usually at the entrance to an RFQ accelerator, converging (Twiss alpha parameters $\alpha_{\text{Twiss}} > 0$) and similar particle distributions in both x and y planes are desired, as shown in Graph (a) in Fig. 5.2. But at the exit of an RFQ, typically the output beam is converging in one transverse plane and diverging ($\alpha_{\text{Twiss}} < 0$) in another one, as shown in Graph (b) in Fig. 5.2. This makes the transition between two RFQ cavities demanding and the matching problem can become very critical at high beam current.

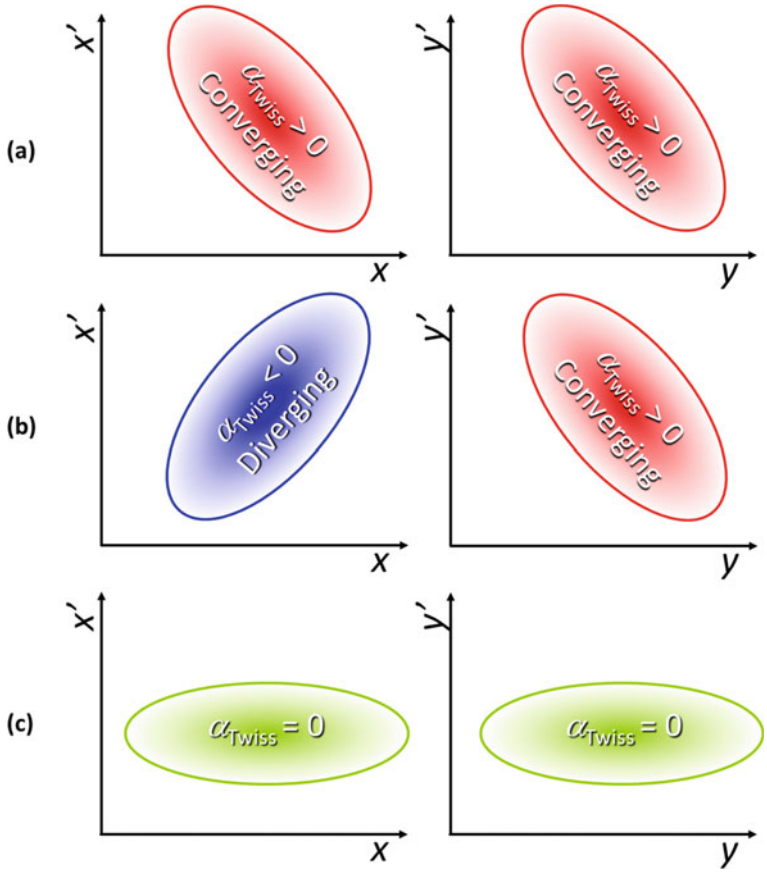

Fig. 5.2 Schematic plots for **a** typical required RFQ input distributions, **b** typical RFQ output distributions (x and y phase planes can be exchanged), and **c** suggested $\alpha_{\text{Twiss}} = 0$ distributions for the transition between two RFQ cavities [3]

For the SNL and PIAVE projects, low beam currents up to eμA were required, so no special care was necessary between two separated cavities. EURISOL has been planned to work in two beam modes: heavy ion beams with negligible currents (CW operation) and up to 7.5 emA light ion beams (pulsed operation) [12]. In the EURISOL design, two RFQ structures are mounted inside the same tank and they are separated by a thin RF shielding wall (the gap between the two sets of electrodes is 1.7 cm long), thus accomplishing a short transition [12].

To investigate the realization of efficient long RFQs using multiple shorter and independent cavities with not only improved field stability and easy RF tuning but also reach high beam transmission and good beam quality, even at high current, the > 9-m-long HSI RFQ has been adopted as an example. The main design parameters of the two constructed HSI RFQs can be found in Table 3.7.

In the RF study performed for the first HSI RFQ [13], one can see that (1) for the full-length tank, the frequency difference between the operating mode and the nearest mode is around 2 MHz; (2) for short tank segments, the higher resonant modes are by about a factor of 8 above the fundamental mode.

Instead of using a non-constant mid-cell aperture r_0 varied from 5.2 to 7.8 mm like the Version-1998 RFQ (see Table 3.7), the Version-2008 adopted an almost constant r_0 (~6.0 mm) [14] for the main part of the RFQ, in order to keep the distributed capacitance along the accelerator nearly constant for easier tuning. This has no influence on the frequency gap for the mode separation (still ~2 MHz).

Another remarkable change in the Version-2008 design is that the inter-vane voltage U was increased from 125 to 155 kV [14]. On the one side, it is because of a higher design beam current (from 16.5 to 20 emA). On the other side, this is necessary for meeting the demand of having a constant r_0 for such a long machine. However, this change required more RF power (the power is proportional to U^2).

Both the Version-1998 HSI RFQ and the Version-2008 HSI RFQ adopted a > 9-m-long cavity. For this study, a new solution using MUltiple Shorter and Independent Cavities (MUSIC) to realize a long RFQ is being proposed with the following advantages [3]:

- It increases the frequency gap for mode separation (improves the longitudinal field stability) and eases the RF tuning.
- One can use smaller and lower-cost power amplifiers.
- It allows designing the different parts of the long accelerating channel more reasonably, flexibly, and efficiently. One can adapt the cavities to the changing beam situation along the beam line, e.g.: (1) almost constant but different r_0 values can be applied for different cavities, which eases tuning; (2) the inter-vane voltage of each cavity can be chosen individually according to the different space-charge situations.
- It supports to add beam diagnostics and knobs between cavities for beam matching and tuning in the operation.

To apply the MUSIC solution for the > 9-m-long HSI RFQ, different scenarios have been investigated:

- The RFQ was cut into two pieces with a drift space in between.
- The RFQ was cut into two pieces with a Medium Energy Beam Transport (MEBT) section in between.
- The RFQ was cut into three pieces with drift spaces in between.

The HSI RFQ covers the energy range of 2.2–120 keV/u. No matter for a 2-piece solution or for a 3-piece solution, therefore, the transition energy W_{trans} between the cavities will be much lower than those of the three above-mentioned Tandem-RFQs (SNL: $W_{\text{trans}} = 1.22$ MeV/u [10]; PIAVE: $W_{\text{trans}} = 341.7$ keV/u [11]; EURISOL: $W_{\text{trans}} = 260$ keV/u [12]). Furthermore, the much higher design beam current, 20 emA, will make the design work very challenging, especially for the first RFQ cavity.

Different from the resonant coupling approach that divides a long RFQ into several segments with short (a few mm long) gaps as transitions, which has only one radial matching section and one fringe field section, the multi-cavity approach used by this study has multiple radial matching sections and exit fringe field sections. Each cavity has to be treated separately, not only from an RF point of view but also in the sense of beam dynamics.

To allow a smooth beam matching between two cavities, an idea is to let the output beam distributions in both transverse planes of the front cavity have $\alpha_{\text{Twiss, t, out}} \approx 0$, as shown in Graph (c) of Fig. 5.2 [3]. This can be realized by introducing two transition cells to the exit part of the electrodes in the front RFQ cavity (see Fig. 4.13) [3].

In addition, to reach good beam quality and high transmission for a MUSIC-style RFQ at high current, the MEGLET and SEGLER methods are also very important for controlling emittance growths and reducing beam instability.

5.2 HSI MUSIC-RFQ (Solution 1): Cavity + Drift + Cavity

For the HSI RFQ, a first solution using two RFQ cavities with a drift space in between has been developed. Each cavity should have a structure length that is roughly half of the original RFQ length, i.e., ~4.64 m. Because the first cavity (RFQ 1) is more important for bunching and the second one (RFQ 2) is more important for acceleration, the transition energy has been chosen as 53.6 keV/u which means that the RFQ 1 should cover an energy gain less than half of what is required for the whole HSI RFQ.

The design of the RFQ 1 is very important and relatively more difficult, because it performs the main bunching at lower energy and sees stronger space-charge effects. Therefore, the design has been optimized by following the MEGLET method in order to reach good beam quality with minimum emittance growths. To obtain $\alpha_{\text{Twiss}} \approx 0$ transverse beam distributions at the exit of the RFQ 1, the length of the Transition Cell 2 (see Fig. 4.13) has been chosen as 3.2 cm.

As the "$\alpha_{\mathrm{Twiss}} \approx 0$" method cannot provide an ideal matching as shown in Graph (a) of Fig. 5.2, a conventional radial matching section (with large starting aperture, $\varphi_s = -90°$, and $m = 1$) has still been adopted for the RFQ 2. Because the RFQ 2 receives an already bunched input beam, a two-cell radial matching section is already sufficient for a good transition. Afterwards, the electrode aperture, the synchronous phase and the modulation parameter can be quickly changed to the values close to those at the RFQ 1 output.

In Fig. 5.3, the main design parameters along this 9.28-m-long, 36.136 MHz linac with two RFQ cavities (4.64 m and 4.63 m long, respectively) and a drift space (drift length $d = 1$ cm) in between are shown. This solution is referred to as "2-RFQ with drift" in the following text.

It can be seen that (1) the inter-vane voltage values have been set differently for the two cavities; (2) in the second cavity, all parameters are held almost constant, except some parameters, e.g., φ_s, have been modified at the entrance and at the exit for better matching.

A comparison of the mid-cell aperture r_0 values between the new solution and the designs of the two built HSI RFQs is given in Fig. 5.4. Compared to the Version-1998 and Version-2008 RFQs, the 2-RFQ solution has a much larger r_0 at the entrance, which helps to increase the transverse acceptance as well as the beam transmission. Then, its r_0 value becomes smaller than those of the other two designs, which supports using lower U and saving RF power. Last but not least, the r_0 value is quasi-constant in the main part of the first cavity as well as in the entire second cavity, which allows for easy RF tuning.

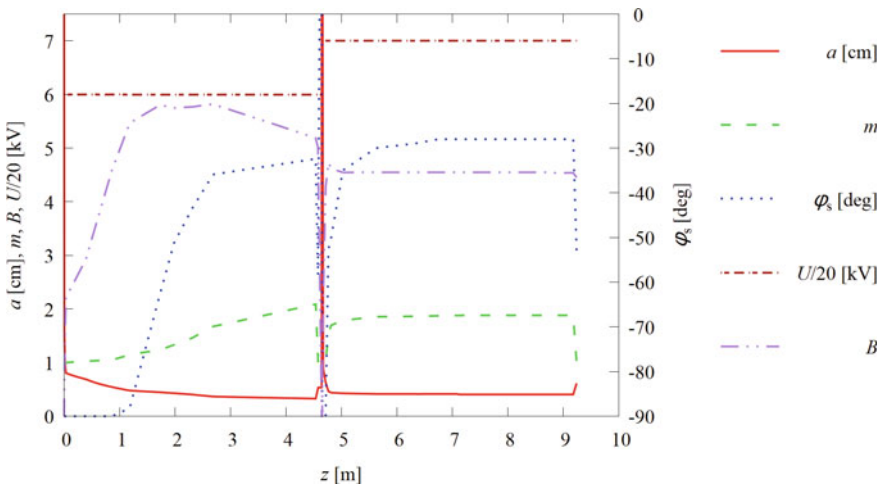

Fig. 5.3 Main design parameters of the "2-RFQ with drift" solution [3]

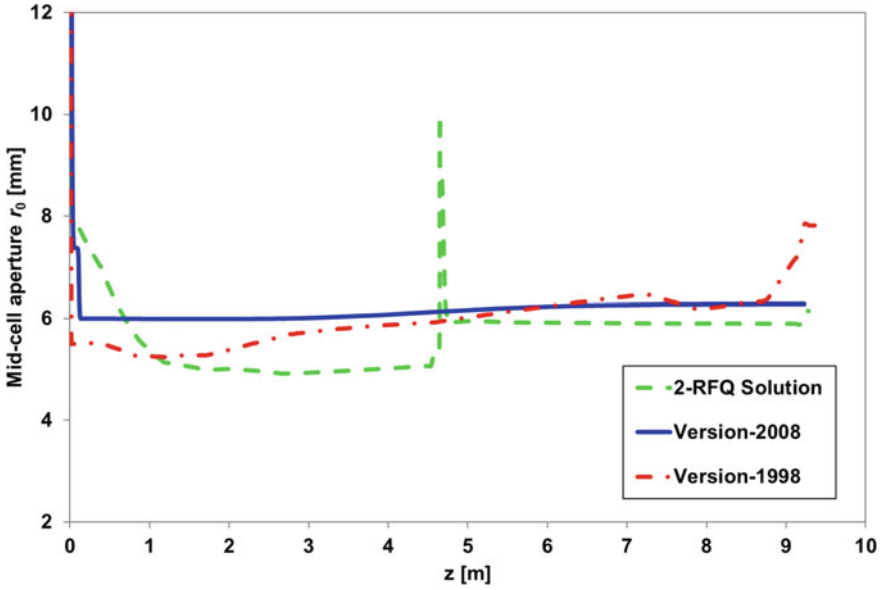

Fig. 5.4 Evolution of the mid-cell aperture along the accelerating channel (compared with the Version-1998 and Version-2008 RFQs)

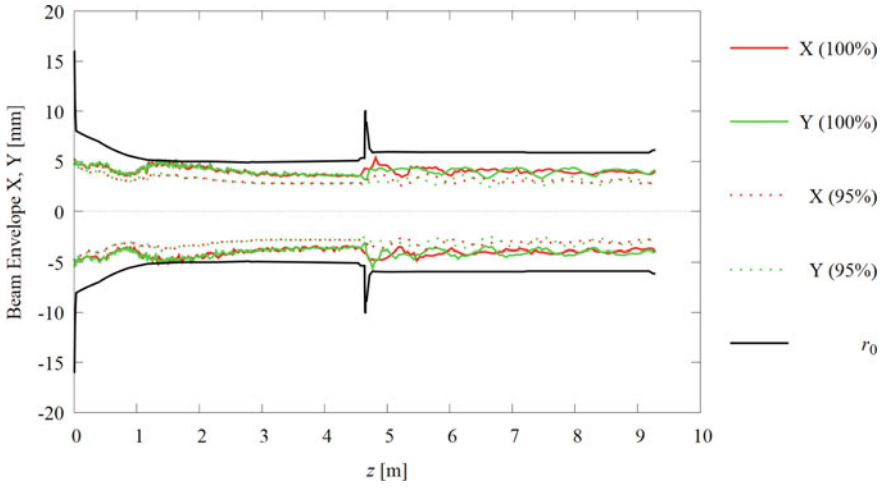

Fig. 5.5 Transverse beam envelopes for all particles as well as for 95% of the beam

The beam dynamics simulation of this MUSIC-RFQ has been performed using the PARMTEQM code. The 20 emA U^{4+} input beam has a 4D-Waterbag distribution, and its transverse emittance is 210 π mm mrad (unnormalized, total) or 0.076 π mm mrad (normalized, rms), the same value as that used by the Version-2008 RFQ. The transverse beam envelopes for all particles as well as for 95% of the beam are shown in Fig. 5.5, where the black curves represent the available aperture

based on the mid-cell aperture of the RFQs and the aperture radius of the beam hole in the RF shielding wall between the RFQ cavities. The total beam transmission of the linac is 96.05% and most losses happened in the range of $z = 1$–2 m, so at low energy.

In Fig. 5.6, the transverse emittances are relatively constant as functions of the longitudinal position, while the longitudinal emittance for all particles increases in the range of $z = 2$–7 m, but the longitudinal emittance curve for 99% of the beam indicates that this increase is due to only $\leq$1% of halo particles. It can be also seen that in the RFQ 1, the emittance ratio has been successfully held around $\frac{\varepsilon_l}{\varepsilon_t} = 1.0$. Although there are some additional emittance growths at the transition, the emittance ratio in the RFQ 2 is still well inside the range of $1.2 \leq \frac{\varepsilon_l}{\varepsilon_t} \leq 1.4$. In short, this is a MEGLET-style linac and the beam quality has been well maintained along the entire accelerating channel.

The output distribution of the RFQ 1 (see the top graphs of Fig. 5.7) shows that the introduced transition cell has successfully provided $\alpha_{\text{Twiss}} \approx 0$ transverse beam distributions for entering into the RFQ 2. The beam distribution at the end of the entire linac (see the bottom graphs of Fig. 5.7) is still very concentrated. Its phase spread and energy spread for the main part of the beam are well within $\pm 30°$ and $\pm 1\%$, respectively.

The above results are based on the 2-RFQ solution with a short drift between the two RFQ cavities (the drift length $d = 1$ cm, and the distance between two sets of electrodes is 3.1 cm). A batch of simulations has been performed by varying d from 1 to 11 cm with an interval of 2 cm. Fig. 5.8 shows that the beam transmission is still ~90% when $d = 8$ cm.

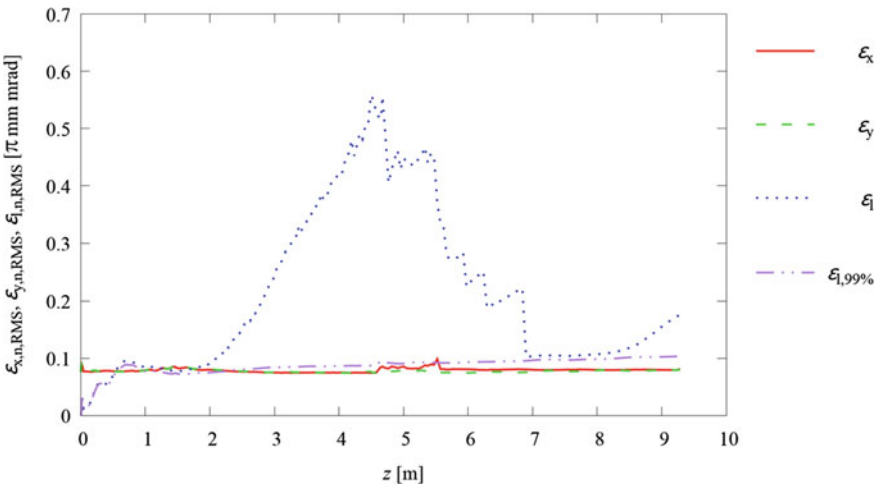

Fig. 5.6 Emittance evolutions along the linac (red: x plane, green: y plane, blue: longitudinal plane for all particles, and purple: longitudinal plane for 99% of the beam)

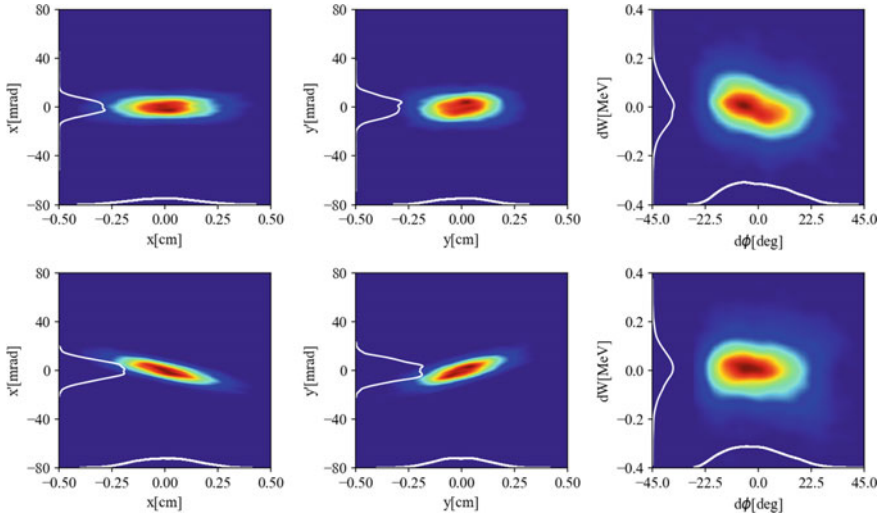

Fig. 5.7 Particle distributions at the RFQ 1 output (top) and at the RFQ 2 output (bottom)

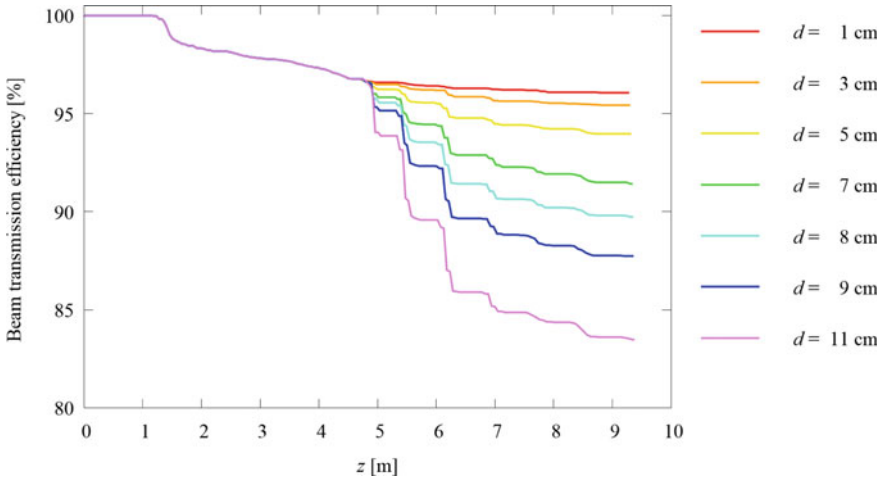

Fig. 5.8 Beam transmission curves for different drift lengths ($d = 1$–11 cm)

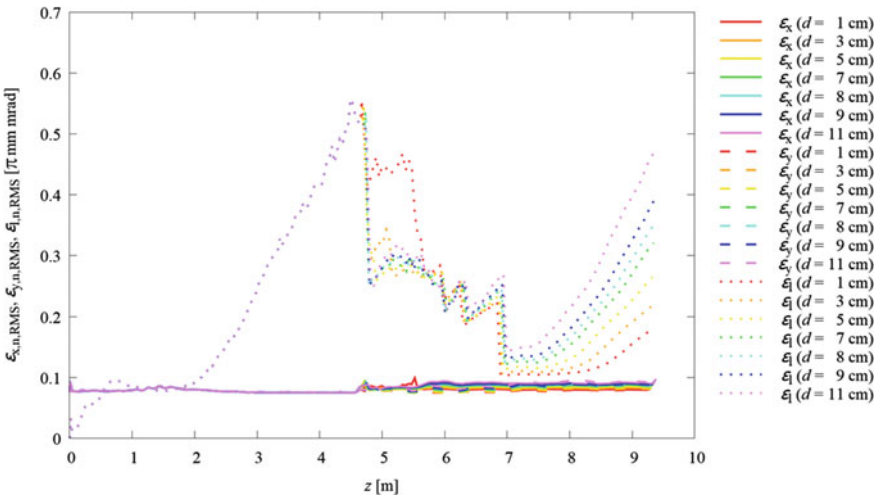

Fig. 5.9 Emittance evolution curves for different drift lengths ($d = 1$–11 cm)

Figure 5.9 shows the evolution of the transverse and longitudinal emittances for different drift lengths. It can be seen that the change of the d value has very little influence on both transverse emittance curves. Up to $z = 7$ m, the evolutions of the longitudinal emittance values for the different cases are still very similar.

Afterwards, a larger d leads to a larger longitudinal output emittance, e.g., 0.176 π mm mrad at $d = 1$ cm and 0.350 π mm mrad at $d = 8$ cm. However, their 99% longitudinal output emittance values, 0.106 π mm mrad and 0.131 π mm mrad for $d = 1$ and 8 cm, respectively, are still relatively close.

Based on these results, different possible schemes can be applied to connect the two RFQ cavities whilst still obtaining reasonable beam transmission. One method is using a 1–5-cm-thick wall to separate the RF fields of the two RFQs (see Fig. 5.10). Actually, it is also possible to have two individual end plates if $d \geq 4$ cm.

In case of 5 cm $\leq d \leq 8$ cm, one beam diagnostic element, e.g., an AC Current Transformer (ACCT), can be introduced into this drift space and integrated with the end plate as shown in Fig. 5.11. The aperture diameter at the two ends of the added element can be kept at 2 cm for good RF shielding and then enlarged to 4 cm in the middle.

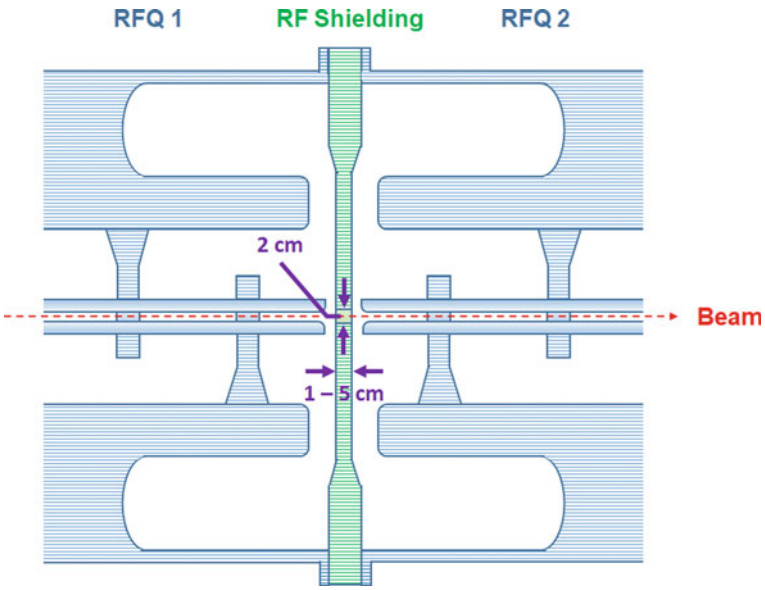

Fig. 5.10 Schematic plot for the connection of two RFQs by an RF shielding wall (the distance between two sets of electrodes excluding the RF shielding wall is 2.1 cm) [3]

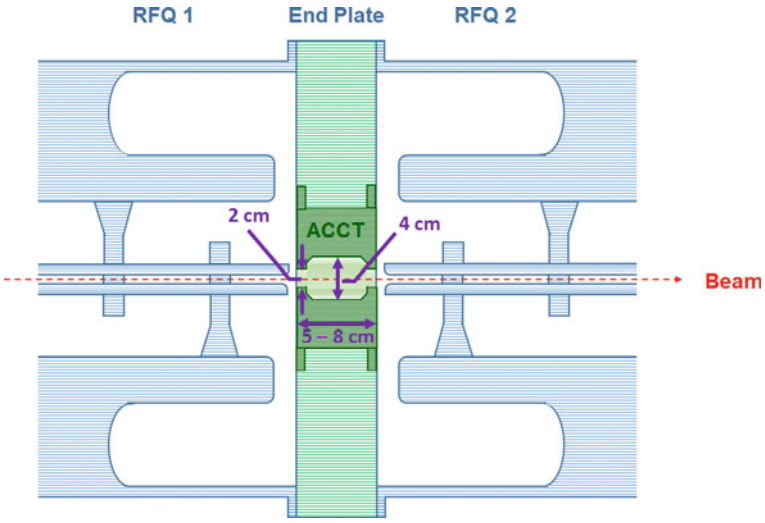

Fig. 5.11 Schematic plot of the connection between two RFQs for 5 cm $\leq d \leq$ 8 cm [3]

5.3 HSI MUSIC-RFQ (Solution 2): Cavity + MEBT + Cavity

To allow more inter-tank elements, e.g., XY-steerer and Beam Position Monitor (BPM) for a better beam matching and orbit correction in the real operation, the 2-RFQ solution has been further extended by including an MEBT section. As schematically shown in Fig. 5.12, the MEBT section consists of two 65-cm-long triplets and one 3-gap rebuncher cavity. At 36.136 MHz, a spiral structure [15] or a split-ring structure is a good candidate for the rebuncher. The main design parameters of the MEBT section are listed in Table 5.1.

For this solution, the RFQ 1 mentioned in Sect. 5.2 is chosen due to its good performance. The MEBT has been designed in a way that its output distribution should be close to that of the RFQ 1 so that the matching to the following RFQ cavity will be as smooth as possible. The RFQ 2 also uses the same design, except

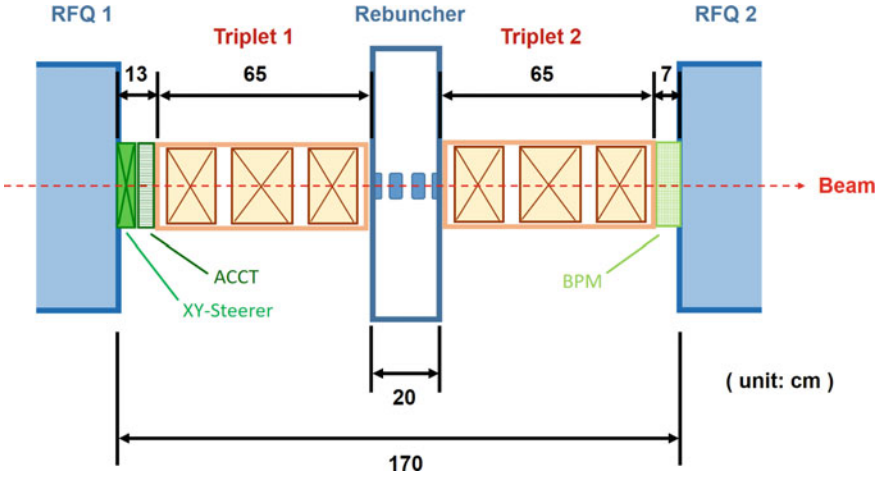

Fig. 5.12 Schematic plot of the connection between two RFQs with an MEBT [3]

Table 5.1 Main design parameters of the MEBT section [3]

Parameter	Triplet 1	Rebuncher	Triplet 2
Quadrupole length (cm)	16/20/16		16/20/16
Quadrupole inner diameter (cm)	3		3
Quadrupole pole-tip field (T)	$\leq$1.14		$\leq$1.17
Resonant frequency (MHz)		36.136	
Period length (cm)		4.45	
Effective gap voltage (kV)		68	
Tube inner diameter (cm)		2.4	

the starting part has been slightly modified for the adaptation to the beam from the MEBT.

Using the RFQ 1 output distribution (see the top graphs of Fig. 5.7) as the input distribution, the open source DYNAC code [16] has been adopted for the beam dynamics simulation of the MEBT section. The DYNAC code originated at CERN and has undergone continuous development for several decades. The code can simulate all standard linac elements, e.g., quadrupoles, RFQ, DTL, and XY-steerers. DYNAC has been benchmarked with other codes, e.g., TRACK, TraceWin/TOUTATIS, IMPACT and LORAS (now: LORASR); it was also used to aid the commissioning of the LINAC3 at CERN and the ReA3 at Michigan State University; and it is being used to support the operations of the ReA3 [17–23].

For a benchmark, the LORASR code [24] has been taken. Both codes gave very similar results. Although the magnetic focusing for such a very low β and very heavy ion beam is difficult, a 94.5% beam transmission has been achieved and the total transverse emittance growths are lower than 15%. The transverse beam envelopes (see Fig. 5.13) have only some obvious oscillations in the MEBT part, but in the RFQ cavities, they are still very similar to those of the "2-RFQ with drift" solution.

Figure 5.14 shows the transverse emittances are still relatively constant along the accelerating channel, despite the presence of the 1.7-m-long MEBT. The longitudinal emittance has a little more growth with the new solution, but the 99%-emittance curve is still flat.

Figure 5.15 shows the particle distributions at the MEBT exit and the exit of the entire linac. They are still comparable to the distributions shown in Fig. 5.7.

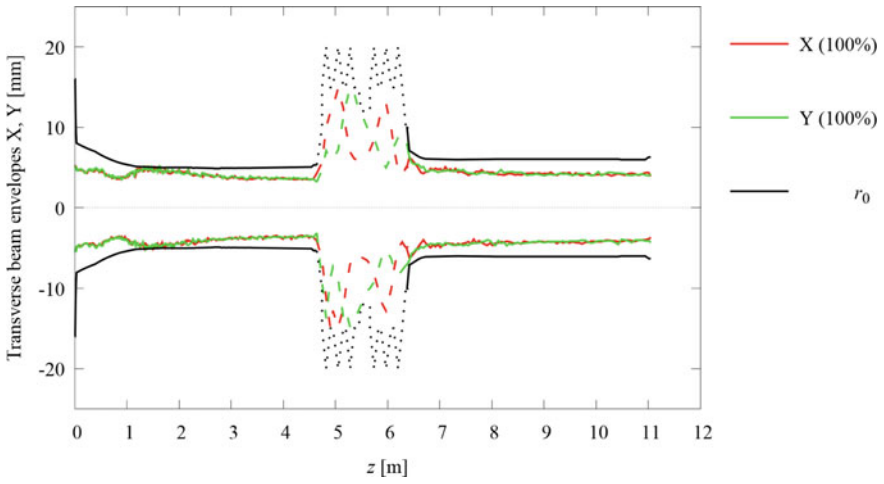

Fig. 5.13 Transverse beam envelopes for all particles along the MUSIC-RFQ (the solid lines are for the RFQ cavities and the dashed lines are for the MEBT section, respectively)

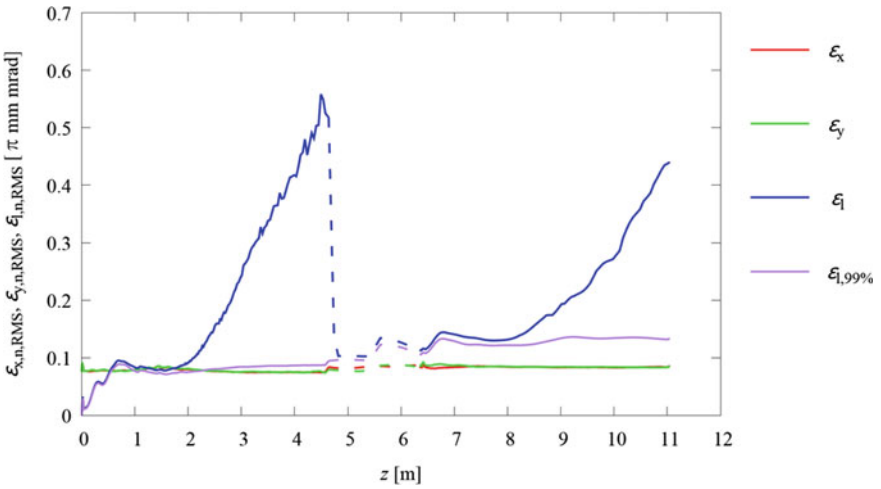

Fig. 5.14 Emittance evolutions along the MUSIC-RFQ with an MEBT (the solid lines for the RFQs, the dash lines for the MEBT section, and the purple curve for 99% of the beam)

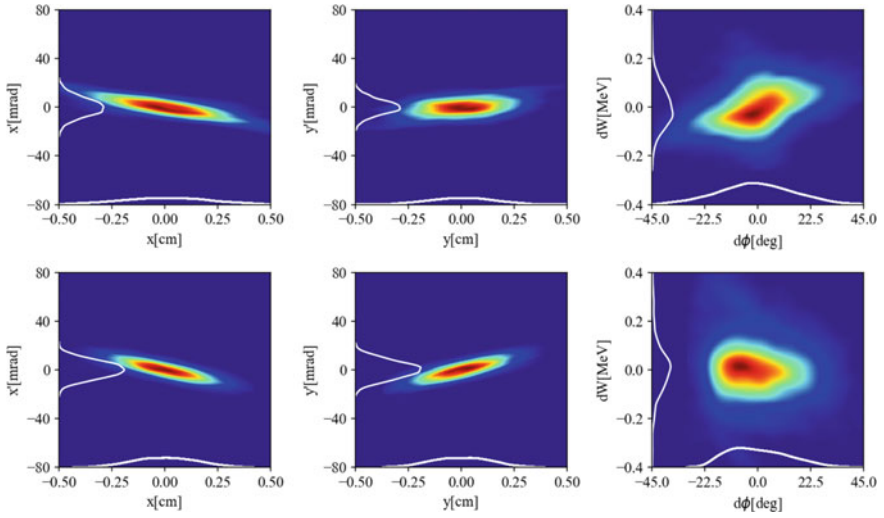

Fig. 5.15 Particle distributions at the MEBT output (top) and at the RFQ 2 output (bottom)

5.4 HSI MUSIC-RFQ (Solution 3): Cavity + Drift + Cavity + Drift + Cavity

Finally, a design using three RFQ cavities with drifts in between has been made. The transition energy values between the cavities have been chosen as 32.6 and 78.5 keV/u, respectively. Due to the different output energy, the RFQ 1 design has been modified, but still following the MEGLET design guideline and the concept to have $\alpha_{\text{Twiss}} \approx 0$ transverse output beam distributions. The main design parameters of the new linac are shown in Fig. 5.16, where the RFQ 1, the RFQ 2, and the RFQ 3 are 3.5 m, 2.9 m and 2.9 m long, respectively. For this plot, the drift length between the cavities is 1 cm. Generally speaking, the parameters are varying in a similar way to those in the 2-RFQ case (see Fig. 5.3).

The beam dynamics simulation of the "3-RFQ with drift" solution has also been performed using the PARMTEQM code. As the RFQ 1 stops at even lower output energy, the beam dynamics of this linac is more challenging due to the space charge. Nevertheless, the total length is only 3 cm longer and the total transmission is only 1.6% lower, compared with the "2-RFQ with drift" case. Further simulations show that the transmission is still ~90% when d is prolonged to 6 cm (without modification and optimization of the RFQ 2 and the RFQ 3). A comparison of the main parameters between this solution and the 2-RFQ solutions is given in Table 5.2.

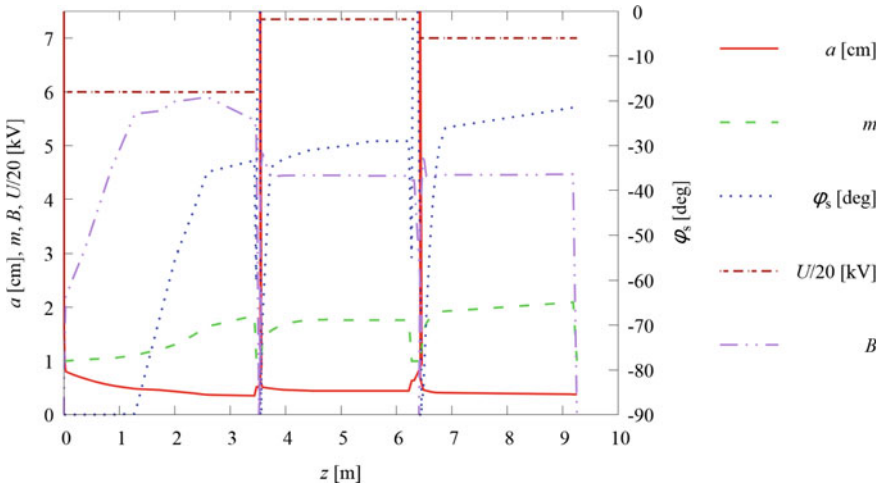

Fig. 5.16 Main design parameters of the "3-RFQ with drift" solution [3]

Table 5.2 A comparison of the 2-RFQ and 3-RFQ solutions (input emittance = 0.076 π mm mrad)

Parameter	2-RFQ w. drift		2-RFQ w. MEBT	3-RFQ w. drift	
Number of RFQ cavities	2	2	2	3	3
Transition between cavities	Drift	Drift	MEBT	Drift	Drift
Transition length d (cm)	1	8	170	1 (each)	6 (each)
$E_{s,\,max}$ (MV/m)	30.9	30.9	30.9	30.9	30.9
U (kV)	120/140		120/140	120/147/140	
$\Delta\varepsilon_x$ (%)					
For 100% beam For 99% beam	7.9 3.9	21.1 15.8	13.2 9.2	13.2 9.2	23.7 18.4
$\Delta\varepsilon_y$ (%)					
For 100% beam For 99% beam	6.6 2.6	14.5 10.5	11.8 7.9	10.5 6.6	23.7 18.4
$\varepsilon_{1,\,out,\,n,\,rms}$ (π mm mrad)					
For 100% beam For 99% beam	0.176 0.106	0.350 0.131	0.440 0.134	0.464 0.117	1.142 0.144
Total length L (m)	9.28	9.35	11.05	9.31	9.41
Total beam transmission T (%)	96.1	89.7	94.5	94.5	89.3

From Table 5.2, one can see that:

- The maximum surface electric field $E_{s,\,max}$ for all these solutions is 30.9 MV/m, lower than that of both the Version-1998 RFQ (31.8 MV/m) and the Version-2008 RFQ (31.2 MV/m).
- The inter-vane voltage for the solutions is between 120 and 147 kV, lower than 155 kV used by the Version-2008 RFQ.

These indicate that the new solutions can support a more reliable and more efficient (the power is proportional to U^2) operation.

In addition, the end-to-end evolution curves of synchronous energy and beam transmission are plotted in Figs. 5.17 and 5.18, respectively, for the three reference cases. Generally speaking, they are very comparable, if the MEBT is skipped.

5.5 MUSIC-RFQ for High Brilliance Neutron Source

In Chap. 3 and in Chap. 4, a small-scale neutron source and a large-scale neutron source, FRANZ and MYRRHA, were introduced, respectively. This section will focus on a middle-scale neutron source, the High Brilliance Neutron Source (HBS) [26], which is currently under development at IAP of Goethe University Frankfurt for Forschungszentrum Jülich, Germany.

The HBS driver linac will need to accelerate a 100 emA proton beam to 70 MeV with a beam duty cycle of up to 6% (11% RF duty cycle) and should be able to

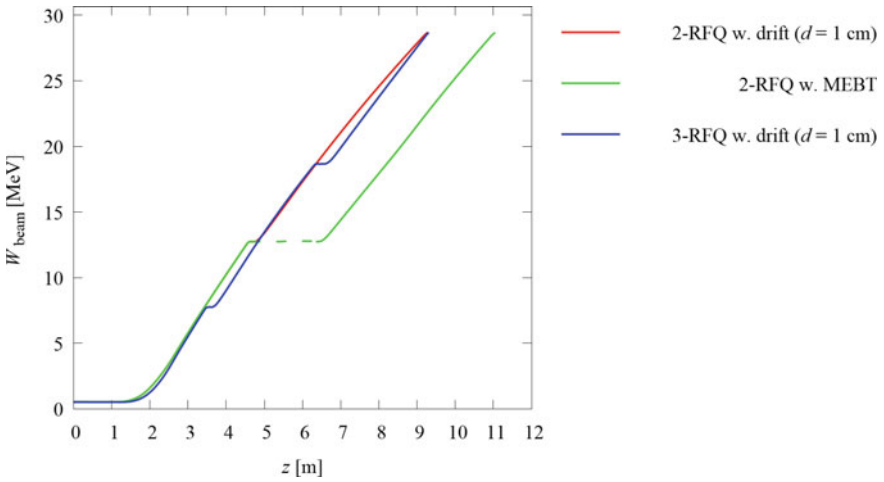

Fig. 5.17 Evolution of the synchronous energy for the three reference cases

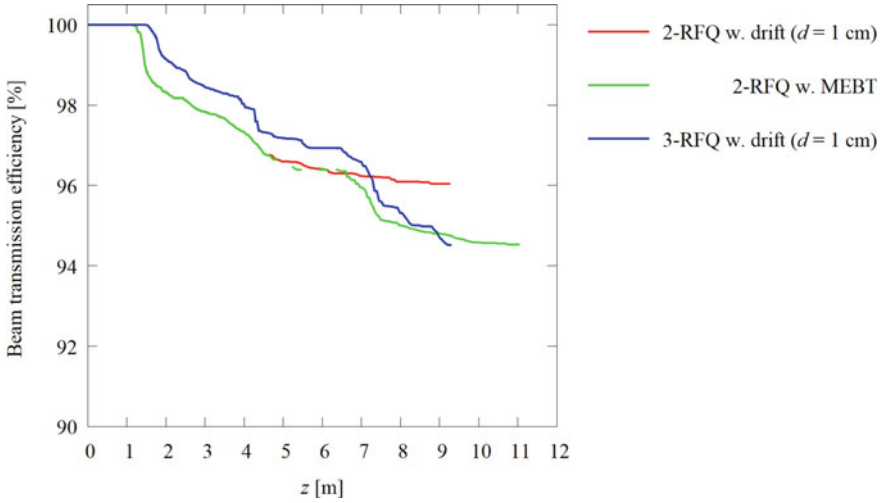

Fig. 5.18 Evolution of the beam transmission for the three reference cases

simultaneously deliver three pulse lengths (52, 208 and 833 μs) for three neutron target stations, respectively [25]. As shown in Fig. 5.19, the HBS driver linac with a peak beam power of 7 MW (an average beam power of 420 kW) will be clearly a high power linac. Therefore, a good beam quality is required along the linac for minimizing beam losses.

The β_{out} value for the HBS driver linac is ~0.37. As shown in Fig. 1.5, one may use only NC cavities or a mixture of NC and SC cavities for this linac. For the latter case, an important parameter is the transition energy between the NC and SC sections. In

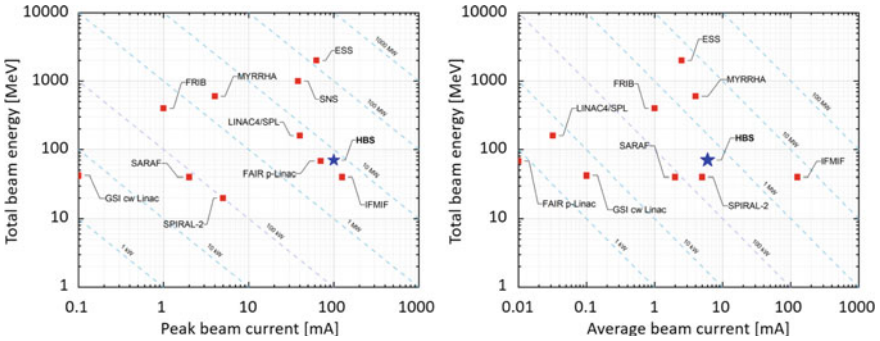

Fig. 5.19 Peak (left) and average (right) beam power of modern hadron linacs (Courtesy of Holger Podlech, with small modifications)

general, the higher the duty cycle and the lower the beam current, the smaller the transition energy should be (see Fig. 5.20) [26]. For the 100 emA, 11% dc HBS linac, therefore, the NC-SC transition energy should be relatively high. In this case, a fully NC linac is preferred due to the much simpler technology which avoids a cryogenic plant, the development of cryo-modules, and associated power couplers [26].

For the HBS front end, NC RFQ and CH cavities will be used as the accelerating structures. The choices for the basic parameters of this part are mainly based on the following considerations:

- With some safety margins, the design current I_{in} and the design input emittance $\varepsilon_{\mathrm{t,\,in,\,n,\,rms}}$ have been chosen as 105 emA and as 0.4 π mm mrad, respectively.
- Compared to the 5 emA MYRRHA RFQ, the 105 emA HBS RFQ will need to use much higher beam energies both at the input (according to the Child–Langmuir law) and at the output (for an injection into the DTL part with less strong space charge effects). Therefore, these two values were taken as 100 keV and 2.5 MeV, respectively.

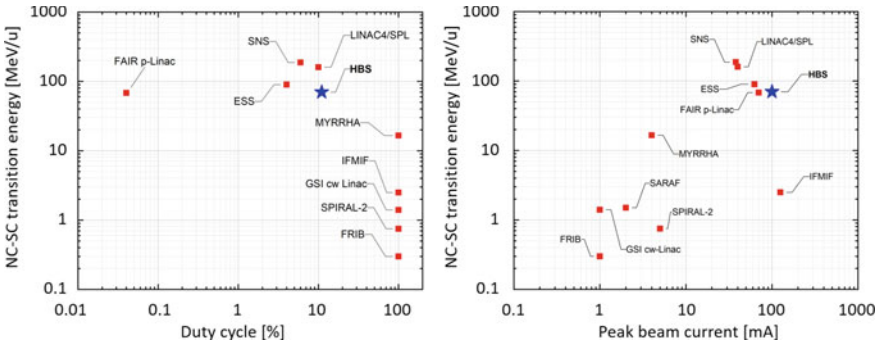

Fig. 5.20 Transition energy as a function of the duty cycle (left) or as a function of the peak beam current (right) for modern hadron linacs, where the transition energy for the fully NC linacs is the final energy (Courtesy of Holger Podlech, with small modifications)

- To benefit from IAP's extensive expertise in the 4-rod RFQ development over decades, the 4-rod structure typically operating at ≤200 MHz was adopted.
- Due to the good experience with the design, construction, and operation of the MYRRHA RFQ (see Chap. 4) and its reasonable R_p (measured value = 73 kΩm [27]), the same frequency, i.e., 176.1 MHz has been adopted.
- For ensuring a reliable operation at the RF duty cycle of 11%, the inter-vane voltage of the HBS RFQ has been conservatively chosen as $U = 85$ kV in order to keep the Kilpatrick factor lower than 1.8, a safe value proven by the LEDA experiments for CW operation.
- Based on all above-mentioned choices, the estimated length of the HBS RFQ will be much longer than 4 m. To avoid demanding RF tuning and a large power amplifier, it was decided to develop a MUSIC-style RFQ (two cavities with an MEBT in between) for the HBS project. The MEBT can also provide knobs for some operational flexibilities.

In Table 5.3, it can be seen that the choices of the basic parameters for the HBS RFQ are conservative, compared to the other $I_{in} \geq 100$ emA, duty cycle ≥ 10% RFQ accelerators.

Table 5.3 Design parameters of the HBS RFQ and the operated RFQs with $I_{in} \geq 100$ emA, duty cycle ≥ 10% in the world

Parameter	FMIT [28]	JAERI BTA [29]	IPHI [30]	LEDA [28]	IFMIF/ LIPAc [31]	HBS
I_{in} (emA)	105	100	100	105	125	105
RF duty cycle (%)	100	10	100	100	100	11
Particle	H_2^+	H^+	H^+	H^+	D^+	H^+
RF structure	4-vane	4-vane	4-vane	4-vane	4-vane	4-rod
f (MHz)	80	201.25	352.2	350	175	176.1
W_{in} (keV)	75	100	95	75	100	100
W_{out} (MeV)	2	2	3	6.7	5	1.25 (Cavity-1) 2.50 (Cavity-2)
U (kV)	185	113	87–123	67–117	79–132	85
Kilpatrick factor	1.7	1.68	1.7	1.8	1.8	≤1.8
$\varepsilon_{t,\,in,\,n,\,rms}$ (π mm mrad)	0.17	–	0.25	0.2	0.25	0.4
P_c (kW)	407	363	1166	1900	841	300–400* (each)
L (m)	4.00	3.35	6	8	9.78	3–4* (each)
T (%)	–	94	>99.3	95	93.7	≥90%

*: Updated design requirements for the HBS RFQ

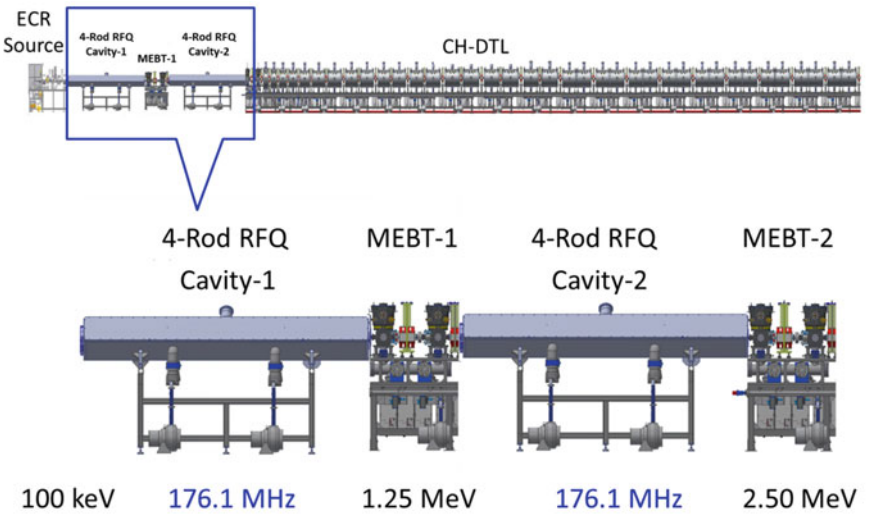

Fig. 5.21 Conceptual layout of the HBS driver linac (remade based on [25])

Table 5.4 Comparison of the design requirements between the HBS RFQ Cavity-1 and the MYRRHA RFQ

Parameter	MYRRHA RFQ Design CZ2013	HBS RFQ Cavity-1
f (MHz)	176.1	176.1
W_{in} (keV)	30	100
W_{out} (MeV)	1.50	1.25
I_{in} (emA)	5	105
Duty cycle (%)	100	11
U (kV)	44	85
$\varepsilon_{t,\,in,\,n,\,rms}$ (π mm mrad)	0.2	0.4
L (m)	4.03	3–4
T (%)	98.6 (simulation result, not requirement)	$\geq$90%

The schematic layout of the proposed HBS driver linac including the planned MUSIC-RFQ is shown in Fig. 5.21. As mentioned, for a MUSIC-RFQ, to design the first cavity is more demanding than to design the second one. The design requirements for the HBS RFQ Cavity-1 are listed in Table 5.4 together with those of the MYRRHA RFQ. The HBS RFQ Cavity-1 should reach a similar output beam energy with a structure length comparable to the MYRRHA RFQ. Although the U value of the HBS RFQ Cavity-1 is almost double that of the MYRRHA RFQ, its input beam has ~20 times the beam current, 2 times the input emittance, and >3 times W_{in} (for

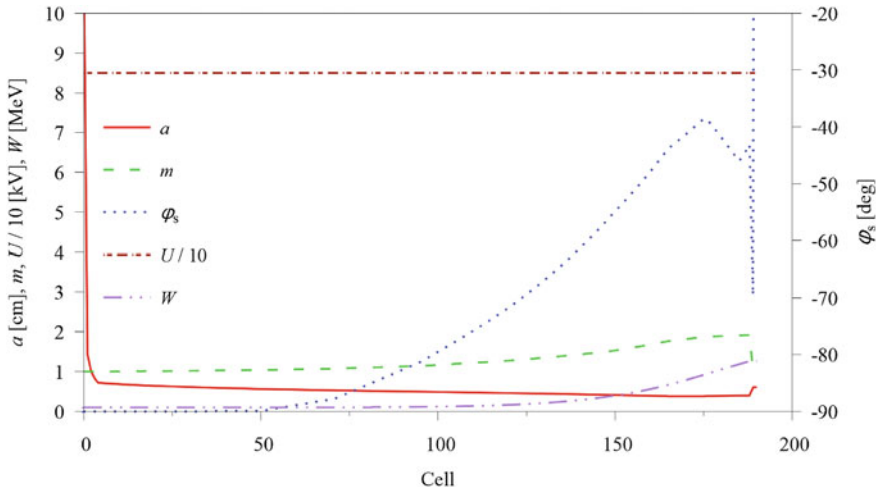

Fig. 5.22 Main design parameters of the HBS RFQ Cavity-1

an RFQ, the length of the bunching section is usually proportional to $\sim \beta_s^3$, see Sect. 2.7). At these given conditions, it is not possible for the HBS RFQ Cavity-1 to hold the emittance ratio inside the MEGLET optimum range, i.e., $0.9 \leq \frac{\varepsilon_l}{\varepsilon_t} \leq 1.4$ like the MYRRHA RFQ, and larger emittance ratios have to be accepted. Fortunately, the HBS RFQ is not a CW machine and does not require an extremely high level of reliability like the MYRRHA RFQ, so some emittance growths will be acceptable. For the design of the HBS RFQ Cavity-1, the SEGLER method was used. The main design parameters of the HBS RFQ Cavity-1 are shown in Fig. 5.22.

Figure 5.23 shows that the emittance ratio is ~2.0 after the pre-bunching and ~3.0 at the exit of the HBS RFQ Cavity-1. The average emittance ratio for the main part of the RFQ is 2.5. On the Hofmann chart for $\frac{\varepsilon_l}{\varepsilon_t} = 2.5$, the tune footprints of the HBS RFQ Cavity-1 have been confined inside the "safe ¼ ellipse" as required by the SEGLER method (see Fig. 5.24). As the "safe ¼ ellipse" is not as clean as the "safe rectangle" (parts of the $\frac{\sigma_l}{\sigma_t} = \frac{1}{2}$ and $\frac{\sigma_l}{\sigma_t} = \frac{1}{3}$ resonance peaks are inside), the tune trajectories especially the longitudinal one touched the two resonance peaks and some emittance growths occurred.

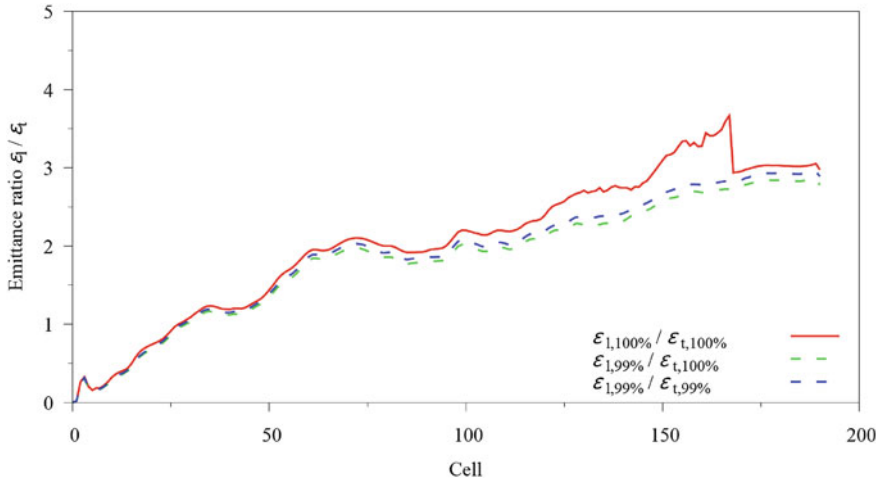

Fig. 5.23 Evolution of emittance ratio along the HBS RFQ Cavity-1

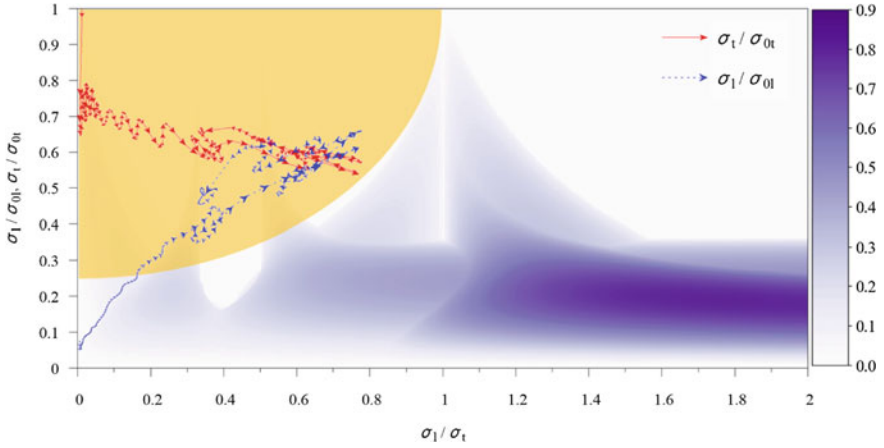

Fig. 5.24 Tune chart for the HBS RFQ Cavity-1 (overlapped with the Hofmann chart for $\frac{\varepsilon_l}{\varepsilon_t} = 2.5$)

The output particle distribution of the HBS RFQ Cavity-1 is still concentrated (see the top graphs in Fig. 5.25). Based on this distribution, an MEBT mainly consisting of one triplet, one 3-gap rebuncher cavity, and another triplet has been designed with the goal to provide an as smooth as possible beam matching for the HBS RFQ Cavity-2 [32].

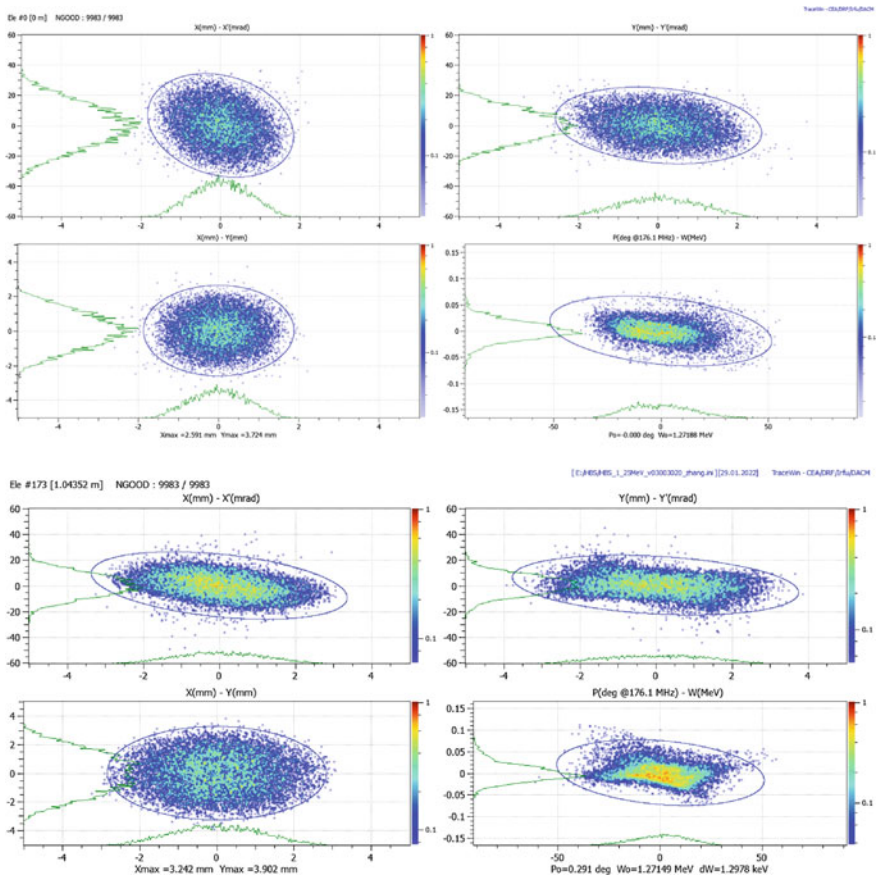

Fig. 5.25 Input (top) and output (bottom) particle distributions of the HBS MEBT-1 (graphs from [32])

The beam energy in the MEBT-1, 1.25 MeV, is still relatively low. This brought some space charge challenges for the transverse beam dynamics in the MEBT-1, as the magnetic force is velocity-dependent. Performed using the TraceWin code, the beam dynamics simulation for the MEBT-1 showed that for a good transverse beam matching, the length of the MEBT-1 should be longer than 1 m. This made the longitudinal beam dynamics in the MEBT-1 also difficult (see Fig. 5.26). The output particle distribution of the MEBT-1 is shown in the bottom graphs of Fig. 5.23. Some wing-like halo particles can be seen, especially in the y and longitudinal phase spaces. Fortunately, the emittance ratio at the entrance to the HBS RFQ Cavity-2 was still kept at $\frac{\varepsilon_l}{\varepsilon_t} \approx 3.0$.

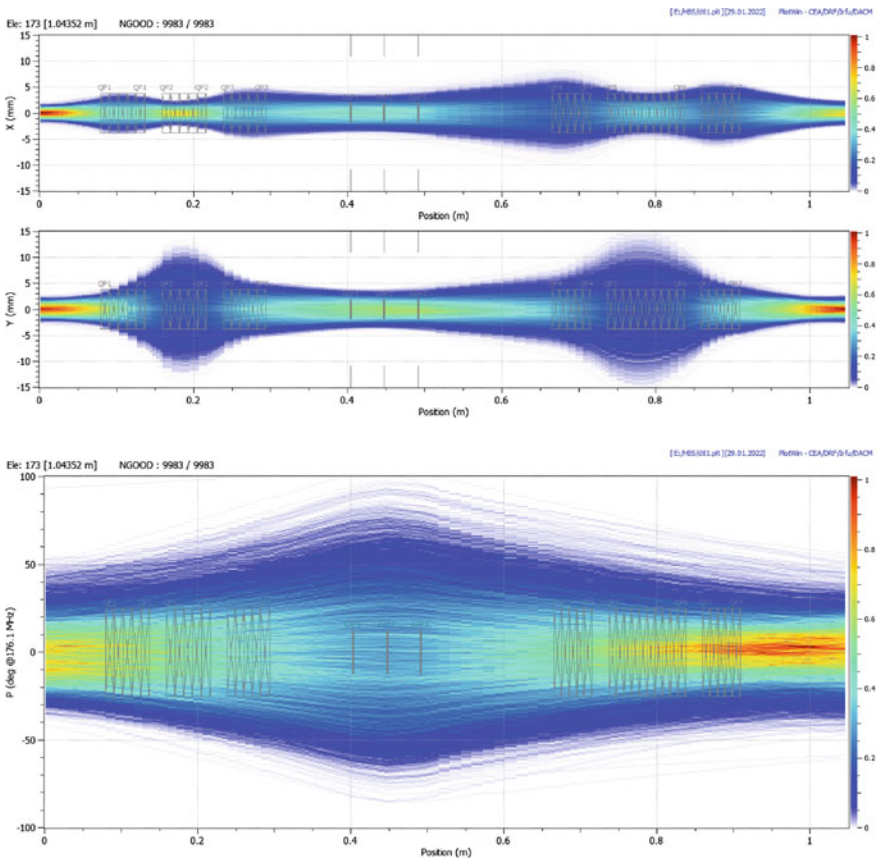

Fig. 5.26 Transverse (top) and longitudinal (bottom) beam envelopes in the HBS MEBT-1 [32]

The design of the HBS RFQ Cavity-2 (see Fig. 5.27) is still based on the SEGLER method. Figure 2.16 shows that the $\frac{\sigma_l}{\sigma_t} = \frac{1}{3}$ resonance peak vanishes gradually from $\frac{\varepsilon_l}{\varepsilon_t} = 2.0$ to $\frac{\varepsilon_l}{\varepsilon_t} = 3.0$. Therefore, the tune trajectories of the HBS RFQ Cavity-2 only touched the $\frac{\sigma_l}{\sigma_t} = \frac{1}{2}$ resonance peak very shortly (see Fig. 5.28). In Fig. 5.29, it can be seen that all emittance curves are quite flat and the emittance ratio is ~3.0 throughout the HBS RFQ Cavity-2.

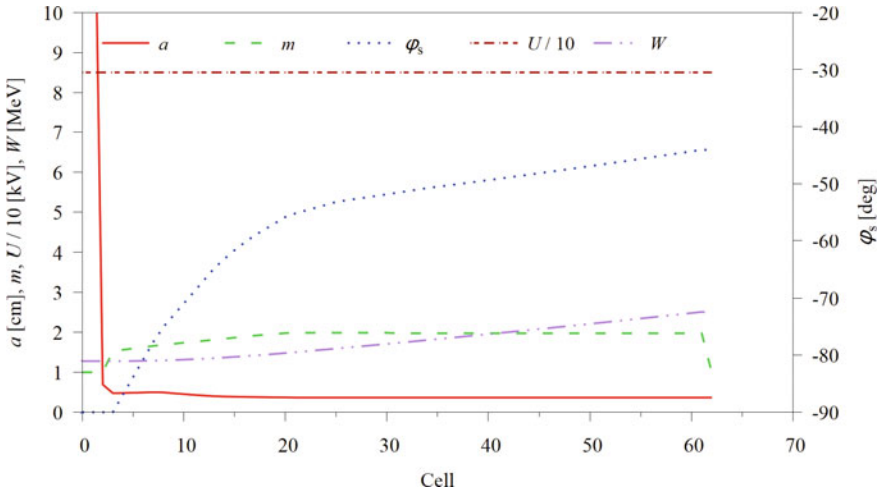

Fig. 5.27 Main design parameters of the HBS RFQ Cavity-2

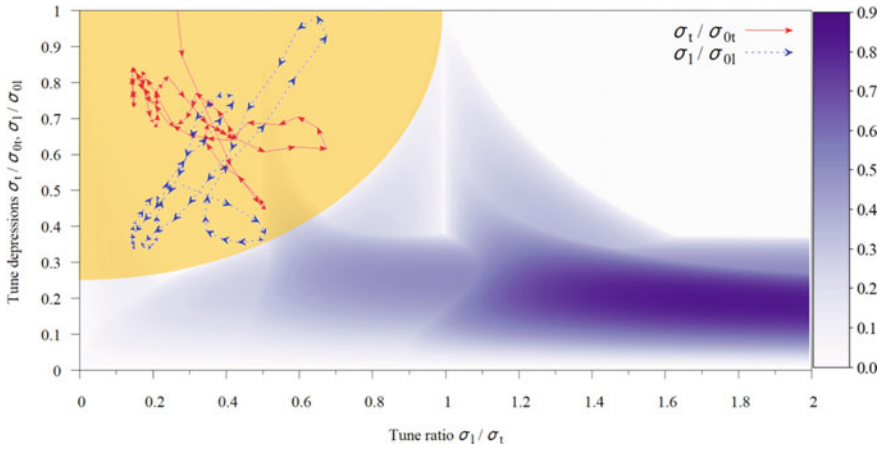

Fig. 5.28 Tune chart for the HBS RFQ Cavity-2 (overlapped with the Hofmann chart for $\frac{\varepsilon_l}{\varepsilon_t} = 3.0$)

The design parameters and simulation results for the two HBS RFQ cavities are summarized in Table 5.5. All parameters fulfilled the design requirements. Figure 5.30 shows that at the end of the HBS RFQ Cavity-2, the wing-like halo particles from the MEBT-1 disappeared in the transverse phase spaces, but still existed in longitudinal phase space. However, the preliminary design study of the downstream CH-DTL (using the Cavity-2 output distribution as the input distribution) proved that these longitudinal halo particles could be again captured and accelerated without losses [33].

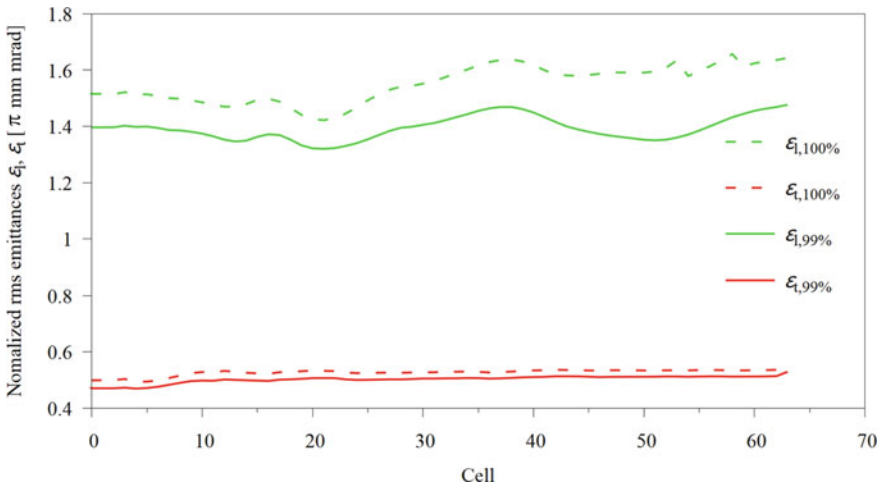

Fig. 5.29 Longitudinal and transverse emittances along the HBS RFQ Cavity-2

Table 5.5 Design parameters and simulation results for the HBS RFQ cavities

Parameter	Cavity-1	Cavity-2
f (MHz)	176.1	176.1
W_{in} (MeV)	0.100	1.25
W_{out} (MeV)	1.25	2.50
I_{in} (emA)	105	105
U (kV)	85	85
Kilpatrick factor	1.51	1.45
$\varepsilon_{x,\text{ out, n, rms}}$ (π mm mrad)	0.46	0.59
$\varepsilon_{y,\text{ out, n, rms}}$ (π mm mrad)	0.47	0.57
$\varepsilon_{z,\text{ out, n, rms}}$ (π MeV deg)	0.27	0.33
L (m)	3.60	3.28
Total transmission T (%)	99.83	98.60

The HBS MUSIC-RFQ design has been accepted as the reference design by the project and will be further improved.

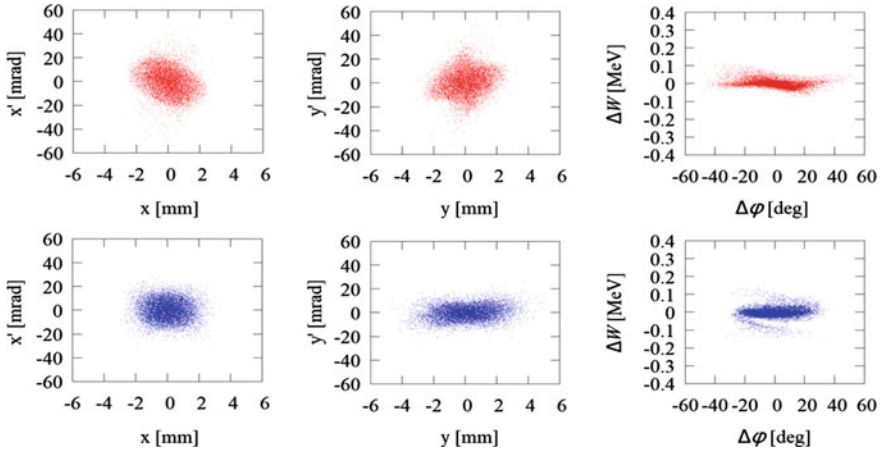

Fig. 5.30 Input (top) and output (bottom) particle distributions of the HBS RFQ Cavity-2

References

1. R.E. Laxdal, RFQ-IH radioactive beam linac for ISAC. AIP Conf. Proc. **473**, 546 (1999)
2. U. Ratzinger, K. Kaspar, E. Malwitz, S. Minaev, R. Tiede, The GSI 36 MHz high-current IH-type RFQ and HIIF–relevant extensions. Nucl. Instrum. Methods Phys. Res. Sect. A **415** (1998)
3. C. Zhang, H. Podlech, E. Tanke, Realizing long radio-frequency quadrupole accelerators with multiple shorter and independent cavities. Phys. Rev. Accel. Beams **23**, 042003 (2020)
4. D.D. Armstrong, W.D. Cornelius, F.O. Purser, R.A. Jameson, T.P. Wangler, RFQ development at Los Alamos. LANL report no. LA-UR-84-498 (1984)
5. R.A. Jameson, Introduction to RFQ session, in *Proceedings of LINAC* (1984)
6. L.M. Young, Tuning and stabilization of RFQ's, in *Proceedings of LINAC* (1990)
7. M.J. Browman, L.M. Young, coupled radio-frequency quadrupoles as compensated structures, in *Proceedings of LINAC* (1990)
8. L.M. Young, Operations of the LEDA resonantly coupled RFQ, in *Proceedings of PAC* (2001)
9. A. Pisent, M. Comunian, A. Palmieri, G.V. Lamanna, D. Barni, TRASCO RFQ, in *Proceedings of LINAC* (2000)
10. F.D. McDaniel et al., The tandem-RFQ linac booster at Sandia National Laboratories. AIP Conf. Proc. **680**, 986 (2003)
11. G. Bisoffi et al., Superconducting RFQ's ready for ion beam operation at INFN-LNL, in *Proceedings of EPAC* (2002)
12. A. Bechtold, H. Podlech, Proposal of a normal conducting CW-RFQ for the EURISOL post-accelerator and a dedicated β-beam linac concept, in *Proceedings of EPAC* (2006)
13. K. Kaspar, U. Ratzinger, Design of the GSI 36 MHz RFQ accelerator on the base of mafia calculations, in *Proceedings of EPAC* (1996)
14. A. Kolomiets et al., Upgrade of the unilac high current injector RFQ, in *Proceedings of LINAC* (2008)
15. A.K. Mitra, R.L. Poirier, High power test of the 35 MHz spiral re-buncher cavity for the TRIUMF ISAC facility, in *Proceedings of EPAC* (2000)
16. https://github.com/dynac-source/dynac-source
17. Y. Bylinsky et al., Dynamics and tolerances for the CERN interdigital H linac, in *Proceedings of LINAC* (1992)

18. P. Lapostolle, E. Tanke, S. Valero, Comparison of computational methods and results concerning the simulation of IH structures with the codes LORAS and DYNAC. CERN report no. PS/Hi/Note 92-02 (1992)
19. J.-H. Jang, I.S. Hong, H. Jang, D. Jeon, H. Jin, H.J. Kim, Beam optics of RISP linac using dynac code, in *Proceedings of IPAC* (2015)
20. E. Tanke et al., Benchmark of beam dynamics code DYNAC using the ESS proton linac, in *Proceedings of LINAC* (2014)
21. E. Tanke, M. Eshraqi, Y. Levinsen, A. Ponton, S. Valero, Status of and plans for the beam dynamics program DYNAC, in *Proceedings of LINAC* (2016)
22. W. Wittmer et al., Online modeling of the rare isotope reaccelerator – ReA3, in *Proceedings of IPAC* (2014)
23. T. Yoshimoto, M. Ikegami, IMPACT model for ReA and its benchmark with DYNAC, in *Proceedings of LINAC* (2016)
24. R. Tiede et al., LORASR code development, in *Proceedings of EPAC* (2006)
25. H. Podlech et al., Conceptual design of the proton LINAC for the high brilliance neutron source HBS, in *Proceedings of IPAC* (2019)
26. T. Brückel, T. Gutberlet (eds.), Conceptual design report – Jülich high brilliance neutron source (HBS). ISBN 978-3-95806-501-7 (2020)
27. H. Podlech et al., The MYRRHA-project, in *Proceedings of NAPAC* (2019)
28. D. Schrage et al., CW RFQ fabrication and engineering, in *Proceedings of LINAC* (1998)
29. K. Hasegawa et al., Development of a high intensity RFQ at JAERI. J. Nucl. Sci. Technol. **34**(7) (1997)
30. R. Ferdinand, P.Y. Beauvais, The IPHI project, in *Proceedings of HB* (2004)
31. E. Fagotti et al., Beam commissioning of the IFMIF EVEDA very high power RFQ, in *Proceedings of IPAC* (2018)
32. M. Droba, HBS MEBT1 design. Internal report, IAP Frankfurt (2022)
33. M. Schwarz et al., Proton linac design for the high brilliance neutron source HBS, in *Proceedings of IPAC* (2022)

Chapter 6
Frequency Jump Using 704.4 MHz RFQ and CH Accelerators

Abstract This chapter introduces an advanced application of the RFQ accelerator, which also sets a new record for the beam velocity, i.e., $\beta \approx 0.2$ applied to the RFQ accelerator. A large-scale H^+ or H^- accelerator often requires a jump in radio frequency, typically in the beam velocity range of $\beta = 0.4$–0.6. The 600 MeV MYRRHA linac has two frequency jumps: one from 176.1 MHz to 352.2 MHz at $\beta \approx 0.2$ and another one from 352.2 MHz to 704.4 MHz in the typical beam velocity range at $\beta = 0.56$. Using the MYRRHA linac as an example, this study investigates two new solutions, whereby the frequency jump in the range of $\beta = 0.4$–0.6 can be eliminated. A single frequency jump from 176.1 MHz to 704.4 MHz at $\beta \approx 0.2$ can shorten the entire linac as well as reduce the construction and operation costs considerably. The proposed frequency jump sections will use 704.4 MHz RFQ and CH-DTL cavities. To ensure a safe and reliable CW operation at such a high frequency for these kinds of accelerating structures, careful design studies with respect to beam dynamics and RF structures including water-cooling channels have been performed. The results demonstrated the feasibility of both solutions. Due to the compactness of such structures, it is being investigated to realize them using additive manufacturing (3D-printing) technologies.

6.1 Frequency Jump in Large-Scale Accelerators

In order to maintain high RF efficiency as well as to save construction costs, accelerating cells need to be kept reasonably short. At higher beam velocities, therefore, a large-scale H^+ or H^- accelerator often requires a jump in the radio frequency at which the cavities operate. Table 6.1 gives examples of existing accelerators and those under construction that use a radio-frequency jump (hereinafter abbreviated as frequency jump). It can be seen that most of them have only one frequency jump in the beam velocity range of $\beta = 0.4$–0.6, except the MYRRHA linac, which has two frequency jumps with its first frequency jump at $\beta \approx 0.2$.

The driver linac design of the MYRRHA project is based on the R&D studies by a series of European ADS projects (see Chap. 4). During the previous EUROTRANS project, the driver linac also had only one frequency jump from

C. Zhang, *Radio-Frequency Quadrupole Accelerators*, Particle Acceleration and Detection, https://doi.org/10.1007/978-3-031-40967-7_6

Table 6.1 An overview of some large-scale H^+ or H^- accelerators with a frequency jump

Project	Frequency before jump (MHz)	Frequency after jump (MHz)	Frequency jump factor	Transition energy (MeV)	Status
LANSCE [1]	201.25	805	4	100	In operation
SNS [2]	402.5	805	2	86.8	In operation
J-PARC [3]	324	972	3	190.8	In operation
ESS [4]	325.21	704.42	2	216	Under construction
MYRRHA [5]	176.1 352.2	352.2 704.4	2 2	16.6 172	Under construction

352.2 MHz to 704.4 MHz at $\beta = 0.56$. In its subsequent MAX project, a new frequency jump from 176.1 MHz to 352.2 MHz was introduced at $\beta \approx 0.2$. The advantages of using a lower frequency for the injector part are: (1) the feasibility of using the cost-saving 4-rod RFQ structure instead of the 4-vane structure; (2) higher shunt impedance; and (3) easier water-cooling (see Chap. 4 or [6]).

After a frequency jump, the beam-bunch length in terms of degrees is also multiplied, resulting in a reduction of the safety margin for the beam with respect to the longitudinal acceptance. Therefore, it is usually crucial to have a proper transition for minimizing the risks of beam losses at the frequency jump and in the subsequent accelerating structures.

It is well known that: (1) the phase width of the beam decreases and the energy width increases during acceleration in a linac due to the phase damping effect [7]; (2) the repulsive space-charge effect decreases with the increased beam velocity [8]. For the MYRRHA linac (see Fig. 4.4), therefore, the second frequency jump, which happens in the range of $\beta = 0.4$–0.6 (similar to the other linacs mentioned in Table 6.1), is less critical than the first frequency jump at $\beta \approx 0.2$ from beam dynamics point of view.

Taking the MYRRHA linac as an example, this study is focusing on new solutions for the frequency jump at $\beta \approx 0.2$. It should be mentioned that this study is not related to the MYRRHA project. In this study, the frequency jump factor of the first frequency jump for the MYRRHA linac is increased to four. It is corresponding to a jump from 176.1 MHz to 704.4 MHz so that the entire driver linac will just need one frequency jump and the 352.2 MHz section between 16.6 MeV and 172 MeV can be shortened considerably. As the MYRRHA linac is a CW machine and it uses only superconducting cavities after the first frequency jump, the transition has to be treated very carefully to avoid beam quality degradation and beam losses.

To accomplish the new frequency jump from 176.1 MHz to 704.4 MHz, a section dedicated to the frequency jump will be placed directly at the end of each injector and will follow the same reliability strategy for the injector. It should have a compact layout, but the energy gain is not a design goal. The design beam current and the duty cycle are still 5 emA and 100%, respectively, same to those of the MYRRHA linac.

The design of the frequency jump section is challenging from both beam dynamics and RF cavity design points of view, because: (1) almost no beam loss will be allowed according to the generally accepted beam loss limit $\leq$1 W/m for hands-on maintenance; (2) an output beam with acceptable phase width and energy width as well as good beam quality should be provided to the downstream superconducting main linac; and (3) last but not least, the RF parameters of the cavities have to be chosen carefully in order to ensure a very safe and reliable CW operation required by the ADS application. For the MYRRHA linac, the beam trips longer than 3 seconds must be very rare [5].

6.2 Frequency Jump Using 704.4 MHz CH Cavities

Covering the energy range from 30 keV up to 16.6 MeV, the 176.1 MHz MYRRHA injector [9, 10] mainly consists of one 4-rod RFQ and fifteen NC CH cavities (see Fig. 4.4). This study starts from a position that is 20 cm behind the last CH cavity of the injector.

The first idea is to still adopt the NC CH structure for the frequency jump section. In Fig. 6.1, one can see that up to now the highest frequency of the constructed NC and SC CH cavities is 360 MHz. The frequency jump CH proposed in this study has almost double that frequency, so the transverse dimensions of the structure will become very small. In view of a safe and reliable CW operation of such a new structure, a cavity design study with carefully chosen parameters has been performed.

At 16.6 MeV and 704.4 MHz, the cell length $\beta\lambda/2 = 4$ cm is very similar to that of the CH-0 cavity for the GSI CW linac (now: HELIAC) [12]. The HELIAC CH-0

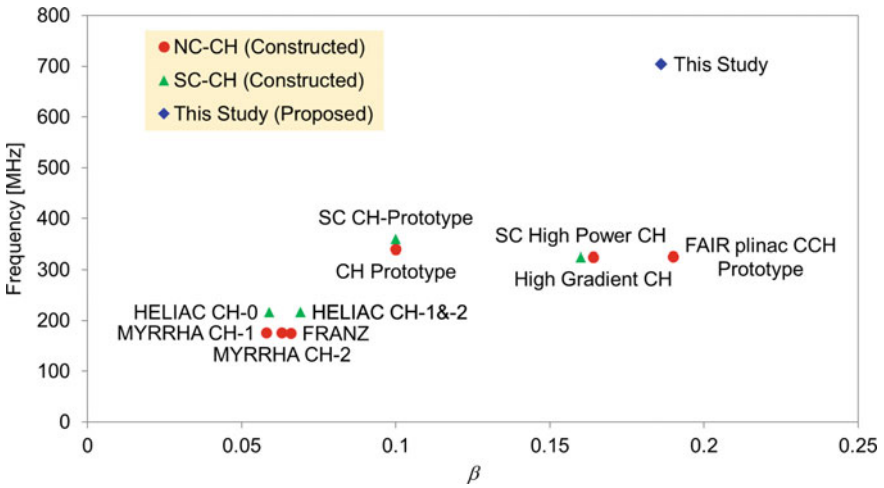

Fig. 6.1 Constructed CH cavities and the proposed frequency jump CH [11]

cavity has been built and successfully tested with beams, so its tube dimensions can be applied for the 704.4 MHz CH as well. Based on this, a 7-gap, $\beta = 0.186$, $f = 704.4$ MHz CH cavity has been designed. It is an NC cavity made of copper. Instead of aiming for a high acceleration gradient, the focus of the cavity design is how to minimize RF power consumption and fulfill the requirements for working at the CW mode safely and reliably.

The main design parameters of the 704.4 MHz CH cavity as well as the simulation results given by the MWS software are summarized in Table 6.2. The cavity has an acceleration gradient of 0.5 MV/m and a Kilpatrick factor of 0.24, which are both very conservative for CW operation. The effective shunt impedance predicted by the MWS software is $Z_{\text{eff, MWS}} = 53.46$ MΩ/m. The CH development experience at Goethe University Frankfurt shows that the measured shunt impedance of a CH cavity is typically ~90% of the simulated value given by MWS, e.g., [13]. In this study, the RF power consumption P_c has been calculated using $Z_{\text{eff, MWS}} \times 85\%$. For this 704.4 MHz CH cavity, P_c is 1.5 kW with a distribution of 60.6% on the stems, 32.2% on the drift tubes, and 7.2% on the tank wall.

Figure 6.2 shows the thermal simulation results using ~20 °C input cooling water for the 704.4 MHz CH structure. The adopted water-cooling concept (see Fig. 6.3) is as follows:

- Each pairs of stems (including the tube) will be cooled by a water circuit (in darker blue).
- The tank wall will be cooled additionally by eight water channels (in lighter blue).

In order to test the robustness of the cooling design with a large safety margin, 2.5 kW of input RF power (including ~70% of additional RF power in terms of $Z_{\text{eff, MWS}} \times 85\%$) was applied as a heat load to the CH cavity in the simulation.

In Fig. 6.2, it can be seen that even with 2.5 kW of input RF power:

- Most parts of the cavity have no obvious temperature increase.

Table 6.2 Design parameters of a 7-gap, 704.4 MHz CH cavity [11]

Parameter	Value
f (MHz)	704.4
β	0.186
Gap number	7
Tank length (mm)	337
Tank inner radius (mm)	80
Tank outer radius (mm)	110
Tube inner aperture radius (mm)	10
E_{acc} (MV/m)	0.5
$Z_{\text{eff, MWS}}$ (MΩ/m)	53.46
P_c (kW)	1.5 (using $Z_{\text{eff, MWS}} \times 85\%$)
Kilpatrick factor	0.24

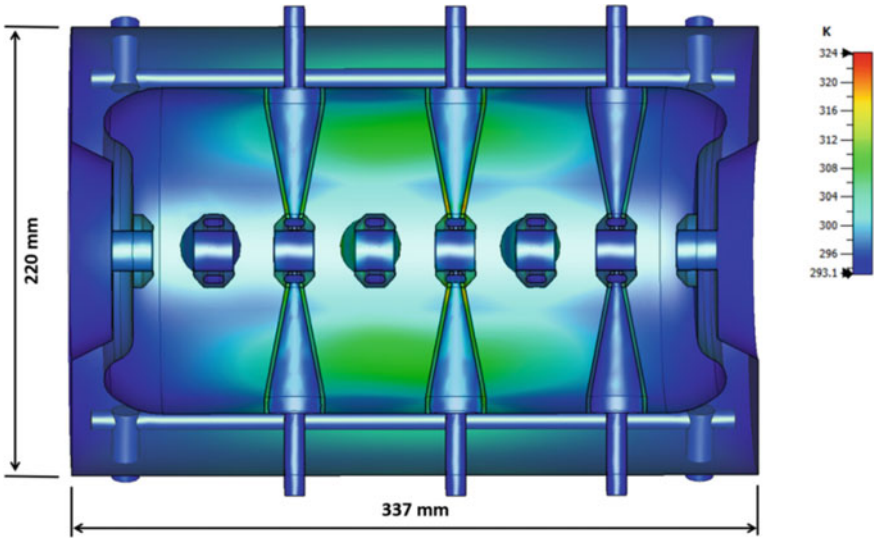

Fig. 6.2 Temperature distribution of the 704.4 MHz CH with 2.5 kW of input RF power and water-cooling [11]

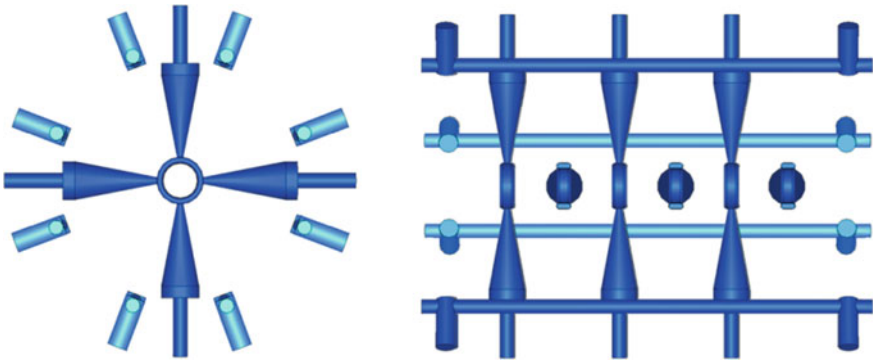

Fig. 6.3 Water-cooling concept for the proposed 704.4 MHz CH (left: front view; right: side view; darker blue: cooling channels for the stems and tubes; lighter blue: cooling channels for the tank wall) [11]

- The hottest spots locate on the middle stem and are close to the drift tube.
- The highest temperature is 324 K, corresponding to a maximum temperature increase of ~30 K.

According to the testing experience with the CH structures for the MYRRHA injector, this temperature distribution is safe for the CW operation.

In short, all above-shown results indicate that the 704.4 MHz, $\beta \approx 0.2$ NC CH is feasible for CW operation from both mechanical and RF cavity design points of view.

As a next step, a beam dynamics design including two triplets and four 704.4 MHz CH cavities has been made for the frequency jump section. Each triplet is 36 cm long, the aperture radius of each quadrupole is 2.5 cm, and the upper limit for the quadrupole pole-tip fields is 1.2 T.

As shown in Fig. 6.4 schematically, the whole layout is 2.71 m long, where two XY-steerer pairs (marked in magenta) have been added in front of the first and last CHs, respectively, for possible orbit corrections required by the real operation. With a design field integral up to 0.005 Tm, each XY-steerer pair is 10 cm long and its aperture radius is also 2.5 cm.

Figure 6.5 shows that after the frequency jump the phase width (in terms of degrees) of the particles at the entrance to the first CH becomes four times as large as the one before the frequency jump as expected. This distribution includes 98,596 macro particles and it has been obtained using the simulated output distribution of the MYRRHA injector as the input distribution. The phase spread of the particle distribution after the frequency jump ranges from –57° to 47°, so the frequency jump section needs to provide a proper bunching before the beam is injected into the downstream DTL cavities. Due to the 1 W/m beam loss limit, almost no particle should be lost in the frequency jump section, which is challenging for the beam dynamics design.

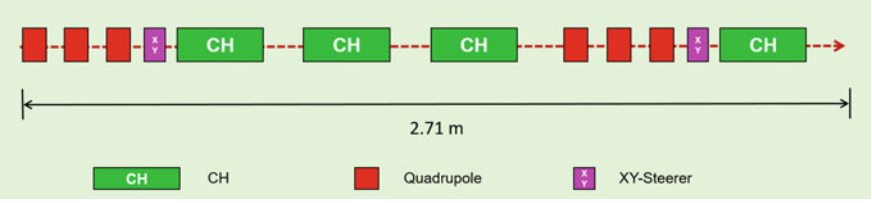

Fig. 6.4 Schematic layout of the frequency jump section based on four 704.4 MHz CHs [11]

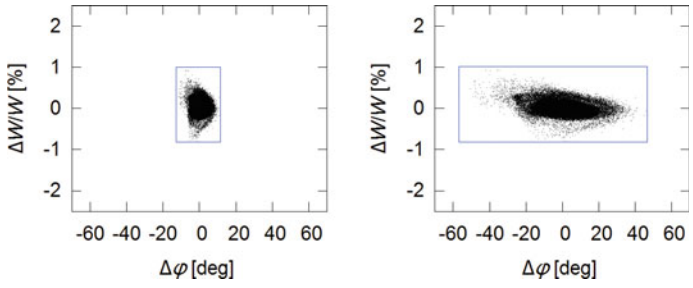

Fig. 6.5 Longitudinal particle distributions before (left) and after (right) frequency jump at the entrance to the first CH (the blue rectangles indicate the boundaries of the particle distributions)

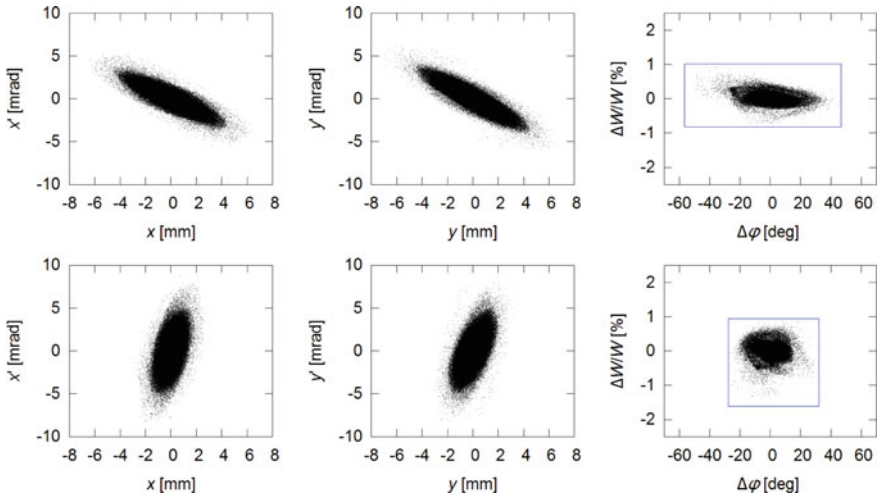

Fig. 6.6 Particle distribution at the entrance to the first CH after frequency jump (top) and particle distribution at the exit of the frequency jump section (bottom), where the blue rectangles indicate the boundaries of the particle distributions

For each CH, a constant synchronous phase φ_s has been used for its all gaps. The synchronous phase values for the 4 CHs are –75°, –40°, –40°, and –40°, respectively, along the beam line. The choice of $\varphi_s = -75°$ for the first CH is for the purpose of capturing all particles in the distribution after the frequency jump.

For the beam dynamics simulation, the DYNAC code [14] has been used. In the simulation, no beam loss has been found during the beam transport. The transverse emittance values are almost constant throughout the frequency jump section, and the emittance growth in the longitudinal plane is only 2.5%. Figure 6.6 compares the particle distribution at the entrance to the first CH (after the frequency jump) with the particle distribution at the exit of the frequency jump section. It can be seen that the total phase width of the beam has been decreased by more than 40° with an increase in the total energy width by only <1%. This output phase width can be well accepted by a downstream cavity operating at $\varphi_s = -40°$, which is typical for DTLs. More detailed simulation results will be presented in the next section of the paper for a comparison with another solution.

6.3 Frequency Jump Using a 704.4 MHz RFQ-CH Combination

In Fig. 6.6, one can see that the transverse beam size is roughly ±7 mm at the entrance to the first CH and ±3 mm at the exit of the frequency jump section. For the first solution (hereafter also referred to as the CH-only solution), an inner aperture radius

of 10 mm has been adopted for all drift tubes. Limited by the ~4 cm cell length, it is difficult to be further enlarged. For having a larger safety margin in the beginning part of the frequency jump section, another idea is to realize this section using a 4-vane RFQ accelerator. In addition, the RFQ electrodes can be more easily cooled than the small drift tubes, so this will be more favorable for CW operation.

However, different from in a CH cavity, the electric field in an RFQ has a large component in the transverse direction. To avoid a too long RFQ, the new solution will only replace the first three CHs of the CH-only solution by an RFQ and the fourth CH will be kept. One important reason for having a short RFQ is because the sensitivity to RF tuning errors for a 4-vane RFQ is proportional to $(L/\lambda)^2$, where L is the RFQ length and λ is the free-space wavelength [15–17]. The two 750 MHz RFQs, which have been successfully constructed and tuned by CERN, are ~5λ [18] and ~2.5λ long [19], respectively. For the 704.4 MHz RFQ, the length limit, $\leq 3\lambda$, has been taken between these two values.

The evolution of the main beam dynamics design parameters along the 704.4 MHz RFQ is shown in Fig. 6.7.

The main design parameters as well as the RF simulation results of the 704.4 MHz RFQ are summarized in Table 6.3. The RFQ has a total structure length of 123 cm, which is equivalent to 2.9λ. The Kilpatrick factor of the 704.4 MHz RFQ is only 0.14, which is very safe for CW operation. As defined in Eq. (2.35), the RFQ shunt impedance simulated by MWS is $R_{\mathrm{p,\,MWS}} = 42.8$ kΩm. The RF power consumption

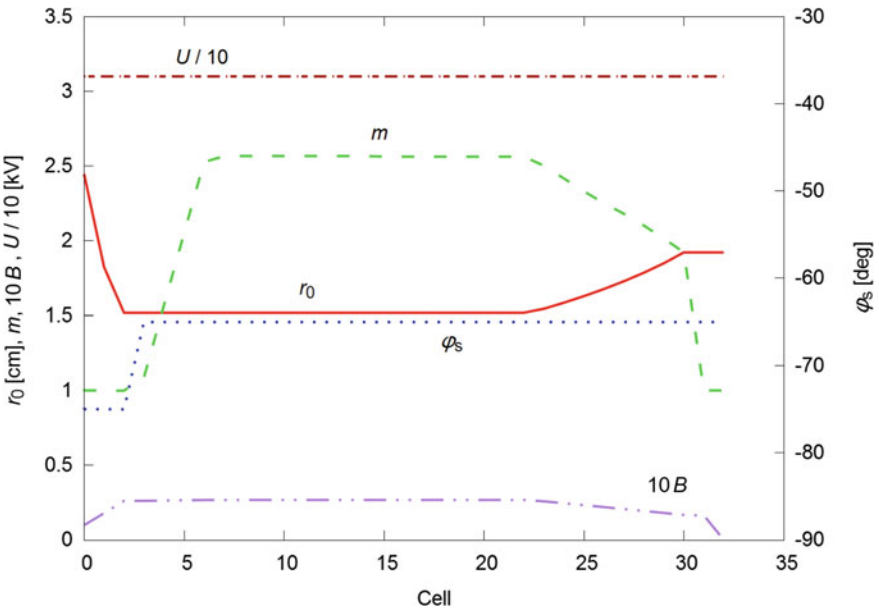

Fig. 6.7 Main design parameters of the 704.4 MHz RFQ [11]

Table 6.3 Design parameters and simulation results of the 704.4 MHz RFQ [11]

Parameter	Value
f (MHz)	704.4
W_{in} (MeV)	16.6
W_{out} (MeV)	16.8
U (kV)	31
Kilpatrick factor	0.14
$r_{0,\text{avg}}$ (cm)	1.59
$R_{\text{p, MWS}}$ (kΩm)	42.8
P_{c} (kW)	32.6 (using $R_{\text{p, MWS}} \times 85\%$)
L (m)	1.23

calculated using $R_{\text{p, MWS}} \times 85\%$ is $P_{\text{c}} = 32.6$ kW with a distribution of 58.8% on the electrodes, 41.1% on the tank wall, and the rest on the endplates.

In Fig. 6.8, the transverse dimensions of the 704.4 MHz RFQ are shown. The 28 blue dots schematically represent the water-cooling channels (each has a diameter of 10 mm) based on a simplified model for a preliminary thermal calculation presented below. In the future follow-up studies, other required auxiliary components, e.g., tuners, will be included for a detailed cavity design.

The temperature increase ΔT as a function of the cooling-water flow rate can be calculated using Eq. (6.1), where ΔT is the temperature increase, P_{c} is the RF power consumption, $\dot{m}$ is the water flow rate per cooling channel, N_{channel} is the number of cooling channels, and C_{w} is the specific heat capacity of water.

$$\Delta T = \frac{P_{\text{c}}}{\dot{m} N_{\text{channel}} C_{\text{w}}} \tag{6.1}$$

In the Test-RFQ built for the MAX project, the water flow rate measured for a cooling channel, which has a diameter of ~5 mm, is 4.8 l/min at a water pressure of 1 bar or 16.8 l/min at 6 bars, the design water pressure [20, 21]. According to Eq. (6.1), the temperature increase of the 704.4 MHz RFQ is only 3.5 K at $\dot{m} = 4.8$ l/min or only 1 K at $\dot{m} = 16.8$ l/min with the RF power consumption $P_{\text{c}} = 32.6$ kW. This is very favorable to lead to a reliable CW operation for the 704.4 MHz RFQ.

Shown in Fig. 6.9, the layout of Solution 2 (hereafter also referred to as the RFQ-based solution) for the frequency jump section has a very similar total length as that of the CH-only solution. Same triplets and XY-steerers have been adopted. Also working at $\varphi_{\text{s}} = -40°$, the CH used by the RFQ-based solution is almost identical to the last CH of the CH-only solution (only some small differences due to the adaption for slightly different beam energy).

The end-to-end beam dynamics simulation for the RFQ-based solution has also been performed using the DYNAC code. No beam loss has been found in the beam dynamics simulation.

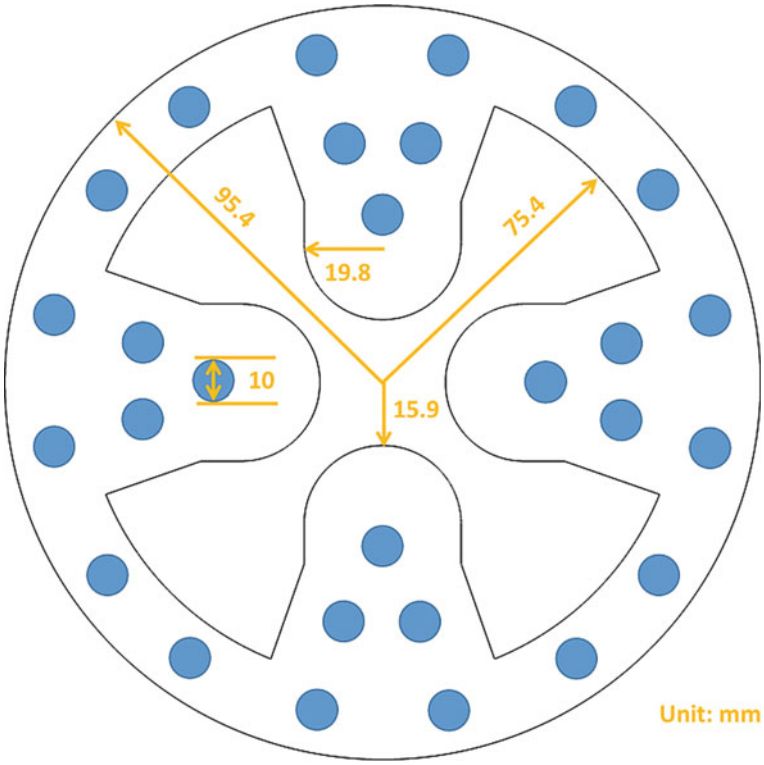

Fig. 6.8 Front view of the 704.4 MHz RFQ with 28 water-cooling channels (blue dots) [11]

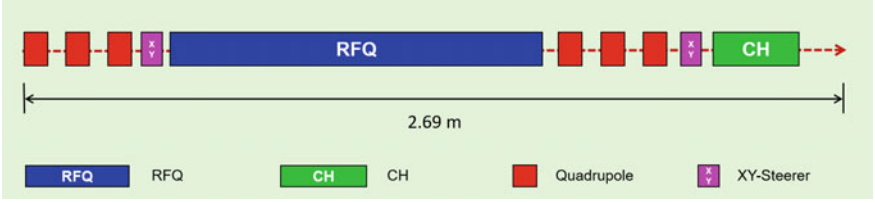

Fig. 6.9 Schematic layout of the frequency jump section based on a combination of one 704.4 MHz RFQ and one 704.4 MHz CH [11]

Figure 6.10 plots the transverse and longitudinal beam envelopes of both solutions, where the red and blue curves stand for the CH-only solution and the RFQ-based solution, respectively. One can see that the performance of both solutions is very similar.

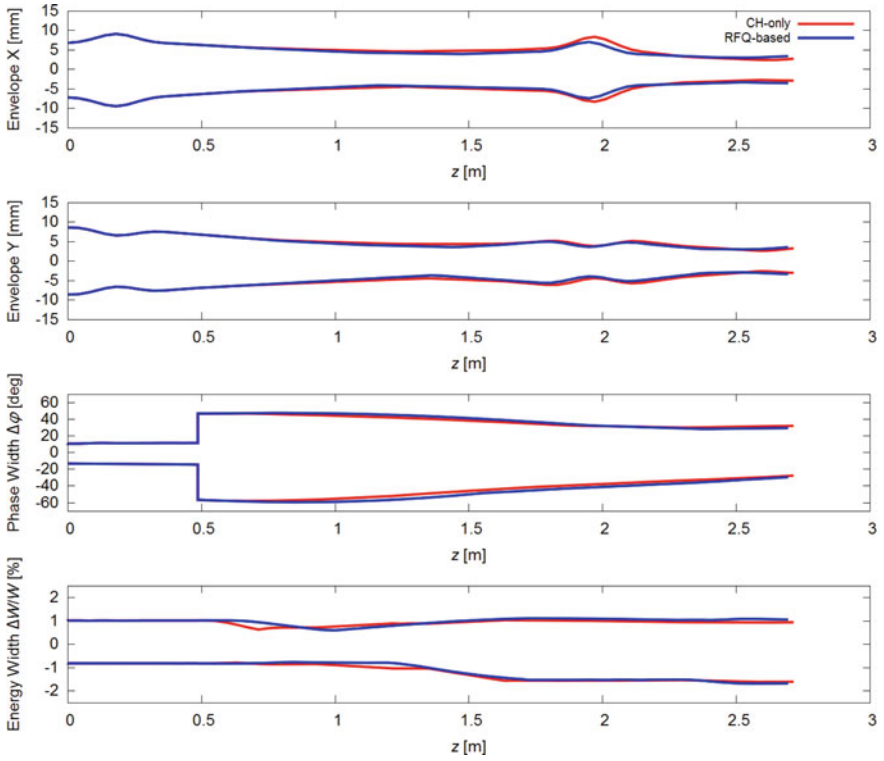

Fig. 6.10 A comparison of the transverse and longitudinal beam envelopes between the two solutions

Figure 6.11 shows the particle distributions at the entrance to the RFQ (after frequency jump) and at the exit of the frequency jump section, respectively. Generally speaking, the output distributions of the RFQ-based solution are comparable to those of the CH-only solution (see Fig. 6.6).

The transverse and longitudinal rms emittances as functions of position along the beam line are plotted in Fig. 6.12, where the solid and dashed curves stand for the CH-only solution and the RFQ-based solution, respectively. All emittance growths are very small: (1) <0.6% in the transverse planes; (2) only 2.5% and 5.6% in the longitudinal plane for the CH-only solution and the RFQ-based solution, respectively.

In Fig. 6.13, a further comparison of the phase width evolutions between the two solutions is given. From the position $z \approx 0.5$ m (location of the frequency jump) to the exit of the frequency jump section, the 100% total phase width has been reduced from ~100° to ~60° and the rms total phase width has been reduced from ~3.9 mm to ~2.7 mm in both cases, although the ways of bunching are different for the two solutions. In the RFQ-based case, the phase width has even an increase after the frequency jump point. This is because the bunching strength in the beginning of the RFQ-based solution is lower than that of the CH-only solution. Different

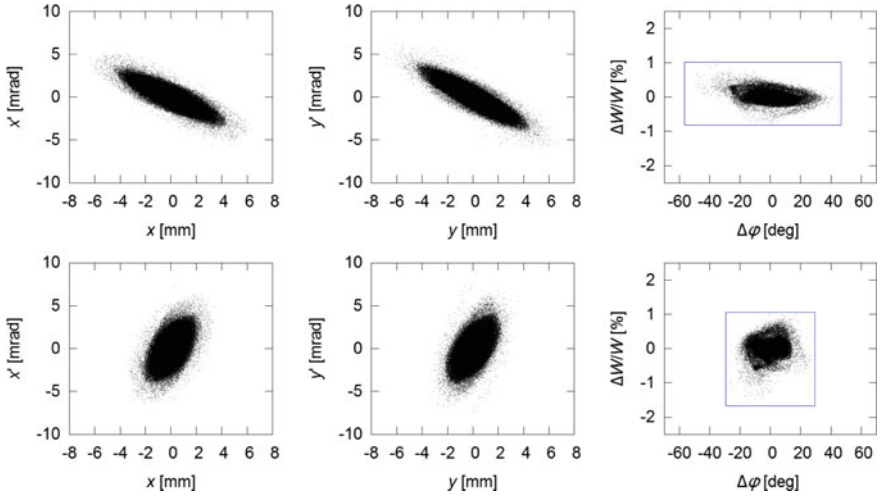

Fig. 6.11 Particle distribution at the entrance to the RFQ after frequency jump (top) and particle distribution at the exit of the frequency jump section (bottom), where the blue rectangles indicate the boundaries of the particle distributions

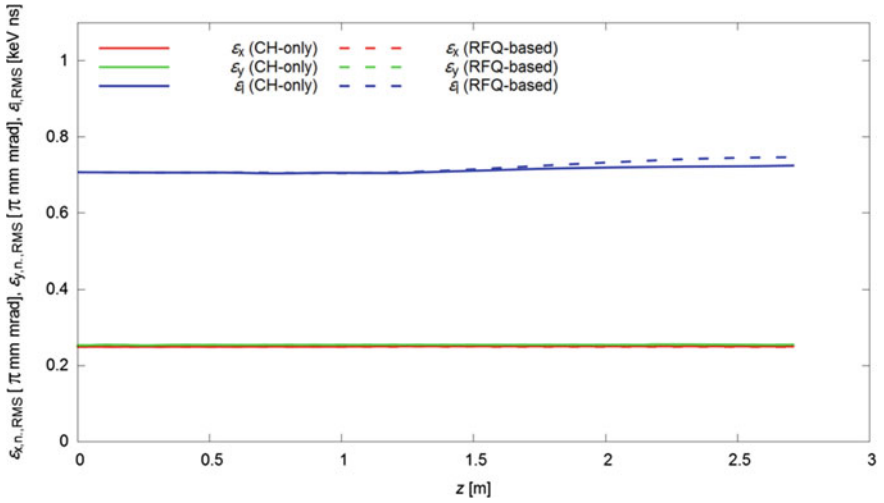

Fig. 6.12 A comparison of the transverse and longitudinal emittance evolutions for the two solutions

from in a DTL, the electric field between the RFQ electrodes has a large transverse component, especially at the entrance where the modulation parameter is 1 for radial matching. Further downstream, the longitudinal electric field strength increases, and as a consequence the bunching effect increases as well. The main design results of the two solutions are summarized in Table 6.4.

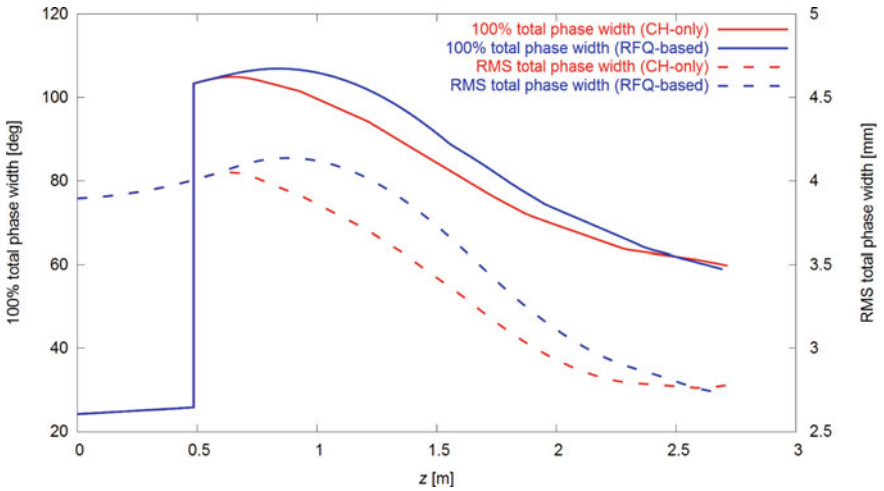

Fig. 6.13 A comparison of the phase width evolutions between the two solutions

Table 6.4 Comparison between the CH-only solution and the RFQ-based solution [11]

Parameter	CH-only	RFQ-based
f (MHz)	704.4	704.4
Number of cavities	4 NC CHs	1 RFQ + 1 NC CH
$W_{\text{in}}/W_{\text{out}}$ (MeV)	16.6/17.0	16.6/16.9
$\varepsilon_{x,\text{ in, n, rms}}$ (π mm mrad)	0.249	0.249
$\varepsilon_{y,\text{ in, n, rms}}$ (π mm mrad)	0.254	0.254
$\varepsilon_{\text{l, in, n, rms}}$ (π keV ns)	0.707	0.707
$\Delta\varepsilon_x$ (%)	0.51	0.06
$\Delta\varepsilon_y$ (%)	0.52	0.21
$\Delta\varepsilon_{\text{l}}$ (%)	2.48	5.57
Total layout length L_{layout} (m)	2.71	2.69

6.4 Error Studies

Based on the three settings defined in Table 6.5, systematic error studies have been carried out for both solutions. The following different kinds of errors have been included:

- Transverse offsets of the input beam with respect to (w.r.t.) the ideal beam axis (IBOF).
- Roll-pitch-yaw rotations of the input beam w.r.t. the ideal beam axis (IBRO).
- Transverse offsets of the magnetic lenses w.r.t. the ideal beam axis (LOFF).
- Roll-pitch-yaw rotations of the magnetic lenses w.r.t. the ideal beam axis (LROT).
- Transverse offsets of the tanks w.r.t. the ideal beam axis (TOFF).

Table 6.5 Settings of the ranges for generating random errors

Error type	Error range setting for Batch 1	Error range setting for Batch 2	Error range setting for Batch 3
IBOF (mm)	±0.2	±0.3	±0.4
IBRO (mrad)	±2.0	±3.0	±4.0
LOFF (mm)	±0.2	±0.3	±0.4
LROT (mrad)	±2.0	±3.0	±4.0
TOFF (mm)	±0.2	±0.3	±0.4
TROT (mrad)	±2.0	±3.0	±4.0
VERR (%)	±2.0	±3.0	±4.0
PERR (°)	±2.0	±3.0	±4.0

- Roll-pitch-yaw rotations of the tanks w.r.t. the ideal beam axis (TROT).
- Voltage amplitude errors for the tanks (VERR).
- Phase errors for the tanks (PERR).

For each solution, three batches of error studies have been performed. Every batch includes 1040 runs with randomly generated and mixed errors. From Batch 1 to Batch 3, the error ranges are gradually enlarged. For an easy description of the six batches, each batch is named by a four-character code, e.g., S1B1 which means "Solution 1 (CH-only), Batch 1" and S2B2 which means "Solution 2 (RFQ-based), Batch 2".

The statistics results of the beam transmission efficiency, T, for the six batches are summarized in Table 6.6. In the table, $T_{\max}$ and $T_{\min}$ are the highest and lowest transmission for each batch, respectively, while $N_{\text{runs, } T\geq 99\%}$, $N_{\text{runs, } 90\%\leq T<99\%}$, and $N_{\text{runs, } T<90\%}$ are the ratio of the runs in a batch with T higher than 99%, between 90 and 99%, and lower than 90% respectively. It can be seen that the RFQ-based solution shows better robustness against errors than the CH-only solution. With the Batch-1 setting, 0.1% of the CH-only runs have <5% beam losses and all RFQ-based runs have 100% of beam transmission. With the Batch-2 setting, the CH-only solution starts to have runs with obvious beam losses, while only 0.1% of the RFQ-based runs have <2% beam losses. With the Batch-3 setting, two of 1040 CH-only runs lost all particles, but 96.25% of RFQ-based runs still have $T \geq 99\%$.

In Fig. 6.14, the beam transmission efficiency values of the Batch-3 runs are visualized for both solutions. Up to now, no orbit correction has been applied. For the CH-only solution, >30% of runs have >1% beam losses and the lowest transmission is 0%, while for the RFQ-based solution, <4% of runs have >1% beam losses and the lowest transmission is >34%. It can be seen again that the RFQ-based solution has a much larger tolerance to the errors than the CH-only solution.

In addition, the so-called additional emittance growth $\delta\varepsilon$, defined in Eq. (6.2), has been compared for the six batches.

$$\delta\varepsilon = \frac{\varepsilon_{\text{out}}^{\text{with errors}} - \varepsilon_{\text{out}}^{\text{without errors}}}{\varepsilon_{\text{in}}} \tag{6.2}$$

Table 6.6 An overview of the beam transmission efficiency values for the six batches*

	S1B1	S1B2	S1B3	S2B1	S2B2	S2B3
T_{max} (%)	100	100	100	100	100	100
T_{min} (%)	95.25	10.67	0	100	98.46	34.07
$N_{runs,\ T\geq 99\%}$ (%)	99.9	89.82	69.93	100	99.9	96.25
$N_{runs,\ 90\%\leq T<99\%}$ (%)	0.1	6.15	12.01	0	0.1	2.69
$N_{runs,\ T<90\%}$ (%)	0	4.03	18.06	0	0	1.06

*: S1B1 means "Solution 1 (CH-only), Batch 1", S2B2 means "Solution 2 (RFQ-based), Batch 2", and so on for the other batch codes

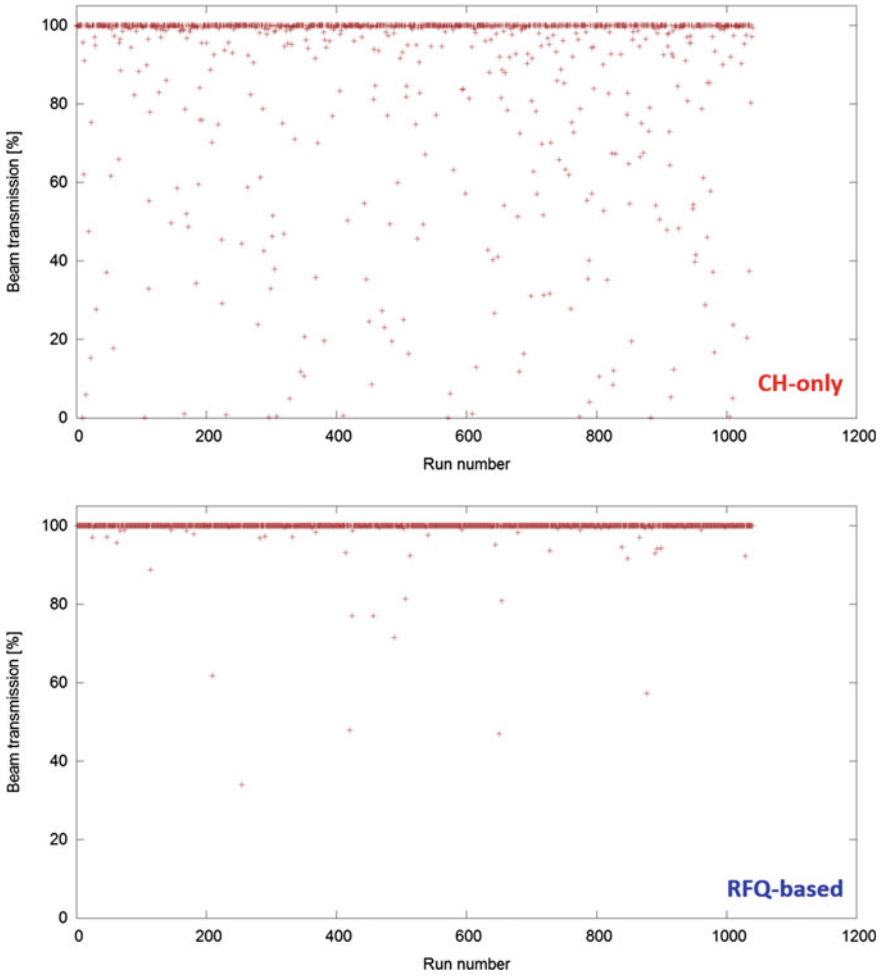

Fig. 6.14 Beam transmission efficiency as a function of the run number for Batch 3 of the CH-only solution (top) and Batch 3 of the RFQ-based solution (bottom), respectively

Table 6.7 An overview of the additional emittance growths for the six batches*

	S1B1	S1B2	S1B3	S2B1	S2B2	S2B3
$\delta\varepsilon_{x,\,\max}$ (%)	0.54	0.72	0.93	0.02	0.03	2.83
$\delta\varepsilon_{x,\,\min}$ (%)	−5.11	−52.40	−71.63	−0.18	−4.04	−53.98
$\delta\varepsilon_{y,\,\max}$ (%)	0.62	2.99	3.32	0.03	0.26	4.43
$\delta\varepsilon_{y,\,\min}$ (%)	−0.96	−44.29	−72.80	−0.07	−0.48	−34.60
$\delta\varepsilon_{z,\,\max}$ (%)	1.17	1.98	62.48	0.82	2.42	5.32
$\delta\varepsilon_{z,\,\min}$ (%)	−0.41	−6.56	−8.99	−0.42	−0.62	−5.60
$N_{\text{runs},\,\lvert\delta\varepsilon_x\rvert>1\%}$ (%)	0.19	9.32	27.19	0	0.38	4.52
$N_{\text{runs},\,\lvert\delta\varepsilon_y\rvert>1\%}$ (%)	0	6.69	25.46	0	0	3.26
$N_{\text{runs},\,\lvert\delta\varepsilon_z\rvert>1\%}$ (%)	1.06	11.04	28.43	0	2.02	9.90

*: S1B1 means "Solution 1 (CH-only), Batch 1", S2B2 means "Solution 2 (RFQ-based), Batch 2", and so on for the other batch codes

For each batch, the maximum and minimum $\delta\varepsilon$ in all three planes are listed in Table 6.7. Except a few Batch-3 runs of the CH-only solution have large positive additional emittance growths in the longitudinal plane, the $\delta\varepsilon$ values for all other runs are small or negative. The large $|\delta\varepsilon_{\min}|$ values in the transverse planes for some batches are due to beam losses. Furthermore, the ratio of the runs with $|\delta\varepsilon| > 1\%$ are also calculated for all batches and listed in the table. It can be seen that the $\delta\varepsilon$ values of most runs for the RFQ-based solution are within the range of $\pm 1\%$.

Figure 6.15 plots the output emittances of all Batch-3 runs as a function of the run number for both solutions. It again clearly shows that with the Batch-3 setting the RFQ-based solution is much less sensitive to the errors than the CH-only solution. The obviously decreased output emittances have been caused by beam losses.

As shown in Figs. 6.4 and 6.9, for both solutions, one XY-steerer pair after each triplet has been foreseen. The design field integral for the steerers is up to 0.005 Tm. Based on these steerers, orbit corrections have been performed for the worst cases of the S1B3 and S2B3 batches. Here, the worst case is defined as the run with the lowest beam transmission. When the number of runs with the lowest transmission in a batch is more than one, the run which reaches this transmission at the earliest will be taken as the worst case.

Figures 6.16 and 6.17 show the transverse and longitudinal beam envelopes before and after the orbit correction for the worst runs of S1B3 and S2B3, respectively. For a better comparison, the design envelopes (without errors) have also been shown. For both worst runs, the beam losses happened in the transverse planes (for the worst run of S1B3: losses mainly located in the CH1, CH2 and CH3 cavities; for the worst run of S2B3: losses mainly located in the RFQ).

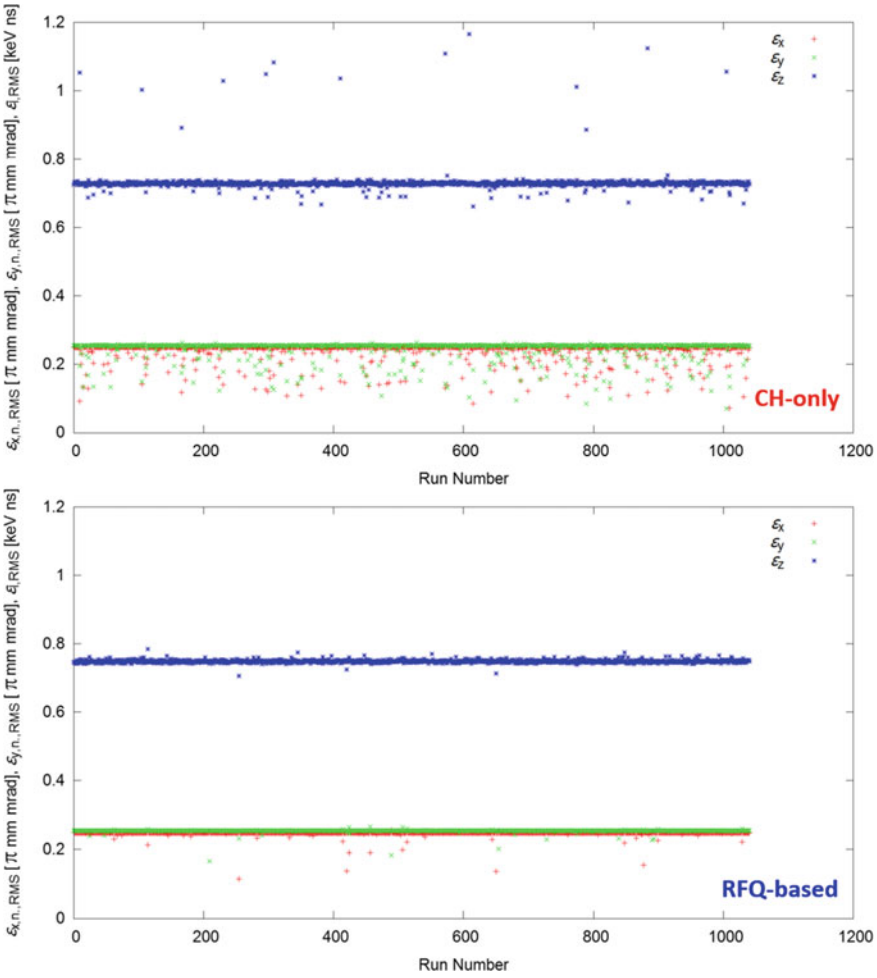

Fig. 6.15 Output emittances as a function of the run number for Batch 3 of the CH-only solution (top) and Batch 3 of the RFQ-based solution (bottom), respectively

The orbit-correction results are as follows: (1) the beam losses for both cases have disappeared; (2) the corrected longitudinal envelopes almost overlap with the nominal ones; (3) at the output, the corrected transverse beam sizes are very close to the nominal ones; and (4) the new additional emittance growths are $\delta\varepsilon_x = -0.21\%$, $\delta\varepsilon_y = 0.32\%$, $\delta\varepsilon_z = 0.43\%$ and $\delta\varepsilon_x = -0.05\%$, $\delta\varepsilon_y = 0.01\%$, $\delta\varepsilon_z = 0.33\%$ for the two runs, respectively.

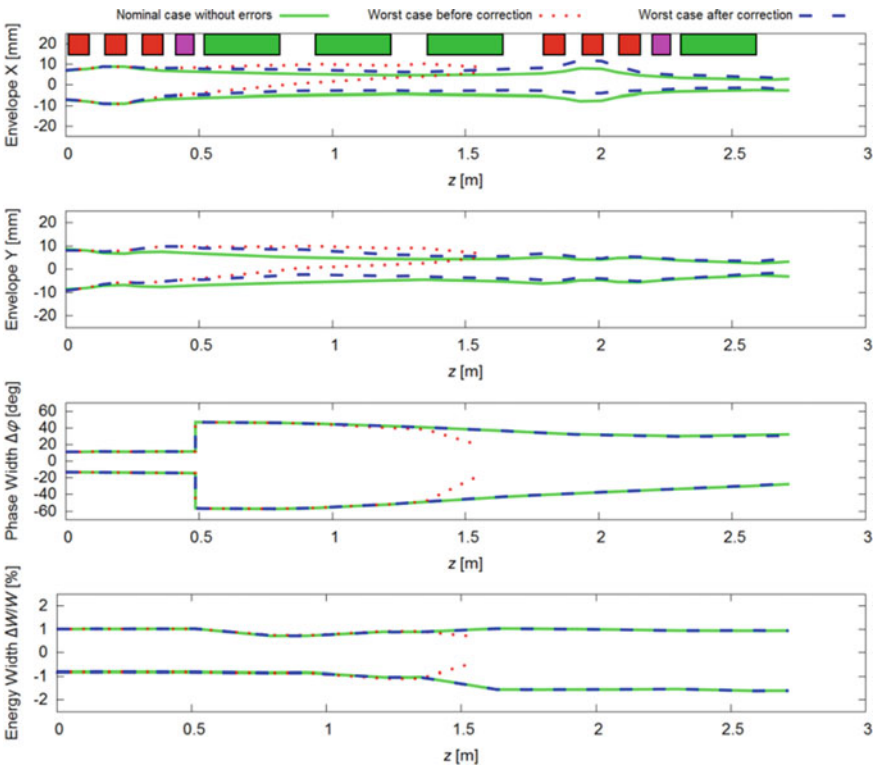

Fig. 6.16 Transverse and longitudinal beam envelopes of the worst run in S1B3 (green: nominal case without errors; red: worst case before correction; blue: worst case after correction)

6.5 Potential Applications and Future Development

Two new solutions for a frequency jump at $\beta \approx 0.2$ have been introduced. The first solution is mainly based on four 704.4 MHz NC CH cavities, while the second one is mainly using a combination of one 704.4 MHz RFQ and one 704.4 MHz NC CH.

The frequency jump sections provided by the two solutions are both only ~2.7 m long. It is worth adding such a short section, as it allows the replacement of a potentially long lower frequency section (~140 m long at 352.2 MHz in the MYRRHA example) with a more compact, higher frequency section (at 704.4 MHz in the MYRRHA example). For the same β, the cell length at 704.4 MHz is half the one at 352.2 MHz, so a 704.4 MHz cavity will have double the number of cells per cavity than a 352.2 MHz one if they have the same length. The current MYRRHA main linac has two 352.2 MHz sections [22]:

- One uses the SC single (2 cells) spoke cavities with a design $E_{\mathrm{acc}} = 7$ MV/m.
- The other uses the SC double (3 cells) spoke cavities with a design $E_{\mathrm{acc}} = 6.8$ MV/m.

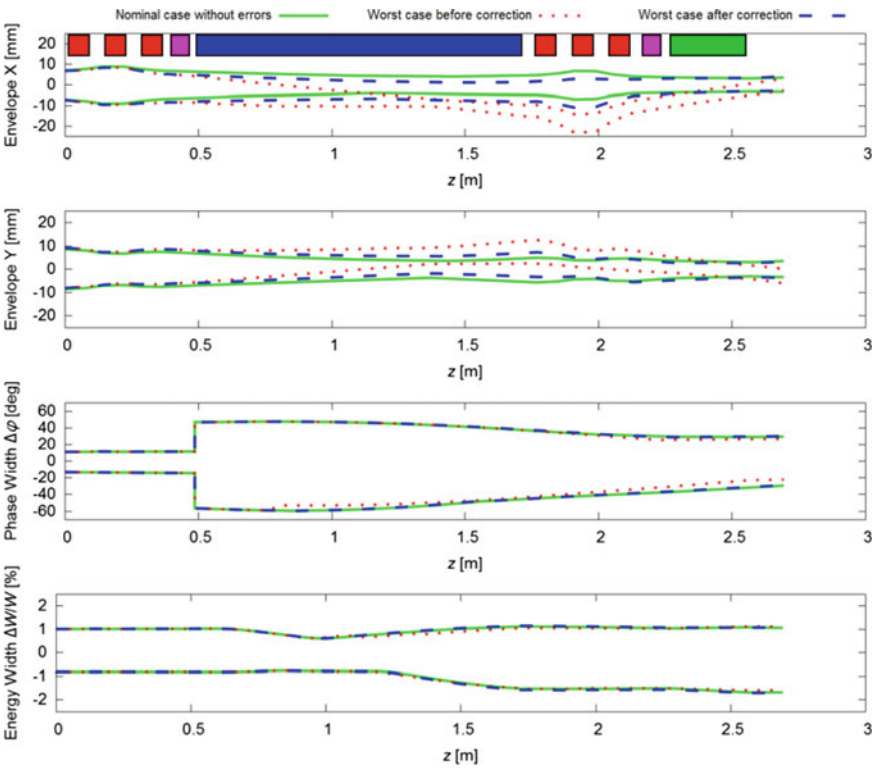

Fig. 6.17 Transverse and longitudinal beam envelopes of the worst run in S2B3 (green: nominal case without errors; red: worst case before correction; blue: worst case after correction)

In case 704.4 MHz spoke cavities with 4 or 6 cells are not available, the SC CH structure [23] can be a potential candidate to replace the two groups of 352.2 MHz spoke cavities. For this, 4-cell and 6-cell 704.4 MHz SC CH cavities could be used. The SC CH structure was originally developed as a kind of efficient multi-cell SC structure [23]. A 7-cell SC CH cavity has been built and successfully tested with beams [12]. For this study, an MWS simulation of a 7-cell, $\beta = 0.2$, SC CH cavity shows that this kind of structure also works at 704.4 MHz. Lowering the E_{acc} values from 7 MV/m and 6.8 MV/m to 5.5–6 MV/m for a larger safety margin, a calculation has been performed for the acceleration using the 4-cell and 6-cell 704.4 MHz SC CH cavities between the frequency jump section and the elliptical-cavity section. To reach the end energy values of the two original 352.2 MHz sections, 101 and 172 MeV, the required numbers of 4-cell and 6-cell SC CH cavities are 46 and 14, respectively. For both sections, the number of required cavities is reduced by ~25% (in the original design, 60 and 18 cavities were adopted, respectively [22]). Accordingly, less magnets and beam diagnostic elements will be needed. This shows the efficiency of the proposed frequency jump solutions.

The two frequency jump solutions have very similar beam performance at their nominal settings, e.g., in terms of beam transmission, beam envelopes, and the evolution of the emittances. Both longitudinal output distributions have a half phase width of ~30° and a half energy width of 1.3%, which are also within the longitudinal acceptance of the current MYRRHA main linac [22] if the small energy difference is ignored.

The performed error studies have shown that: (1) by means of two XY-steerer pairs, one can avoid all losses for the worst cases of both solutions via the orbit correction; (2) the correction can restore the beam sizes as well as the emittances of the output beam close to those of the nominal cases; and (3) the RFQ-based solution is more robust in the presence of errors than the CH-only solution.

At 704.4 MHz, the cavities used by the two solutions have relatively small transverse dimensions. In view of reliable CW operation, different water-cooling concepts have been developed. The thermal calculation has shown that: (1) the temperature increases of the RFQ and CH cavities will be low enough for a reliable CW operation; and (2) at 704.4 MHz, the RFQ electrodes can be more easily cooled than the small CH drift tubes.

In short, both solutions for the frequency jump are feasible, but the RFQ-based solution can provide larger safety margins for both beam transport and heat load. Although the RFQ-based solution will be more expensive in construction and operation, it is worthy to adopt this solution, because:

- The RFQ-based solution can provide a safer and more reliable operation than the CH-only solution, which is very important for the ADS application.
- The increased costs in construction and operation will be partially and possibly completely mitigated, as the frequency jump solution will shorten the whole linac considerably.

For this frequency jump study, to ensure an extremely reliable CW operation was a high priority when developing these two solutions. For pulsed machines, higher electrode voltages will be feasible, so the beam bunching with the two solutions could be performed even more efficiently. Especially for the RFQ-based solution, if the bunching provided by the RFQ with higher electrode voltage is sufficient, one can have a pure RFQ solution for the frequency jump. For example, spallation neutron source applications with a duty cycle of several percent can be promising candidates for the proposed frequency jump solutions.

The prototyping of the proposed 704.4 MHz cavities has been started firstly with the novel 704.4 MHz NC CH, as CERN has successfully built two 750 MHz RFQs [18, 19]. For the construction of such a “table-top” cavity, the additive manufacturing (3D-printing) technology was foreseen as an attractive choice [11]. Some recent results for one CH electrode printed with copper can be found in [24]. In parallel, the 704.4 MHz SC CH (or at cryogenic temperature like the Cold-Copper-Collider concept [25]) is being further studied as a candidate structure to cover the acceleration between the frequency jump section and the elliptical-cavity section.

References

1. R.W. Garnett, LANSCE accelerator update and future plans. IOP Conf. Ser.: J. Phys.: Conf. Ser. **1021** (2018)
2. N. Holtkamp, Status of the SNS linac: an overview, in *Proceedings of LINAC* (2004)
3. Y. Liu et al., Progresses of J-PARC linac commissioning, in *Proceedings of the 14th Annual Meeting of Particle Accelerator Society of Japan* (2017)
4. I.D. Kittelmann et al., Ionisation chamber based beam loss monitoring system for the ESS linac, in *Proceedings of IBIC* (2019)
5. H. Podlech et al., The MYRRHA-project, in *Proceedings of NAPAC* (2019)
6. C. Zhang et al., From EUROTRANS to MAX: new strategies and approaches for the injector development, in *Proceedings of IPAC* (2011)
7. T.P. Wangler, *RF Linear Accelerators* (Wiley-VCH Verlag GmbH & Co. KGaA, 2008). ISBN: 978-3-527-40680-7
8. K. Schindl, Space charge. CERN Accelerator School: Intermediate Course on Accelerator Physics (2003)
9. D. Mäder et al., Status and development of the MYRRHA injector, in *Proceedings of IPAC* (2018)
10. K. Kümpel et al., Status of the MYRRHA CH cavities, in *Proceedings of IPAC* (2018)
11. C. Zhang, D. Koser, N. Petry, H. Podlech, E. Tanke, Frequency jump using 704.4 MHz radio-frequency quadrupole and cross-bar H-type drift tube linear accelerators. Phys. Rev. Accel. Beams **24**, 040101 (2021)
12. W. Barth et al., First heavy ion beam tests with a superconducting multigap CH cavity. Phys. Rev. Accel. Beams **21**, 020102 (2018)
13. N.F. Petry et al., Test of a high power room temperature CH DTL cavity, in *Proceedings of IPAC* (2017)
14. https://github.com/dynac-source/dynac-source
15. D.D. Armstrong, W.D. Cornelius, F.O. Purser, R.A. Jameson, T.P. Wangler, RFQ development at Los Alamos. LANL report no. LA-UR-84-498 (1984)
16. R.A. Jameson, Introduction to RFQ session, in *Proceedings of LINAC* (1984)
17. L.M. Young, Tuning and stabilization of RFQ's, in *Proceedings of LINAC* (1990)
18. M. Vretenar et al., High-frequency compact RFQs for medical and industrial applications, in *Proceedings of LINAC* (2016)
19. H.W. Pommerenke, V. Bencini, A. Grudiev, A.M. Lombardi, S. Mathot, E. Montesinos, M. Timmins, U. van Rienen, M. Vretenar, RF design studies on the 750 MHz radio frequency quadrupole linac for proton-induced X-ray emission analysis. Phys. Rev. Accel. Beams **22**, 052003 (2019)
20. H. Podlech et al., Design of the MYRRHA RFQ and associated short test section. MAX project deliverable no. 2.4 (2014)
21. M. Vossberg, C. Lenz, H. Podlech, A. Schempp, A. Bechtold, RF measurement during CW operation of an RFQ prototype, in *Proceedings of IPAC* (2013)
22. F. Bouly, M. Baylac, A. Gatera, D. Uriot, Superconducting linac design upgrade in view of the 100 MeV MYRRHA phase I, in *Proceedings of IPAC* (2019)
23. H. Podlech et al., Superconducting CH structure. Phys. Rev. ST Accel. Beams **10**, 080101 (2007)
24. C. Zhang, M. Heilmann, A. Japs, C. Will, H. Podlech, Development of a 704.4 MHz CH cavity using additive manufacturing, in *Proceedings of IPAC* (2023)
25. M. Nasr, E. Nanni, M. Breidenbach, S. Weathersby, M. Oriunno, S. Tantawi, Experimental demonstration of particle acceleration with normal conducting accelerating structure at cryogenic temperature. Phys. Rev. Accel. Beams **24**, 093201 (2021)